Extreme Jet Bends in Nearby Radio Galaxies

Josephine Rawes

A thesis submitted to the University of Bristol
in accordance with the requirements of the degree of
Doctor of Philosophy
in the Faculty of Science

Department of Physics,
H.H. Wills Physics Laboratory,
Tyndall Avenue,
Bristol,
BS8 1TL

March 2017

$\sim 60,000$ words

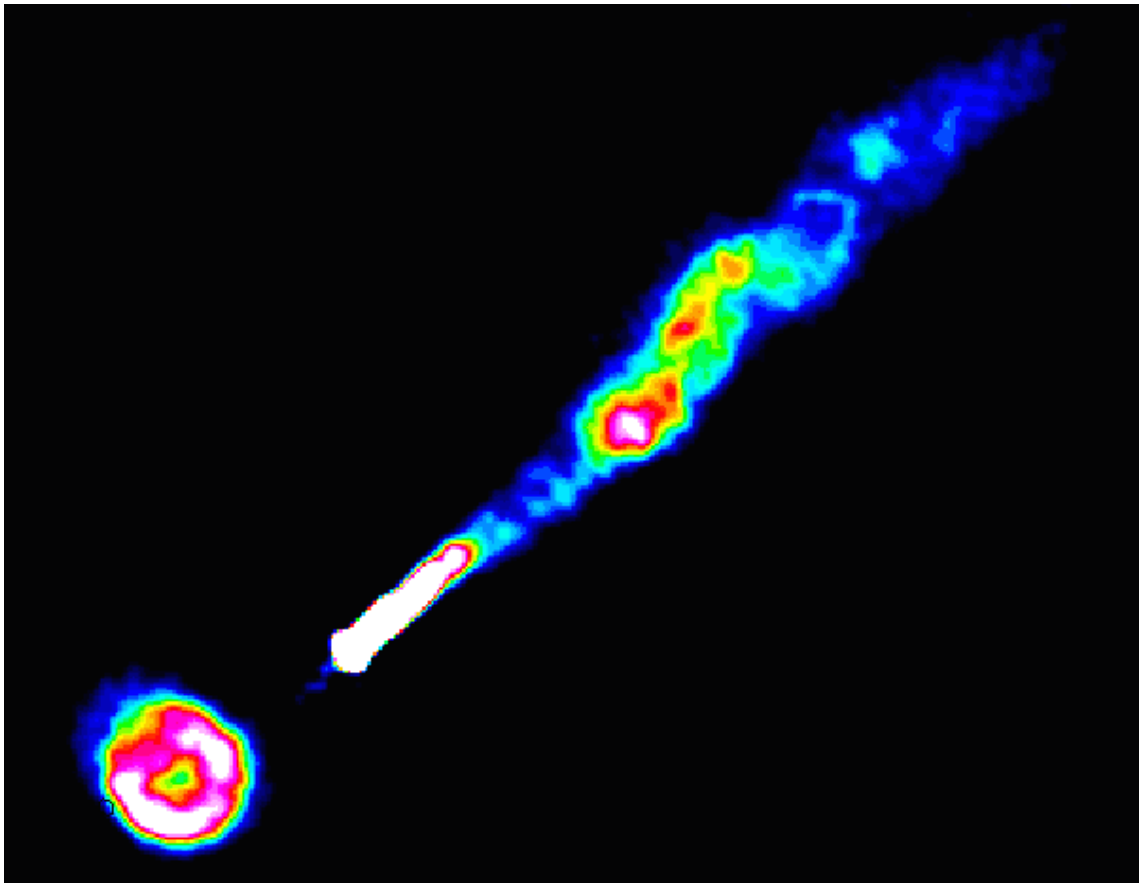

Figure 1: The swirl-like structure in NGC 6109 at 2.99 GHz (see chapter 5).

Abstract

In this thesis, I use radio observations to examine large scale jet bends in nearby radio galaxies. I complement the radio data with optical and X-ray observations in order to create a detailed picture of the host environment of these sources and explain the unusual jet structures.

I present a detailed radio study of the low-power FR I-type radio galaxy NGC 7385, using archived and new VLA observations. I find evidence for a 180° jet bend, and interpret this to be due to a jet-cloud interaction causing disruption of the path of the jet. This cloud is visible in HST images of the galaxy, and I discuss the possible origins and excitation mechanisms for this cloud. I examine the rotation measure structure in the interacting region, and suggest that the estimated magnetic field is due to entrainment of the cloud into the boundary layers of the radio jet. I also report the discovery of optical and X-ray emission from the brighter radio jet using data from HST and *Chandra*. The jet has a projected length of 5 kpc and a similar morphology to other known optical jets in low-power radio galaxies. The spectral energy distribution from radio to X-ray shows the synchrotron process to be responsible for the emission at all wavelengths.

The radio galaxy NGC 6109 is a second source exhibiting a large scale jet bend in the form of a remarkable swirl-like structure. I present an in-depth analysis of the radio emission associated with this galaxy and I discuss the possible mechanisms which could lead to such a morphology. I use polarisation studies to investigate the magnetic field structure and carry out rotation measure synthesis to explore possible interactions between the jet and the external environment. I find no evidence for optical features associated with the radio emission or any X-ray structure beyond the core. I suggest that an interaction with magnetised plasma could produce the observed jet bend, although jet precession on a kpc scale is also viable. Low frequency radio observations (e.g. LOFAR) are required to constrain these mechanisms further.

Observations of such extreme jet distortions are rare and offer the chance to examine

how emission from radio galaxies can be influenced by the external environment and in turn how local IGM material is disrupted by collisions with radio jets. I discuss a few jet distortions observed in quasars and CSS sources and present observations of NGC 7016, which shows a similar jet bend to NGC 6109. I draw parallels between the two sources, and suggest that such swirl-like features could be produced as a result of interactions with trails of radio plasma. Finally, I discuss the prevalence of large scale jet bends within radio galaxy samples and give details of future surveys and instruments which should constrain the jet dynamics within NGC 7385 and NGC 6109 and have the potential to reveal a large number of similar sources in the radio sky.

Contents

List of Figures

List of Tables

Acknowledgments

There are many people who have helped and supported me throughout my PhD studies. Firstly I am hugely grateful to my supervisors, Mark Birkinshaw and Diana Worrall, for their continuous support and insightful discussions and suggestions. Their guidance and patience made my graduate experience both enjoyable and rewarding. I would also like to thank Mark for his helpful and thorough editing of all my manuscripts, and for encouraging me to pursue a career in research.

I am grateful to my friends and family, for their encouragement and kindness over the last few years. In particular I thank Georgie for her relentless optimism, my parents for helping me through university and teaching me how to persevere and Sophie for her life-long friendship and support.

The work presented here has made use of NASA's Astrophysics Data System (ADS), the NASA/IPAC Extragalatic Database (NED), the High Energy Astrophysics Science Archive Research Center (HEASARC), provided by NASA's Goddard Space Flight Center, the *Chandra* Data Archive, part of the Chandra X-Ray Observatory Science Center (CXC) which is operated for NASA by the Smithsonian Astrophysical Observatory, the *XMM-Newton* Science Archive, operated by the European Space Agency, and the National Radio Astronomy Observatory Very Large Array (VLA) electronic archive. The National Radio Astronomy Observatory is a facility of the National Science Foundation operated under cooperative agreement by Associated Universities, Inc.

Declaration

I declare that the work in this dissertation was carried out in accordance with the Regulations of the University of Bristol. This work is original except where indicated by special reference in the text and no part of the dissertation has been submitted for any other degree. Any views expressed in the dissertation are those of the author and in no way represent those of the University of Bristol. The dissertation has not been presented to any other university for examination either in the United Kingdom or overseas.

Josephine Rawes
March 2017

Chapter 1

Introduction

1.1 Active Galaxies

In the majority of galaxies, the intensity of the light peaks at visible wavelengths, comes mainly from stars and is evenly distributed throughout the galaxy. For a small number of galaxies, the light comes mainly from gas and the intensity peaks at radio wavelengths. These so-called radio loud 'active galaxies' have a bright compact, central region from which we observe substantial non-thermal emission. This core is referred to as the 'active galactic nucleus' (AGN).

The first class of AGN was discovered by Carl Seyfert in 1943. Seyfert reported the discovery of galaxies with bright, point-like nuclei and broader emission lines than expected for the usual motion of stars within a galaxy. Such high velocities implied the presence of material orbiting around a large compact mass. The physics of these objects remained poorly understood until Woltjer (1959) noted that these AGN have exceptionally large luminosities (of order comparable to the sum of the stellar luminosity of the host galaxy). Theories including supernova chain reactions and thermonuclear emission from a supermassive star (e.g. Hoyle and Fowler, 1967) were invoked to explain the phenomenal power of AGN. It is widely believed today however, that AGN are powered by accretion onto a central supermassive black hole. In this process material falls under the influence of gravity towards a central compact object, loses angular momentum, and through viscous forces it radiates a fraction of its energy away.

AGN may be subdivided according to, for example, the properties of their optical emission lines, their radio activity and their brightness. AGN radiate over a range of wavelengths, but may be particularly bright over a specific portion of the electromagnetic

spectrum. The widely accepted 'Unified model' (e.g. Urry and Padovani, 1995) is shown in Figure 1.1 and forms a basic framework for explaining the diversity of AGN characteristics observed. Within this framework, a central black hole is surrounded by an accretion disk. This disk produces UV light and X-rays and is orbited by fast moving line-emitting clouds and an obscuring torus. The accretion disk can cause the formation of jets, due to the strong magnetic field that arises from the hot material in the disk. Particles (some combination of electrons and positrons, or electrons and protons) travel from these jets at relativistic speeds and are visible at various wavelengths, dependent on the amount of material they eject and their temperature. The whole disk is at most a few parsec across, so direct observations can only be carried out via optical interferometry if the disk is unobscured (e.g. by the future VLT instrument GRAVITY, Eisenhauer et al., 2009). X-ray spectra and polarisation detection can give a detailed account of conditions in this compact region: the radiation is thermal thus the continuum spectra should be able to provide a measure of the temperature (although this is far from uniform over the disk). The dusty torus can obscure the view of the accretion disk and the clouds and the angle at which the torus is viewed by the observer determines the AGN classification.

Optical spectral lines are observed from AGN, predominantly from a small number of atomic species (e.g. H, He, C, N, O), as seen in H II regions. An outstanding characteristic of these optical lines is extreme broadening, and this is accounted for by the rotation and turbulent motion close to the disk. For many AGN the lines show a spectrum with two distinct components; one with line widths corresponding to velocities $\approx 10^5$ km s^{-1} (known as a broad-line region, or BLR), and the other with widths corresponding to a few hundred km s^{-1} (narrow line region, or NLR). It has been proposed that the BLR is the accretion disk itself (e.g. Collin-Souffrin, 1987; Collin-Souffrin and Dumont, 1990), however the photoionisation models computed by these authors could not reproduce the observed high-ionisation lines. Emmering et al. (1992) suggested that the BLR consisted of condensations in a hydromagnetic accretion-disk wind, and extensions of this model explain the acceleration of the wind in terms of radiation pressure, magnetic pressure or a combination of the two (e.g. Murray and Chiang, 1997; Everett, 2003). The NLR is a more extended region, above the disk. This means that when the AGN is seen from the side, the torus obscures the radiation from the BLR, while the NLR is still observable. The existence of the torus is largely deduced from observations of optical spectra, however excess infrared radiation from AGN also points to the presence of a dust cloud. Direct observation of the torus in a typical AGN requires an angular resolution ≈ 1 milliarcsec.

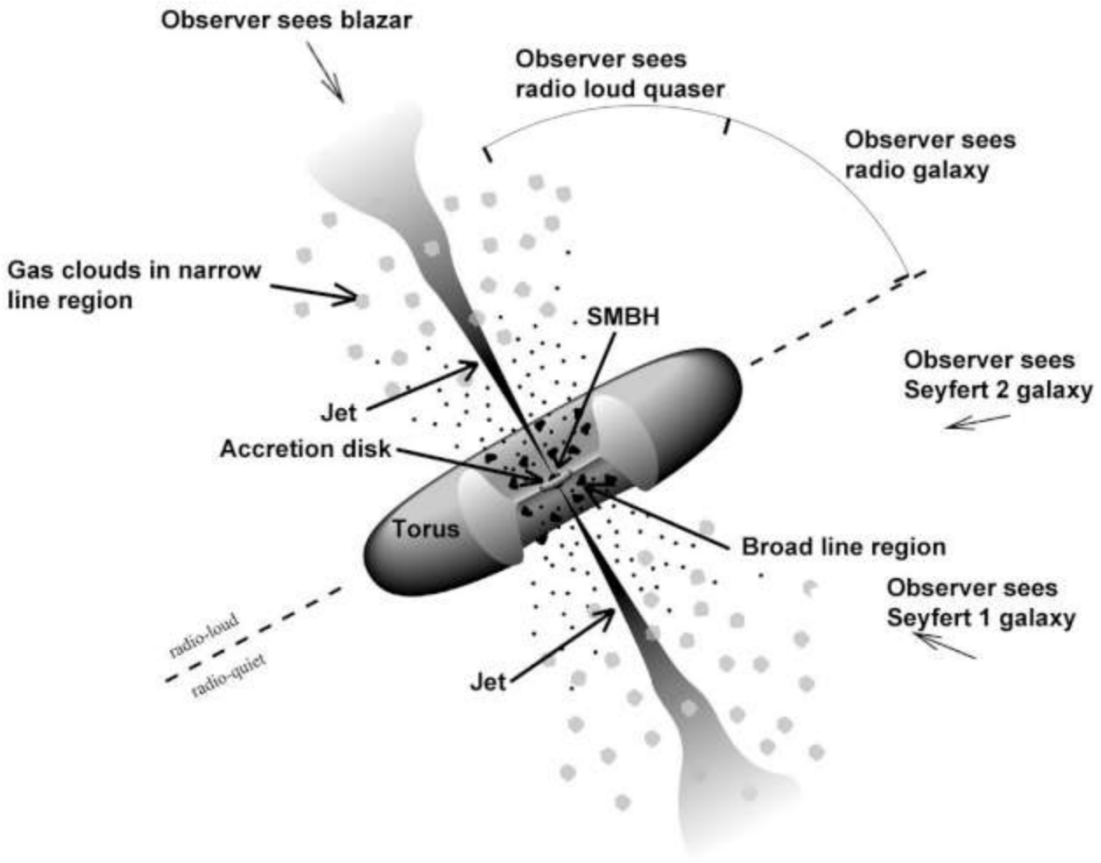

Figure 1.1: Schematic illustration of the standard AGN-unification model reproduced from Urry and Padovani (1995). A central accreting black hole is surrounded by fast moving line-emitting clouds and an obscuring torus. Classification of the different types of AGN discussed in the text and labelled here is dependent on the viewing angle of the observer and jet beaming effects.

Sources radiating strongly at radio wavelengths are subclassified as 'radio-loud', compared to sources with weak radio emission deemed 'radio quiet'. An AGN is described as radio-loud if $L_{5\,\mathrm{GHz}}/L_B > 10$, where L_B is the rest-frame B-band luminosity (Visnovsky et al., 1992). Characteristics of the 4 main types of AGN include :

1. Seyfert galaxies : These are spiral galaxies with extremely bright nuclei. The luminosity of Seyfert galaxies ranges from 0.1 to 10 times the luminosity of our galaxy. The basic classification scheme proposed by Seyfert (1943) was extended by Khachikian and Weedman (1974), who subdivided the population into two distinct classes based on their optical line emission properties. Type I Seyfert galaxies have broad emission lines together with narrow forbidden lines with widths of only a few hundred km s^{-1}. Type II Seyfert galaxies differ from Type I galaxies in that only the narrow emission lines are detected.

2. Quasars : Quasars are the most energetic form of AGN. They exhibit a range of host galaxy morphology and some show evidence for recent galaxy mergers. The optical spectra are similar to those of Seyfert galaxies, although they have weaker stellar absorption features. Quasars emit a significant amount of energy at UV and optical wavelengths and about 5-10% of quasars are characterised as radio loud. These radio-loud quasars emit jets from their central regions, often with an FR II-type morphology (see section 1.2.2.2).

3. Blazars : These AGN, like quasars, were first discovered as 'quasi-stellar' points of light. Blazars can vary significantly in brightness over less than a day, indicating that the jet makes a small angle to the line of sight, and the effects of relativistic beaming dominate their observed properties. Blazars can be subdivided into two classes: BL Lac objects and Optically Violent Variables. The former objects have featureless continuum spectra, are strongly polarised and rapidly variable. The latter are similar to BL Lac objects, although they occur at higher redshifts ($0.1 < z < 2$) and have strong and broad optical emission lines.

4. Radio galaxies : This class of AGN is noted for its strong radio emission. Radio galaxies are elliptical, with collimated twin jets of gas extending away from the central nucleus. The jets emit radio waves by the synchrotron process and may extend to distances exceeding 100 kpc. Radio galaxies can be subdivided into Fanaroff-Riley Type 1 (FR I) or Type 2 (FR II) in nature (Fanaroff and Riley, 1974) and their morphology and luminosity are found to be closely related (e.g. Ledlow and Owen, 1996).

This thesis is primarily concerned with radio galaxies and the morphology of the jets that emanate from the central nucleus of these AGN.

1.2 Features of Radio-Loud Galaxies

Radio galaxies exhibit a broad range of morphological structures at radio wavelengths. The most common features are discussed below, although not all are present in every radio galaxy.

1.2.1 The core

A compact radio core is detected in about 80% of radio galaxies and is usually found to coincide spatially with the optical nucleus of the galaxy. The core emits radiation over the entire electromagnetic spectrum and occupies a volume similar to that of our solar system. The strength of the nuclear optical line emission observed from these regions subdivides these objects into high-excitation radio galaxies (HERG) and low-excitation radio galaxies (LERG). The radio spectrum of a core is usually found to be flat $(\alpha \approx 0)$ at cm wavelengths. The core is the origin of the jets emitted along the polar directions; where these jets occur, the core and the jets may be regarded as continuous.

1.2.2 Jets, lobes and hotspots

Outside the core, the structure of a typical radio galaxy is determined by the interaction of energetic jets with hot diffuse gas filling and surrounding the host galaxy. AGN jets are believed to extract rotational energy from the twisting of magnetic fields in the accretion disk (Hawley and Krolik, 2006). It has also been suggested that black hole spin is directly correlated to the radio-loudness of an AGN (Fanidakis et al., 2011). Jets are composed of radiative plasma, comprising of electrons, positrons and/or protons. They can extend into the IGM on scales ranging from parsecs to hundreds of kpcs. The jets initially follow trajectories related to the structure of the core, but ultimately they are confined by an external medium through which they drive a tunnel. In this process, ambient gas must be entrained in the jets, but the main source of radiation is the population of particles that radiate after they are ejected from the core. Radio lobes can develop when the jets are stopped by the ram pressure of the diffuse gas; at this point 'hotspots' of radiation can form, from which the more diffuse lobes spread out and are left behind as the hotspots advance through the external medium. Jets are emitted along the polar directions of the core, however often only one jet is dominant. This can be explained either in terms of an intrinsic asymmetry in the core, or due to the effects of Doppler brightening. Small bright patches along a jet can sometimes be seen; these 'knots' represent turbulent interactions with the surrounding interstellar and intergalactic medium. A high degree of polarisation is found along jets which indicates the presence of well ordered magnetic fields. The magnetic field is usually found to be directed along the jet for most of its length, and becomes transverse at the hotspots or lobes where the jet culminates.

Fanaroff and Riley (1974) reported that the location of high and low surface brightness regions in the lobes and hotspots of radio galaxies are directly related to their radio luminosities. This conclusion followed observations of 57 radio galaxies and quasars from the complete 3CR catalogue (Bennett, 1962) which at 1.4 GHz or 5 GHz could be resolved into multiple (≥ 2) distinct components. Fanaroff & Riley classified this sample according to the ratio R of the distance between the regions of highest surface brightness on opposing sides of the core, to the total extent of the radio source. Sources with $R < 0.5$ were classified as FR I-type, and sources with $R > 0.5$ as FR II-type. They found that this classification system divided sources neatly by overall luminosity, with the luminosity boundary at 178 MHz given by

$$L(178\text{MHz}) < 2 \times 10^{25} \tag{1.1}$$

in units of W Hz^{-1} sr^{-1}. In addition, Owen and Ledlow (1994) observed that the transition between FR I and FR II-type radio-morphology is a function of the optical magnitude of the host galaxy. These sources exhibit different morphological properties, highlighting a direct link between the luminosity of a source and the mechanism by which energy is transported from the core and converted to radio emission in the outer parts of a galaxy.

1.2.2.1 Fanaroff-Riley Class I (FR I)

These sources have their brightest regions closest to the central core and become fainter as one approaches the outer extremities of the lobes. In these outer regions the spectra are the steepest, indicating an older population of electrons. An example of the structure of an FR I-type source is given in Figure 1.2. This is the radio galaxy 3C 31, observed with the VLA at 1.4 GHz and with 5.5 arcsec resolution (Laing et al., 2008). 3C 31 is optically identified with a dusty elliptical host galaxy at a redshift z = 0.0169. It exhibits twin jets, emanating from a bright core, which undergo a series of bends before terminating in diffuse lobes. FR I-type sources may entrain the external medium and tend to be found locally in rich environments (Wing and Blanton, 2011; Bicknell, 1995). The jets are interpreted as decelerating to subsonic speeds closer to the core than their higher luminosity counter-parts.

Resolved multi-wavelength emission from kpc scale jets in low-power FRI-type radio galaxies has been detected in the X-ray with *Chandra* (e.g. Worrall et al., 2001; Hardcastle et al., 2002), and optically for a few sources including M 87 (Biretta et al., 1999), 3C 264 (Crane et al., 1993) and 3C 15 (Martel et al., 1998). These optical counterparts

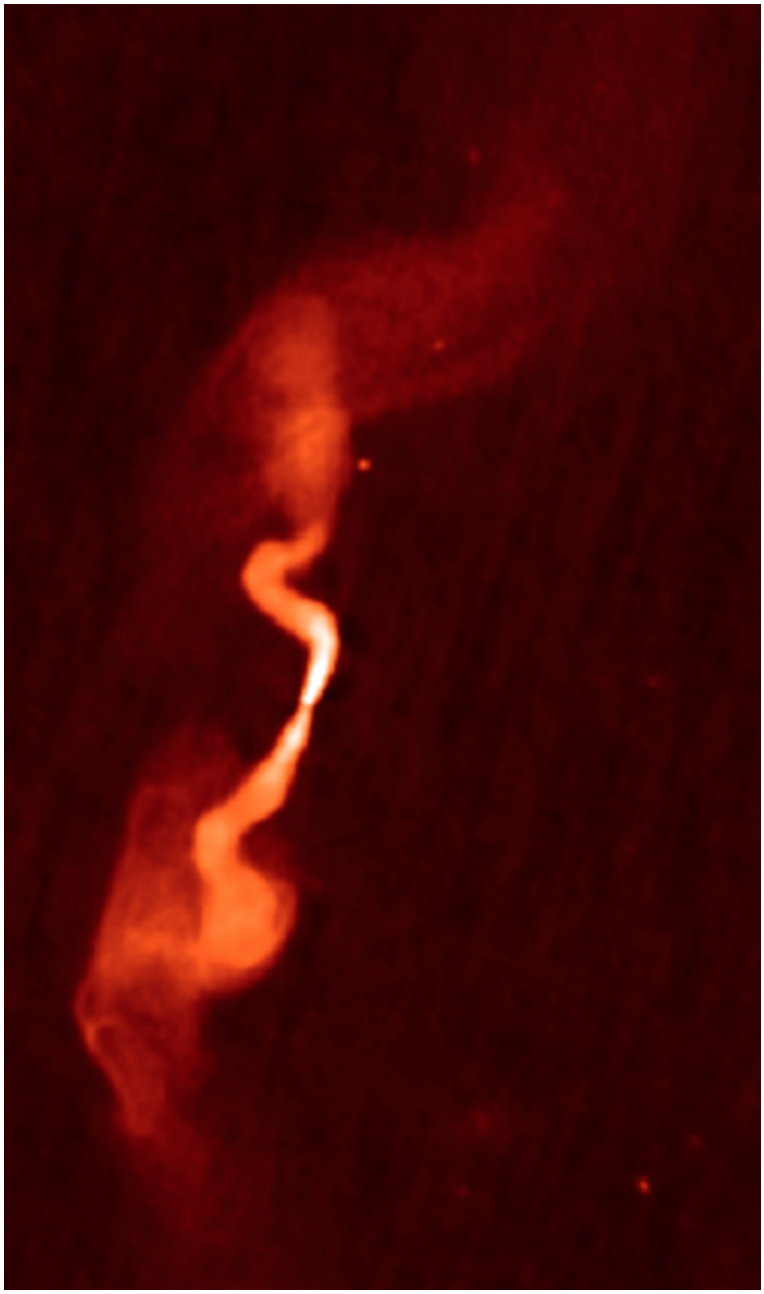

Figure 1.2: 1.4 GHz VLA image of the inner regions of the FR I-type radio galaxy 3C 31 with angular resolution 5.5 arcsec. Reproduced from Laing et al. (2008). The characteristic 'centre-brightened' morphology, twin jets and radio plumes are clearly seen.

are difficult to image due to poor contrast with starlight from the host galaxy. For the confirmed detections however, it is believed that synchrotron emission is responsible for the radio, optical and X-ray emission of these jets and that the spectrum can be described with a broken power law (e.g. Hardcastle and Croston, 2005; Evans et al., 2005).

1.2.2.2 Fanaroff-Riley Class II (FR II)

Due to the overall higher luminosity of this type of source, the cores and jets of these objects are brighter than those in FR I-type galaxies but relative to the lobes these features are much fainter. Jets are detected in less than 10% of these luminous radio galaxies, but in nearly all quasars. The jets have small opening angles and a magnetic field predominantly parallel to the jet axis. An example of an FR II-type object is given in Figure 1.3, which shows a VLA map of the radio quasar 3C 47 (Leahy et al., 1996). This source has a one-sided jet, and a bright hotspot on the same side as the jet. The lobe on the opposite side does not qualify as a hotspot, according to the criteria of Bridle et al. (1994). The kpc scale jets are distinctly more collimated and symmetric than those of FRI-type radio galaxies. FR II-type sources are thought to transport their energy more effectively along their jets, inflating radio lobes with internal pressure that is equal to, or exceeds that of the external medium (Scheuer, 1974).

FR II-type sources are generally associated with normal giant elliptical galaxies and their environments show no evidence for enhanced galaxy clustering (Owen and Laing, 1989). Since the nature of the host galaxies and the environments of the FR I and FR II-type sources are not the same, it is possible that they may not related to each other through an evolutionary sequence but in fact be intrinsically different types of source.

1.2.2.3 FRI/II boundary sources

Worrall and Birkinshaw (2017) estimate that half of the total jet power in the local Universe should be from sources with radio powers within a factor of three of 3×10^{25} W Hz^{-1} at 1.4 GHz. Sources within this range show morphologies between FR I and FR II-type, and are defined by Worrall and Birkinshaw (2017) as FRI/II boundary sources. Within the 3CRR catalogue (Laing et al., 1983) (see chapter 6 for further details) there are 16 FRI/II boundary sources at $z < 0.1$, and a significant amount of this subsample (Birkinshaw et al., in preparation) show jet-gas interactions (e.g. 3C 35, Mannering et al., 2013; 3C 305, Hardcastle et al., 2012; 3C 310, Kraft et al., 2012). The environments of these boundary sources are investigated to assess whether they dominate radio galaxy

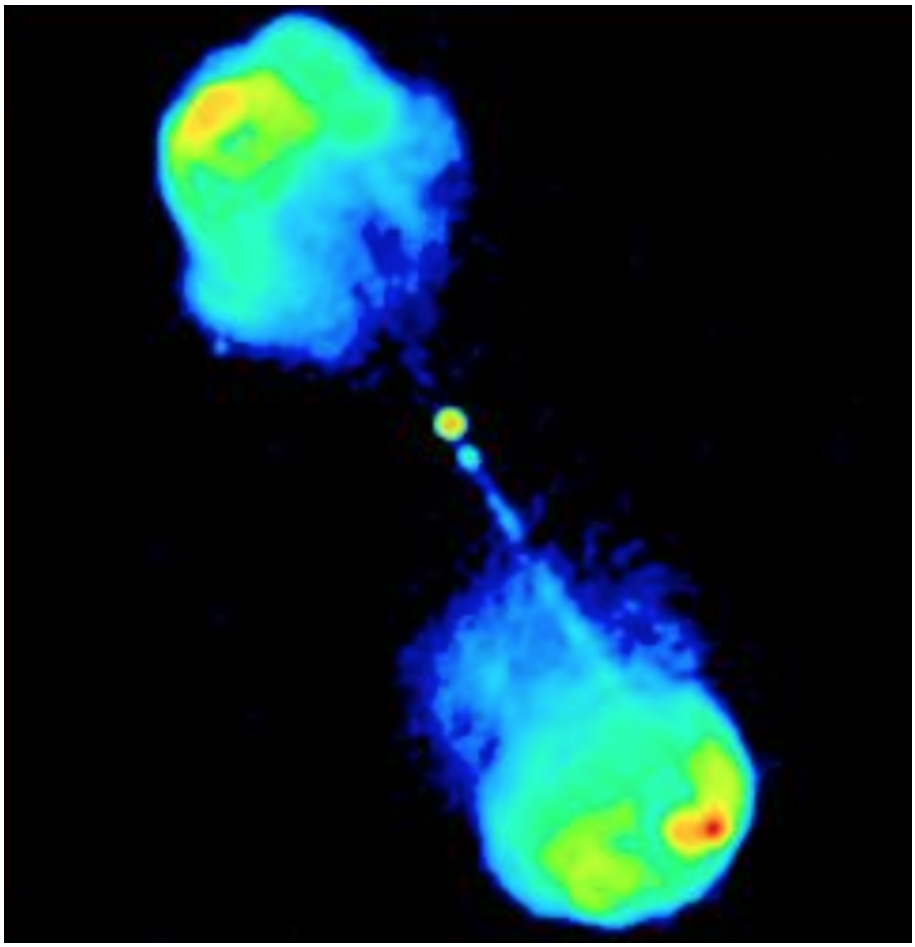

Figure 1.3: 1.65 GHz VLA image of the FR II-type radio quasar 3C 47 with angular resolution 1.0 arcsec. Reproduced from Leahy et al 1996. The map clearly shows the edge-brightened morphology, with twin jets and radio hotspots.

heating in the local Universe; the next generation of X-ray telescopes should help with these studies.

1.2.2.4 Recurrent radio activity

An important question in studies of AGN is whether their nuclear activity is episodic in nature. Recurrent AGN activity could have significant implications within feedback processes and the evolution of galaxies. Saikia et al. (2010) give a review of the increasing evidence for recurrent activity, both in X-ray and radio observations, although only a handful of cases have been confirmed. A signature of episodic activity is seen in radio-loud objects where multiple distinct lobes are observed. These sources are referred to as double-double radio galaxies (DDRG's), although Brocksopp et al. (2007) suggest that the galaxy B 0925+420 may exhibit three cycles of activity.

1.2.3 The spectra of AGN

The spectra of AGN can extend over the entire electromagnetic spectrum. Within this range radiation is emitted by a variety of processes, some thermal and some non-thermal. The contributions from these processes depend on the orientation of the AGN and the jet component may be affected by Doppler boosting. Despite these complications, the overall spectrum can be roughly represented by a simple power law $s = \nu^{\alpha}$ where $\alpha \approx -1$. Often, there is a 'blue bump' in the blue part of the spectrum, attributed to radiation from the accretion disk. At high frequencies, there is an additional component from inverse Compton effects (discussed below). The radio wavelengths are the most variable part of the spectrum. When a compact core can be distinguished, the spectrum is flat ($\alpha \approx 0$) and this appears to be the combination of several opaque sources with a range of optical depths. The jets and lobes are 'optically thin', with $\alpha \approx -0.7$. The outer parts of the lobes have steeper spectra than the jets, as expected if the jets are feeding high energy particles into the lobes.

1.2.4 Feedback from jets

The role of AGN feedback in galaxy formation is one of the main debated problems in astrophysics. This feedback takes place through an interaction between the energy and radiation generated by accretion onto the black hole and the gas in the host galaxy. Jets can strip the galaxy of interstellar gas, terminate star formation and through lack of fuel

for accretion, terminate the AGN. Observational evidence for AGN feedback is found in Brightest Cluster Galaxies (BCGs) in cool core clusters of galaxies. Without energy input through kinetic feedback, many BCGs would be yet more massive and appear as brilliant, giant starbursts. AGN feedback also features in many theoretical, numerical and semi-analytic simulations of galaxy growth and evolution (e.g. Kauffmann and Haehnelt, 2000; Croton, 2006; Hopkins and Hernquist, 2006). Radio galaxies are thought to provide the strongest feedback and therefore affect structure formation on the largest range of mass scales: quantitative estimates based on the energetics of cavities in dense X-ray emitting gas show that the energy provided by radio galaxies can easily reverse gas in falls on scales of hundreds of kpc. Although sufficient energy input is available from jets, neither the way in which feedback is regulated nor the processes which heat the IGM are fully understood. To resolve this, it is necessary to quantify the mass, momentum and energy inputs from jets and explore how they interact with their surroundings. Studies of individual AGN which show significant interactions between jets and the host environment could help to address these issues.

1.3 Radiative Processes

The propagation of radio waves is governed by the laws of radiative transfer (see Rybicki and Lightman, 2008 for an in depth discussion). If the characteristics of the emitted radiation do not depend on the temperature of the source and cannot be represented by the spectrum of thermal bremsstrahlung or black body radiation, then the radiation is referred to as 'non-thermal'. In astronomy, there are three common types of non-thermal radiation :

1. Synchrotron emission : generated by charged particles spiralling around magnetic field lines at relativistic speeds. The non-relativistic equivalent is cyclotron radiation.

2. Compton scattering : the process in which electrons are deflected by high energy photons, which impart some of their energy.

3. Stimulated emission : where electrons in a metastable state decay to the ground state after passing a photon with the same energy as the difference between the two levels.

These non-thermal processes describe the light emitted by astrophysical objects in the Universe, such as supernovas, pulsars and radio galaxies. The processes important to the interpretation of sources studied in this thesis are the synchrotron mechanism and inverse Compton emission, and these are discussed below.

1.3.1 Synchrotron radiation

High energy astrophysics is dominated by the emission of synchrotron radiation. This is the radiation emitted by relativistic electrons as they gyrate in a magnetic field. This process is responsible for the radio emission that we detect from the jets, lobes and hotspots of AGN. It is not limited to radio wavelengths, as it can also explain the non-thermal optical and X-ray emission observed in the Crab Nebula.

The equation of motion for a single relativistic particle of rest mass m_0, charge q and Lorentz factor $\gamma = (1 - v^2/c^2)^{-1/2}$ in a uniform magnetic field **B** is given by

$$\frac{d}{dt}(\gamma m_0 \mathbf{v}) = q(\mathbf{v} \times \mathbf{B}) \tag{1.2}$$

The magnetic field does no work on the particle because the force is always perpendicular to the velocity vector **v**. The particle therefore will travel with a helical trajectory, with uniform circular motion perpendicular to **B**.

The left hand side of equation 1.2 can be expanded as follows:

$$m_0 \frac{d}{dt}(\gamma \mathbf{v}) = m_0 \gamma \frac{d\mathbf{v}}{dt} + m_0 \gamma^3 \mathbf{v} \frac{(\mathbf{v} \cdot \mathbf{a})}{c^2} \tag{1.3}$$

In a magnetic field, the acceleration vector $\mathbf{a} = d\mathbf{v}/dt$ is always perpendicular to **v** and consequently $\mathbf{v} \cdot \mathbf{a} = 0$. As a result,

$$\gamma m_0 \frac{d\mathbf{v}}{dt} = qvB \sin\theta \tag{1.4}$$

where the pitch angle θ is the angle between the direction of motion and the magnetic field. The motion of the particle is a spiral path with a constant pitch angle; this consists of a constant velocity along the direction of **B** and circular motion with radius r about it. This radius r is the gyroradius of the particle, and the angular gyrofrequency of the particle in its orbit ω_g is given by

$$\omega_g = v_\perp / r = qB/\gamma m_0 \tag{1.5}$$

The corresponding gyrofrequency ν_g is

$$\nu_g = \omega_g/2\pi = qB/2\pi\gamma m_0 \tag{1.6}$$

The characteristic radius r of the electron path is found by equating equation 1.4 with the centrifugal force in the relativistic regime, such that

$$r = \frac{\gamma m_0 v_\perp}{qB} \tag{1.7}$$

The rate of loss of energy of the charged particle is determined from the relativistic generalisation of the Larmor formula, which gives the power radiated by a point charge as it accelerates,

$$-\left(\frac{dE}{dt}\right) = 2\sigma_T c\gamma^2\beta^2 u_B sin^2\theta \tag{1.8}$$

where σ_T is the Thomson cross section, and u_B is the energy density of the magnetic field ($u_B = B^2/2\mu_0$). As σ_T is inversely proportional to the square of the mass of the particle, the power emitted by a heavier particle, such as a proton, is significantly less than that of an electron.

This result applies for electrons of a specific pitch angle θ. Particles of a particular energy E, or Lorentz factor γ are expected to have an isotropic distribution of pitch angles. It is therefore necessary to work out their average energy loss rate by averaging over such a distribution $p(\theta)d\theta = 1/2\sin\theta d\theta$, giving

$$-\left(\frac{dE}{dt}\right) = 2\sigma_T c\gamma^2\beta^2 u_B \frac{1}{2}\int_0^\pi \sin^3\theta d\theta = \frac{4}{3}\sigma_T c\gamma^2\beta^2 u_B \tag{1.9}$$

1.3.1.1 Relativistic beaming

The following analysis is reproduced from Longair (2011), and constructs the typical frequency of synchrotron emission.

The spectrum of synchrotron emission is dominated by a characteristic frequency. This frequency is governed by the fraction of the orbit during which the observer receives radiation. In the frame of the electron, the emitted radiation has a characteristic dipole shape dependent on the direction of the acceleration. In the observers frame however, most of the particle's energy is beamed into a cone of opening angle ϕ, where

$$\phi \approx \gamma^{-1} \tag{1.10}$$

For an electron gyrating about a magnetic field at a pitch angle θ = 90°, it takes a length of time given by ϕ/ω_L to move through angle ϕ, in the frame of the electron. The leading t_1 and the trailing t_2 times of the pulse are related by

$$t_2 - t_1 = \frac{\phi}{\omega_L} \tag{1.11}$$

In the observers frame, these parameters become

$$t_1' = t_1 + \frac{D + \delta D}{c} t_2' = t_2 + \frac{D}{c} \tag{1.12}$$

where D is the distance between the trailing edge of the pulse and the observer and δD is the distance the pulse has travelled during time t_2'. In the observers frame, the duration of the pulse $\Delta t'$, is

$$\Delta t' = t_2 - t_1 - \frac{\delta D}{c} = \frac{\phi}{\omega_L} - \frac{v\phi}{c\omega_L} = \left(1 - \frac{v}{c}\right) \frac{\phi}{\omega_L} \tag{1.13}$$

The term $(1 - v/c)$ can be approximated by

$$\left(1 - \frac{v}{c}\right) = \frac{(1 - \frac{v}{c})(1 + \frac{v}{c})}{(1 + \frac{v}{c})} = \frac{1 - \frac{v^2}{c^2}}{1 + \frac{v^2}{c^2}} \approx 2\gamma^{-2} \tag{1.14}$$

The observer therefore will observe a pulse of radiation for a time period $2\gamma^{-2}$ times that of the gyration period in the frame of the particle. The duration of the pulse can be rewritten as

$$\Delta t' = \left(\frac{1}{2\gamma^2}\right) \frac{\phi}{\omega_L} = \frac{1}{2\gamma^3 \omega_L} \tag{1.15}$$

The spectrum is calculated by taking the Fourier transform of the power times series. The observed frequency of the pulse is given by $\nu \approx (\Delta t')^{-1}$, so that the particle emits most of its power at a frequency ν_s, related to the relativistic angular frequency ν_L and the non-relativistic gyrofrequency ν_g as

$$\nu_s \approx \gamma^3 \nu_L \approx \gamma^2 \nu_g \tag{1.16}$$

Consequently, the energy of the electron and the frequency of the observed radiation are closely related. In the above analysis it has been assumed that the particle moves in a circle with a pitch angle θ = 90°. For an arbitrary pitch angle, the result becomes

$$\nu_s \approx \gamma^2 \nu_g \sin\theta \tag{1.17}$$

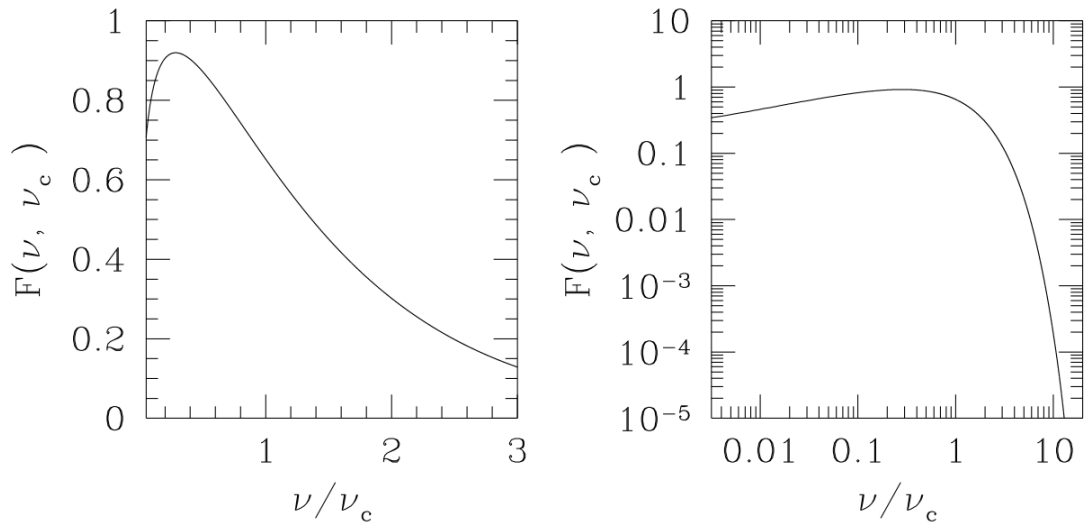

Figure 1.4: The linear *(left)* and logarithmic *(right)* form of the spectral distribution of synchrotron emission from a single electron. Adapted from Worrall and Birkinshaw (2006). The spectrum peaks at ν = 0.29 ν_c and falls off exponentially at $\nu > \nu_c$. At low frequencies synchrotron self-absorption becomes important.

These equations show that the relativistic beaming of radiation is a general property that is independent of the force causing the acceleration.

The critical frequency of a single electron for any pitch angle can be defined as

$$\nu_c = \frac{3}{2}\nu_s \sin\theta \tag{1.18}$$

and ν_c can approximate the frequency of emission. A population of mono-energetic electrons has a frequency-dependent spectral distribution given by

$$F(X) = X \int_X^\infty K_{5/3}(z)dz \tag{1.19}$$

where X = ν/ν_c and $K_{5/3}(z)$ is a modified Bessel function of order 5/3.

The form of this spectrum is shown in both linear and logarithmic form in Figure 1.4. The broad maximum is centred roughly at the frequency $\nu \approx \nu_c$ and the peak of the emission spectrum has value $\nu_{\rm max} = 0.29\nu_c$.

The high frequency emissivity of the electron is given by an expression of the form

$$F(\nu, \nu_c) \propto \nu^{1/2} e^{-\nu/\nu_c} \tag{1.20}$$

which is dominated by the exponential cut-off at frequencies $\nu >> \nu_c$. This reflects the fact that there is little radiation emitted by the electron at angles $\theta << \gamma^{-1}$. At

low frequencies ($\nu << \nu_c$) the spectrum is proportional to $\nu^{1/3}$. The behaviour at low frequencies is not usually observed in practice due to synchrotron self-absorption as the source becomes optically thick (see section 1.3.2).

1.3.1.2 Emission from a population of electrons

In practice, the observer will not detect emission from a single electron but will detect the superposition of pulses from a population of electrons. This population will have a range of different energies and phases. The emitted spectrum of electrons of energy E is sharply peaked near the critical frequency ν_c. It is therefore assumed that all the radiation of an electron of energy E is radiated at the critical frequency. This gives

$$\nu \approx \nu_c \approx \gamma^2 \nu_g = \left(\frac{E}{m_e c^2}\right)^2 \nu_g \tag{1.21}$$

where

$$\nu_g = \frac{eB}{2\pi m_e} \tag{1.22}$$

The energy of radiation in the frequency range ν to $\nu + d\nu$ can therefore be attributed to electrons with energies in the range E to $E + dE$. This energy range is assumed to have a power-law of the form $N(E) = kE^{-p}$, where k is the normalisation of the particle spectrum. Following Worrall and Birkinshaw (2006), the luminosity per unit frequency for a spectrum of electrons can be expressed as

$$L_\nu = 2\pi\sqrt{3} c m_e r_e \nu_g \sin\theta \int F(\nu, \nu_c) N(E) dE \tag{1.23}$$

where m_e and r_e are the mass and radius of the electron, respectively. For frequencies between $E_{min}^2 \nu_g < \nu < E_{max}^2 \nu_g$ and assuming an isotropic pitch angle, the luminosity is given by

$$L_\nu = A(p) c m_e r_e \nu_g^{(p+1)/2} k \nu^{-(p-1)/2} \tag{1.24}$$

where $A(p)$ is weakly dependent on p, the power-law index of the electron energy distribution. The spectral index of synchrotron emission α is defined as $L(\nu) \propto \nu^{-\alpha}$ and the shape of the spectral distribution for synchrotron emission depends on the energy distribution of the electrons, since α is related to p as $\alpha = (p-1)/2$.

1.3.1.3 Spectral ageing

In the optically thin regime of sources of synchrotron radiation, spectral breaks or cutoffs are often observed. In addition, variations in the spectral index may be seen within different regions of the same source. These phenomena are due to the effects of ageing of the spectrum of the electrons and therefore provide useful information about timescales. The lifetimes τ of the electrons within a region are

$$\tau = \frac{E}{-dE/dt} \propto (BE)^{-1} \tag{1.25}$$

The particle injection rate and synchrotron lifetime determine the evolution of the particle spectrum, which is represented by the diffusion-loss equation

$$\frac{dN(E)}{dt} = \frac{d}{dE}\left[N(E)\left(-\frac{dE}{dt}\right)\right] + Q(E,t) + D\nabla^2 N(E) \tag{1.26}$$

where Q gives the particle injection rate. The final term describes the spatial diffusion of particles away from a source and for simplicity here it is assumed to be negligible. As energy is lost, new particles (with spectrum kE^{-p}) are injected in order to balance the system, and the diffusion loss equation becomes

$$\frac{d}{dE}\left[N(E)\left(-\frac{dE}{dt}\right)\right] = -kE^{-p} \tag{1.27}$$

This equation has a solution (assuming $N \to 0$ as $E \to \infty$)

$$N(E) = \frac{kE^{-(p-1)}}{(p-1)(-\frac{dE}{dt})} \propto E^{-(p+1)} \tag{1.28}$$

This analysis describes the effect of continuous synchrotron energy loss upon the initial spectrum of high energy electrons. For different radiative loss mechanisms, a different signature in the spectrum will appear. This is also the case when high energy electrons for which $\tau << t$ (where t is the age of the source), are subject to synchrotron cooling. This means that their energy spectrum will be steeper than the initial spectrum by one power of E. For low energy electrons that have not yet had time to cool, the observed energy spectrum will correspond to the injection spectrum described above.

1.3.1.4 Minimum energy

An important consideration involving calculations of synchrotron radiation is the estimation of the minimum energy requirements in terms of electrons and magnetic fields, which

are able to produce the observed synchrotron emission (Burbidge, 1959).

The luminosity of a synchrotron emitting source at frequency ν can be expressed in terms of the magnetic field B as

$$L_\nu = A(\alpha) V k B^{1+\alpha} \nu^{-\alpha} \tag{1.29}$$

where the electron energy spectrum per unit volume is $N(E)dE = kE^{-p}dE$, the power law index of the election energy distribution is given by $p = 2\alpha + 1$ and $A(\alpha)$ is a constant dependent on α. Expressing the energy density in relativistic electrons as ϵ_e, the total energy present in the source is

$$W_{\text{total}} = V\epsilon_e + V\frac{B^2}{2\mu_0} = V\int kEN(E)dE + V\frac{B^2}{2\mu_0} \tag{1.30}$$

Equation (1.29) shows that the observed luminosity L_ν may be produced by a large flux of relativistic electrons in a weak magnetic field, or vice versa. From measurements of the luminosity, it is not possible to distinguish between the two cases. This introduces the requirement for a minimum total energy, where the energies of the particles and fields are approximately equal. To account for the energy of the particles, the contribution from relativistic protons must be included. If protons have energy K times that of electrons, the energy density in particles, u_p can be given as

$$u_p = (1 + K)u_e = \eta u_e \tag{1.31}$$

and equation (1.30) can be rewritten as

$$W_{\text{total}} = \eta V \int_{E_{\text{min}}}^{E_{\text{max}}} kEN(E)dE + V\frac{B^2}{2\mu_0} \tag{1.32}$$

The maximum intensity of synchrotron radiation occurs at a frequency

$$\nu = \nu_{\text{max}} = 0.29\nu_c = 0.29\frac{3}{2}\gamma^2\nu_g = CE^2B \tag{1.33}$$

for a non-relativistic gyro-frequency ν_g and C = 1.22 $\times$ 10^{10} / $(m_e c^2)^2$. The range of electron energies can therefore be expressed as

$$E_{\text{max}} = \left(\frac{\nu_{\text{max}}}{CB}\right)^{1/2} \tag{1.34}$$

$$E_{\text{min}} = \left(\frac{\nu_{\text{min}}}{CB}\right)^{1/2} \tag{1.35}$$

The energy in the particles is then

$$W_{\text{particles}} = \eta V \int_{E_{\text{min}}}^{E_{\text{max}}} kEN(E)dE = \frac{\eta V k}{(p-2)}(CB)^{(p-2)/2}\left[\nu_{\text{min}}^{(2-p)/2} - \nu_{\text{max}}^{(2-p)/2}\right] \quad (1.36)$$

Substituting for L_ν, Longair (2011) shows that the total energy in the source is given by

$$W_{\text{total}} = G(\alpha)\eta L_\nu B^{-3/2} + V\frac{B^2}{2\mu_0} \quad (1.37)$$

where $G(\alpha)$ is a constant which depends weakly on α, ν_{max} and ν_{min}. The variation of the energies in particles and magnetic field as a function of magnetic field strength is given in Figure 1.5. There is a minimum magnetic field strength

$$B_{\text{min}} = \left[\frac{3\mu_0 G(\alpha)\eta L_\nu}{2V}\right]^{2/7} \quad (1.38)$$

and this corresponds to an approximate equality of the energy in the particles and in the magnetic field. This is referred to as the equipartition of energy and gives a minimum total energy of

$$W_{\text{total}}(\text{min}) = \frac{7}{6\mu_0}V^{3/7}\left[\frac{3\mu_0}{2}G(\alpha)\eta L_\nu\right]^{4/7} \quad (1.39)$$

This expression describes the minimum energy needed to account for the observed luminosity of a source.

The minimum-energy assumption can be tested by combining measurements of synchrotron and inverse-Compton (see section 1.3.3) emission from the same electron population. If the measured X-ray emission can be ascribed to the inverse Compton process and the properties of the photon field are known, then the X-ray flux density can be determined (see Worrall, 2009 for an in-depth discussion). The combination of the radio (from synchrotron observations) and X-ray flux density allows a value for the magnetic field strength B to be inferred and compared to the value calculated from minimum energy arguments.

The X-ray telescopes *Chandra* and *XMM-Newton* have made important advances in tests of minimum energy and results generally find magnetic field strengths within a factor of a few of their minimum energy values (e.g. Hardcastle et al., 2001; Brunetti et al., 2002; Migliori et al., 2007).

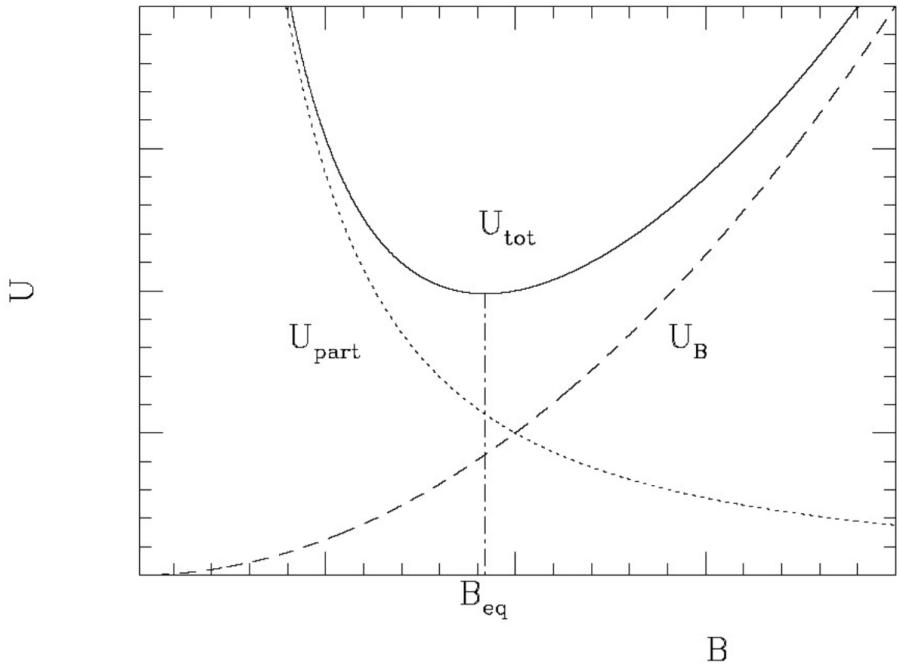

Figure 1.5: The variation of energy U in magnetic field and particles as a function of magnetic field strength B. The particle energy $U_{\text{part}} \propto B^{-3/2}$, and the magnetic field energy $U_{\text{B}} \propto B^2$.

1.3.1.5 Polarisation

The synchrotron emission detected in AGN has a high degree of linear polarisation. The polarisation properties of a synchrotron-emitting source can reveal insights on the magnetic field structure in that region, making it a fundamental tool for understanding the physics within active galaxies. Polarimetric observations in optical astronomy are difficult, due to the lower typical level of polarisation detected by optical instruments. In radio astronomy however, polarimetric observations are much simpler.

The polarisation of a transverse wave is given by the orientation of the electric field vector E. The E vector can be described by a plane wave with phase shift $\delta_{x,y}$ as

$$E_x = E_{0x} \cos(kz - \omega t + \delta_x) \tag{1.40}$$

$$E_y = E_{0y} \cos(kz - \omega t + \delta_y) \tag{1.41}$$

Dividing by the amplitudes E_{0x} and E_{0y} and using the double angle trigonometric formulae gives

$$\frac{E_x}{E_{0x}} = \cos(kz - \omega t)\cos(\delta_x) - \sin(kz - \omega t)\sin(\delta_x) \tag{1.42}$$

$$\frac{E_y}{E_{0y}} = \cos(kz - \omega t)\cos(\delta_y) - \sin(kz - \omega t)\sin(\delta_y) \tag{1.43}$$

Rearranging and squaring these equations yields

$$\frac{E_x^2}{E_{0x}^2} + \frac{E_y^2}{E_{0y}^2} - 2\frac{E_x E_y}{E_{0x}E_{0y}}\cos(\phi) = \sin^2(\phi) \tag{1.44}$$

where $\phi = \delta_y - \delta_x$. This is the equation for an ellipse, thus as E_x and E_y propagate along the z-axis, they appear as an ellipse to an observer looking down the direction of propagation. Special cases of an elliptically polarised wave are linear and circular polarisation. For linear polarisation, the phase difference between E_x and E_y is $\phi = 0$, i.e. the electric field vectors are in phase. For circular polarisation, the phase difference $\phi = \pi/2$, so E_x and E_y are π radians out of phase (the amplitudes E_{0x} and E_{0y} must also be equal for circular polarisation). The handedness of the polarisation is also defined by the phase difference ϕ. Right hand polarisation corresponds to $0 < \phi < \pi$ and the electric field vector rotates counter clockwise. Left hand polarised waves have a phase difference given by $\pi < \phi < 2\pi$ and the rotation is clockwise.

A 'polarisation ellipse' is a useful representation of equation (1.44), and is shown in Figure 1.6. The polarisation ellipse presents some important parameters enabling the characterisation of the state of the polarisation. The rotation angle ϕ is the angle between the x axis and the major axis ϵ. This angle is called the azimuth angle. A second angle β can be defined as $\beta = \arctan(E_{0y}/E_{0x})$ and is known as the auxiliary angle. The ellipticity of the shape is given by the ratio of the major axis b to minor axis a, and the ellipticity angle equals $\chi = \arctan(b/a)$. For linearly polarised light $\chi = 0$; for circularly polarised light $|\chi| = 45°$.

The parameters represented on the polarisation ellipse can be expressed in terms of the Stokes parameters. These are used in radio polarimetry to describe the polarisation state of the radiation. They are given by I, Q, U, V as

$$I = E_{0x}^2 + E_{0y}^2 \tag{1.45}$$

$$Q = I\cos(2\chi)\cos(2\phi) \tag{1.46}$$

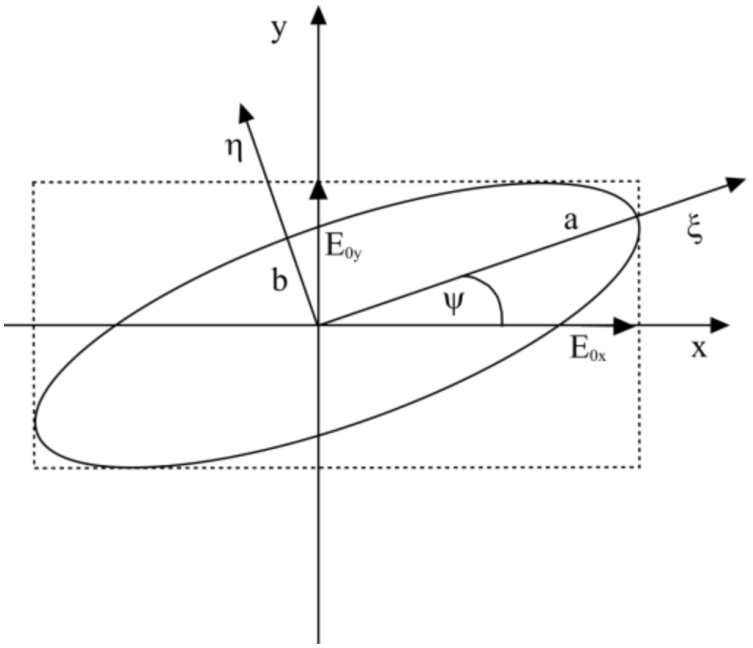

Figure 1.6: A diagram showing the polarisation ellipse, adapted from Perlicki and Yasin (2015). Axes x and y are the initial, unrotated axes. ϵ and η are a new set of axes along the ellipse. The rotation angle ϕ is the angle between the x axis and the major axis ϵ. This angle is called the azimuth angle. The ellipticity of the shape is defined as the ratio of the major axis b to the minor axis a.

$$U = I\cos(2\chi)\sin(2\phi) \tag{1.47}$$

$$V = I\sin(2\chi) \tag{1.48}$$

where I describes the total intensity of the radiation, Q and U describe the linear and orthogonal linear polarisation respectively and V describes the circular polarisation state of the radiation. These parameters can be represented on a Poincare sphere, where $I, 2\phi$ and 2χ are the spherical coordinates of the polarisation state. The factors of two before ϕ and χ highlight the fact that any polarisation ellipse is indistinguishable from one rotated by 180°. A representation of the Poincare sphere is given in Figure 1.7. The poles of the sphere represent circular polarisations, thus linearly polarised radiation will lie on the equator. The upper-hemisphere represents left-hand circularly polarised radiation and the lower hemisphere denotes right-hand circularly polarised radiation.

For monochromatic, fully polarised radiation, $I^2 = Q^2+U^2+V^2$. In general however, radiation is incoherent and only partially polarised, thus $I^2 > Q^2 + U^2 + V^2$. Parameters that directly describe the polarisation vector can be derived from the Stokes parameters:

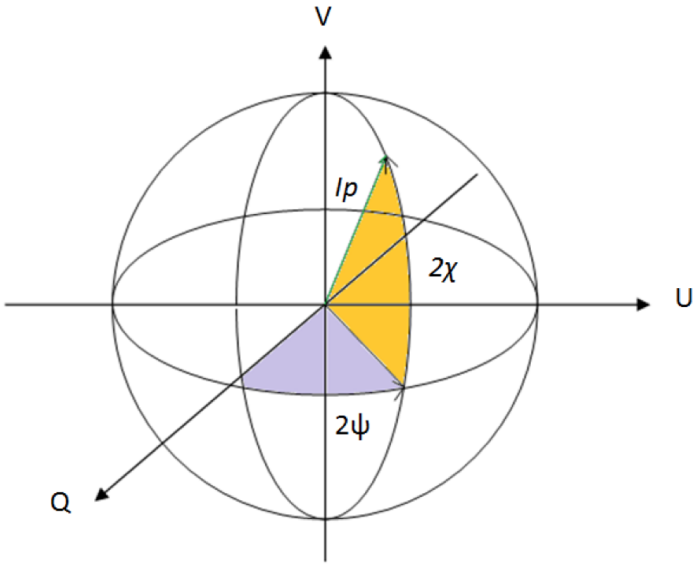

Figure 1.7: This illustration shows the parameterisation of the Stokes parameters in spherical coordinates onto a Poincare sphere, adapted from Collett (2005). I is the total intensity and p is the degree of polarisation, thus the length of the vector Ip represents the degree of polarisation.

$$P = \sqrt{Q^2 + U^2} \tag{1.49}$$

$$\phi = \frac{1}{2} \arctan\left(\frac{U}{Q}\right) \tag{1.50}$$

$$\vec{P} = Pe^{2i\phi} = Q + iU \tag{1.51}$$

where these give the linearly polarised intensity, the polarisation angle and the complex polarisation vector, respectively.

A significant advantage of using Stokes parameters to describe polarisation is that they can be calculated in a simple way from radio telescope outputs. Radio telescopes that have full-polarisation capability have one feed for each polarisation. Those feeds can be built in as either linear or circular feeds. The Stokes parameters can be expressed in terms of feed outputs, and these are given in chapter 2.

1.3.1.6 Faraday effects

A linear polarised wave can be constructed via the superposition of two circularly polarised waves. As these waves propagate through a magnetic medium, right hand and left

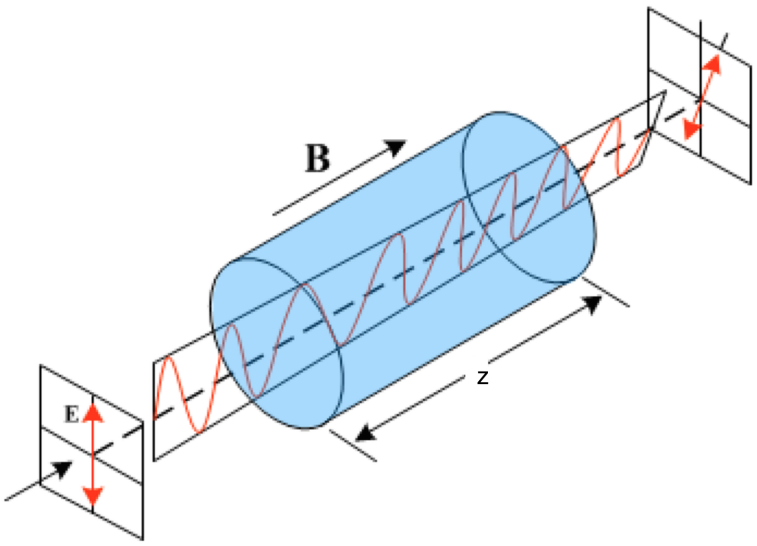

Figure 1.8: This illustration shows how the plane of polarisation is rotated by a magnetic medium due to birefringence. A linearly polarised wave enters the magnetised medium represented by the blue cylinder with path length z and magnetic field strength B. As it propagates, the wave is rotated, and the final wave has a polarisation angle offset from the initial wave angle.

hand circularly polarised waves of the same frequency have slightly different wave numbers. This is a birefringence effect that causes a rotation of the polarisation angle as the wave propagates. This effect is known as Faraday rotation and is illustrated in Figure 1.8. The rate of advance of the polarisation angle with distance travelled by the wave is given by

$$\frac{d\phi}{dz} = \Delta k = \frac{\omega_p^2 \Omega}{2\omega^2 c} = \frac{e^3 n_e B_0}{2\epsilon_0 m_e^2 c \omega^2} \tag{1.52}$$

Hence a linearly polarised wave which propagates through a plasma with an electron number density n_e and component of the magnetic field $B_{||}$ along the line of sight, has its plane of polarisation rotated through a total angle

$$\Delta\phi = \frac{e^3 \lambda^2}{2\pi (mc^2)^2} \int n_e(z) B_{||}(z) dz \tag{1.53}$$

where $\omega = 2\pi c/\lambda$. The integral extends over the line of sight between the source and the observer. This equation is written in terms of the Rotation Measure (RM) as

$$\Delta\phi = RM\lambda^2 \tag{1.54}$$

where

$$RM = 0.81 \int n_e(z) B_{||}(z) dz \tag{1.55}$$

in units of rad m^{-2} for n_e in cm^{-3}, $B_{||}$ in μG and path length z in parsec.

The Faraday rotation effect means it is possible to measure the magnetic field parallel to the line of sight, weighted by the electron density. The Faraday rotation of a plasma is also dependent on the Lorentz factor of electrons γ. Faraday rotation weakens with the increase in γ as $\ln \gamma / \gamma^2$. The electric vector position angle of linearly polarised light will therefore be preserved better if electrons are relativistic. Determination of the intrinsic polarisation angle at the source can be determined from polarisation angle measurements at multiple frequencies, from which the rotation measure can be found as

$$RM = \frac{\phi_2 - \phi_1}{\lambda_2^2 - \lambda_1^2} \tag{1.56}$$

Any polarisation angle measurement however, has an ambiguity of an integer number n of π. It is therefore not possible to distinguish between a polarisation angle of ϕ or $\phi \pm n\pi$. To resolve this ambiguity, three or more reference frequencies are used to determine the gradient of ϕ versus λ^2.

Faraday rotation can lead to depolarisation of the observed radiation. This means that the degree of polarised intensity for radio observations can be significantly lower than the intrinsic value. This depolarisation can either be internal to the radio source or external, caused by a Faraday rotating screen along the line of sight between the observer and the source.

External depolarisation can also be caused by limitations of the instrumental capabilities. Beam depolarisation is due to changes or disturbances in the foreground screen within the observing beam. These changes may be unresolved density or magnetic field inhomogeneities of the external medium through which the radiation propagates and this can lead to spatial variation in the Faraday rotation measure and hence beam depolarisation. Additionally, bandwidth depolarisation can occur when the polarisation position angle rotates significantly across the bandwidth of the observations.

Depolarisation due to the spatial extent in size of the radio emitting source can also occur. This is referred to a differential Faraday rotation, where the plane of polarisation along a given line of sight within a source is Faraday rotated by different amounts due to the different path length, i.e. the plane of polarisation at the far end of the source will be rotated more than that closest to the observer. The observed degree of polarisation for the source therefore is reduced. If the Faraday rotation is intrinsic to the source, then the

source can be described by an homogeneous optically thin slab (e.g. Burn, 1966) and the degree of polarisation varies as

$$P_{\text{obs}}(\lambda) = \lambda_{\text{int}} \frac{\sin(RM'\lambda^2)}{RM'\lambda^2} \tag{1.57}$$

where the rotation measure through the source is given by RM′. Internal and external Faraday depolarisation can be distinguished with high resolution polarisation data at multiple frequencies. Internal depolarisation is correlated with the Faraday rotation measure, so regions with small values of rotation measure should exhibit little depolarisation. External depolarisation due to gradients in the rotation measure structure will be correlated with the amount of variation.

1.3.2 Synchrotron self absorption

In the previous sections, it has been assumed that all of the synchrotron radiation emitted by each electron reaches the observer. This is not always the case however, since photons emitted via the synchrotron mechanism can scatter off an electron. This process is known as synchrotron self absorption. A source is defined as optically thick if the mean free path of the photon is smaller than the size of the source. For an optically thick spectrum, an effective temperature T_{eff} can be assigned to the electrons in the synchrotron plasma

$$k_B T_{\text{eff}} \approx \gamma m_e c^2 \tag{1.58}$$

This equation indicates that the electron emits at a characteristic frequency, given by

$$k_B T_{\text{eff}} \propto E \propto \nu^{\frac{1}{2}} \tag{1.59}$$

Even though the electrons are not in a thermal distribution, at any frequency they cannot emit radiation more efficiently than a black-body. T_{eff} can therefore be used in the Planck formula to determine the maximum brightness of a self-absorbed synchrotron plasma

$$I_\nu = \frac{2k_B T \nu^2}{c^2} \propto \nu^{5/2} \tag{1.60}$$

Synchrotron self-absorption is observed at the low frequency end of radio-emitting plasma, regardless of the energy distribution. The spectrum in Figure 1.9 shows the distribution expected when synchrotron self absorption becomes important. The flux peaks

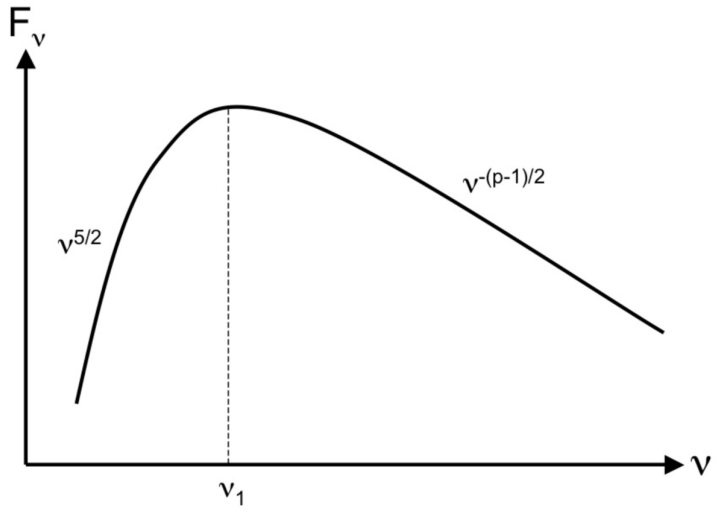

Figure 1.9: The spectral energy distribution when synchrotron-self absorption is important, adapted from Rybicki and Lightman (2008). The flux peaks where the SED turns over from optically thick to optically thin (τ = 1). For AGN, the turnover frequency ranges from $\nu_1 \approx 0.1 - 10$ GHz.

where the SED turns over from optically thick to optically thin. For AGN, the turnover frequency ranges from $\nu \approx$ 0.1-10 GHz.

1.3.3 Inverse Compton emission

In the inverse Compton mechanism (iC), ambient photons are scattered to higher energies by synchrotron emitting electrons. This process is the opposite of the Compton scattering process in which photons lose energy after collisions with electrons. The following approach to determine the electron energy loss due to the iC mechanisms is based on the derivation by Longair (2011).

The power emitted in the rest frame of the electron S' is given by

$$P' = \sigma_T c u'_{\text{rad}} \tag{1.61}$$

where σ_T is the Thomson cross-section which describes the probability of scattering between the photon and the electron, and u'_{rad} is the energy density of radiation in the rest frame of the electron. u'_{rad} is given by

$$u'_{\text{rad}} = u_{\text{rad}}[\gamma(1 + \beta\cos\theta)]^2 \tag{1.62}$$

where θ is the angle of incidence between the photon and electron in the observer's frame. This equation incorporates the relativistic Doppler shift and is dependent on the angle

between the direction of the photons and the electron velocity vector. If the radiation field is isotropic in the frame of the observer, the total energy density can be found as

$$u'_{\rm rad} = u_{\rm rad} \int_0^{\pi} \gamma^2 (1 + \beta \cos\theta)^2 \frac{1}{2} \sin\theta d\theta = \frac{4}{3} u_{\rm rad} (\gamma^2 - \frac{1}{4}) \tag{1.63}$$

The energy gained by the photon field is found by subtracting the initial input energy from the incident photon as

$$-\left(\frac{dE}{dt}\right) = \frac{4}{3}\sigma_T c u_{\rm rad}(\gamma^2 - \frac{1}{4}) - \sigma_T c u_{\rm rad} = \frac{4}{3}\sigma_T c u_{\rm rad}\gamma^2\beta^2 \tag{1.64}$$

The corresponding energy loss due to synchrotron power can be compared to equation (1.9) and gives the relation

$$\frac{L_{\rm iC}}{L_{\rm synch}} = \frac{u_{\rm rad}}{u_B} \tag{1.65}$$

Relativistic electrons subjected to both a radiation and magnetic field therefore emit photons by both the iC and synchrotron mechanism.

The spectrum of iC scattered photons by a power law distribution of electrons results in an intensity spectrum of the scattered radiation of the form

$$L_\nu \propto \nu^{-(p-1)/2} \tag{1.66}$$

As I shall discuss next, these non-thermal radiative processes can be used to characterise the emission within radio galaxies and create a more complete picture of the environments within which they reside.

1.4 The Large Scale Morphology and Magnetic Field Structure of Radio Jets

Most models of jet acceleration and collimation rely on a rotating accretion disk threaded by a perpendicular large scale magnetic field (Blandford and Znajek, 1977; Shu et al., 2000; Pudritz et al., 2007). Magnetic fields play an important role in launching, driving and directing the evolution of jets through the external environment. When jets terminate, enormous amounts of mechanical energy and momentum are deposited into the IGM and their interactions within this medium are closely correlated with the magnetic fields that they carry. The release of gravitational potential energy during accretion is an important

power source for most astrophysical jets. Magnetic torques can easily tap into the shear energy available in the accretion disk that forms due to gravitational collapse. Models of magnetised outflows were developed by Blandford and Payne (1982) and these theories envisage that material from a disk is ejected outwards along open field lines as it rotates with a threading magnetic field. The gas will accelerate as long as the field is strong enough continue rotating with the accretion disk. The inertia of the particles travelling along the field lines results in the field becoming wrapped up in a toroidal like structure, producing a helical magnetic field configuration. This dominant toroidal field component exerts a pinching force on the jet and collimates it in the direction of the axis. This theory also predicts that jets should extract the angular momentum of the host source. Rapidly rotating black holes also provide a source of energy, since electromagnetic torques can efficiently extract rotational energy (Blandford and Znajek, 1977). Large scale magnetic fields are therefore one of natures tools for extracting the energy and angular momentum from rapidly accreting or spinning objects, and directing them into the formation of ordered magnetically collimated outflows. The synchrotron radiation emitted by relativistic electrons spiralling around the magnetic field lines allows one to directly measure the strength and configuration of the magnetic field in the jet. Numerical MHD models of the production of magnetised jets are able to develop jet-like features emerging from a central disk region (e.g. McKinney, 2006; McKinney and Blandford, 2009), but a fully self-consistent treatment taking into account all the relevant mechanisms within the accretion disk and the physical conditions allowing the ejection of material is still missing.

Radio interferometers such as the Very Large Array (VLA) (see chapter 2.2) have greatly advanced the study of radio jets for a number of reasons. The VLA has the sensitivity to detect weak radio emission without long observations, the dynamic range to do so even when there is bright unresolved emission in the galaxy core and the angular resolution to distinctly separate jets and other radio components. It also allows polarisation observations with sufficient sensitivity and resolution to reveal important information about a jet's magnetic field configuration and rotation measure structure. At present, FR I-type jets have been investigated most thoroughly because their relative brightness and proximity ensure that sensitive measurements can be made on both parsec and kpc scales. In addition, both a jet and counter-jet are routinely detected in FR I-type sources, and the assumption that these two structures are intrinsically symmetrical allows the effects of relativistic beaming and aberration to be separated from the intrinsic behaviour of the source.

Some general attributes of radio sources and their magnetic fields have become apparent (e.g. Laing and Bridle, 2014). Well resolved jets are often highly linearly polarised, so their magnetic fields are at least partially ordered. The bases of FR I-type jets are dominated by field components along the jet axes; however further from the AGN the field rotates to become perpendicular (Bridle and Perley, 1984). The effect of Faraday rotation is usually modest outside the core regions, leading to polarisation rotations of around 0-15° at centimetre wavelengths. Jets with misaligned polarisation (i.e. neither close to parallel or perpendicular to the jet axis) that cannot be explained by Faraday rotation are not frequently observed. Some jets exhibit a 'spine-sheath' polarisation structure, where transverse magnetic fields are observed near the central axis of the jet and longitudinal magnetic fields are detected near the jet edges (e.g. Attridge et al., 1999). This structure is often interpreted as a combination of transverse shocks compressing an initially tangled magnetic field so that it has become ordered in the plane of compression (the transverse 'spine') and the action of shear that has enhanced the longitudinal component of the field in a layer surrounding the jet (the 'sheath') (Hughes et al., 1989; Laing, 1996).

Alternatively these polarisation structures can be used as evidence for a helical magnetic field carried by the jets (e.g. Lyutikov et al., 2005). Within this interpretation, jets with longitudinal magnetic fields carry helical fields with relatively large or small pitch angles. The appearance of 'spine-sheath' polarisation structure can be explained by a jet carrying a helical magnetic field, with the azimuthal component dominating near the central axis of the jet and the longitudinal component becoming dominant near the edges.

These two possible interpretations for the polarisation structure observed within jets are not easily distinguished. Faraday rotation distributions however, offer a unique tool for testing the existence of a helical magnetic field configuration. An observational signature of a jet carrying a helical magnetic field is the presence of a gradient in the rotation measure structure transverse to the jet direction. This is currently tested primarily on a parsec scale (e.g. Zavala and Taylor, 2005; Gabuzda et al., 2004), however Gabuzda et al. (2012) reported the detection of Faraday rotation gradients across the kpc scale jets and lobes of six AGN. This is significant if true, because if the jets contain helical magnetic fields, then these should be present wherever the jets propagate, i.e. on both parsec and kpc scales. Therefore the ability to reliably measure the polarisation properties across AGN jets is key to probing the nature of the magnetic field.

The lobes of radio galaxies are also often strongly polarised, with the typical apparent magnetic field direction being parallel to contours of constant total intensity surface

brightness. Because of the large spatial scales and strong polarisation, lobes are the best places for detailed studies of Faraday rotation intrinsic to the source or its local environment.

1.4.1 Bent jets

Interactions between galaxies and the intracluster medium as they travel within a galaxy cluster can cause irreversible changes to the morphology of the galaxies themselves. Ryle and Windram (1968) reported the first examples in two members of the Perseus cluster, IC 310 and NGC 1265. Each galaxy exhibits an extended (0.1-1 Mpc) radio tail on one side (at large linear scales), and these are classified as 'head-tail' sources (see Sarazin, 1988 for more examples). Head-tail sources are often interpreted as an AGN-driven jet swept back by ram pressure as it moves through the intracluster medium (Miley et al., 1972; Rudnick and Owen, 1976). Radio sources with less extreme bending are known as wide-angle tail galaxies, and they are often associated with central galaxies within clusters. McBride and McCourt (2014) classify all sources with radio morphologies that appear to be produced due to the motion of their galaxy through the external medium, regardless of the scale of the bending as 'bent-double' sources. The association between these bent-double sources and galaxy clusters is so significant that they have been used as a probe for discovering galaxy clusters in radio surveys (Blanton et al., 2001; Wing and Blanton, 2011) and to estimate the gas density within galaxy group environments (Freeland et al., 2008).

The majority of head-tail sources which show jet bending have been resolved into U-shaped twin jets. They are modelled as an effect of the relative motion of the host galaxy in the ICM and their symmetrical jet morphology in the presence of bending suggests that the jets have sub-relativistic velocities and moderate Mach numbers (O'Dea and Owen, 1985). A few sources with asymmetric jets have been found, where one jet shows extreme jet bending and the other remains relatively straight. The morphologies of these sources cannot be explained within the framework of ram pressure exerted by external gas unless the scale size of the extended gas is less than the size of the source. Detailed multifrequency observations are therefore required to attempt to interpret their structure.

Investigating the magnetic field structure within bent jets can help to interpret the deflecting components and while the magnetic field may not dominate the dynamics of the large-scale structures, it may still have some role to play. It has been noticed (e.g. Bridle et al., 1994) that the magnetic field direction often follows bends in a jet very closely and is thus a good indicator of complex structure.

1.5 This thesis

In this thesis, I present VLA observations of two highly unusual low-power FR I-type radio galaxies. There are three main goals to my work :

1. To create sensitive radio images of the sources in order to investigate the morphology and polarisation structure of the jets and radio features

2. To use X-ray and optical observations to complement the radio data and create a more complete picture of the source environment

3. To explain how the extreme jet distortions can be produced and to what extent they may occur for other similar radio sources

This thesis is organised as follows. In chapter 2, I provide an overview of the capabilities of the VLA, and describe the techniques and analysis required for radio synthesis imaging. In chapter 3, I present an overview of the multi-wavelength properties of all the sources that I study in this thesis. In chapter 4, I present archival and new JVLA radio data for the FRI-type radio galaxy NGC 7385. I present evidence for an optical and X-ray synchrotron jet, and images of an optical gas cloud interacting with the radio counter-jet. This counter-jet then undergoes a series of extreme deflections as a result of the collision. In chapter 5, I present observations of the radio galaxy NGC 6109, which shows a remarkable 'swirl' like radio feature. I discuss the possible mechanisms responsible for the unusual structure, including helical jet precession on a kpc scale and large scale helical jet bending. In chapter 6, I compare the two unusual objects with other sources that show 180° jet bends and discuss how more of these sources may be observed. Finally, in chapter 7, I provide a brief summary of the results of the work in this thesis, and also make some suggestions of future work that could lead on from these studies.

Chapter 2

Radio Synthesis and Imaging Techniques

In this chapter I explain the basic principles of radio synthesis as applied to creating images of radio galaxies. I describe the techniques I have developed to process interferometric radio data and produce maps of the total intensity and polarisation structure of individual AGN. These techniques include the methods I have used to mitigate the effects of radio frequency interference (RFI), and the different models for the rotation measure structure of a polarised source that I have investigated. The procedures described in this chapter are therefore of interest to any radio astronomer considering reducing polarisation data for radio-loud AGN.

Radio astronomy is one of the most important methods of astronomical observation. The first detection of radio waves from an astronomical object was carried out in 1930, when Karl Jansky was trying to determine the origin of a source of noise picked up by 20 MHz radio receivers. After Jansky deduced that this radiation was from the Milky Way, electronics engineer Grote Reber set about designing the first radio telescope, a 9m dish built in his own garden. Radio telescopes have since evolved from single dishes to interferometers: arrays of telescopes with the effective resolution of a single telescope many miles in diameter. These arrays are capable of synthesised beams with less than 1 milliarcsecond resolution.

Radio telescopes led to the discovery of new objects such as pulsars, quasars and radio galaxies, not originally identified through optical astronomy. These objects represent the sites of some of the most extreme and energetic physical processes in the Universe.

2.1 Fundamentals of Radio Interferometry

For a single dish radio telescope, the resolution of the image is limited by the diameter D of the dish and lacks the capability to resolve small sources in the sky. The angular resolution of a telescope θ is a measure of the minimum angular distance between two objects that will allow them to be distinguished as separate entities. It is given by $\theta \sim \lambda/D$, where λ is the observed wavelength in metres. The largest fully-steerable radio dish is located at Green Bank, where a 100m telescope provides $\theta \approx 10$ arcsec at 90 GHz; however to match the resolution of an optical telescope, the diameter of a radio dish would have to exceed a kilometre. To overcome this problem, arrays of smaller telescopes separated at large baselines are used increase the effective dish diameter.

A basic interferometer is a system of two telescopes whose voltage outputs are correlated. Larger systems of N elements can be treated as $N(N-1)/2$ independent interferometer pairs. A two-element interferometer is shown in Figure 2.1. The dishes 1 and 2 are separated by a baseline vector $\mathbf{b}$. The array observes in a narrow frequency range $\Delta\nu$ centred on $\nu_c = \omega$ / 2π. This frequency range is termed the bandwidth.

The correlator multiplies and time averages the voltage outputs V_1 and V_2 from each antenna. The voltage outputs differ by a geometric delay factor τ_g = **b** $\cdot\hat{s}$ / c, where **b** is the vector baseline between the antennas and $\hat{s}$ is the unit vector in the direction of the distant source. The output response R of the system is given by

$$R = \langle V_1 V_2 \rangle = \left(\frac{V^2}{2}\right)\cos(\omega\tau_g) \tag{2.1}$$

where the output amplitude $V^2/2$ is proportional to the point source flux density.

Extended sources are treated as the sum of independent point sources, and a complex correlator is used to account for both the odd and the even parts of the intensity distribution I by inserting a $\pi/2$ phase offset in one of the signal paths in Figure 2.1. The response to the source from a two element interferometer at a single frequency ν is given in equation (2.2) by the complex visibility function V_ν, in terms of the intensity $I_\nu(s)$ on the sky integrated over an element of solid angle $d\Omega$ and $A(s)$ which accounts for the finite size of the antennas.

$$V_\nu = \int A(s) I_\nu(s) e^{-2\pi i b\cdot s/\lambda} d\Omega \tag{2.2}$$

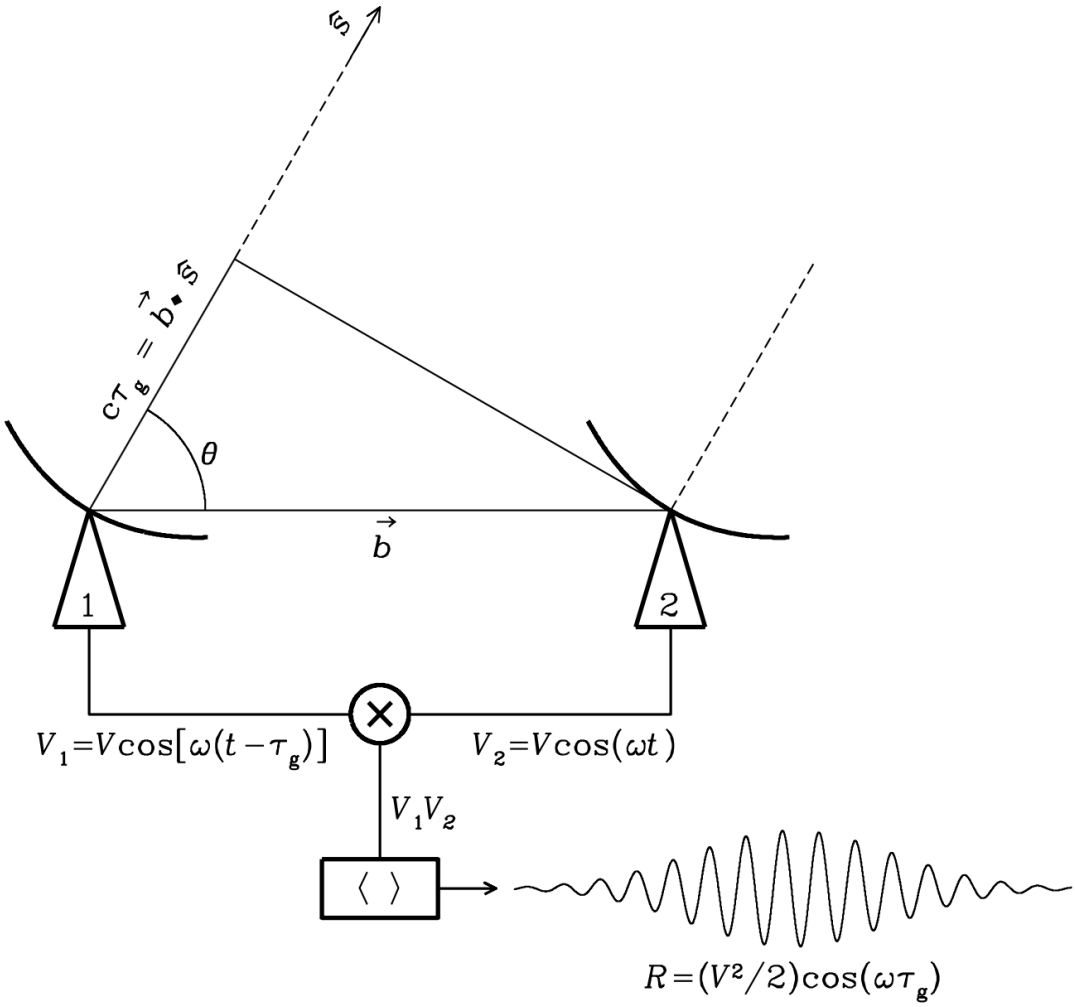

Figure 2.1: Simplified schematic diagram of a two element interferometer, observing in a narrow frequency range centred on $\nu = \omega/2\pi$. $\hat{s}$ is the unit vector in the direction of the target source, and $\vec{b}$ is the baseline vector between the antennas 1 and 2. The output voltage V_1 of antenna 1 is the same as V_2 of antenna 2 except for some geometric delay factor τ_g. The voltages are amplified, multiplied and time averaged by the correlator to produce an output response with an amplitude R. The phase of R is dependent on the delay τ_g and the frequency of the observation. This diagram was adapted from Wilson et al. (2009).

2.1.1 Coordinate system for imaging

The intensity distribution of the radiation I_ν from the radio source can be determined by inverting the complex visibility function V_ν. To apply equation (2.2) in practice, a coordinate system needs to be introduced where measurements can be made in a plane and the vector spacing of the separation variable **b** can be measured in terms of the wavelength λ; that is **b** = $\lambda(u, v, w)$. In this coordinate system, the components of the unit vector $\hat{s}$ are (l, m, n). A diagram of this coordinate system is given in Figure 2.2, where w is chosen to lie in the direction of the centre of the synthesised image $\vec{s}$. The following parameters are used to derive the interferometer response:

$$\frac{\mathbf{b} \cdot \hat{\mathbf{s}}}{\lambda} = ul + vm + wn \tag{2.3}$$

$$\frac{\mathbf{b} \cdot \tilde{\mathbf{s}}}{\lambda} = w \tag{2.4}$$

$$d\Omega = \frac{dldm}{n} = \frac{dldm}{\sqrt{1 - l^2 - m^2}} \tag{2.5}$$

In terms of this coordinate system, equation (2.2) can be rewritten as

$$V_\nu(u, v, w) = \int\int A_\nu(l, m) I_\nu(l, m) e^{-2\pi i(ul+vm+w(\sqrt{1-l^2-m^2}-1))} \frac{dldm}{\sqrt{1 - l^2 - m^2}} \tag{2.6}$$

This equation can be simplified into the form of a 2D Fourier transform, under the conditions that the vector baselines are coplanar and the w axis lies in the direction of the celestial pole so that w = 0. Equation (2.6) then becomes

$$V_\nu(u, v) = \int\int A_\nu(l, m) I_\nu(l, m) e^{-2\pi i(ul+vm)} dldm \tag{2.7}$$

This two-dimensional Fourier transform can be inverted to give the intensity $I(l, m)$ of the distant radio source as

$$A(l, m)I(l, m) = \int\int V(u, v) e^{2\pi i(ul+vm)} dudv \tag{2.8}$$

Some 2D arrays (e.g. the VLA) have baselines that are not aligned in the E-W direction and the rotation of the Earth causes the baselines to be moved into planes that are offset from their initial orientation. This introduces a component of the baseline in the direction of the source (w direction) and results in a phase error of $\pi(l^2 + m^2)w$ for

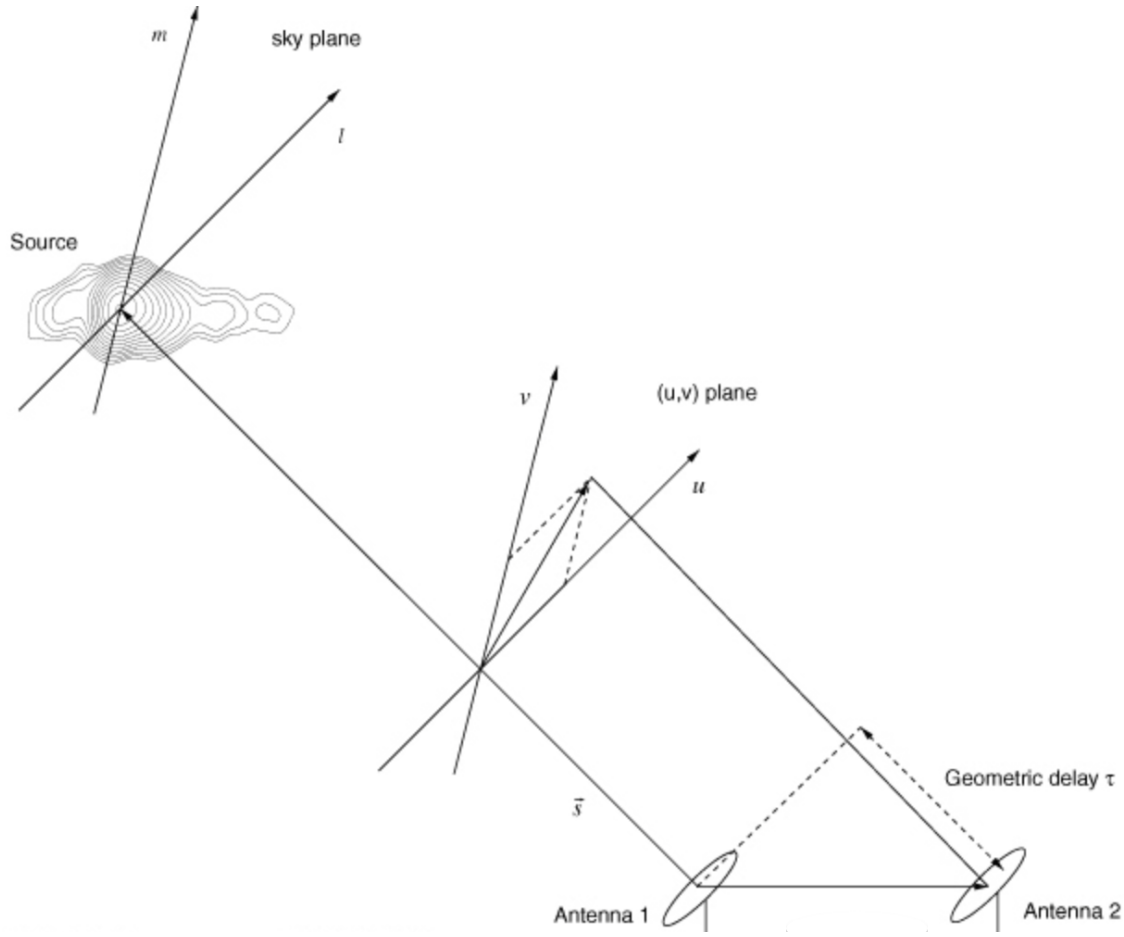

Figure 2.2: The (u, v, w) and (l, m, n) coordinate systems used to express the interferometer baselines and the source brightness distribution, respectively. Reproduced from Middelberg and Bach (2008). The target source is observed in the direction of the line of sight vector $\vec{s}$, and the sky coordinates are the direction cosines l and m. The (u, v) plane is perpendicular to $\vec{s}$ and yields the (u, v) coordinates of the antennas in units of the observing wavelength. There is a geometric delay τ_g between the two antennas.

radiation from the point (l, m). This places a limit on the size of the source that can be imaged without distortion. For a pair of antennas with a non-coplanar baseline, the largest w component, w_{max}, occurs when the source being observed is at a low angle of elevation and an azimuth close to that of the baseline. In this case, $w_{\text{max}} \approx b_{\text{max}}/\lambda$ and therefore the half-power width of the synthesised beam θ_{HPBW} can be expressed in terms of the longest baseline b_{max} as

$$\frac{1}{\theta_{\text{HPBW}}} \approx \frac{b_{\text{max}}}{\lambda} \approx w_{\text{max}} \tag{2.9}$$

There are a variety of established methods for dealing with non-coplanar baseline effects, including the W-projection algorithm (Cornwell et al., 2005) and W-snapshots (Cornwell et al., 2012).

2.1.2 Bandwidth smearing

The design of a synthesis array is based upon obtaining visibility measurements uniformly distributed over the (u, v) plane within the range determined by the angular resolution. If the source brightness and the response of the interferometer are constant for a finite bandwidth $\Delta\nu$ with central frequency ν_c, then equation (2.7) can be rewritten as:

$$V_\nu = \int \left[(\Delta\nu)^{-1} \int_{\nu_c - \Delta\nu/2}^{\nu_c + \Delta\nu/2} A(s) I_\nu(s) e^{-2\pi i b \cdot s/\lambda} d\nu \right] d\Omega \tag{2.10}$$

$$V_\nu = \int \left[(\Delta\nu)^{-1} \int_{\nu_c - \Delta\nu/2}^{\nu_c + \Delta\nu/2} A(s) I_\nu(s) e^{-2\pi i \nu \tau_g} d\nu \right] d\Omega \tag{2.11}$$

If I_ν is a weak function of ν then the integral in square brackets is the Fourier transform of a rectangle function, and thus equation (2.11) can be expressed as

$$V_\nu = \int A(s) I_\nu(s) \,\text{sinc}(\Delta\nu\tau_g) e^{-2\pi i \nu_c \tau_g} d\Omega \tag{2.12}$$

This equation implies that for a finite bandwidth $\Delta\nu$ the fringe amplitude is attenuated by the factor $\text{sinc}(\Delta\nu\tau_g)$. This attenuation can be removed by introducing a compensating delay $\tau_0 \approx \tau_g$ into the signal of the leading antenna. The delay needs to adjust to track the rotation of the Earth, with the requirement $|\tau_0 - \tau_g| << (\Delta\nu)^{-1}$. The angular radius of the field of view may be limited by the variation of τ_g with offset $\Delta\theta$ from the direction of $\vec{s}$. At large offsets, bandwidth smearing will radially broaden the synthesised beam by convolving it with a rectangle of angular width $\Delta\theta\Delta\nu/\nu$. To avoid this problem the total

bandwidth can be separated into a number of narrow frequency channels. These channels must satisfy the condition

$$\Delta\theta\Delta\nu << \theta_{\text{HPBW}}\nu \tag{2.13}$$

where θ_{HPBW} is the synthesised beam width and $\theta_s \approx \lambda/b$.

The time averaging of the visibility data at the correlator results in another form of smearing. The data from each correlator are separated into consecutive time intervals of length Δt and only the average value for each interval is retained. The averaged visibility samples are assigned (u, v) values corresponding to the mid-points of the averaging intervals. Excessive averaging times will cause time smearing. This effect can be minimised with the following condition, where P is the sidereal rotation period of the Earth:

$$\Delta\theta\Delta t << \frac{\theta_s P}{2\pi} \tag{2.14}$$

2.2 The Very Large Array

The Very Large Array (VLA) in Socorro, New Mexico, is a 27 dish two-dimensional array built between 1973-1980 as a component of the National Radio Astronomy Observatory (NRAO). It is configured in a Y shape (see Figure 2.3) to obtain adequate coverage of the (u, v) plane while using an economical geometry (Thompson et al., 1980; Napier et al., 1983). Each arm of the configuration measures up to 13 miles long. The array is capable of achieving an angular resolution of about 0.04 arcseconds. The frequency coverage is 74 MHz to 50 GHz and each dish has a diameter of 25m.

The VLA was upgraded in 2011 to the Expanded Very Large Array (eVLA) and renamed the Jansky Very Large Array (JVLA) in 2012. This upgrade built upon the existing infrastructure of the VLA. A comparison of the capabilities of the upgraded JVLA with the VLA is given in Table 2.1.

By reconfiguring the antennas, the JVLA can vary its spatial resolution by a factor of 50. The baselines for each configuration are given in Table 2.2 and reconfiguration occurs approximately every 4 months. Hybrid configurations can also be set up (e.g. B and A). There are 8 wide-band receivers, from 1-50 GHz (see Table 2.3 for frequency ranges and synthesised beamwidths θ_{HPBW}) with up to 8 GHz instantaneous bandwidth per polarisation. Full Stokes parameter imaging is available and new post-processing pipelines have been set up to calibrate data before they are released. Figures 2.4 and 2.5

Figure 2.3: An aerial view of the VLA in D configuration looking South, with one antenna not tracking (far right). Photo credit : Dave Finley, NRAO.

Parameter	VLA	JVLA	Factor
Point Source cont. sensitivity (1σ, 12hr)	10 μJy	1 μJy	10
Maximum BW in each polarisation	0.1 GHz	8 GHz	80
Number of freq. channels at max. BW	16	16384	1024
Max. number of freq. channels	512	4194304	8192
Coarsest frequency resolution	50 MHz	2 MHz	25
Finest frequency resolution	381 Hz	0.12 Hz	3180
Number of full-polarisation SPW	2	64	32
(log) Frequency coverage (1-50 GHz)	22%	100%	5

Table 2.1: A comparison of the capabilities of the VLA and JVLA radio array.

Configuration	A	B	C	D
B_{max} (km)	36.4	11.1	3.4	1.03
B_{min} (km)	0.68	0.21	0.035	0.035

Table 2.2: Basic antenna configurations of the JVLA. The antennas can also be set up into hybrid configurations.

Band	Range (GHz)	Synthesised Beamwidth (arcsec)			
		A	B	C	D
L	1.0-2.0	1.3	4.3	14	46
S	2.0-4.0	0.65	2.1	7.0	23
C	4.0-8.0	0.33	1.0	3.5	12
X	8.0-12.0	0.23	0.73	2.5	8.1
Ku	12.0-18.0	0.13	0.42	1.4	4.6
K	18.0-26.5	0.089	0.28	0.95	3.1
Ka	26.5-40.0	0.059	0.19	0.63	2.1
Q	40.0-50.0	0.043	0.14	0.47	1.5

Table 2.3: The observable frequency ranges and corresponding synthesised beam widths of the JVLA, assuming uniform weighting.

show the configuration of the antennas and the (u, v) coverage respectively, for a JVLA observation of radio galaxy NGC 7385 in the A array at L band.

All of the VLA receivers accept dual, circularly polarised signals. The L, S and C-band systems use quad-ridged orthomode transducers (OMTs) to separate the orthogonal linearly polarised components of the signal. The right-hand circular polarisation signal (RCP) of one antenna is correlated with the left-hand circular polarisation (LCP) of another, to obtain the cross-polarisation products RL and LR. The parallel-hand circular polarisation cross-products are given as RR and LL. All data with the VLA are taken in spectral line mode even if one is conducting continuum science, therefore bandpass solutions are required to account for gain variations with frequency.

The assumption that visibility data are taken at $w = 0$ (see section 2.1.1) can not be applied to the JVLA (except for snapshot observations). Solutions to the problem of imaging wide-field data taken with non-coplanar arrays have been implemented into the calibration and editing software.

The primary data reduction package for the VLA is the CASA (Common Astronomy Software Applications) package. This package can process both interferometric and single dish data. Data reduction processes are described in the CASA user reference manual and cookbook (see casaguides.nrao.edu for CASA guides and examples).

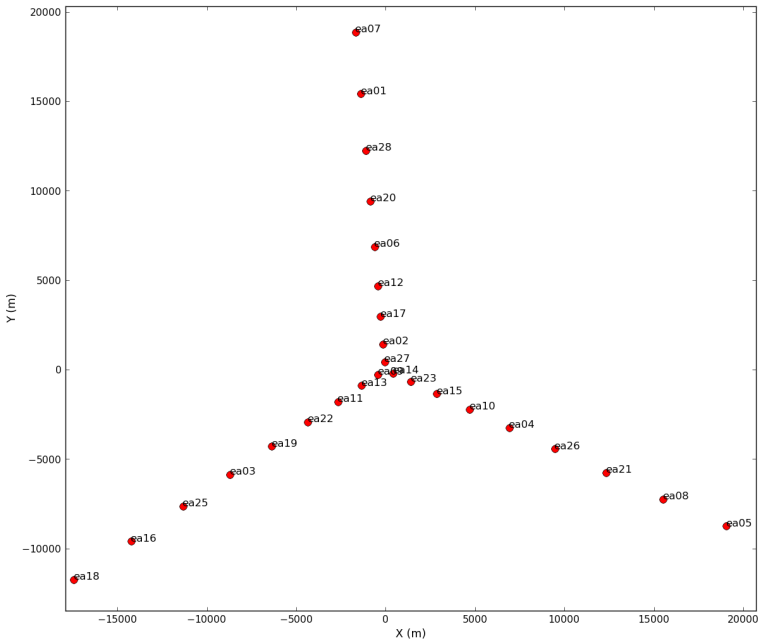

Figure 2.4: The configuration of the 27 antennas of the VLA in A array for observations of NGC 7385. eaNN refers to VLA antenna NN.

2.3 Calibration and Editing

The spatial coherence function given in equation (2.7) can be referred to as the *true* visibility function V_{ij}, with the subscripts indicating which pair of antennas are involved. The role of calibration and editing of a dataset is to recover the *true* visibility from the *observed* visibility. These quantities differ for a multitude of reasons, including antenna tracking inaccuracies and bad weather. Throughout this section, the observed visibility will be represented by $\tilde{V}_{ij}(t)$.

The basic calibration formula is given by equation (2.15) where t is the time of the observations, $\varsigma_{ij}(t)$ is the baseline-based complex gain, $\epsilon_{ij}(t)$ is a baseline based complex offset and $\eta_{ij}(t)$ is a stochastic complex noise.

$$\tilde{V}_{ij}(t) = \varsigma_{ij}(t)V_{ij}(t) + \epsilon_{ij}(t) + \eta_{ij}(t) \tag{2.15}$$

The complex gain $\varsigma_{ij}(t)$ can be approximated by the product of the individual antenna complex gains $g_i(t)$ and $g_j(t)$,

$$\varsigma_{ij}(t) = g_i(t)g_j^*(t)g_{ij}(t) = a_i(t)a_j(t)a_{ij}(t)e^{i(\phi_i(t)-\phi_j(t))+\phi_{ij}(t)} \tag{2.16}$$

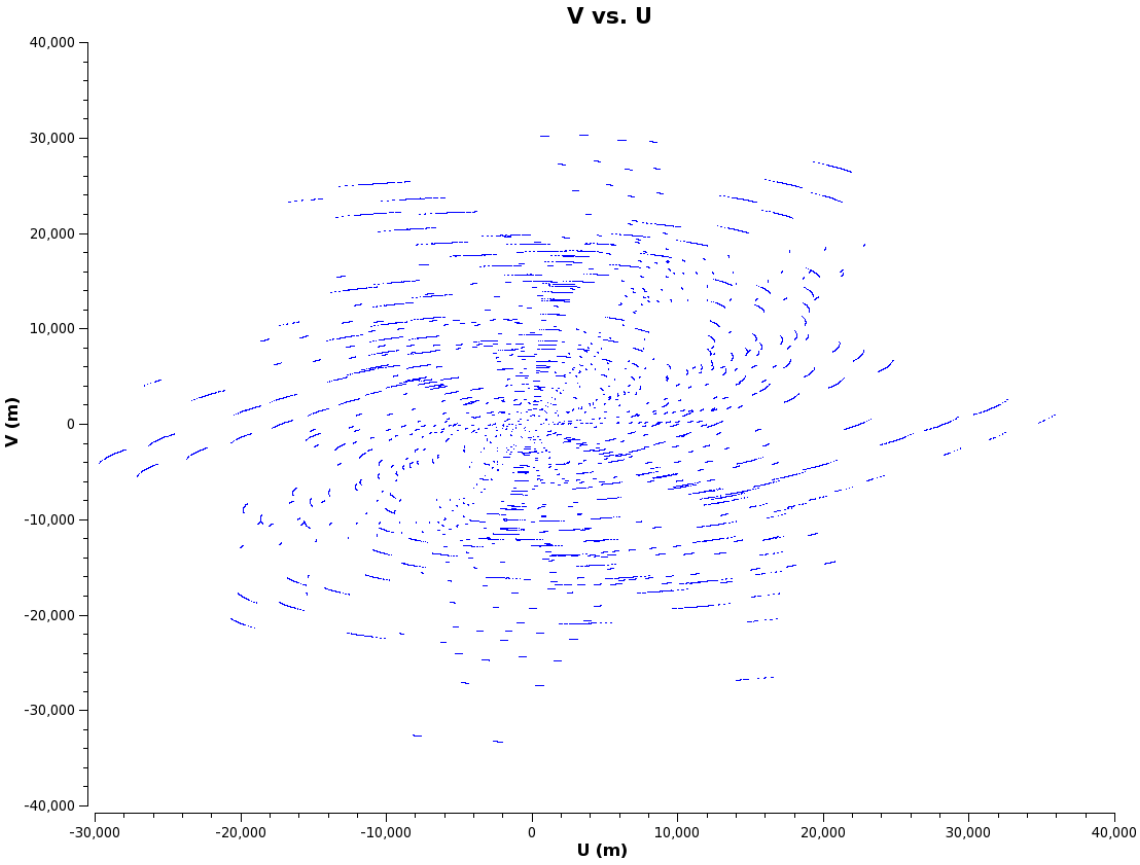

Figure 2.5: The uv coverage of an L band JVLA continuum observation of NGC 7385 in A array. Note the incomplete coverage and the central hole in the (u, v) plane.

where $a_i(t)$ is an amplitude correction and $\phi_i(t)$ is the antenna based phase correction. The term $g_{ij}(t)$ is the residual baseline-based complex gain and $g_{ij}(t) \approx 1$ is assumed in this thesis. This residual is usually within 1% of unity. Observations of calibrator sources in the sky determine the complex gain $\varsigma_{ij}(t)$ for each baseline. Calibrator sources are also used to monitor the stability of the phase of the array and phase changes caused by the atmosphere.

Before observations of a radio source can begin, instrumental parameters of the array must be determined. This includes the antenna pointing error, which is the difference between the actual pointing position and the desired position. Multiple effects can cause a misalignment between the two (e.g. Clark, 1973) including gravitational deformation, heating of the structure and atmospheric refraction. Interferometric observations of calibration sources are used to determine these offsets. Delay errors also occur; these can be geometric for the baseline (τ_g) or instrumental due to mis-calibration of the required delay (τ_r). Other instrumental parameters include path length changes due to the Earth's atmosphere and time and position errors of the calibration sources (see Fomalont and Perley, 1999 for a review).

Equation (2.8) indicates that the brightness distribution $I(l, m)$ is modified on the sky by the primary beam of the individual antennas $A(l, m)$. The primary beam for each observatory and antenna type is different, and for the VLA the primary beam is modelled on an Airy disk fitted to the measurements. The effects due to the primary beam are accounted for when the visibility functions are deconvolved, after the data have been calibrated.

2.3.1 Radio frequency interference

Significant amounts of the data recorded by a radio telescope can be of poor quality, due to array malfunctions or external effects such as radio frequency interference (RFI). Bad data can range from a few seconds per scan on a particular antenna pair to an entire antenna, or even an antenna arm throughout a long observation. Looking through the data for affected points is done manually, although CASA has a few automatic flagging programs which can detect outliers (e.g. *rflag*; Greisen, 2011). Data of poor quality are worse than no data at all, thus it is important to ensure that all scans look consistent and sensible.

Array problems such as broken elements or correlator malfunctions have relatively straightforward flagging protocols. RFI however, can cause problems across multiple

parameters including: antennas, time steps, frequencies and baselines. This makes it difficult to excise the bad data, leading to a reduced image sensitivity and poor calibration results. RFI is more problematic at low frequencies ($\leq$ 1.5 GHz) and the most significant contributors are satellites, radio channels and aeroplane communications. Most interfering sources radiate either in a fixed range of frequency or produce a broadband peak within a short time range.

For data which are strongly affected by RFI, Gibbs ringing may cause artefacts (Gibbs, 1899). Gibbs ringing can be removed by applying a Hanning-smoothing algorithm to the data. This algorithm is a running mean across the spectral axis with a triangle as a smoothing kernel. The channels are weighted differently, with a weighting of 0.5 for central channels and 0.25 for adjacent channels. This smoothing significantly reduces effects due to the Gibbs phenomenon, but degrades the spectral resolution of any images produced. Figure 2.6 shows a data set in CASA before and after applying the Hanning-smoothing algorithm. The smoothing has removed some of the prominent RFI peaks, most noticeably the peak at 1.09 GHz and between 1.24 and 1.26 GHz. Although some regions of errant data remain, performing this algorithm before RFI excision should allow one to retain as much good data as possible.

RFI flagging can be carried out manually or using an automatic flagging algorithm. The latter provides a much less time-consuming solution, although all scans should still be checked on a TV device (e.g. *plotms* in CASA). *rflag* is an auto-flag algorithm based on a sliding window statistical filter (Greisen, 2011). The data is iterated through chunks of time and statistics for these chunks are calculated. Flags are then applied to the data based on pre-defined or auto-calculated thresholds. Reports and plots are generated to show which channels have been flagged for specified antenna and spectral windows. An example is given in Figure 2.7 for spw = 1 (shown in Figure 2.6 coloured red between 1.075-1.130 GHz) and antenna pair 02 & 09. The top panel shows the pre-flagged data (flagged only from Hanning smoothing) and the bottom row shows the flags generated by *rflag*. The four windows correspond to different polarisation products, the x-axis represents the channel number for the assigned spectral index and the y-axis gives all integrations included in a time chunk. The threshold can be set by changing how sensitive the algorithm is to deviations from the calculated rms. In this example, *rflag* has increased the data flags from 52.8% to 59.7%.

RFI can also be automatically detected with the external package AOFlagger (Offringa

et al., 2010). This flagging framework uses several different methods to excise RFI. Implemented algorithms include the SumThreshold method, background fitting techniques (smoothing, sliding window, filters) and morphological operators. This program is used by default for the LOFAR radio telescope, and has been successfully used for the WRST, JVLA, ATCA and others.

2.3.2 Choosing a calibrator

To ensure that the instrument is producing reliable measurements, observations are calibrated by inserting a known signal at the input and analysing the resulting signal at the output. The calibration measurement will provide the corrections that need to be applied to the output signal in order to obtain the true representation of the incoming signal. The standardised uncorrected output signal from the instrument is known as the instrumental response. Determining the response for an interferometer is achieved by observing a point source in the sky with a constant and known flux density, polarisation and absolute sky position. It is assumed that calibrations are performed at a similar time to the target source so that corrections can be interpolated over the target observation.

The following calibrator requirements are needed to fully process interferometric radio data. A full description of each calibration step is given in subsequent sections.

- Absolute flux calibration : the correlator products RR, LL, RL and LR need to be adapted to represent the flux density as measured from the sky visibilities. This involves observing a calibrator with a known flux density at a given frequency. The most common flux calibrators observed by the VLA are 3C 138, 3C 147, 3C 286 and 3C 48. The model flux densities at multiple wave bands are available in CASA so that they can be used as the primary calibration source for most observations. The model scale used is based on the Perley-Butler standard (Perley and Butler, 2013) between 1-50 GHz, this scale is similar to the Baars scale (Baars et al., 1977).
- Pointing and delay calibration : inaccurate antenna positions or timings can cause small deviations from the correlator model. These deviations alter the phase of the data as a function of frequency. Observations of a strong source over a short time interval can correct for these effects and the primary flux calibrator is a good choice for this.
- Bandpass calibration : small errors in the frequency dependent part of the gain ς_{ij} also need to be corrected for. A good bandpass calibrator is a bright, flat spectrum source

with featureless spectra. The structure of the bandpass calibrator can be examined in CASA to check the channel to channel variation of the phase and amplitude with frequency before applying it to the desired source. An example of this calibration check is shown in the Figure 2.8. The primary flux calibrator is often used to calibrate the bandpass.

- Phase and amplitude gain calibration : time variable instrumental imperfections such as from environmental effects cause fluctuations in the antenna gain. These can be corrected by repeatedly observing a calibrator source in order to measure the change in visibility amplitude and phase with time. These changes are then interpolated over the target source scans. The gain amplitudes are determined by reference to a standard flux density calibrator. The gain phase calibrator needs to be a source close to the target source in order to minimise differences in signal through the atmosphere.
- Polarisation calibration : in order to obtain the correct polarisation characteristics of the target source, two different calibrations have to be carried out. The first calibration solves for the leakage between orthogonal signals and this can be achieved by observing an unpolarised source or a source with an unknown polarisation but a wide-range in parallactic angle. Secondly, a reference source with a known polarisation needs to calibrate for the polarisation angle. A list of appropriate sources and their polarisation angles for different frequencies is given in the VLA Polarimetry Manual.

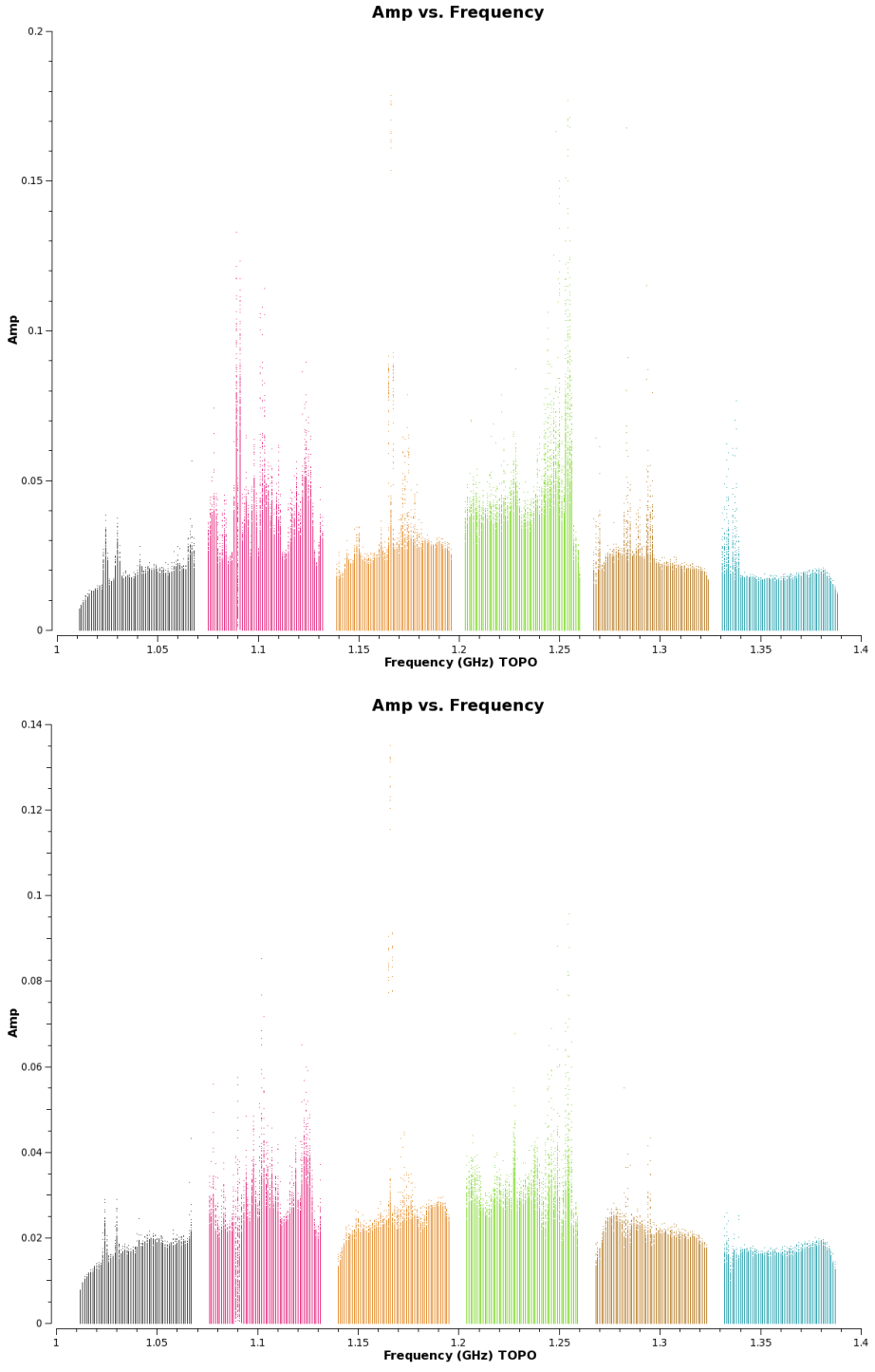

Figure 2.6: Plot of the frequency against amplitude for an L band dataset affected by RFI, taken with the JVLA in A array. The frequency ranges have been colourised by spectral window. *Top:* before Hanning-smoothing. *Bottom:* the dataset after it has been Hanning smoothed. There is a noticeable decrease in data spikes in the bottom image, particularly at $\sim$1.09 GHz.

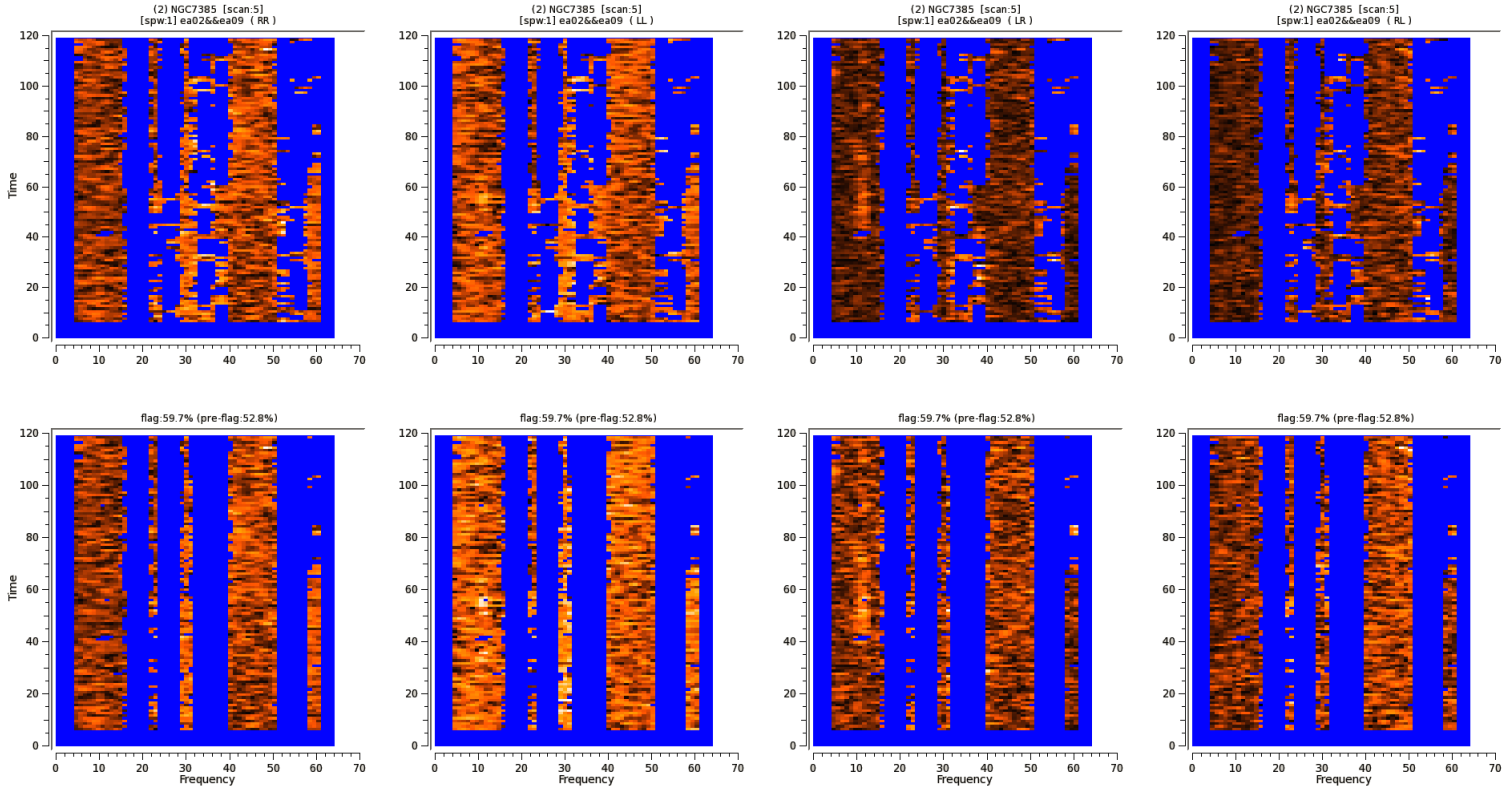

Figure 2.7: Results from applying *rflag* in CASA. The top panels show the pre-flagged data for the correlations RR, LL, LR and RL respectively, and the lower panels show the flags after *rflag* has been calculated for these same correlations. For this task, σ = 5 for both time and frequency. The image shows the results for spw = 1 and antenna pair = 02 & 09 for the pre-calibrated VLA data for radio source NGC 7385.

2.3.3 Bandpass calibration

Bandpass calibration is the process of measuring and correcting the frequency dependent part of the gain ς_{ij}. Bandpass calibration is important in spectral line observations where radio sources may emit most of their radiation in a narrow frequency range, and the resolution in frequency needs to be sufficient to separate emission regions at different radial velocities. For continuum measurements, it is assumed that there are no important changes in the visibility within the integrated band and that effects of chromatic aberration are negligible. However these conditions may not be met, in which case it is important to generate the coherence as a function of frequency since bandpass errors can limit the dynamic range of the observations.

A strong calibrator source with a flat spectrum is observed to determine the relative frequency response of a set of frequency channels. Since the true visibility is identical in all channels for a calibrator, the bandpass complex correlator based gain function for the baseline $i-j$ and the k^{th} frequency channel is the observed visibility $\tilde{V}_{ij}(\nu_k)$ divided by the true visibility $V_{ij}(\nu_k)$. The individual frequency-dependent, baseline-dependent gains can be factored into products of antenna based gains, giving antenna based amplitude and phase calibrations. The bandpass function does not vary strongly with time and only one calibration per observing block is required.

2.3.4 Gain calibration

Gain calibration is carried out to remove long term atmospheric and instrumental gain variations. To derive corrections for the complex antenna gain $\varsigma_{ij}(t)$, you can assume that for a point source calibrator of known flux density S, the phase is zero. This gives

$$\varsigma_{ij}(t) = \frac{\tilde{V_{ij}}(t)}{S} \tag{2.17}$$

This assumes that the offset term $\epsilon_{ij}(t)$ from equation 2.15 has been removed or is negligible and that the noise term $\eta_{ij}(t)$ is negligible after data have been averaged in the scan. From equation 2.16, the complex gain $\varsigma_{ij}(t)$ can be separated into expressions for amplitude A_{ij} and phase ϕ_{ij} as:

$$A_{ij}(t) = a_i(t)a_j(t)a_{ij}(t) \tag{2.18}$$

$$\phi_{ij}(t) = \phi_i(t) - \phi_j(t) + \phi_{ij}(t) \tag{2.19}$$

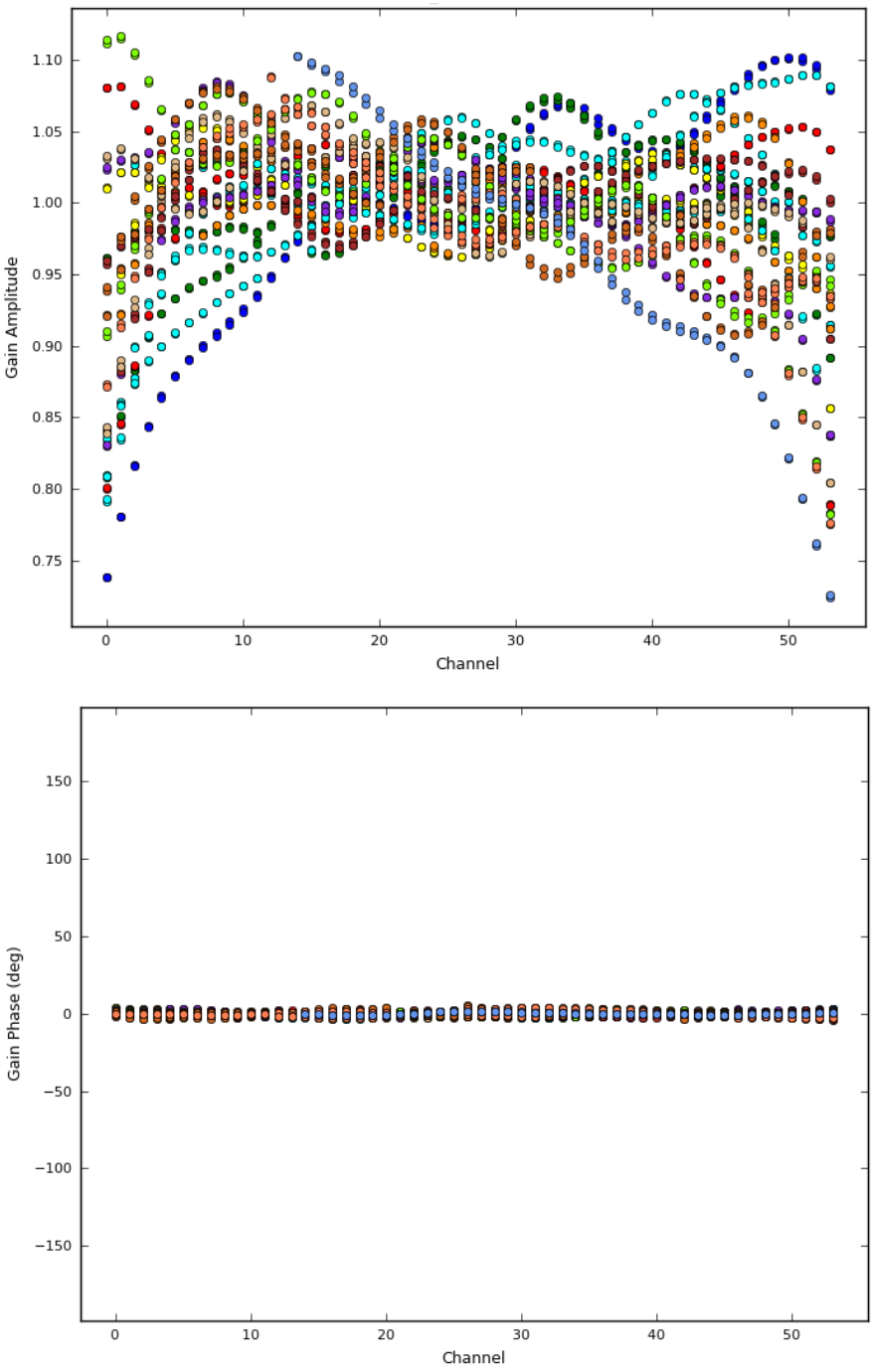

Figure 2.8: Plots of the bandpass calibrator 3C 48 showing the amplitude *(top panel)* and phase *(bottom panel)* variation with channel for the first antenna in the array. The different colours indicate different frequency bands and polarisations, R and L. There is a noticeable drop in the gain amplitude at the edge channels, so these are excluded from the calibration. The gain phase is stable across all channels.

If the true visibility is represented as $V_{ij} = A_{ij} \exp i\phi_{ij}$, and the observed visibility as $\tilde{V}_{ij} = \tilde{A}_{ij} \exp i\tilde{\phi}_{ij}$ then for the point source calibrator

$$\tilde{A}_{ij} = a_i a_j a_{ij} S \tag{2.20}$$

$$\tilde{\phi}_{ij} = \phi_i - \phi_j + \phi_{ij} \tag{2.21}$$

These equations can be solved for a_i and ϕ_i for all N antennas, provided that g_{ij} is close to unity.

Antenna-based calibration values are preferred to baseline-based values because instrumental variations are related to particular antennas. The number of baselines in an array of N elements is far larger than N, and so the computer storage capacity is significantly reduced using antenna-based values. Additionally, the antenna-based values are fitted from $N_{\text{vis}} >> N$ data points, giving high redundancy and cross-checks.

Figure 2.9 shows the gain phase and amplitude solutions for the calibrator 3C 48. These plots are useful to ensure that smooth solutions for each antenna are produced as a function of time.

2.3.5 Polarisation calibration

As described in chapter 1, the synchrotron radiation produced in the jets of radio sources is polarised. An elliptically polarised wave can be well described as the superposition of two orthogonal linearly polarised waves. Polarisation measurements are made using a pair of feeds on each interferometer element. These feeds are sensitive to either orthogonal circular or linear polarisations, and for the VLA it is the former.

The spatial coherence of the electric field vector can be described by four correlations. If the dual polarisation feeds measure the right circular polarisation R and the left circular polarisation L, then the four visibility functions are $R \cdot R, L \cdot L, R \cdot L$ and $L \cdot R$.

There are a number of effects that can corrupt or change the polarised signals. An instrumental contribution to the measured polarised signal is introduced by antenna feeds even for unpolarised sources, and the phase relation of the signals detected by the two feeds for any interferometer element can be distorted by both ionospheric Faraday rotation and by the interferometer electronics.

The four visibility functions can be expressed in terms of the Stokes parameters

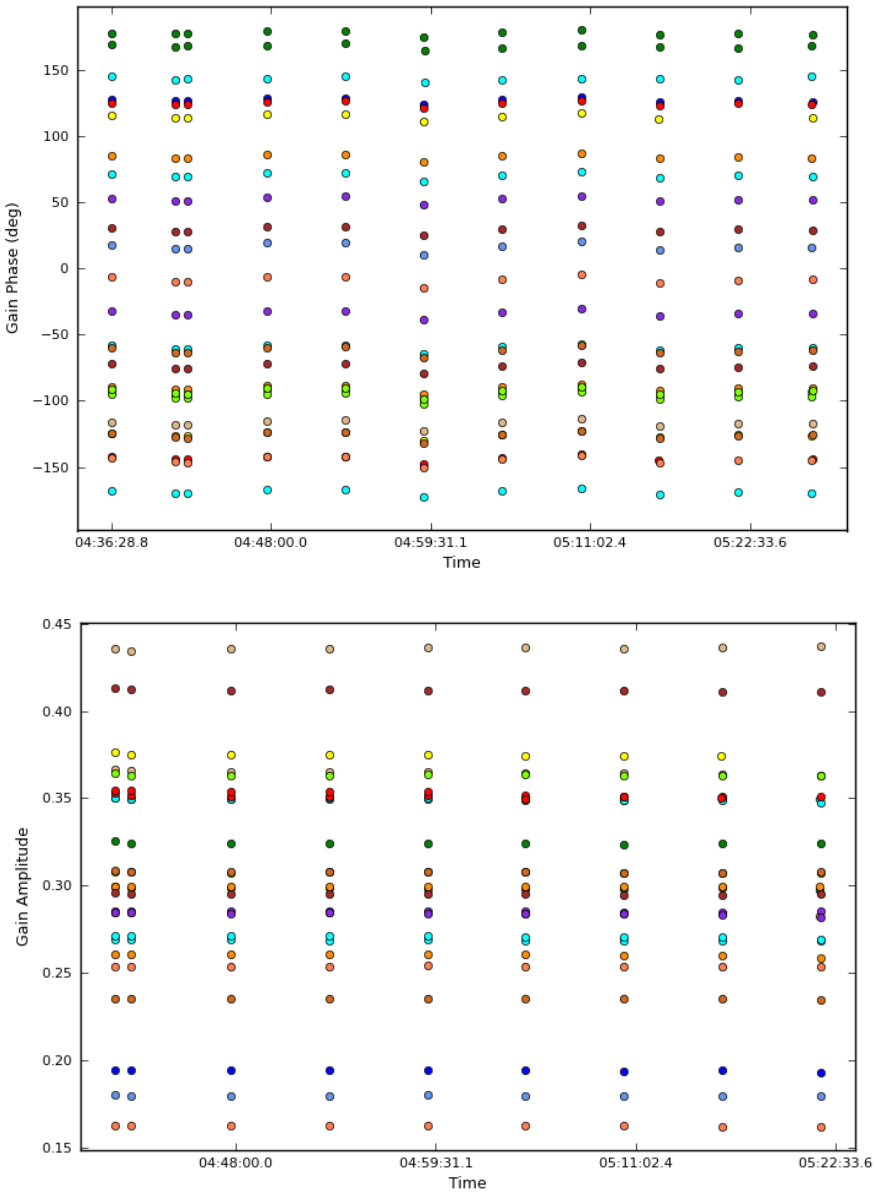

Figure 2.9: Plots of the gain calibrator 3C 48 showing the phase *(top panel)* and amplitude *(bottom panel)* variation with time for the first antenna in the array. The different colours indicate different frequency bands. Each frequency band shows a smooth variation in gain phase with time, and a stable amplitude.

I, Q, U and V. The interferometer produces a linear combination of the Stokes parameters and this information can be used to characterise the polarisation state of the radiation from the target. The I, Q, U and V visibilities are related to the correlated voltages as

$$\tilde{V}[R \star R] = \tilde{V}_I + \tilde{V}_V \tag{2.22}$$

$$\tilde{V}[L \star L] = \tilde{V}_I - \tilde{V}_V \tag{2.23}$$

$$\tilde{V}[R \star L] = (\tilde{V}_Q + i\tilde{V}_U)e^{-2i\chi} \tag{2.24}$$

$$\tilde{V}[L \star R] = (\tilde{V}_Q - i\tilde{V}_U)e^{2i\chi} \tag{2.25}$$

where χ is the parallactic angle which determines the orientation of the feed with respect to the sky and $\star$ denotes the cross correlation between the two visibility functions.

2.3.5.1 Leakage terms

When observing in a continuum mode the cross hand correlations RL and LR are produced automatically for each channel. Because the circular feeds are not exactly orthogonal, a small amount of right circular polarisation can show up in the left channel and vice versa.

The response of an antenna i with orthogonally polarised feeds p and q can be expressed using Jones matrices. A detailed discussion of these matrices can be found in Sault et al. (1996). In this formalism, the antenna response to the polarisation leakage J_i is defined in terms of a number of physically different components:

$$J_i = G_i D_i P_i \tag{2.26}$$

The gain term, G_i describes the uncorrected effects of the atmosphere and electronics and is represented in terms of complex gain factors g_{ip} and g_{iq} for the two orthogonal signals as:

$$G_i = \begin{pmatrix} g_{ip} & 0 \\ 0 & g_{iq} \end{pmatrix} \tag{2.27}$$

The D_i term represents the imperfections in the feed polarisation response, with terms d_{ip} and d_{iq} that describe how much polarisation is 'leaking' into a given feed. This term is expressed as:

$$D_i = \begin{pmatrix} 1 & d_{ip} \\ -d_{iq} & 1 \end{pmatrix} \tag{2.28}$$

The final factor P_i includes the effects of the rotation of an alt-az mounted antenna (e.g. VLA, VLBA, ATCA). It is expressed in terms of the parallactic angle χ, which is dependent on the source declination δ, the latitude of the antenna λ and the source hour angle h as:

$$\chi = \tan^{-1}\left(\frac{\cos(\lambda)\sin(h)}{\sin(\lambda)\cos(\delta) - \cos(\lambda)\sin(\delta)\cos(h)}\right) \tag{2.29}$$

The parallactic angle χ has an effect on the measured signals from a circular feed given by

$$P_i = \begin{pmatrix} e^{-j\chi} & 0 \\ 0 & e^{j\chi} \end{pmatrix} \tag{2.30}$$

In this matrix, $j = \sqrt{-1}$ to avoid confusion with the antenna i.

These equations assume that the p feed is oriented north-south when observing a source on the meridian and that the q feed is at 90° to this. If the feeds are rotated from this orientation, it will be incorporated into the calibrator solution tables.

The polarisation leakage J_i can be expressed in terms of the interferometer response to polarised radiation as $\nu = (qq, qp, pq, qq)$. Hamaker et al. (1996) show that the response for circularly polarised feeds on baseline $i - k$ can be expressed as:

$$\nu_{pp} = \frac{1}{2} g_{ip} g^*_{kp} (I + V) \tag{2.31}$$

$$\nu_{pq} = \frac{1}{2} g_{ip} g^*_{kq} ((d_{ip} - d^*_{kq})I + e^{-2j\chi}(Q + jU)) \tag{2.32}$$

$$\nu_{qp} = \frac{1}{2} g_{iq} g^*_{kp} ((d^*_{kp} - d_{iq})I + e^{2j\chi}(Q - jU)) \tag{2.33}$$

$$\nu_{qq} = \frac{1}{2} g_{iq} g^*_{kq} (I - V) \tag{2.34}$$

The leakage terms can be calculated by observing a strong, unpolarised and unresolved source so that the observed visibility in the cross hand channels are simply the sum of two leakage terms. Alternatively, D terms can be determined from a source with unknown polarisation but good parallactic angle coverage. This is because as the parallactic angle changes the polarisation of the calibrator will appear to rotate in the sky while the instrumental contribution remains constant. For the VLA, D values can be up to 5% in the centre of channels and worse at the edges, therefore it is often necessary to ignore the edge channels when solving for the leakage terms.

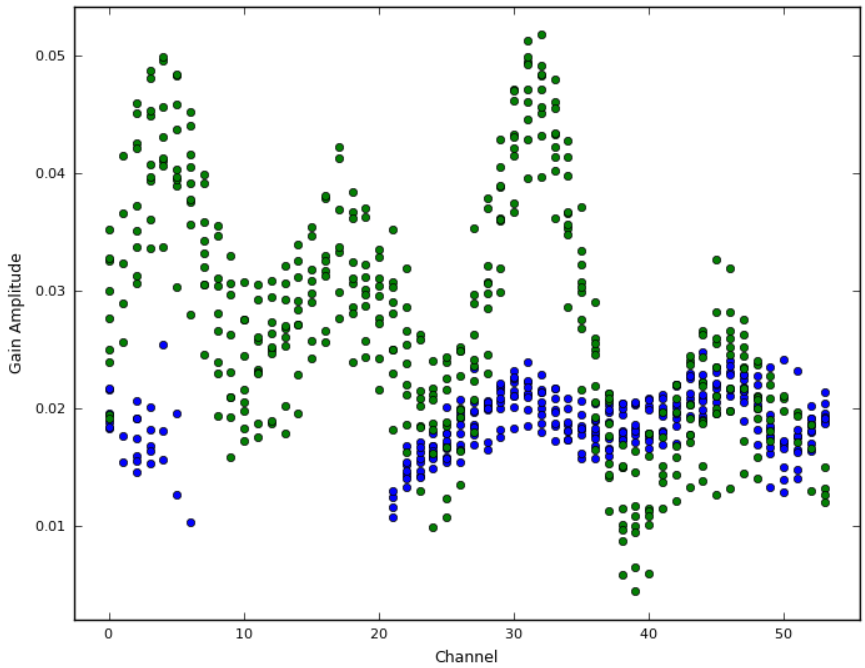

Figure 2.10: The D terms for a polarisation calibrator for a single antenna and across a single frequency band. The different colours represent the R and L hand correlations. The amplitude shows a maximum of approximately 5% for channels in the range 0-5 and 25-35.

Figure 2.10 shows the amplitude against channel plots for the D terms calculated from a polarisation calibrator; here the leakage is just over 5%. After calibration, residual D terms should be around 0.1%.

2.3.5.2 R-L polarisation angle calibration

Independently calibrating the p and q circular systems will leave an unknown phase difference between them. This phase difference will cause a rotation of the Stokes parameters $Q + iU$, resulting in a rotation of the polarisation position angle of the source. Although this angle offset will not affect the quality of the final image or measures of the fractional polarisation of the source, it will produce the wrong polarisation position angle. Calibration of the phase difference can be accomplished by observing a strongly linearly polarised radio source with known $Q + iU$ values and choosing a reference antenna with a gain phase set to zero. The calibrator source should have a stable fractional polarisation and polarisation position angle over the observed frequency range.

2.3.5.3 Ionospheric Faraday rotation

As discussed in chapter 1, the orientation of an electromagnetic wave can rotate as it propagates through a magnetised medium. Radio waves passing through the Earth's ionosphere are subject to Faraday rotation due to free electrons in the plasma. Since ionospheric rotation is time variable, it can produce incorrect polarisation angles for observations. It is also dependent on the density of electrons, which can increase near a maximum in solar activity. It is mainly a problem for low frequency observations, below about 2 GHz.

Ionospheric corrections used for the VLA are derived from a GPS receiver, by monitoring the total electron content along the line of sight to GPS satellites above the horizon at any one time. A model of the ionosphere at the time of the observations is then created from the measurements (Erickson, 1999).

2.3.6 Applying the calibrations

After carrying out polarisation and gain calibrations, the gain amplitude for the primary flux calibrator can then be scaled onto the other calibrators. This allows the true flux density of the secondary calibrators to be determined. The output can be checked in the VLA Calibrator Manual for consistency, although many of the calibrator sources are highly variable at high frequencies.

All the calibration solutions can then be applied to the actual target source. The gain solutions from the phase calibrator are linearly interpolated onto the target. Despite the gains on the phase calibrator being derived at a different time and different position on the sky, this is a reasonable approximation to make if the calibrator is sufficiently close to the target and the weather at the time of observing was stable.

2.4 Imaging

One of the foundations of radio synthesis imaging is that the visibility $\tilde{V}(u,v)$ observed with an interferometer as a function of baseline coordinates can be Fourier transformed to give the sky brightness distribution $I(l,m)$ as a function of sky coordinates. These functions are related by equation (2.8):

$$A(l,m)I(l,m) = \int\int \tilde{V}(u,v)e^{2\pi i(ul+vm)}dudv \tag{2.35}$$

This relation holds provided that $|w(l^2 + m^2)| << 1$. The primary beam $A(l, m)$ is corrected for as part of the imaging process, so for simplicity I will use $I(l, m)$ to denote the modified sky brightness, $A(l, m)I(l, m)$ for the rest of this section.

The visibility function $\tilde{V}$ after calibration is expressed in units of flux density (Janksy, 1 Jy = 10^{23} erg cm^{-2} s^{-1} Hz^{-1}), while I has units of surface brightness (flux density per unit of solid angle). The standard unit for I is Jy / beam area.

Aperture synthesis is based on the idea of sampling the $\tilde{V}(u, v)$ plane at enough (u, v) points using an array of antennas to synthesise a larger aperture antenna of size $(u_{\text{max}}, v_{\text{max}})$. If an array has N antennas then it can cover $N(N - 1)$ samples at a time. In addition, the rotation of the Earth can fill in the (u, v) plane over time.

In practice, the function V is not known everywhere but is sampled at particular places on the (u, v) plane. This introduces the discrete sky brightness distribution I^D as

$$I^D(l, m) = \int\int V_\nu(u, v)S(u, v)e^{2\pi i(ul+vm)}dudv \tag{2.36}$$

here the sampling function $S(u, v)$ can be expressed in terms of the Dirac delta function at M sampling locations (u_k, v_k):

$$S(u, v) = \sum_{k=1}^{M} \delta(u - u_k, v - v_k) \tag{2.37}$$

It is useful to introduce the sampled visibility function V^S, such that $V^S = S\tilde{V}$:

$$V^S(u, v) = \sum_{k=1}^{M} \delta(u - u_k, v - v_k)\tilde{V}(u_k, v_k) \tag{2.38}$$

Let $\mathcal{F}$ denote the Fourier transform operator, then the discrete sky brightness distribution I^D is given by

$$I^D = \mathcal{F}V^S = \mathcal{F}(S\tilde{V}) = (\mathcal{F}S) * (\mathcal{F}\tilde{V}) \tag{2.39}$$

by the convolution theorem (e.g. Bracewell, 1986). The Fourier transform of the sampling pattern is the called the point spread function (PSF). Radio astronomers often refer to I^D as the 'dirty image', which is the true image convolved with the 'dirty beam'.

It is difficult to do science with the dirty image, so it is deconvolved with the dirty beam to give a model image of $\tilde{V}$. Deconvolution uses non-linear techniques to interpolate samples of $V(u, v)$ into unsampled regions on the (u, v) plane. In order to find a sensible model of $\tilde{V}$, some assumptions need to be made.

2.4.0.1 Weighting

Weighting functions $W(u,v)$ can be used to control the shape of the synthesised beam. Weighting modifies the sampling function to give

$$S_w(u,v) = S(u,v)W(u,v) \tag{2.40}$$

The weighting function is defined by $W(u,v)$ = $R_k T_k D_k$, where R, T and D are weights assigned to the visibility points k. The coefficient R_k describes the reliability of the k^{th} visibility point and is dependent on the system temperature, integration time and bandwidth. D_k is the density weighting and is used to simulate more uniform (u,v) coverage, and T_k is the tapering function which suppresses sidelobes and increases the beam width. Different configurations of these coefficients describe different weighting functions used in radio synthesis imaging.

A 'natural' weighting is provided when D_k = 1 and $W(u,v)$ = 0 in unoccupied cells. This weighting maximises the point source sensitivity and therefore gives the best signal to noise ratio for detecting weak sources. It generally gives excess weight to short baselines however, resulting in poorer images for sources with both large scale and small scale structure.

'Uniform' weighting describes $D_k = 1/N_s(k)$, where $N_s(k)$ is the number of data points within a region of width s. $W(u,v)$ is therefore inversely proportional to the local density of the (u,v) points, filling the plane more uniformly and lowering the sidelobes of the dirty beam. This gives more weight to long baselines, thus enhancing the angular resolution but decreasing the sensitivity.

'Briggs' or 'robust' weighting is a variant of uniform weighting that allows for continuous variation between maximum point source sensitivity and angular resolution. A more detailed discussion of this weighting scheme is given by Briggs (1995).

2.4.0.2 Gridding

Two methods are commonly used to approximate the Fourier transform. These are the 'direct Fourier transform', and the 'fast Fourier transform' (FFT) techniques. The second algorithm is much faster than the first, however it involves interpolating the data onto a rectangular grid. Aperture synthesis does not provide $V(u,v)$ on a regularly spaced grid thus 'gridding' must be used to resample $V(u,v)$ for FFT. This interpolation is achieved

by convolving the weighted, sampled measurement distribution with some chosen function C. Some typical choices for C are

- A 'pillbox' function
- An exponential function
- A sinc function
- A prolate spheroidal function

For an in depth discussion of these functions, see Schwab (1984).

2.4.0.3 Imaging parameters

Before deconvolving the weighted, sampled and gridded visibility function, some imaging decisions need to be made in order to achieve the best resolution and field of view for the required target source. The size of the pixels must satisfy the sampling theorem for the longest baselines, i.e.

$$\Delta l \leq \frac{1}{2u_{\text{max}}} \tag{2.41}$$

$$\Delta m \leq \frac{1}{2v_{\text{max}}} \tag{2.42}$$

In addition, 3-5 pixels across the dirty beam is optimal to aid deconvolution and the size of the image is usually chosen to represent the full extent of the primary beam $A(l, m)$. These parameters can be controlled with the CASA inputs 'cell size' and 'imsize' respectively.

2.4.0.4 CLEAN algorithm

The CLEAN algorithm (Högbom, 1974) is a method of deconvolution in radio astronomy, which assumes that $\tilde{V}$ is a collection of point sources in an otherwise empty field of view. An iterative approach is used to locate and measure the flux of the point sources, and the final deconvolved image is the sum of these point sources convolved with a CLEAN beam. The basic Högbom CLEAN algorithm works as follows:

1. Initialise a 'residual' map, which is the dirty image I^D before any iterations have been carried out.
2. Identify the highest peak in the residual map as a point source.

3. Subtract from the residual map, at the position of the peak, some fraction of the strength (some factor of the dirty beam, termed the gain γ).
4. Record the position and the magnitude of the point source in a CLEAN component list.
5. Return to step 1, unless the remaining peak strength is below a user-specified level.
6. Convolve the set of point sources with an elliptical Gaussian CLEAN beam fitted to the central lobe of the dirty beam.
7. Add the residuals of the dirty image to the CLEAN image with all point source components.

The resulting CLEAN image is an estimate of the true sky brightness. The units of the restored image are usually Jy / beam area, where I Jy = 10^{-26} W m^{-2} Hz^{-1}.

Figure 2.11 shows images to accompany the steps involved in the algorithm for the radio source NGC 6109. The CLEAN parameters use a Briggs weighting with robust parameter 0.5, a cell size = 0.1 arcsec and an image size = [1024, 1024] pixels. The first image shows the dirty map generated by the initial run of CLEAN. The second shows the CLEAN components after 1000 iterations, the third shows the residual map after these iterations have been subtracted and the final image shows the restored image after 1000 iterations.

The quality of a restored image can be improved by using a mask to advise CLEAN where the emission is deemed to be real can reduce the noise within an image. Furthermore, it is also possible to set a stopping threshold to define when CLEAN should finish iterating. This threshold could be a multiple of the rms noise or some fraction of the dirty map maximum, if the dynamic range is limited. The number of CLEAN iterations N_{cl} and the gain γ determine how deep the dirty image is cleaned. The residual left over for a point source on the dirty image is (1-γ)$^{N_{cl}}$ of the initial peak. For synthesis imaging with the VLA and using CASA, $0.1 \leq \gamma \leq 0.25$ is usually adopted.

The CLEAN algorithm of Högbom was developed further by Clarke (1980). Clarke's algorithm uses a two-dimensional FFT and finds approximate positions and strengths of the components via CLEAN using only a small patch of the dirty beam. This is much faster than the calculation of the PSF by Högbom; however this is less effective if there is poor uv-coverage. The CASA task *clean* has both algorithms which can be selected using the 'psfmode' parameter.

Another process for improving the dirty map is the Maximum Entropy Method (MEM). This method looks for the most probable solution to the determination of the true source

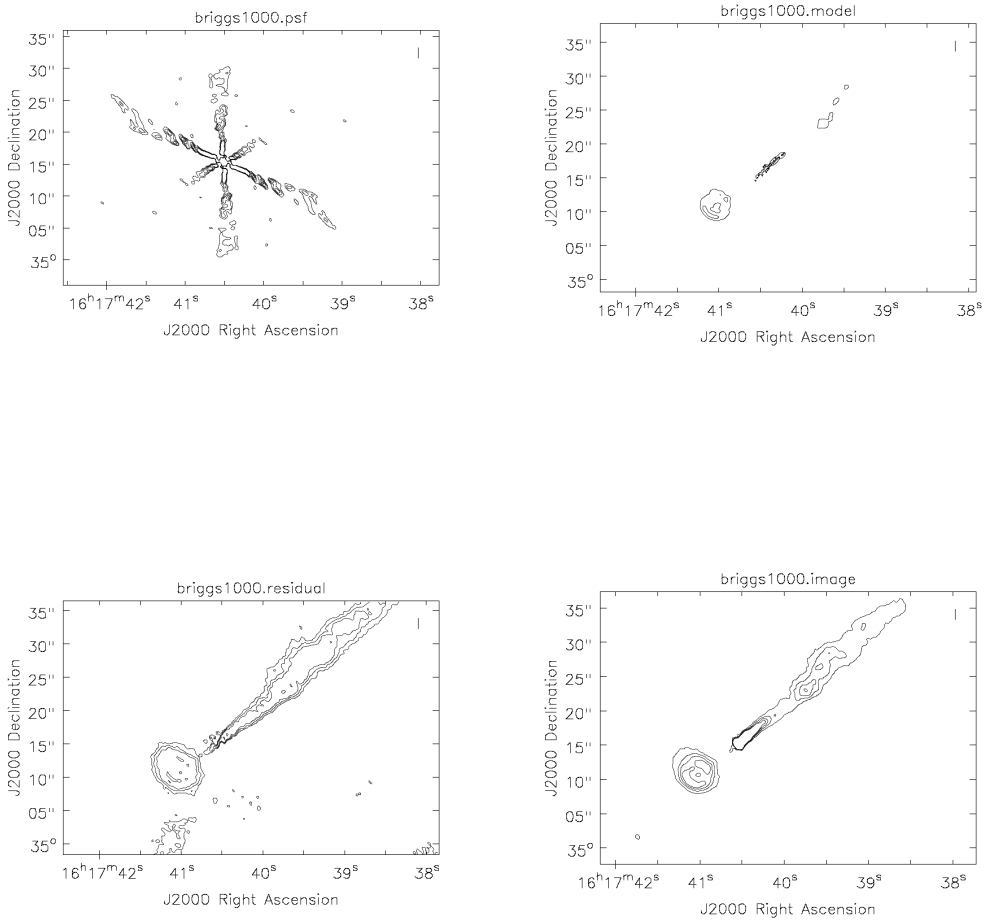

Figure 2.11: The different stages of the CLEAN process. *(a)* shows the contours of the dirty beam, with levels 60, 120, 180 and 240 mJy beam^{-1}; *(b)* shows the CLEAN components after 1000 iterations with contour levels 0.08, 0.16, 0.24 and 0.32 mJy beam^{-1}; *(c)* shows the residual / beam map after these iterations have been subtracted with contour levels 0.4, 0.8, 1.2 and 1.6 mJy beam^{-1}; *(d)* shows the restored image after 1000 iterations with contour levels 1, 2, 3 and 4 mJy beam^{-1}. CLEANing wasn't taken to its usual depth (to remove most of the source flux density) for this example.

structure by forcing all regions of a map to display a positive brightness temperature and compressing the range of pixel values (Narayan and Nityananda, 1986). MEM is often preferred for very large data sets since it requires less CPU time but has the problem that the effective synthesised beam-size depends on the local signal to noise ratio of the features.

2.4.0.5 Multi-frequency synthesis imaging

For wide-band imaging, broad-band receivers are used to increase the continuum sensitivity. Multi-frequency synthesis (MFS) imaging involves gridding visibility data from different frequency channels separately to eliminate bandwidth smearing. This process also augments the deconvolution process to take into account spectral variations across the observing band. The aim of MFS algorithms are to increase the uv-coverage used in deconvolution (Conway et al., 1990) and produce continuum images with a high dynamic range. Observing at a number of frequencies N_f enhances the measured baselines from $N(N-1)/2$ to $N_f N(N-1)/2$, which is the equivalent effect of introducing roughly $\sqrt{N_f}$ extra antennas.

Simple MFS algorithms assume that the source has a flat spectrum across the frequency band. If the spectrum is not flat, all visibility values after combined gridding of multi-channel data do not represent the same source flux and deconvolution errors will occur. MFS in the CASA task *clean* uses the Sault-Wieringa (Sault and Wieringa, 1994) cleaning method to model the wide-band sky brightness as a linear combination of Gaussian-like functions with amplitudes that follow a Taylor polynomial in frequency. This algorithm models the source spectrum in terms of both an amplitude and a frequency slope. This allows the user to produce both a continuum and spectral index map and is more effective in recovering the full dynamic range of the image (Rau and Cornwell, 2011). The Taylor expansion is usually stopped after a few terms and may not be valid over large bandwidths. This is due to effects of combining measurements from a large range of frequencies, namely varying ranges of sampled spatial scales and array-element response functions. In addition, including multiple Taylor terms does not automatically support primary beam correction and flux variations across the chosen frequency range must be more than twice the channel noise level in order to obtain reliable spectral indices.

2.4.1 Self-calibration

Calibration using external calibrators will never yield perfect results because the calibrators were observed at a different time and direction to the target source; both tropospheric and ionospheric effects are time variable and non-uniform across the sky. Improvements are possible however, because the array gives over-determined information. There are residual errors in the phase and amplitude for each element N in the array. Assuming that a reference antenna is chosen, there are then $2N - 2$ error parameters. Since there are $N(N - 1)$ complex visibilities, this is higher than the number of error parameters provided that $N > 3$ for a subset of VLA antennas. Schwab (1984) describes the most commonly used method for using the redundant information, known as self-calibration.

It is possible to self-calibrate the target source, by combining corrections for the antenna based phase and amplitude errors with imaging. This is an iterative process which creates a source model with the following steps:

1. Assume a source model constructed from the calibrated visibilities, usually from the first run of CLEAN.
2. Solve for time dependent gains, using the target source as the gain source and apply these calibrations to the target source.
3. Form a new source model from the corrected data using CLEAN.
4. Repeat step 2, until some assigned signal to noise level has been reached.

Schwab's procedure minimises the difference between the model visibility and the observed visibility in a least-squares sense. Since it is a non-linear procedure, no convergence proofs have been found for self calibration. Cornwell and Fomalont (1989) showed that the procedure works best when initially only the phases of the complex gains are varied, and then, when there seems to be a strong convergence of the phase-only solutions, the amplitudes are included.

Self-calibration is also effective at improving the dynamic range of the image, i.e. the ratio of peak brightness to noise in a region with no emission.

2.4.2 Image analysis

Once images have been produced to a good standard, they can be used to investigate a wide variety of physical properties of the source. In this thesis I am interested in determining the polarisation properties of radio sources and so the methods for producing polarisation maps are discussed below.

2.4.2.1 Primary beam correction

After a good quality image has been produced, the image must be corrected for the relative sky sensitivity. This is the primary beam correction and is modelled by a power law expansion of the form of equation (2.43), where $X = \theta_{\text{arcmin}}\nu_{\text{GHz}}$ and the coefficients are given by Napier (1982) for the VLA.

$$\frac{1}{A} = \sum a_i X^{2i} \tag{2.43}$$

Problems may arise for primary beam correction if the primary beam is not circularly symmetric for antennas with azimuth-elevation mounting. This is because the primary beam changes over a period of hours thus there is no unique primary beam associated with the target observations. In addition, at the VLA the primary beam correction for the four correlation channels is different. Therefore each correlation must be processed independently and then combined after it has been corrected for its individual beam. The primary beam of the antennas can be accounted for during the CLEAN phase of the data reduction. If only one Taylor term is modelled in the deconvolution, *clean* can correct for the primary beam during imaging. Primary beam correction can also be carried out after imaging, using the task *impbcor* for regular datasets, and *widebandpbcor* for those that use multiple Taylor term expansion. The primary beam must be accounted for before flux densities can be extracted from the image.

2.4.2.2 Magnetic field structure and spectral index

Image display is an important aid in image analysis. In CASA, the *viewer* task displays grey-scale and colour maps essential for highlighting the intensity distribution of a source. It can also display contours and vectors to draw attention to small scale structure and field directions.

Running a full polarisation CLEAN will yield four separate images of the I, Q, U and V Stokes parameters. Checking that the V image shows no structure is a good consistency check for the calibration applied. Any significant V emission could also indicate unflagged RFI within the data.

The separate Stokes images can be combined to produce maps of the fractional polarisation P and the polarisation position angle χ, as given by

$$P = \frac{\sqrt{Q^2 + U^2}}{I} \tag{2.44}$$

$$\tan 2\chi = \frac{U}{Q} \tag{2.45}$$

It is important to specify the threshold intensity of the linear polarisation, so that the position angle and fractional polarisation is not biased by the noise. In addition, contour maps of the primary beam corrected intensity can also be created. These maps then allow one to inspect the apparent magnetic field structure within the target source, by rotating the polarisation position angle by 90°.

The spectral index α of synchrotron emission is related to the source flux S at frequency ν by $S \propto \nu^{-\alpha}$ and it can be mapped in two ways. Firstly, through first-order Taylor expansion during the imaging process (see section 2.4.0.5) and secondly α can be extracted from the radio flux densities at two different frequencies, as α = - log($S_{\nu 1}$/ $S_{\nu 2}$) / log(ν_1 / ν_2). This is the safer option to use since the MFS imaging method is still experimental and can produce poor results in low signal to noise regions near bright components. α is a useful parameter that can convey information about the emission mechanism, the optical depth of the source, and the energy distribution of the population of synchrotron particles.

2.4.3 Sensitivity and image errors

In an observation of a weak and unresolved target source, the image sensitivity is equal to the sensitivity of all the interferometer combinations over the integration time of the target. This noise limit reveals the weakest source of radio emission that can be detected. The derivation of image sensitivity is given by Walker (1995), who finds that the sensitivity of a single polarisation image formed from an array with N antennas can be given by

$$\Delta I_m = \frac{\sqrt{2} k_B T_{\text{sys}}}{A\eta\sqrt{N(N-1)\Delta\nu t_{int}}} \tag{2.46}$$

in units of Jy / beam area. Here, T_{sys} is the system temperature, A is the area of each antenna, η is the aperture efficiency, $\Delta\nu$ is the observing bandwidth and t_{int} is the integration time. Extending this to dual polarisation data, the sensitivity of an image of Stokes parameter I, Q, U or V follows

$$\Delta I = \Delta Q = \Delta U = \Delta V = \frac{\Delta I_m}{\sqrt{2}} \tag{2.47}$$

The sensitivity of many modern interferometers after a few minutes of integration is $\sim$ 100 μJy / beam. Image sensitivity can be degraded by effects that lead to high noise levels at the edges of images (Crane and Napier, 1989). This could be due to FFT issues or antenna primary beam gain patterns. Self-calibration of the data can also lead to a reduced sensitivity by a factor of $\sqrt{(N-1)/(N-3)}$ (Cornwell and Fomalont, 1989).

2.4.3.1 Image errors

A key property of Fourier transforms is that a sharp peak in one domain transforms to a broad feature in the other, and vice versa. Therefore the Fourier transform of a serious error in the (u, v) plane may have little to no effect on the image; however an error which is spread out in the (u, v) plane can greatly affect the final image. This is highlighted by how it is possible to make a reasonable quality radio image even when not all of the (u, v) plane has been sampled.

If the errors are in the (u, v) plane, then plotting the visibility amplitudes will often show the outlying data points. Figure 2.12 shows four examples of bad data points in visibility amplitude plots. These points can easily be flagged out of the data set and then the source can be re-imaged and self-calibrated.

Errors in the image plane are evident from non physical features in the restored image, such as stripes, rings, or negative structures. A few diagnostic tests to try and locate the problem include checking that the image is big enough to cover all the significant emission, ensuring the resolution is low enough to detect the emission, and ensuring that the cell size is appropriate for the beam size. Figure 2.13 shows a few typical effects seen in the image plane.

In general, errors $\epsilon(u, v)$ can be divided into different types, depending on how they modify the visibility data.

1. Additive errors : V + $\epsilon \Leftrightarrow$ I + $\mathcal{F}\epsilon$

   The Fourier transform $\mathcal{F}\epsilon$ of these errors is added to the image I and is independent of the position and amplitude of other structure in the image. Examples of additive errors include solar interference, cross talk between antennas, and noise.
2. Multiplicative errors : V $\epsilon \Leftrightarrow$ I * $\mathcal{F}\epsilon$

   In this case, the Fourier transform of the error is convolved with the source distribution

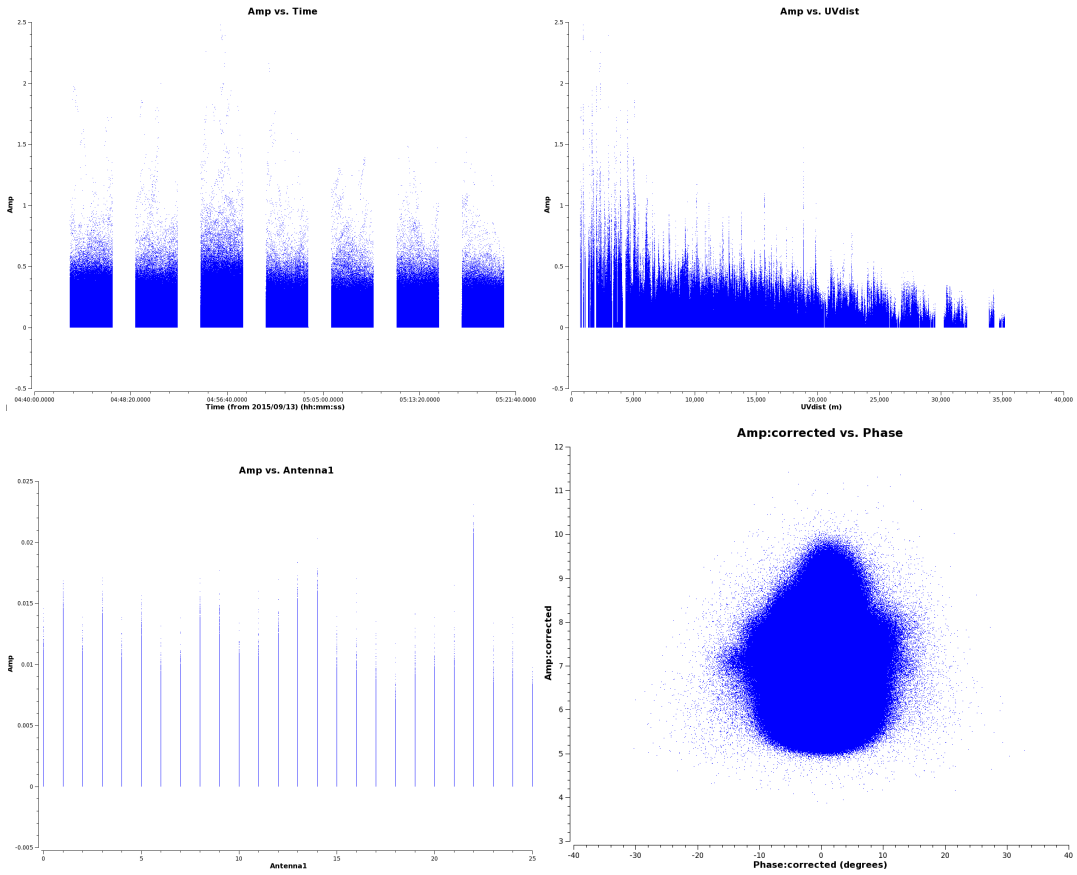

Figure 2.12: An example of errors in the (u, v) plane. *a* shows an amplitude vs time plot for a dataset with bad channels; *b* gives the amplitude vs uv-distance for a dataset with bad channels; *c* gives the amplitude vs antenna for a dataset with a bad antenna; *d* gives the amplitude vs phase for a dataset with bad calibration terms, causing asymmetric scatter of the visibility data.

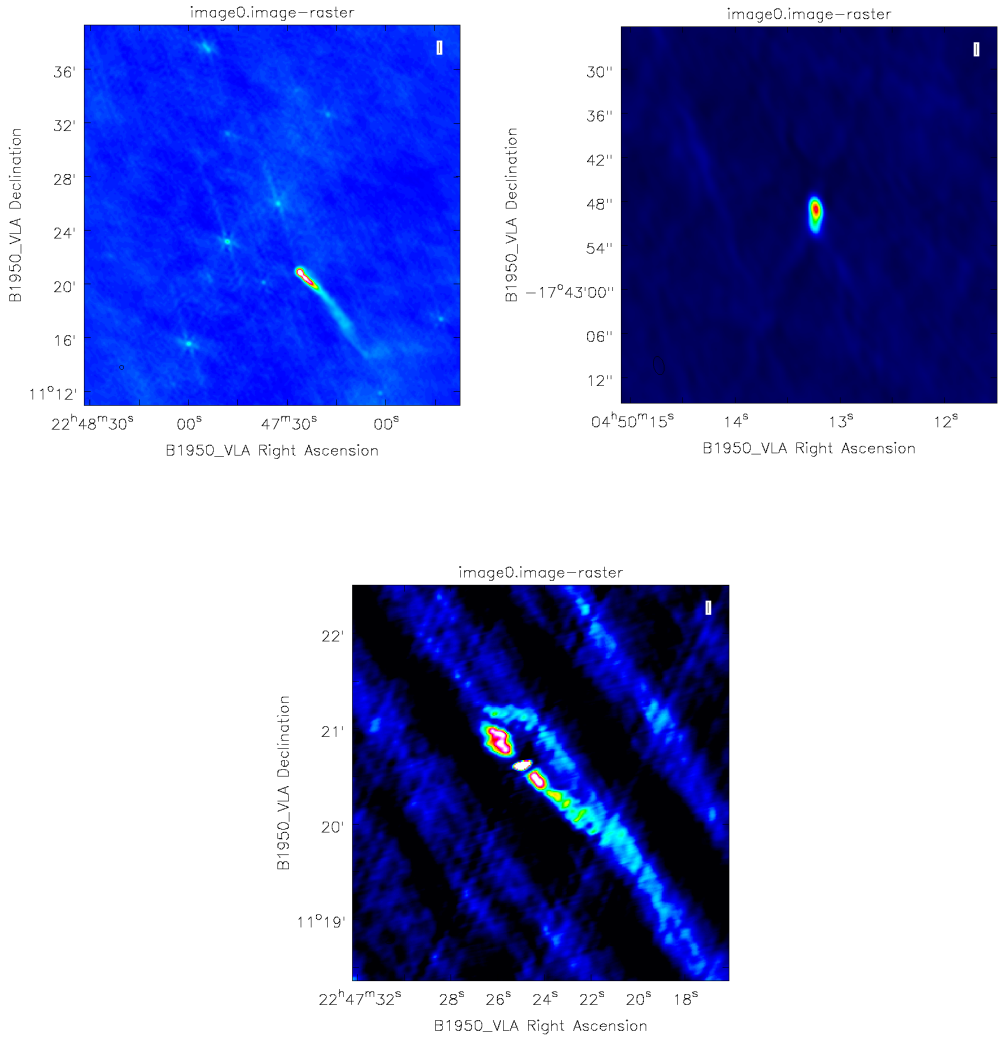

Figure 2.13: An example of errors in the image plane. *(a)* Background sources have not been CLEANed, causing these sources to appear convolved with the dirty beam. The 6-fold symmetric pattern results from the Y configuration of the VLA; *(b)* The point source is elongated in the N-S direction, when it should be circular due to a calibration error; *(c)* shows large stripes across the image, indicative of antenna errors at short baselines.

in the image. A common error in an image is caused by (u, v) coverage effects, due to missing information in the (u, v) plane. These missing data cause the visibility function $V(u, v)$ to be multiplied by zero. Deconvolution algorithms such as CLEAN attempt to correct this effect however the success of these algorithms is dependent on the extent of the missing spacings. Evidence for these coverage effects can be found in the point spread function. Gain calibration errors are also multiplicative. The real part of $\epsilon(u, v)$, i.e. the amplitude errors, give symmetric error patterns associated with each source in the image. Imaginary parts of $\epsilon(u, v)$ i.e. phase errors, generate asymmetric patterns.

3. Convolutive errors : V * $\epsilon \Leftrightarrow$ I $\mathcal{F}\epsilon$

   For errors due to a convolution of the observed visibility function, the image will be multiplied by the Fourier transform of the error function. An example is the effect of the primary beam of the array.

Low resolution images are a good diagnostic tool for assessing the quality of the image, because they can highlight extended emission and are computationally fast. This allows the user to evaluate the radio emission in the image and either continue with imaging if no problems are obvious or re-check the (u, v) data for outliers.

2.5 Rotation Measure Fitting

The amount of Faraday rotation between a source and the observer is characterised by the Faraday rotation measure (RM) :

$$RM = 0.81 \int_{\text{source}}^{\text{observer}} n_e B \cdot dl \tag{2.48}$$

where n_e is the electron density in units of cm^{-3}, the magnetic field B is expressed in μG and the path length l is given in parsecs. The polarisation angle is modified by Faraday rotation via the expression :

$$\chi(\lambda) = \chi_0 + RM \cdot \lambda^2 \tag{2.49}$$

where χ_0 is the intrinsic polarisation angle (i.e. the polarisation angle at zero wavelength) and $\chi(\lambda)$ is the polarisation angle observed at wavelength λ.

The rotation measure is usually found by investigating $\chi(\lambda)$ as a function of λ^2 and performing a least-squares fit to the data. This approach is used in the CASA task *rmfit*.

This task uses Stokes Q and U images at several different frequencies to determine the rotation measure and the position angle at zero wavelength using the algorithm of Leahy et al. (1986). The task requires the user to specify the maximum absolute RM value that should be solved for, thus some a priori information needs to be supplied. This task will provide output images of the rotation measure structure, the zero wavelength position angle and the errors associated with both.

There are numerous problems determining the rotation measure in this way. Firstly, the observed polarisation angle is only known modulo π radians; thus if measurements do not span enough frequency bands, then the rotation measure fit can be arbitrary. This problem is illustrated in Figure 1 of Rand and Lyne (1994). Different methods have been devised to attempt to circumvent this problem, for example the 'Pacerman' method (Vogt et al., 2005) which operates on images and uses spatial continuity arguments to find and correct $n\pi$ ambiguities. Secondly, polarised emission with different values of rotation measure can be present within a single observing beam. The mixture of these signals from different regions makes a linear fit inaccurate. Finally, faint radio emission with a strong rotation measure will not be detected in narrow individual frequency bands due to low signal to noise, and will be undetectable even after all bands have been integrated due to bandwidth depolarisation. This places the implicit constraint that the polarised signal must be bright enough at each observing frequency to allow a fit.

A different, Fourier-based approach was introduced by Burn (1966) and extended and implemented by Brentjens and de Bruyn (2005). This 'RM synthesis' method transforms the complex linear polarisation $Q + iU$ over the spectral axis to the rotation measure axis and is detailed below. The resulting Faraday dispersion spectrum provides much additional information but requires an extensive range of λ^2 for the best results. This method retains the coherent sensitivity of the observing frequency band to polarised emission even if there is possible Faraday rotation within the band, under the assumption that the rotation is well resolved by the λ^2 sampling.

In this thesis, I will use both methods to produce rotation measure maps of radio sources and compare the results.

2.5.0.2 RM synthesis

Burn (1966) showed that the observed complex polarisation vector $P(\lambda^2)$ can be expressed as

$$P(\lambda^2) = \int_{-\infty}^{+\infty} pIe^{2i[\chi_0+\phi\lambda^2]}d\phi \tag{2.50}$$

where the RM from equation (2.49) is now expressed by a generalised quantity ϕ, the Faraday depth. A positive Faraday depth implies a magnetic field pointing towards the observer. This can be rewritten in terms of the Faraday dispersion function $F(\phi)$ which describes the intrinsic polarised flux, as

$$P(\lambda^2) = \int_{-\infty}^{+\infty} F(\phi)e^{2i\phi\lambda^2}d\phi \tag{2.51}$$

The Faraday dispersion function describes radiation emitted at different Faraday depths along a given line of sight. If there is only one source along the line of sight and the plane of polarisation is not modified due to differential Faraday rotation or affected by beam depolarisation, then the Faraday depth ϕ of the source is equivalent to RM across all observing frequencies. In general however, the situation is usually more complex (e.g. Sokoloff et al., 1998; O'Sullivan et al., 2012). This is illustrated in an example given by Brentjens and de Bruyn (2005), shown in Figure 2.14. In this example, the line of sight is complicated by three areas with polarised emission (A, B and C), of which two (A and B) also have internal Faraday rotation. A physical interpretation of this example would be that region A and the rotation only areas adjacent to it reside in our Galaxy, region B and the adjacent rotation only areas are a galaxy cluster, and region C represents a background polarised source with no internal Faraday rotation. The line of sight 1 goes through the cluster, whereas line of sight 2 does not. This causes region C to be at a different Faraday depth for the two lines of sight.

The Faraday dispersion function takes the form of a Fourier transform, and can be inverted to express the intrinsic polarisation in terms of observable quantities:

$$F(\phi) = \int_{-\infty}^{+\infty} P(\lambda^2)e^{2i\phi\lambda^2}d\lambda^2 \tag{2.52}$$

Since it is not possible to observe at wavelengths $\lambda^2 < 0$ and not all values of $\lambda^2 > 0$ are sampled during an observation, Brentjens and de Bruyn (2005) introduced a window function $W(\lambda^2)$, to be non-zero only at values of λ^2 which are sampled by the telescope. They rewrite equations 2.51 and 2.52 to express the observed polarised emission as

$$\tilde{P}(\lambda^2) = W(\lambda^2)P(\lambda^2) = W(\lambda^2)\int_{-\infty}^{+\infty} F(\phi)e^{2i\phi(\lambda^2-\lambda_0^2)}d\phi \tag{2.53}$$

and the reconstructed Faraday dispersion function as

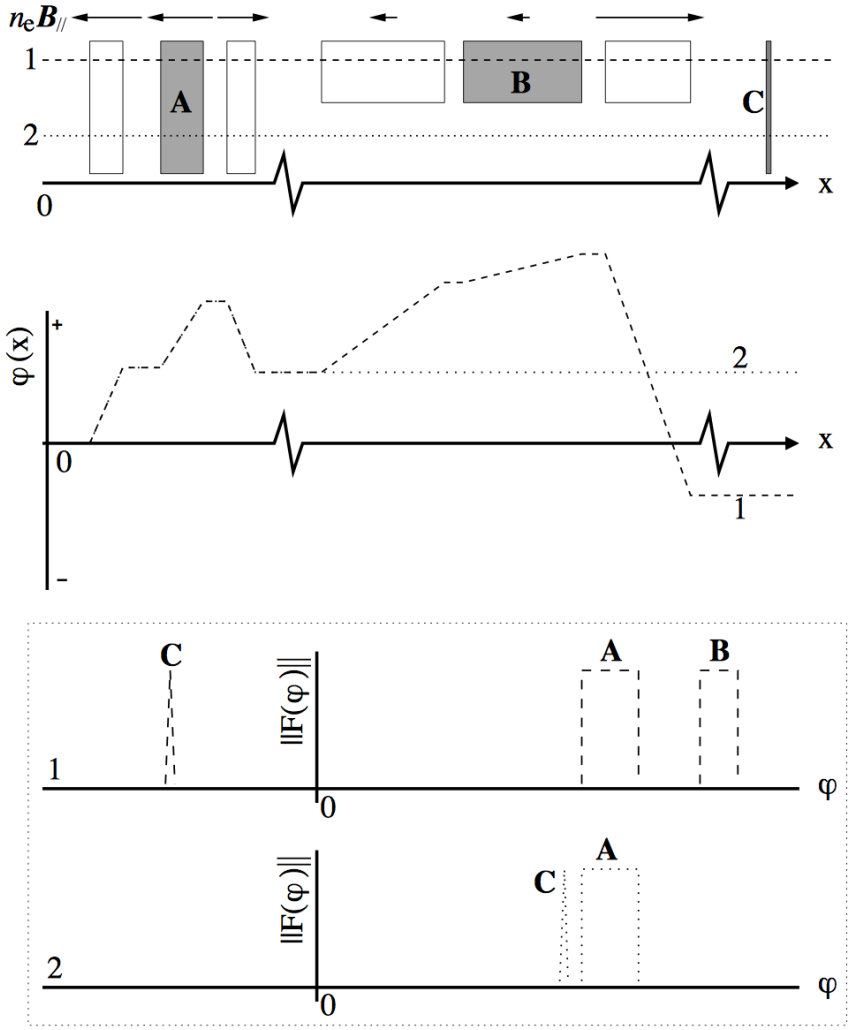

Figure 2.14: An example of how the line of sight can change the observed Faraday spectrum, adapted from Brentjens and de Bruyn (2005). The cartoon sketches the relation between emission $n_e\mathbf{B}_{||}$, Faraday depth ϕ, location x and the observed Faraday spectrum. The top panel depicts the physical situation, with the arrows representing $n_e\mathbf{B}_{||}$. The x coordinate represents the physical distance from the observer, who is located at the far left of the plots. White blocks represent areas with only Faraday rotation, grey areas with arrows have both emission and rotation and grey areas with no arrow have only emission. The middle panel plots Faraday depth ϕ as a function of physical distance x for both lines of sight. The bottom panel shows the observed polarised surface brightness $F(\phi)$.

$$\tilde{F}(\phi) = K \int_{-\infty}^{+\infty} \tilde{P}(\lambda^2) e^{2i\phi(\lambda^2 - \lambda_0^2)} d\lambda^2 = F(\phi) * R(\phi) \tag{2.54}$$

where K is the inverse of the integral over $W(\lambda^2)$ and $R(\phi)$ is the RM transfer function (RMTF) defined by :

$$R(\phi) = K \int_{-\infty}^{+\infty} W(\lambda^2) e^{-2i\phi(\lambda^2 - \lambda_0^2)} d\lambda^2 \tag{2.55}$$

The quality of the reconstruction is dependent on the weight function $W(\lambda^2)$ and the λ^2 coverage, since having fewer gaps in the λ^2 sampling reduces the sidelobes of the RMTF. The RMTF is a complex valued function, with the real part corresponding to the response of the transform parallel to the (Q, U) vector at λ = λ_0 and the imaginary part corresponding to the response orthogonal to it. Brentjens and de Bruyn (2005) showed that the optimal choice of λ_0^2 is the mean of the sampled λ^2 values, weighted by $W(\lambda^2)$. This significantly reduces the rapid rotation of the real and imaginary parts of the RMTF, making it easier to measure accurate polarisation angles in a sampled RM cube (see Brentjens and de Bruyn, 2005, Fig 3 and 4 for further details). The RMTF of a JVLA dataset is shown in 2.15, in terms of its real and imaginary parts. The Q, U vectors have been derotated by the mean of the sampled λ^2 values for the observation.

Brentjens and de Bruyn (2005) also investigated the effect of the emission spectrum of a source on the RM synthesis technique. They proved that it is easy to correct for the spectra of sources that are reliably detected in individual channel maps; however for sources that only show up after averaging the full band then it proves impossible. For the latter objects, it is sensible to make an estimate of the average spectral index and apply it to the entire map. Since the spectral dependence is an amplitude only effect, it has no influence on the location of the Faraday dispersion peak and therefore a slightly wrong estimate does not affect the derived Faraday depth.

A key motivation for carrying out RM synthesis rather than the linear fit approach is to minimise the effects of the nπ ambiguity. By splitting up the observing bandwidth into a large number of narrow frequency channels, only the polarised emission with the highest intensity will be detected above the noise level. The standard error in the RM when obtained by fitting a straight line plot of χ versus λ^2 is given by

$$\sigma_{RM} = \frac{\sigma_\chi}{\sigma_{\lambda^2}\sqrt{N-2}} \tag{2.56}$$

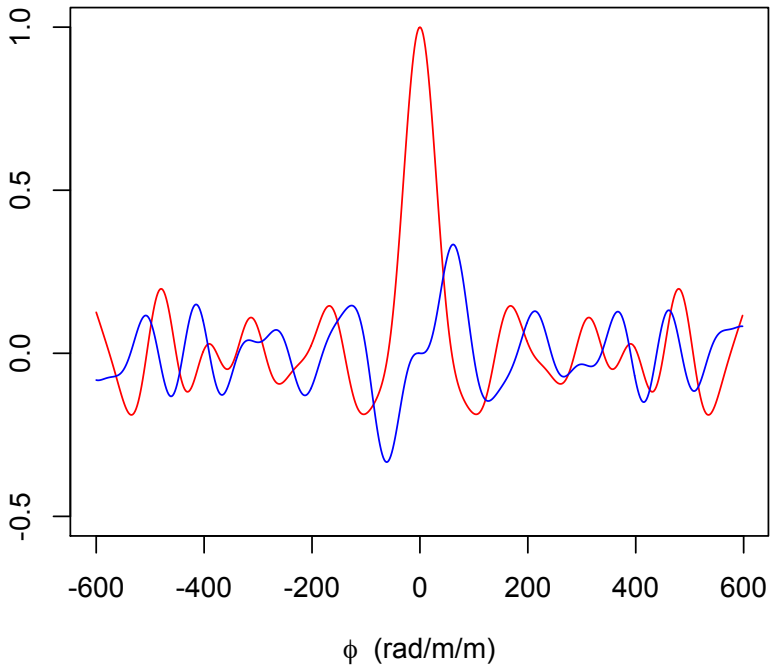

Figure 2.15: The RMTF of a 1.4 GHz dataset taken with the JVLA. There are 10 spectral windows and 64 channels per window within the dataset. The Q, U vectors have been derotated to the average λ^2. The red line shows the real part of the transfer function and the blue shows the imaginary part.

$$\sigma_{\lambda^2} = \sqrt{(N-1)^{-1}\sum_{i=1}^{N}\lambda_i^4 - \lambda_0^4} \tag{2.57}$$

where N is the number of channels. σ_χ is given by either

$$\sigma_\chi = \frac{1}{2}\frac{\sigma}{||P||} \tag{2.58}$$

if $\sigma_Q \approx \sigma_U = \sigma$ or

$$\sigma_\chi = \frac{\sqrt{U^2\sigma_Q^2 + Q^2\sigma_U^2}}{2||P||^2} \tag{2.59}$$

if σ_Q and σ_U differ by more than a factor of two or so.

An additional advantage of the RM synthesis technique is being able to separate out emission at multiple Faraday depths along a chosen line of sight. This is useful, for example, when a background polarised source is observed through a foreground medium which has its own intrinsic RM. In this case, the polarised intensity will appear at different values of ϕ, thus making it possible to disentangle the total RM signal.

Three parameters are used to evaluate the output of a Faraday rotation experiment. These are the channel width $\delta\lambda^2$, the width of the λ^2 distribution $\Delta\lambda^2$, and the shortest wavelength squared λ^2_{min}. These parameters describe the maximum observable Faraday depth, the resolution in ϕ space, and the largest scale in ϕ space to which one is sensitive, respectively. The FWHM of the RMTF which determines the precision with which the RM peak can be deduced in ϕ space, the scale in ϕ space to which sensitivity has dropped to 50% and the maximum Faraday depth to which one has more than 50% sensitivity, are approximated by

$$\delta\phi \approx \frac{2\sqrt{3}}{\Delta\lambda^2} \tag{2.60}$$

$$\text{max scale} \approx \frac{\pi}{\lambda^2_{\text{min}}} \tag{2.61}$$

$$|\phi_{\text{max}}| \approx \frac{\sqrt{3}}{\delta\lambda^2} \tag{2.62}$$

The proportionality constant for $\delta\lambda^2$ is given by Brentjens and de Bruyn (2005) as $2\sqrt{3}$, and reevaluated by Schnitzeler (2008) to be FWHM = 3.8 / $\Delta\lambda^2$ instead.

The search for multiple Faraday screens along the line of sight can be complicated by the RMTF sidelobes (see Figure 2.16, taken from Heald et al., 2009). The sidelobes can be significantly reduced by performing a deconvolution operation, with an algorithm similar to the CLEAN method introduced by Högbom (1974). In the RM synthesis deconvolution, the algorithm searches for the maximum of the Faraday dispersion function ϕ_p, and the values of the real and imaginary parts of $|\tilde{F}(\phi_p)|$ are scaled by a loop gain parameter g. This maximum point is stored as a 'clean component'. A version of the RMTF, shifted and scaled to be equal to $g|\tilde{F}(\phi_p)|$ at $\phi = \phi_p$, is then subtracted from the Faraday dispersion function. The residuals are searched for a new maximum, and the cycle is repeated until the residuals fall below a threshold or maximum iteration parameter specified by the user. The clean components are then convolved with a restoring function and added to the residuals. This method produces a deconvolved Faraday dispersion function, where the peak represents the RM for that pixel. This RM-cleaning algorithm has been implemented within the MIRIAD software package, but is not yet available for CASA.

For deconvolution, it is essential to obtain an accurate RMTF for all sources within the field of view and along the line of sight. The frequency dependence of both the primary beam attenuation and the instrumental polarisation can cause problems; thus frequency dependent instrumental effects must be calibrated before generating an RM cube and the synthesised beam must be the same for every Stokes image at all frequencies.

RMTF sidelobes can be reduced by tapering in λ^2 space. By setting $W(\lambda^2) \neq 1$, the sidelobe levels can be significantly improved. Tapering however, comes at the expense of lower ϕ resolution. The chosen taper should therefore be selected as a reasonable trade-off between sidelobe height and RMTF width.

The frequency coverage $\Delta\lambda^2$, determines whether emission at multiple Faraday depths can be recovered. A single Faraday depth or a few distinct Faraday depths appear as one or more unresolved peaks in the Faraday dispersion function. For regions described as 'Faraday thick' however, the observing frequency must be sufficient to recover polarised emission at a continuous range of Faraday depth. In these regions, emitting and rotating plasma with magnetic fields may be uniformly distributed along the line of sight, this results in synchrotron emission from the far side of the Faraday screen undergoing more Faraday rotation than the side closest to the observer. In a simple model, a uniform level of polarised flux will be detected at a continuous range of Faraday depth. The same effect can be caused by turbulent magnetic fields (e.g. Berkhuijsen et al., 1997). Burn (1966)

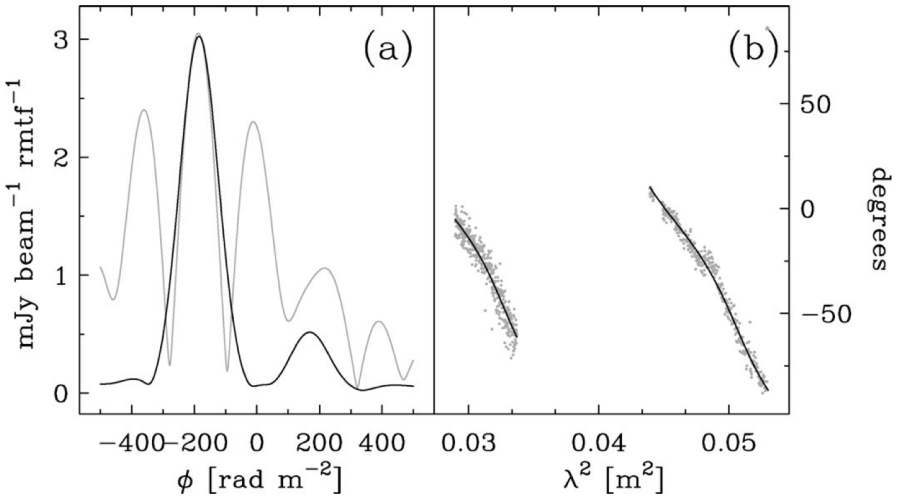

Figure 2.16: An example of RMCLEAN results, taken from Heald (2008). *Left* shows the Faraday dispersion function of a bright polarised point source close to NGC 7331, observed as part of the WSRT-SINGS survey. The grey line is the original reconstructed Faraday dispersion function, and the black line is the Faraday dispersion function after deconvolution. The resulting profile shows two distinct components. *Right* the observed polarisation angle with λ^2 is plotted. The polarisation angle calculated by the clean components extracted from RMCLEAN are shown by a black line. A traditional linear fit would not have accurately represented the data in this case.

showed that the observational signature of a Faraday thick region with a magnetic field gives a $|P(\lambda^2)|$ distribution in the form of a sinc function. Differential Faraday rotation will depolarise the emission at all non-zero frequencies within the region, and is this effect is stronger at larger λ^2. Therefore a smaller $\lambda^2_{\rm min}$ means sampling $P(\lambda^2)$ closer to its peak and recovering more of the intrinsic polarised flux. In order to resolve Faraday thick emission in ϕ space so that internal structure can be investigated, the main peak of the RMTF should be narrower than the maximum scale to which it is sensitive. This gives the additional requirement $\lambda^2_{\rm min} < \Delta\lambda^2$ (see Brentjens and de Bruyn, 2005 for examples).

2.6 A Note on Optical and X-ray Data

In this thesis, I also use optical data from the Hubble Space Telescope (HST), together with X-ray data from the *Chandra* satellite. For the HST data, the main datasets I obtained were from the Wide-Field Planetary Camera 3 (WFPC3). The Space Telescope Science Data Analysis System (STSDAS) pipeline processing software is able to produce calibrated, cosmic ray-rejected datasets from HST observations, so I was then able

to perform simple analysis tasks in IRAF on these data. For the X-ray data, the Chandra Interactive Analysis of Observations package (CIAO) was used to reprocess the data, following the recommended data processing steps. Full details of the optical and X-ray analysis are given for each radio galaxy in the proceeding chapters.

2.7 Summary

In this chapter I have reviewed the data calibration and editing methods for interferometric radio data, and in particular for observations with the VLA. I have discussed the problems of radio frequency interference and the methods I have used to mitigate its effects, as well as the different techniques available to produce rotation measure maps. These techniques and calibration steps are used to produce the results presented in subsequent chapters of this thesis.

Chapter 3

Overview of the Sources Studied in this Thesis

In this chapter I present an overview of the sources that I have studied in this thesis. Two of these sources, NGC 7385 and NGC 6109, are part of the 3CRR catalogue compiled by Laing et al. (1983), which is a sample of 173 bright radio sources in the Northern sky. The radio sources in this catalogue have a flux density $\geq$ 10.9 Jy at 178 MHz, and the majority have been classed as powerful FR II-type radio galaxies and radio loud quasars. 36 of the sample have $z \leq 0.1$, and an overview of the main X-ray properties of all these sources is given by Evans (2005). NGC 7385 and NGC 6109 fall within this low redshift sample, and both have been observed with the VLA and *Chandra* in an attempt to reveal details of radio source physics.

NGC 7016 and NGC 7018 are FR I and FR II-type radio galaxies respectively, located within close proximity of each other in the nearby cluster A3744. The cluster was detected in the ROSAT All-Sky Survey and later observed with *Chandra*, which provided evidence that the two galaxies may be interacting with each other.

This chapter will provide a brief review of the literature available for these sources, before new observations are presented in the subsequent chapters.

3.1 NGC 7385

NGC 7385 (4C 11.71) is a low-redshift (z = 0.026, Wegner et al., 1999) elliptical galaxy located in a poor cluster (Zwicky 2247.3 + 1107). This galaxy is part of the the 3CRR

catalogue, but was not one of the original 3C sources, due to the resolution of the 3C interferometer (Smith et al., 1976). Scott et al. (1977) report on spectroscopic observations of 16 galaxies within Zw 2247.3+1107 and observe that most of the bright galaxies are elliptical and stellar objects. Unlike the environment of other known head-tail galaxies however, the cluster is insufficiently rich to appear in the Abell catalogue. Scott et al. (1977) determined a mean cluster velocity with respect to the Sun of $\langle V_R \rangle$ = 7577 $\pm$ 150 km s^{-1} and a corresponding velocity dispersion σ_T = 965 $\pm$ 129 km s^{-1}. These give an approximate luminosity distance of 109 Mpc for the cluster. The X-ray luminosity of the cluster was calculated to be $L_X \leq 7.9 \times 10^{43}$ erg s^{-1} (Cooke, 1976).

Despite early radio observations showing an interesting jet structure and a head-tail morphology, detailed features of the radio source remain largely unrecognised.

3.1.1 Radio structure

The radio structure of NGC 7385 was first reported by Schilizzi and Ekers (1975). They published observations of NGC 7385 as a new example of a 'head-tail' class of radio source, and only a few others were known at the time (3C 129.1, Hill and Longair, 1971; 5C 4.81, Willson, 1970; several sources in the Perseus cluster, Ryle and Windram, 1968; Miley et al., 1972). The observations of Schilizzi and Ekers (1975) came from the Molonglo Cross Telescope (Mills et al., 1976) at 408 MHz and the Westerbork Synthesis Radio Telescope (WSRT, Brouw, 1971) at 1.415 GHz. Figure 3.1 shows the brightness distribution produced from these observations; a long bright radio tail extends to the S for approximately 510 kpc. This radio tail has an implied age of 3×10^8 years for a galaxy speed 550 km s^{-1}.

Higher resolution images were produced by Hardee et al. (1980) after NGC 7385 was observed with the VLA in 1978 at 5 GHz. The map produced from these observations is given in Figure 3.2. Hardee et al. (1980) attribute the NE component to the ejection of material from the nucleus both parallel and antiparallel to the direction of motion of the galaxy through the intergalactic medium. By assuming that the NE component can be described as a uniformly filled cylinder, Hardee et al. (1980) calculated a radio lobe pressure of $P_R \approx 5.5 \times 10^{-12}$ dyn cm^{-2}, and an equipartition magnetic field strength $B \approx 10$ μG.

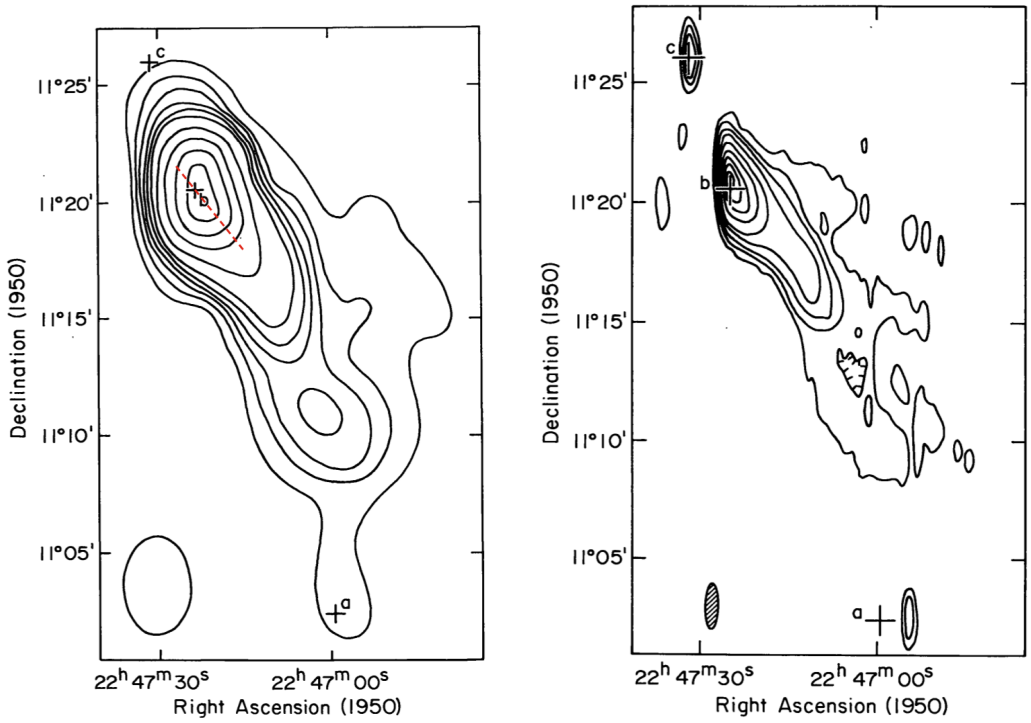

Figure 3.1: The brightness distribution of NGC 7385 published by Schilizzi and Ekers (1975). The optical objects marked (a), (b) and (c) are members of Zw 2247.3+1107; objects (b) and (c) are NGC 7385 and NGC 7386 respectively. *Left:* Molonglo cross telescope observation at 408 MHz with beam size $2.8' \times 4.2'$. The red dashed line indicates the extent of the radio emission seen at 5 GHz in Figure 3.2. *Right:* WSRT brightness distribution at 1.415 GHz with beam size $25'' \times 125''$.

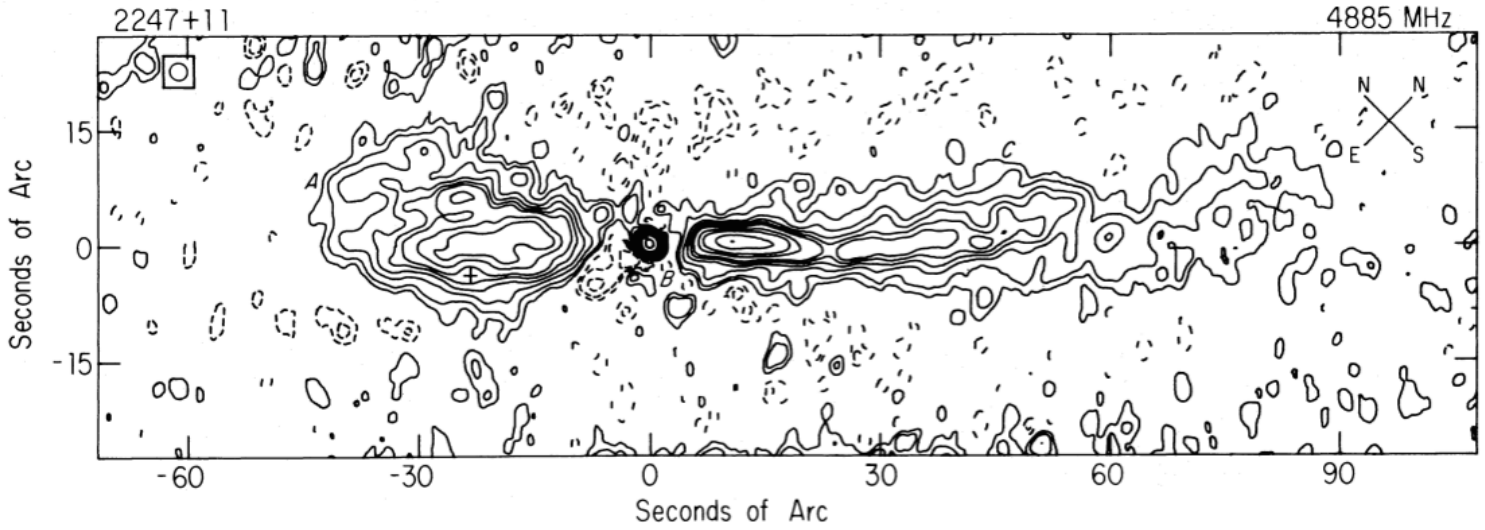

Figure 3.2: VLA 5 GHz total intensity map of NGC 7385 at 2.5″ resolution, published by Hardee et al. (1980). The cross marks the position of an optical object and regions are labelled A-C to mark the positions of a diffuse component, an unresolved nuclear source and the inner 70″ of the jet tail, respectively. The extent of this radio emission compared to the large scale structure observed with the Molonglo cross telescope and WSRT is shown with a red dashed line in Figure 3.1.

Component	Frequency (GHz)	Flux density (Jy)	α	Reference
Entire source	0.408	6.8		1
Entire source	1.415	2.3	0.87	1
Core	5.0	0.121		2
NE component	5.0	0.243	0.8	2
NE component	5.0	0.350	0.5	3
Near tail	5.0	0.340	0.5	3
Far tail	1.4	0.170		3

Table 3.1: Key parameters of NGC 7385 from the literature. The entire source at 0.408 and 1.415 GHz is defined by the radio contours in Figure 3.1, excluding optical objects a and c. The core is labelled as component B in Figure 3.2 and the NE component is labelled as A. Near tail corresponds to the inner 50 kpc of the radio tail and the far tail as any radio emission detected beyond this point. The spectral index α is defined as $S \propto \nu^{-\alpha}$. References : (1) Schilizzi and Ekers (1975), (2) Hardee et al. (1980), (3) Robertson (1981)

Polarised intensity maps of NGC 7385 were published by Robertson (1981) from observations made with the WSRT at 0.6, 1.4 and 5 GHz, in order to examine the physical conditions in the emitting regions and the surrounding intracluster medium. Robertson (1981) found a polarised intensity at 5 GHz of 20-30% along the first 50 kpc of the tail and 17% in the NE component. At 1.4 GHz, the polarised intensity is 4% in the NE component and 20% in the inner tail. Rotation measure values were also reported for the inner tail and NE component between 1.4 and 5 GHz, at -19.9 and -12 rad m^{-2} respectively.

Table 3.1 shows some of the key parameters for NGC 7385 taken from the literature. These will provide a useful comparison for new JVLA observations presented in chapter 4.

3.1.2 Optical observations

An optical knot associated with the NE radio component of NGC 7385 was first noticed on a Palomar Schmidt plate by Simkin and Ekers (1979). The image was taken with a B filter (i.e. with a bandpass in the near ultraviolet). Later spectroscopy (Simkin et al., 1984) found strong nebular emission lines and a blue continuum.

Direct photography and digital spectrophotometry were used by Simkin et al. (1984) to study the optical knot, which when combined with the VLA high resolution image of Hardee et al. (1980), shows the knot to be embedded in the NE radio component. Hardee et al. (1980) suggested that the knot is the result of a thermal instability arising from the

interaction between the radio plasma and the interstellar gas in the galaxy. Simkin et al. (1984) however, favoured an interpretation in which there is a direct interaction between optical line-emitting gas and the radio lobe.

Figure 3.3 shows the optical images presented by Simkin et al. (1984) superposed on the radio contours published by Hardee et al. (1980). The optical image in Figure 3.3a is from three IIIaJ plates which have been summed digitally. The position of the knot measured by Simkin and Ekers (1979) is located at the leading edge of the optical feature. A clearer picture of the relationship between the optical knot and the radio structure is shown in Figure 3.3b. This shows the results of converting the digitised photographic images to relative intensity and subtracting the symmetrical component of the underlying galaxy image (e.g. Butcher et al. 1980). Simkin et al. (1984) interpret this image as a set of at least two knots. They also found that the regions of excess optical emission are significantly bluer than the underlying galaxy.

The measured fluxes for all emission lines are given in Table 2 of Simkin et al. (1984), but the most prominent were [OII], [OIII] and Hβ. Analysis of the positions of the emission lines in the spectra found a velocity difference of 230 $\pm$ 70 km s^{-1} between the knots and the surrounding galaxy and an internal velocity dispersion for the ionised gas of 60 - 90 km s^{-1}. They conclude that the spatial coincidence of the optical knot and the radio emission strongly suggests an interaction, and that photoionisation of the cloud could be caused by some combination of shock heating and a population of early-type stars.

3.1.3 X-ray observations

A study carried out by Miller et al. (1999) investigated the X-ray luminosity for 25 $z \leq$ 0.06 radio galaxies which are not members of Abell clusters, and both NGC 7385 and NGC 6109 were amongst the sources sampled. The X-ray structure of the galaxy environment was studied by means of the ROSAT All-Sky Survey (RASS), ROSAT pointed observations, and the Palomar optical Digitized Sky Survey (DSS). An image of the X-ray environment taken from Miller et al. (1999) of NGC 7385 is given in Figure 3.4. The optical nucleus of NGC 7385 is marked with a cross, and the nearby radio galaxy NGC 7386 can be seen to the N. The X-ray luminosity appears to skirt around the edges of NGC 7385 with the highest luminosity roughly in between the two galaxies.

The X-ray emission within NGC 7385 was analysed by Mannering (2013) using new *Chandra* data. The aim of this study was to search for X-ray gas belt candidates from the 3CRR catalogue and the results for NGC 7385 are shown in Figure 3.5. The diffuse

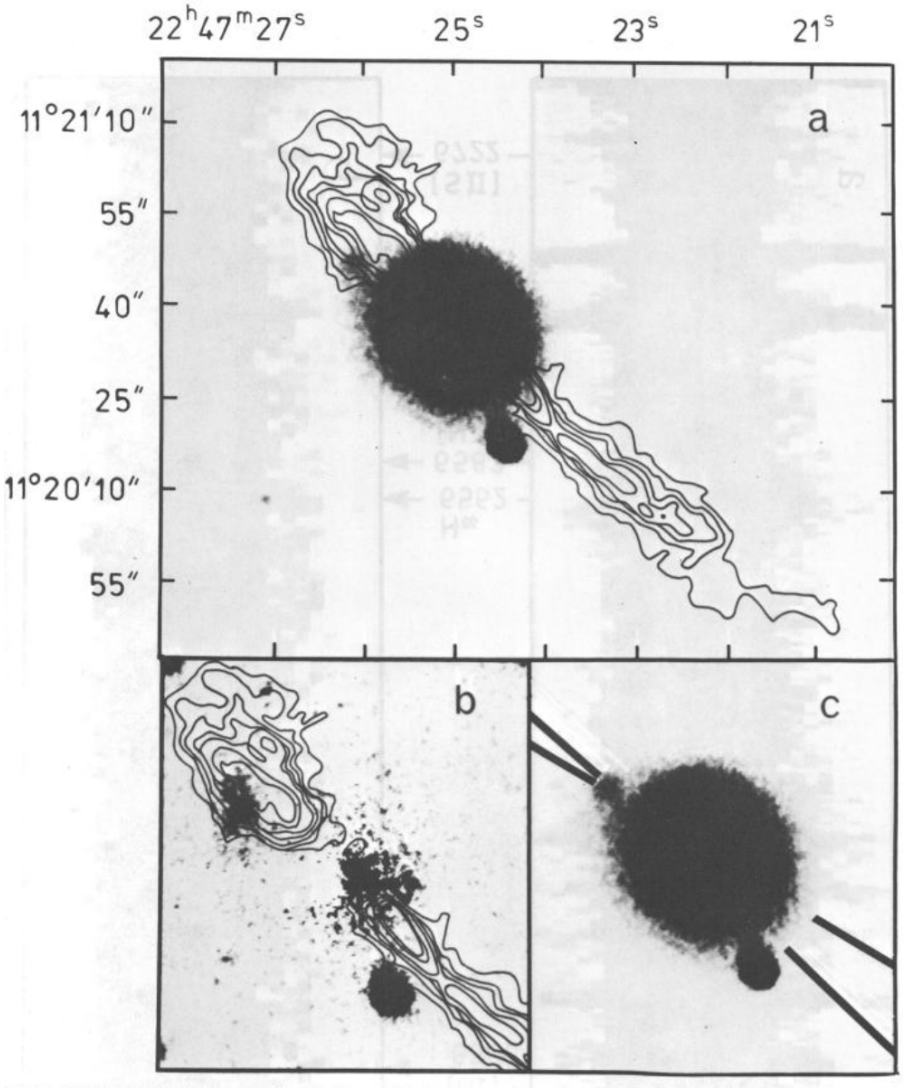

Figure 3.3: Optical observations of NGC 7385 taken with the Palomar Schmidt in 1978 and presented by Simkin et al. (1984) with radio contours from Hardee et al. (1980). a is from three IIIaJ plates, b shows radio contours on the regions of optical excess and c shows the spectrograph slit positions.

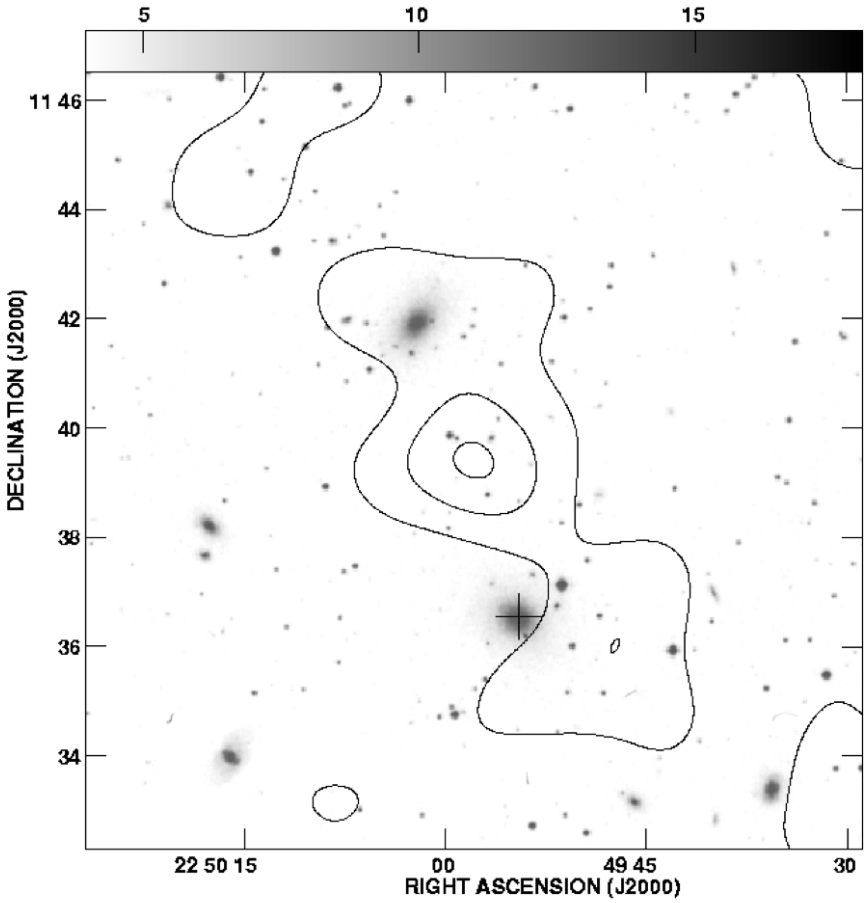

Figure 3.4: X-ray luminosity contours from the RASS in the environment of NGC 7385 overlayed on a DSS optical image, given by Miller et al. (1999). The X-ray image has been smooth with a $2'$ Gaussian and background subtracted. The optical nucleus of NGC 7385 is marked with a cross and the galaxy NGC 7386 is seen to the N within the X-ray contours.

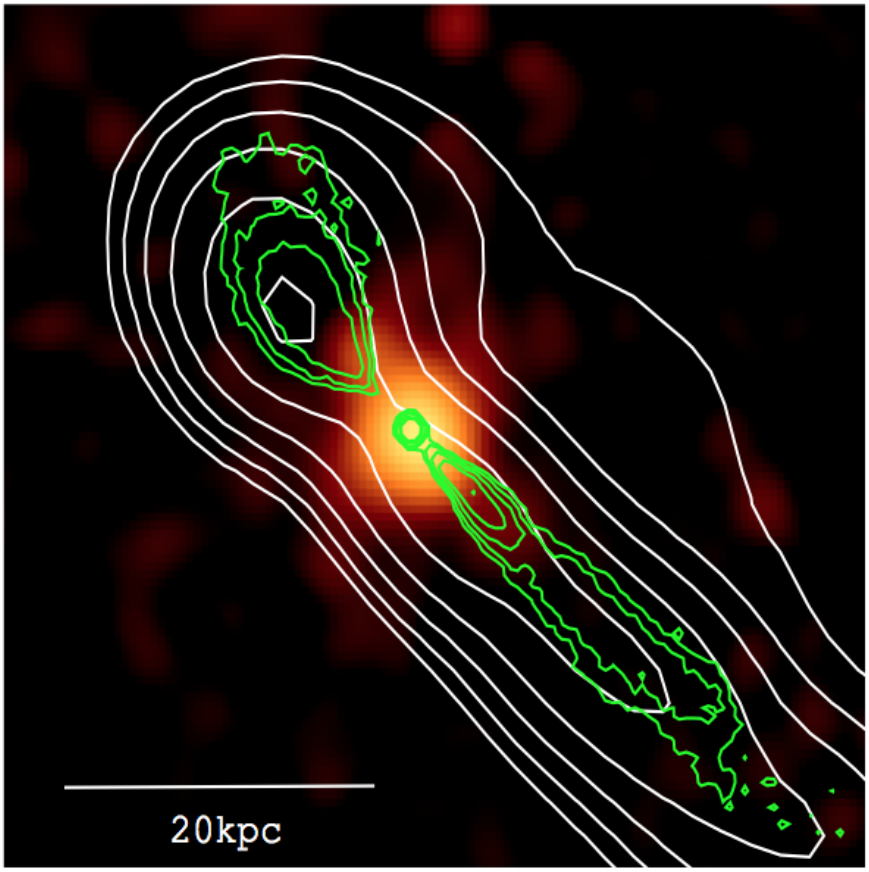

Figure 3.5: A *Chandra* exposure-corrected image of NGC 7385 in the energy range 0.4-8.0 keV, taken from Mannering (2013). The green contours are VLA radio observations at 5 GHz with resolution 1.4″, and the white at 1.4 GHz with resolution 14.8″.

emission associated with the galaxy atmosphere extends out to a 10 kpc radius. Little X-ray emission is seen in the NE component or along the main jet, but see section (4.2.3) for new results.

3.2 NGC 6109

NGC 6109 is an FR I-type head-tail radio galaxy located in a poor cluster with redshift z = 0.0295 (Wegner et al., 1999) and so with an angular diameter distance of 121 Mpc. The host cluster, Zw 1615.8 + 3505 (Zwicky et al., 1961) is described as dynamically young by Tomita et al. (1999), based on the presence of the 'well developed' head-tail radio source NGC 6109 within it (Venkatesan et al., 1994). Tomita et al. (1999) performed optical and CO radio observations of members of the cluster in order to investigate the

morphology and star formation activity of galaxies within this environment. NGC 6109 was found to be an elliptical galaxy with regular morphology, and shows no evidence for star formation.

3.2.1 Radio Structure

The radio morphology of NGC 6109 was first reported by Ekers (1978). They published radio and optical observations of the radio galaxies B2 1615 + 35 (NGC 6109) and B2 1621+ 38 (NGC 6137) to add these sources to the small sample of radio galaxies which showed head-tail structure, despite being located in a poor cluster (NGC 7385 was one of the small sample already published). The radio structure of NGC 6109 was mapped at 0.6, 1.4 and 5.0 GHz with the WSRT and the resulting images are shown in Figure 3.6.

Results from these observations indicated that NGC 6109 has a projected size of approximately 390 $\times$ 45 kpc. A weak leading component SE of the core is visible at 5 GHz and the brightness in the NW tail drops off suddenly at about 150 kpc from the core. In addition, Ekers (1978) found that the spectral index of the radio emission between 0.6 GHz and 5 GHz steadily increases with increasing distance along the tail. The steepening was reported to be more pronounced at higher frequencies, suggesting a break in the radio spectrum. This was interpreted as a result of the energy losses of the relativistic particles via the synchrotron and Compton processes. However, since the velocity dispersion in the cluster was deduced to be approximately 1100 km s^{-1}, relativistic electrons in the outer regions of the tail are too young to have been directly produced in the nucleus, suggesting that electrons are re-accelerated within the radio tail (e.g. Pacholczyk and Scott, 1976).

Building on the results from this initial paper, Fanti et al. (1981) published polarisation maps. They used these observations to determine the internal Faraday rotation, the orientation of the magnetic field and the ratio of the uniform magnetic to random magnetic field. At 5 GHz, they found a fractional polarisation of 40% in the inner regions of the tail (out to about 10 kpc). Beyond this region, the polarisation decreases and the signal to noise prevents further conclusions. The core is found to be unpolarised and the SE 'leading component' has a fractional polarisation of less than 20%. At 1.4 GHz the signal to noise is higher, and the polarisation can be traced out to about 100 kpc. The degree of polarisation increases from 4% in the inner tail to 20% in the outer regions. At 0.6 GHz, the source is found to be unpolarised.

The rotation measure across the source is found to be 16 $\pm$ 20 rad m^{-2}, calculated using the 1.4 GHz and 5.0 GHz observations and combined with results of Parma and

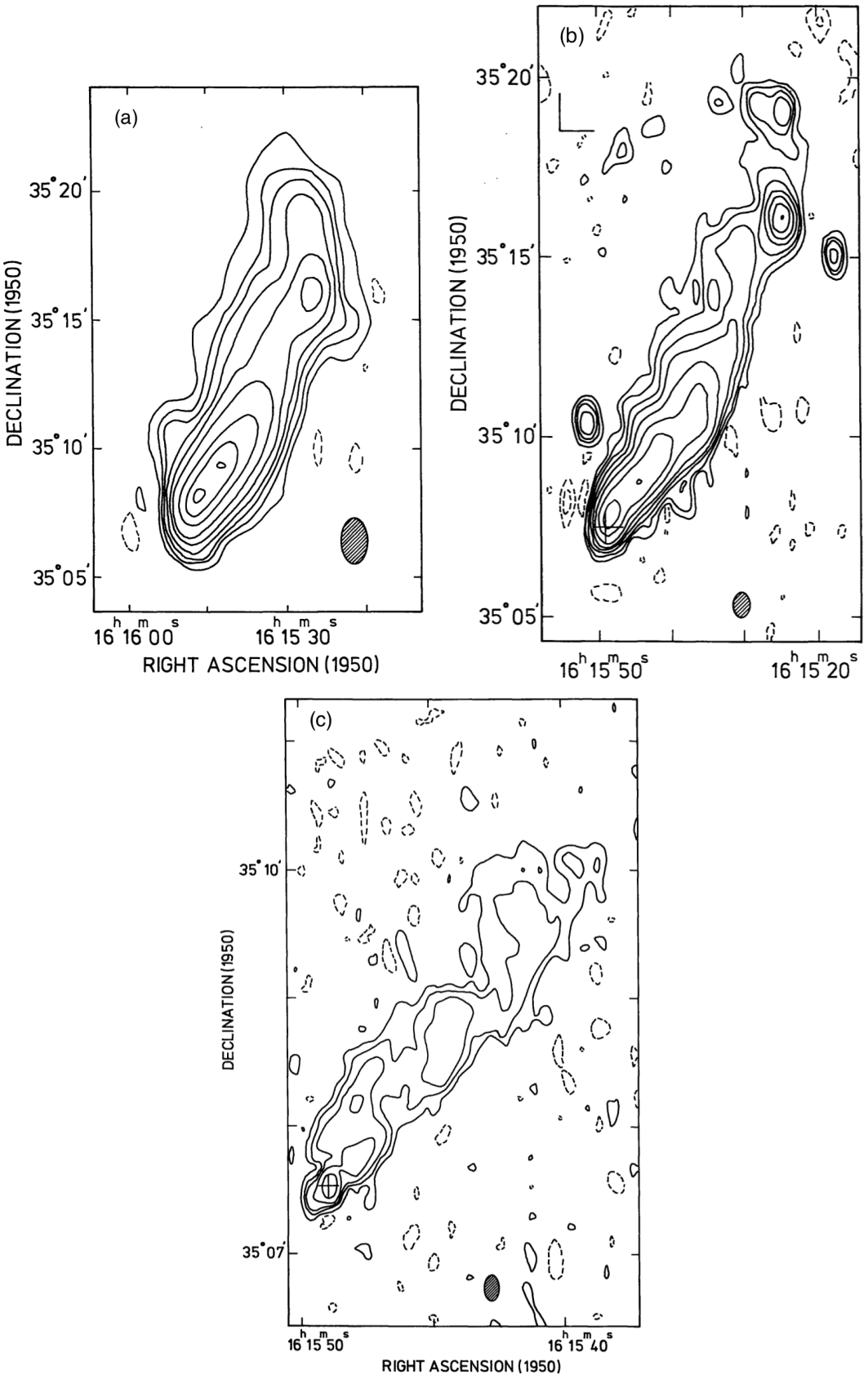

Figure 3.6: The brightness distribution of NGC 6109 published by Ekers (1978) using the WSRT at *(a)* 0.6 GHz, $50'' \times 87''$ resolution *(b)* 1.415 GHz, $24'' \times 42''$ resolution and *(c)* 5.0 GHz, $8'' \times 14''$ resolution. In *(b)* and *(c)* the position of the galaxy NGC 6109 is indicated by a cross.

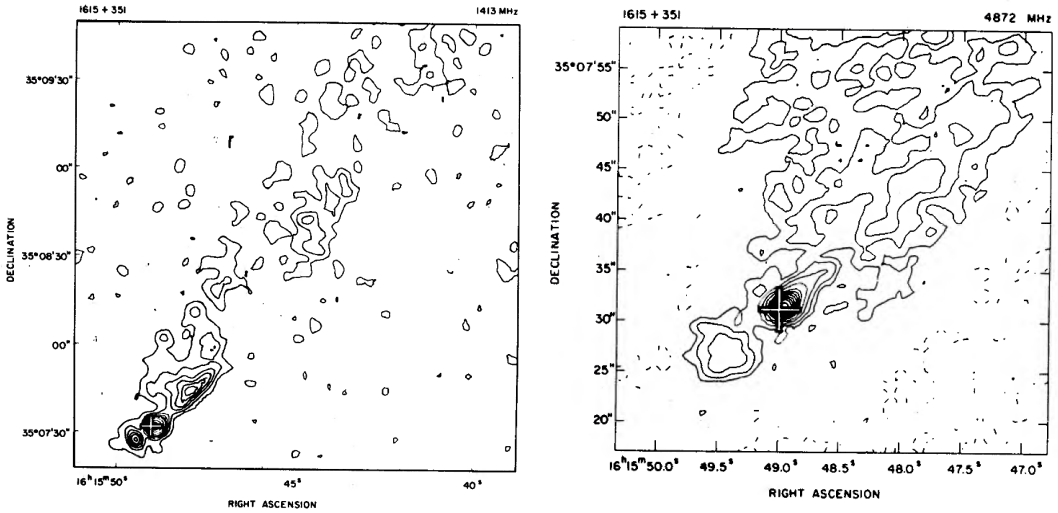

Figure 3.7: VLA maps of NGC 6109 published by Burns and Gregory (1982) at *(left)* 1.41 GHz and $4.6'' \times 4.3''$ resolution, *(right)* 4.87 GHz and $1.7'' \times 1.4''$ resolution. The cross marks the position of the optical nucleus of NGC 6109.

Weiler (1981) using the Effelsberg telescope at 2.7 GHz. The magnetic field is found to align with the tail and significant depolarisation is found between 1.4 and 5.0 GHz, suggesting a large density of thermal plasma in the radio emission.

The radio structure of NGC 6109 was also mapped by Burns and Gregory (1982) with the VLA in the B-configuration at 1.4 and 5.0 GHz, to provide a sample of 4C radio galaxies (Gower et al., 1967) in poor Zwicky clusters. These maps are shown in Figure 3.7. The SE leading component is more discernible in these maps, and Burns and Gregory (1982) describe the galaxy morphology as a 'tadpole-like' tailed source. They proposed that the source may be an example of twin plasma ejections but with the line of ejection along the galaxy velocity vector. The SE component could then be stunted by strong ram pressure produced by ejection into the intracluster medium in the same direction as the galaxy motion.

Some source structure parameters from the literature are given in Table 5.1.

3.2.2 Optical observations

Optical observations by Tomita et al. (1999) classified NGC 6109 as an E1 elliptical galaxy with a diameter $35''$ and ellipticity 0.10 ± 0.05. Optical spectroscopy was also carried out on NGC 6109, although only a few weak emission lines were observed. From the spectra, an estimate of the Hα luminosity was calculated to be $L(H_\alpha) = 5 \times 10^{39}$ erg s^{-1} and the star formation rate was found to be less than 7×10^{-3} $M_\odot$ yr^{-1}. Only one

Component	Frequency (GHz)	Flux density (Jy)	α	Reference
Entire source	0.408	5.4	0.9	1
Entire source	0.610	4.6		1
Entire source	1.415	2.1		1
Entire source	4.995	0.55		1
Core	1.4	0.05		2
Core	4.995	0.054		1
Core	5.0	0.029		2

Table 3.2: Key parameters of NGC 6109 from the literature. The spectral index α is defined as $S \propto \nu^{-\alpha}$. References : (1) Ekers (1978), (2) Burns and Gregory (1982)

galaxy within the cluster Zw 1615.8 + 3505, NGC 6104, showed evidence for strong line emission.

Ekers (1978) carried out optical observations of the cluster Zw 1615.8 + 3505 using the Kitt Peak National Observatory (KPNO) 2.1m and 4m telescopes, to determine the velocity dispersion σ, and the velocity of the radio galaxy with respect to the intracluster medium. These were calculated to be 584 km s^{-1} and 588 km s^{-1} respectively.

The velocity of NGC 6109 with respect to the ICM was also determined by Ulrich (1978) in a study of four head-tailed radio galaxies approximately 100-200 Mpc from the Earth. Their finding chart for the cluster is given in Figure 3.8. This chart shows the situation in the cluster to be complex, and suggests the possibility that there are two clusters, A and B. Cluster A has velocities in the range 8500 - 9800 km s^{-1} and is richer and more extended. Cluster B has velocities in the range 9800 - 10600 km s^{-1}. Alternatively, Zw 1615.8 + 3505 could be a single cluster, with a peculiar distribution of velocities.

3.2.3 X-ray observations

A survey by Price et al. (1990) of the X-ray emission from poor clusters revealed the presence of gas in Zw 1615.8 + 3505. They used the Einstein X-ray satellite to map the X-ray morphology and classified it as a 'T' type cluster; a cluster where the X-ray emission traces the distribution of galaxies and there is no X-ray dominant cluster member. They extracted an X-ray luminosity of L_X = 23.7 $\times$ 10^{42} ergs s^{-1} between 0.5 and 4.5 keV.

NGC 6109 was observed by the ROSAT satellite in 1991, with both the Position Sensitive Proportion Counter (PSPC) and High Resolution Imager (HRI). Using these observations, Feretti et al. (1995) reported on the interaction of the X-ray gas with the extended radio structure. They investigated whether the external gas could confine the radio source and modify its morphology via ram pressure. They also produced high resolution images

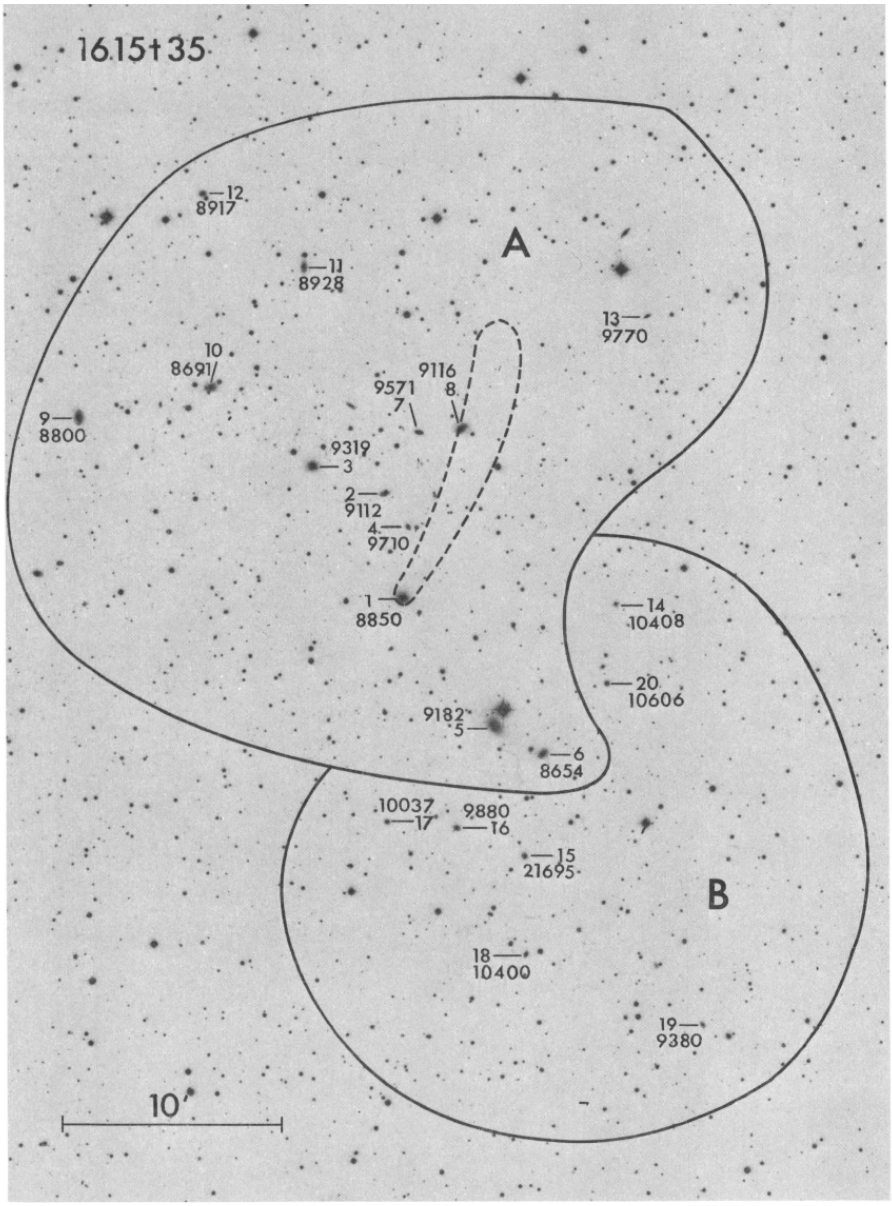

Figure 3.8: Finding chart for cluster Zw 1615.8 + 3505, published by Ulrich (1978). The head-tail radio galaxy NGC 6109 is labelled '1' and given with its velocity in units of km s^{-1}. '5' is associated with NGC 6107. The sub clusters A and B are labelled, and the dashed line approximates the 1.4 GHz contour of the radio tail.

and X-ray spectra. Figure 3.9 shows a grey-scale X-ray image from the PSPC with 0.6 GHz radio contours. Discrete X-ray sources are identified with the tailed radio galaxy NGC 6109 and NGC 6107. An important result from Feretti et al. (1995) is the detection of extended diffuse X-ray emission, which appears to be of thermal origin and related to the intergalactic medium in the group. It looks to be roughly centred between NGC 6109 and NGC 6107, elongated in the N-S direction and has a maximum size of about 800 kpc. NGC 6109 shows only unresolved X-ray emission, probably originating in the galactic nucleus and they calculated a gas temperature of 2.1 $\pm$ 0.6 keV for the diffuse gas.

NGC 6109 was observed with *Chandra* in 2003 for approximately 20 ks. Spectral fitting of the nucleus by Evans (2005) found kT = 0.63 $\pm$ 0.15 keV for a source-centred circle with radius 1.23$''$. Evans (2005) compared the 1-keV flux density from *Chandra* (1.4 nJy) to that with ROSAT (Hardcastle and Worrall, 1999) (12 nJy) and concluded that the discrepancy is due to the enhanced resolution of the *Chandra* images.

Mannering (2013) used the same *Chandra* observations to search for a gas belt in NGC 6109. The *Chandra* exposure-corrected image in the energy range 0.4-8.0 keV is given in Figure 3.10 with VLA contours. Mannering (2013) uses this image to confirm the existence of an X-ray gas belt in the NE-SW direction, with the pressure of the gas constraining the central radio emitting plasma from the jets of NGC 6109.

3.3 NGC 7016 and NGC 7018

PKS 2104-25 is a radio source complex in the central regions of the cluster A 3744. The environment is dominated by two large radio jet sources, associated with the galaxies NGC 7016 and NGC 7018, at z = 0.0381 (Mazure et al., 1996). These sources are in relatively close proximity and exhibit complicated radio structures which suggest an interaction with the cluster atmosphere. Although they show different morphologies and structures, their luminosities are similar. There are two other small radio sources in the vicinity on the sky with no obvious optical counterparts and presumed to be distant background sources unrelated to the cluster. NGC 7018 lies to the N of NGC 7016 and has its radio core in the nucleus of a dumbbell galaxy, whereas NGC 7016 lies within an elliptical E0 galaxy.

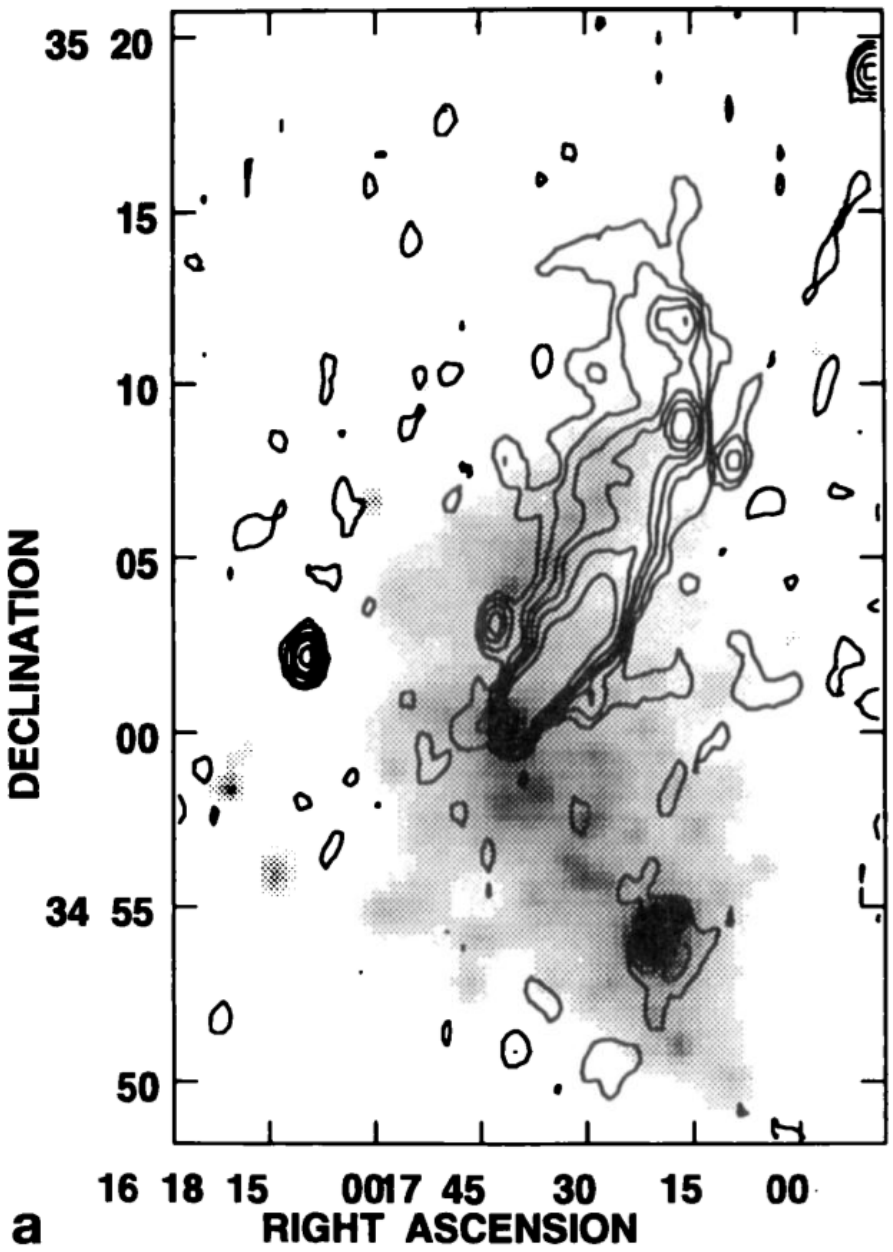

Figure 3.9: A grey scale X-ray image of NGC 6109 from the PSPC with 0.6 GHz WSRT radio contours at $51'' \times 30''$ resolution, published by Feretti et al. (1995). Discrete X-ray sources are associated with NGC 6109 and NGC 6107 (SW of NGC 6109). Other background sources are also visible.

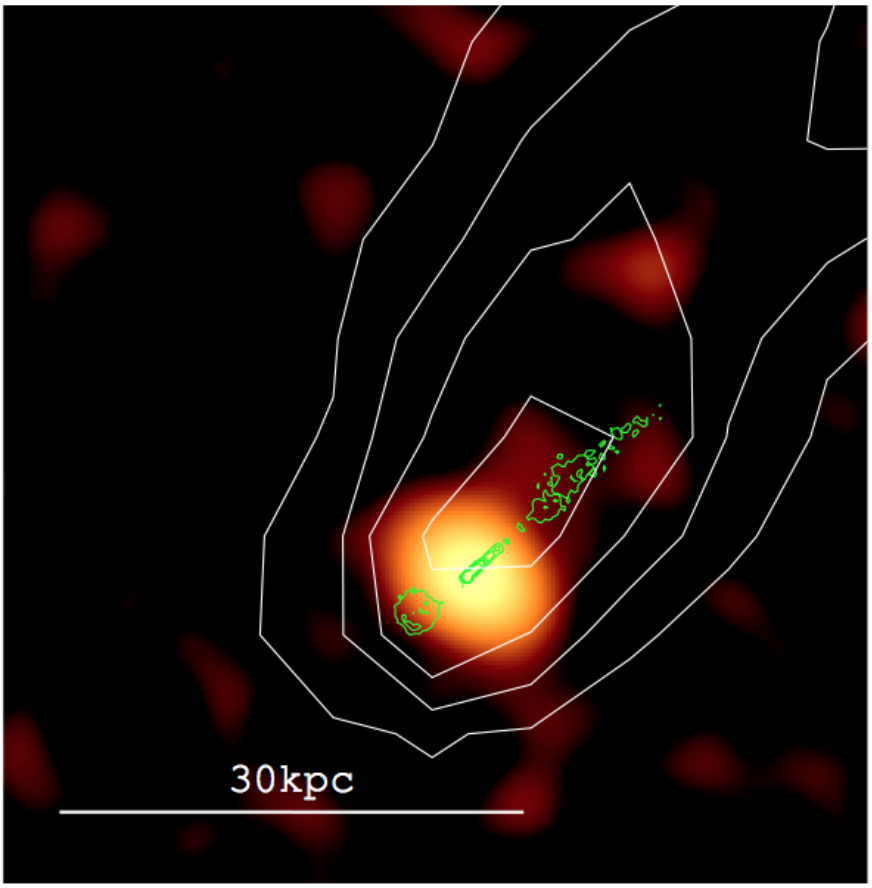

Figure 3.10: A *Chandra* exposure-corrected image of NGC 6109 in the energy range 0.4-8.0 keV, taken from Mannering (2013). The green contours are VLA radio observations at 5 GHz with resolution 1.4″, and the white at 1.4 GHz with resolution 14.8″.

Instrument	Year	Frequency (GHz)	Flux density (Jy)	Reference
MSH	1960	0.086	100	1
Parkes	1964	0.408	31	2
Parkes	1964	1.400	12	2
Parkes	1964	2.650	7.3	2
Parkes	1969	0.408	22	3
Parkes	1969	1.400	9.5	3
Parkes	1969	2.650	5.9	3
Fleurs Observatory	1973	0.029	180	4
Fleurs Observatory	1973	0.408	28.1	5
Culgoora Catalogue	1977	0.080	70	6
Culgoora Catalogue	1977	0.160	50.2	6
VLA	1988	0.080	70	7
VLA	1988	0.160	50.2	7
VLA	1988	1.420	11.2	7
VLA	1988	2.700	6.2	7
VLA	1988	5.000	3.97	7

Table 3.3: Flux densities of the radio complex PKS 2104-25 from the literature. References : (1) Mills et al. (1960), (2) Bolton et al. (1964), (3) Ekers (1969), (4) Finlay and Jones (1973), (5) Robertson et al. (1973), (6) Slee (1977), (7) Ekers et al. (1989)

3.3.1 Radio structure

NGC 7018 has been classified as a FR II-type source and it is one the closest of these type of sources to Earth. This proximity has therefore lead to detailed study of the radio properties of the system. The more southern source in the cluster, NGC 7016, is an example of an FR I-type radio galaxy. Detailed investigation into these sources together provides a unique opportunity to look at the intrinsic differences related to different source morphologies within a similar environment.

The radio source complex PKS 2104-25 has been listed in several different catalogues of southern radio sources. The original MSH catalogue (Mills et al., 1960) lists it as MSH 21-21, an extended source ($>$ 50 arcsec) with a flux density of 100 Jy at 86 MHz. Table 5.1 gives an overview of the flux measurements carried out on this source.

The earliest image of PKS 2104-25 was published by Ekers et al. (1989), who used two-element interferometer fringes measured at 467 MHz and 1.401 GHz to fit a 2-D double elliptical gaussian model to the source. Other radio images of both NGC 7016 and NGC 7018 were published by Wall and Cole (1973) using the Parkes 64 m telescope at 5 GHz and Schilizzi and McAdam (1975) with the Molongolo Cross Telescope at 408 MHz. These observations had insufficient resolution ($>$ 50 arcsec) to reveal the full extent

of the radio structure or reveal the emission to be from two independent sources. The polarisation of PKS 2104-25 was measured by Gardner and Davies (1966), who found a low net polarised flux density ($< 2\%$ of the total flux density).

Heckman et al. (1986) observed PKS 2104-25 with the VLA and distinguished the two individual radio sources, with 1.4 GHz fluxes $\approx$ 11 Jy for each source. They did not however, present images of the galaxies and misclassify NGC 7018 as an FR I-type source.

A comprehensive study of the complex radio structure of this system was carried out by Cameron (1988) using VLA observations at 1.415, 1.635 and 4.860 GHz taken in 1984. Figure 3.11 shows the radio structure of the two sources at 4.86 GHz with 2.5 arcsec resolution. Because of the southern declination of PKS 2104-25, many observations used the VLA in a 'hybrid' configuration, with the northern arm in the next larger configuration than the eastern and western arms, to provide an approximately circular synthesised beam.

The total flux densities of NGC 7018 and NGC 7016 at 1.415 GHz were found to be 6.0 and 4.74 Jy, respectively. The morphology of the sources in Figure 3.11 is complex, with large scale bends seen in both. NGC 7018 displays a N lobe and SW lobe which is extended to the W for 12 arcmin. NGC 7016 shows thin jets emitted in opposite directions. The N jet extends to the NW before bending towards the N and then entering a swirl of radio emission. The S jet bends 90° to the S and then again to the E.

3.3.2 Optical observations

Cameron (1988) investigated the optical properties of the PKS 2104-25 system. NGC 7018 was found to have an unusual double nucleus, with the radio jets emanating from the eastern nucleus. NGC 7016 has a bright nucleus, with no other significant optical features.

3.3.3 X-ray observations

The influence of radio galaxies NGC 7018 and NGC 7016 on cluster gas was investigated by Worrall and Birkinshaw (2014). Prior to this, A3744 had been detected in the ROSAT All-Sky Survey and was one of the members of the REFLEX cluster catalogue (Böhringer et al., 2014). However the archival data were insufficient to probe the cluster substructure.

Sensitive *Chandra* observations of the cluster were made with the Advanced CCD Imaging Spectrometer (ACIS) in 2010 for 75 ks, and an exposure-corrected image is

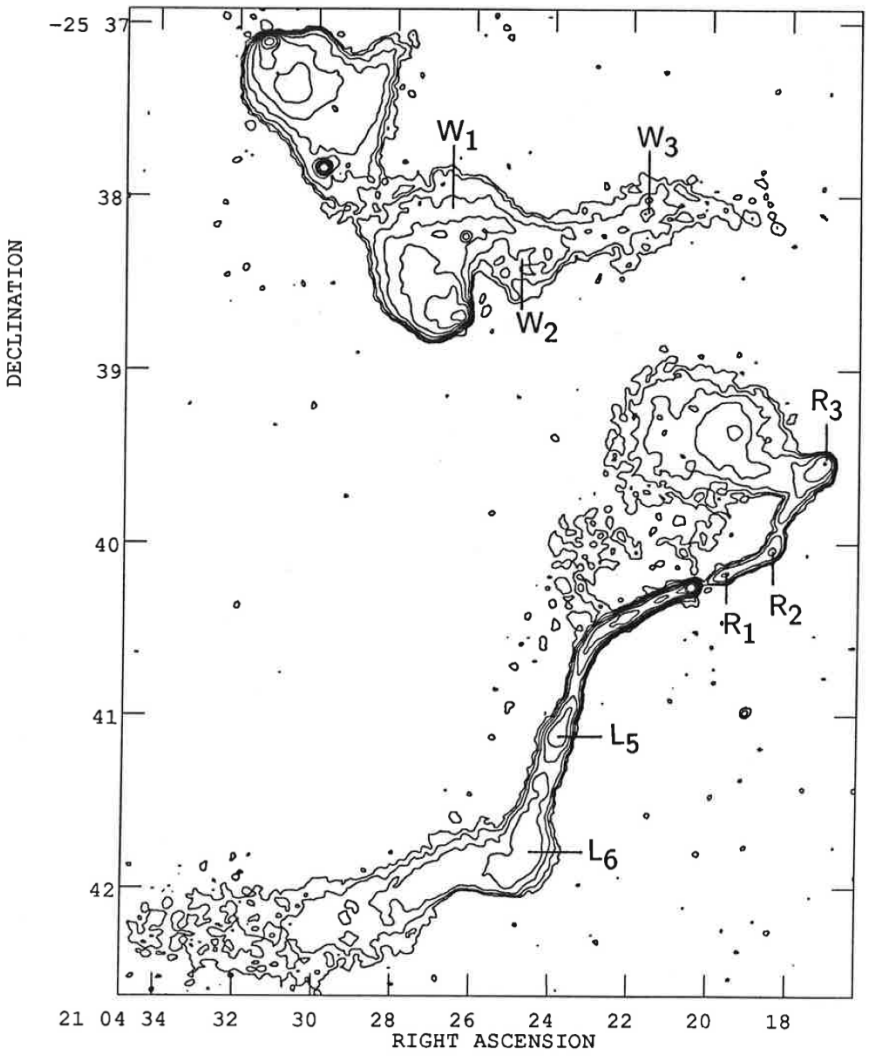

Figure 3.11: Radio contours of NGC 7016 and NGC 7018 from a VLA observation at 4.860 GHz with 2.5 arcsec resolution, published by Cameron (1988). The peak surface brightness in the source is 57.5 mJy beam^{-1}. The contour levels are at -0.2, 0.2, 0.4, 0.8, 1.6, 3.2, 6.4, 12.8 and 25.6 mJy beam^{-1}. The labels refer to distinct regions and are discussed in Cameron (1988).

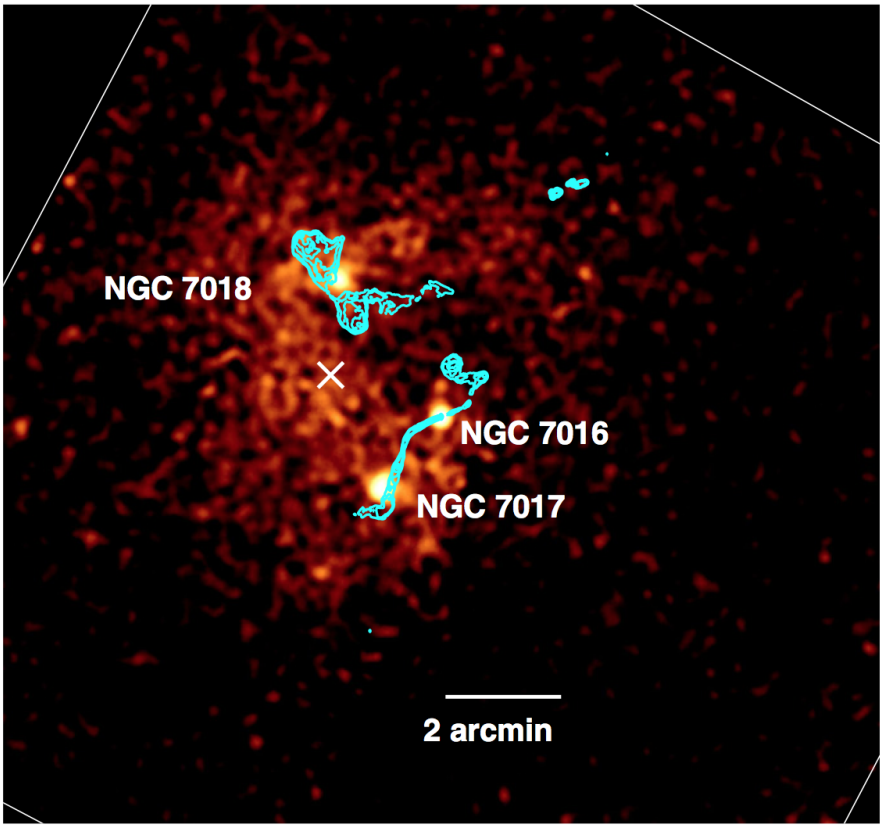

Figure 3.12: A 0.3-5 keV exposure-corrected *Chandra* image of NGC 7016 and NGC 7018, taken from Worrall and Birkinshaw (2014). The image has been smoothed with a 2D Gaussian of radius 20 pixels after removal of point sources. The blue contours are eVLA radio observations at 1.4 GHz with restoring beam $2.16'' \times 1.01''$. The white cross indicates the centre of the cluster gas.

shown in Figure 3.12 with contours from VLA radio observations.

Worrall and Birkinshaw (2014) reported an X-ray cavity coincident with the position of the radio swirl in NGC 7016 and suggested that the radio feature could be produced due to a collision with the radio plasma from NGC 7018 or in the wake of its motion. An important result of their investigation is an X-ray temperature gradient alongside the 'tendril' features of the radio sources. They suggested that because the radio plasma is magnetised, it can act as a barrier to transport between gas layers and reduce the effective viscosity, preserving post-merger gas flows.

The 1 keV X-ray flux was calculated to be 8.6 nJy and 15.8 nJy in NGC 7016 and NGC 7018 respectively and a gas temperature of 0.87 (nuclear) and 1.01 (gas) keV was found for NGC 7016.

3.4 Summary

In this chapter I have given an overview of the sources studied in this thesis, so that maps and parameters given in the literature can be compared to those from more recent observations which are presented in subsequent chapters.

Aspects of the radio sources to be studied in this thesis include:

1. Overall structural details, such as the extents and shapes of the radio sources on large and small size scales, source luminosity, jet sidedness, etc.

2. The surface brightness along the jets (e.g. Killeen et al., 1988).

3. The spectral index evolution along the jets and lobes.

4. Rotation measure structures, which can define the environment of the radio source and provide a means of examining the interaction between a radio source and its environment (e.g. Dreher et al., 1987).

5. Magnetic field structures, showing the evolution of parallel and transverse components of the magnetic field in the radio jets (Bridle 1984, for a review) and regions of compression and shear in the jets and lobes.

Chapter 4

Multi-frequency Observations of the Radio Galaxy NGC 7385

4.1 Introduction

Relativistic outflows of plasma from the central regions of active galactic nuclei (AGN) are often observed as jets extending away from the nuclei of their parent galaxies. At large distances these may develop into large-scale 'plumes' or radio lobes. Jets and lobes play host to some of the most energetic particles in the Universe. NGC 7385 was classified by Schilizzi and Ekers (1975) as having a head-tail morphology. The long bright radio tail extends to the S of the core, approximately 510 kpc in length.

Despite the large number of radio jets that have observed X-ray counterparts, relatively few optical counterparts have been detected (see http://astro.fit.edu/jets and references therein for a complete sample).

Optical synchrotron jets are of particular interest because the energy loss times for high-energy electrons are typically short (and shorter still for X-rays), of the order of 100 years. X-ray and optical synchrotron features localise the sites of particle acceleration, thus studies of optical jets can probe jet interiors and constrain energy transfer processes in radio galaxies. Because of this potential importance to radio-source physics, extensive searches for optical jets have been carried out (e.g. Butcher et al., 1980). As the number of confirmed detections has increased, particularly from the Hubble Space Telescope (HST), some patterns in their properties have emerged. Optical jets show a strong similarity to the radio morphology and a high degree of linear polarisation (e.g. 3C 66B, 3C 78, 3C 264; Perlman et al., 2006), but optical jets are shorter and narrower than their radio

counterparts (Sparks et al., 1995). No optical observations of NGC 7385 have previously revealed evidence for an optical jet, however Simkin and Ekers (1979) detected an optical object associated with the NE radio component.

Radio/optical interactions can provide a better insight into the physical conditions within radio sources and in their environment than radio data alone. The detection of an optical object with emission lines and an underlying continuum in the outer region of a radio galaxy is relatively rare. Sources studied in depth include 3C 277.3 (van Breugel et al., 1985b; Worrall et al., 2016), 3C 305 (Heckman et al., 1982; Reynaldi and Feinstein, 2013), 4C 26.42 (van Breugel et al., 1984), 4C 29.30 (van Breugel et al., 1986), Minkowski's object (van Breugel et al., 1985a; Croft et al., 2006) and PKS 2152-699 (Fosbury et al., 1998; Birkinshaw and Worrall, 2013). These objects are faint, thus making them difficult to study, however a few general conclusions have been reported. The optical emission-line regions form at the edges of radio jets which are propagating through a dense ambient medium. When these jets collide with relatively cool clouds they can ionise the optical gas, producing line emission and disturbing the collimation and polarisation of the radio plasma. Spectroscopic analysis can reveal the excitation mechanism and the velocity field of the optical gas, and polarimetric radio studies can shed light on the magnetic field strength and electron densities in this interacting region.

In this chapter I present multi-frequency observations of the radio galaxy NGC 7385, with archival VLA and recent JVLA observations. I also used data from the Wide Field Camera 3 (WFC3) on the Hubble Space Telescope (HST) in conjunction with *Chandra* observations, taken as part of a survey to look at the X-ray activity of low redshift 3CRR galaxies. A significant amount of this chapter has appeared in Rawes et al (2015), with the exception of the new JVLA observations. These new observations provided good quality polarimetric and rotation measure analysis. Throughout this section I adopt the cosmological parameters H_0 = 70 km s^{-1} Mpc^{-1}, $\Omega_{\Lambda 0}$ = 0.7, Ω_{m0} = 0.3. The redshift of NGC 7385 (z = 0.024, Högbom, 1974) corresponds to a luminosity distance of 106 Mpc and a projected linear scale of 0.49 kpc/arcsec.

4.2 Observations and Analysis

4.2.1 Radio observations: calibration and data reduction

NGC 7385 has been observed with the VLA for 16 different science projects since 1980. I used data from the NRAO VLA archive to map the intensity distribution and polarisation structure of its radio features. The unusual jet morphology discerned from these maps prompted a proposal to the VLA to request further observations with the upgraded JVLA telescope. The enhanced capabilities of this telescope allowed me to probe the polarised emission of this source with higher sensitivity and investigate the RM structure associated with the jet and counter-jet.

4.2.1.1 Archival data

The NRAO archive contains almost all VLA data since observing started in 1976, and all contents are available through the Archive Access Tool (AAT). I selected datasets which had observed NGC 7385 for more than 500 s, had used more than 26 antennas, and had all four correlations available. Table 4.1 gives details of the VLA observations I calibrated and imaged from the archive. I produced maps of all the data given in Table 4.1, however the majority of measurement sets were of insufficient quality to publish.

Project code	Configuration	Date	Frequency (GHz)	Bandwidth (MHz)	Time (s)	Resolution (arcsec)	Flux calibrator
AB 412	C	86-Dec	1.46-1.51	50	540	12	3C 48
AM 0484	A	95-Oct	8.41-8.46	25	540	0.24	3C 48
AW 112	C	84-Jun	4.83-4.89	50	1020	3.9	3C 286
BT 18	B/AB	95-Oct	4.99-8.64	50	3320	1.2	3C 48
AC 243	A	88-Dec	1.46-1.51	50	540	1.4	3C 48, 3C 286
AH 129	A	83-Oct	1.46-14.91	50	4900	1.4/0.14	3C 286
AL 419	C	97-Aug	1.42-1.47	25	10460	12.5	3C 48
AW 136	BC	85-Jun	4.84-4.89	50	1560	1.2	3C 48, 3C 286
AW 87	A	83-Oct	1.51-14.96	50	1260	1.4/0.08	3C 48, 3C 138

Table 4.1: VLA observations used to calibrate and produce images of NGC 7385 from the NRAO data archive.

Different frequency bands and VLA configurations are appropriate for different imaging goals. 1-2 GHz (L band) observations can reveal the structure of radio sources on kpc scales; at 4-5 GHz (C band), observations are unaffected by radio frequency interference. The configuration of the VLA also affects the synthesised beam width (see Table 2.3, chapter 2 for details). For NGC 7385, I used observations at 1-2 GHz in C-array to map the large scale structure of the emission and observations at the same frequency in A-array to highlight the high resolution morphology of the inner jet regions. The polarisation structure of the source was analysed from both 1-2 GHz and 4-5 GHz observations, in order to look for depolarisation and rotation measure between the frequency bands.

The flux calibrators for each project are given in Table 4.1. The flux densities for all these sources are well known and stable. A phase calibrator was chosen by looking for a source close on the sky to NGC 7385 and with a flux density listed in the VLA Calibrator Manual. The polarisation properties of the calibrator 3C 48 are unstable at $\leq$ 3 GHz (Perley and Butler, 2013) and therefore this source was not used to fix the absolute position angle of polarised emission for L band observations. For position angle calibration based on observations of the sources 3C 138 and 3C 286, position angles of -10° and 33° and fractional polarisations of 0.05% and 10% respectively, were assumed at 1-2 GHz. At 4-5 GHz, angles of -11° and 33° and fractional polarisations of 0.1% and 11.2% were used.

Archived VLA data are not passed through any kind of calibration or flagging pipeline prior to release. The data reduction and calibration were carried out using the Common Astronomy Software Applications package (CASA) and closely followed the procedures set out in the CASA cookbook and reference manual. A detailed explanation of the calibration and imaging techniques used to reduce radio data can be found in chapter 2, however in brief the following data reduction steps were carried out:

1. Data were inspected to look for faulty data points. Detected problems included antenna drop outs, baseline amplitude errors and missing data for the first few seconds of each new scan. All data were passed through the flagging algorithm *rflag*, and L band datasets were run through the *aoflagger* software to excise problems due to RFI.
2. An absolute flux density scale for the primary flux calibrators was set.
3. The delays of each antenna relative to a reference antenna were solved for, before amplitude and phase solutions for each of the antenna gains as a function of time were obtained from the phase calibrator and primary flux calibrator.
4. Polarisation calibration was carried out by finding the cross hand leakage gains and the

absolute polarisation position angle. Solving for the gains required using a calibrator with a large range in parallactic angle across the scans. This was the phase calibrator in most cases. Alternatively, if a known, unpolarised source was observed then this could also be used. The polarisation position angle was set using observations of the primary flux calibrator, for which the position angle and fractional polarisation is known and stable.

5. The amplitude gains of the primary calibrator were scaled to the phase calibrator and all calibration tables were then applied to the NGC 7385 visibility data by interpolation between adjacent gain solutions.

Images of the sky brightness distribution were made via Fourier transforms of the visibility data, together with deconvolution of the interferometer diffraction pattern using the CASA task *clean*. This task also corrects for the primary beam of the telescope. Initially only the Stokes I parameter was mapped, so that a general idea of the quality of the image could be obtained without the additional CPU time required to map all four Stokes parameters. Data were then self-calibrated (e.g. Pearson and Readhead, 1984), to correct for residual phase and amplitude errors in the gain solutions. Self-calibration corrects solutions by iteratively converging the visibility data and the CLEAN model of the sky brightness. This allows the removal of gain fluctuations and atmospheric phase disturbances on shorter timescales than the gain solutions obtained from the phase calibrator observations.

Good quality L band total intensity and polarisation images were produced from the projects AL 419 and AH 129. The project BT 18 provided sufficient data to produce C band maps. The final deconvolved Stokes I, Q and U images at each frequency had rms noise levels within a factor of 2 of the expected limiting noise level estimated from the noise temperature of the VLA receivers. The Stokes Q and U images generally had lower rms noise levels than the Stokes I images, because of the smaller dynamic range. Figures 4.1 and 4.2 show the L band intensity distribution of NGC 7385 at 14 arcsec and 1.4 arcsec resolution respectively. Some low-level striping persisted in the higher resolution image; however this minor defect does not affect the information extracted from the image. The C band map from the BT 18 project is shown in Figure 4.3, at 1.3 arcsec resolution. Stokes V images were checked to ensure that they showed no structure; any visible structure could indicate an error in the calibration tables, or unflagged RFI.

Fractional polarisation maps are given in Figures 4.4 and 4.5 at 1.41 and 4.99 GHz respectively, producing by combining the Stokes I, Q and U images in the form

Total flux density (Jy, 1.44 GHz)	2.59 ± 0.0007
Total power (W Hz^{-1}, 1.44 GHz)	$\sim 10^{24}$
Core position (J 2000)	RA 22 49 54.59
	Dec 11 36 30.9
Core flux density (mJy, 1.49 GHz)	71 ± 0.3
(mJy, 4.99 GHz)	115 ± 0.1
Core power (W Hz^{-1}, 1.49 GHz)	$\sim 10^{22}$
NE component position (J 2000)	RA 22 49 55.52
	Dec 11 36 45.59
NE component size (arcsec, 1.41 GHz)	25×15
(arcsec, 4.99 GHz)	38×20
NE component flux density (Jy, 1.49 GHz)	0.47 ± 0.003
(Jy, 4.99 GHz)	0.28 ± 0.004
Core - NE component distance (arcsec)	20
SW tail projected length (arcsec, 1.41 GHz)	60
(arcsec, 4.99 GHz)	52
SW inner jet flux (Jy, 1.49 GHz)	0.23 ± 0.006
(Jy, 4.99 GHz)	0.10 ± 0.004
Tail length (arcsec)	1100
Counter-jet tail length (arcsec)	950

Table 4.2: Morphological parameters of NGC 7385 from the archival observations. The SW inner jet is taken to be up to 20″ from the core.

$$P = \sqrt{\frac{Q^2 + U^2}{I^2}} \tag{4.1}$$

The apparent magnetic field direction can be determined by rotating the polarisation position angle by 90° and these vectors are shown in Figures 4.6 and 4.7. The rotation measure structure cannot be determined for these data due to inadequate frequency coverage with sufficient signal to noise at matched angular resolutions, thus the vectors are uncorrected for Faraday rotation effects.

Table 4.2.1.1 lists some fundamental parameters and measured quantities for the radio galaxy NGC 7385 from the AL 419 (1.44 GHz), AH 129 (1.49 GHz) and BT 18 (4.99 GHz) observations.

4.2.1.2 Radio morphology

Figures 4.1 and 4.2 show a one-sided radio jet extending to the SW of an unresolved core. The NE counter-jet is not detected close to the nucleus, but must be present since it expands into a lobe-like feature. The full length of the jet is evident from Figure 4.1. The collimated part of the emission extends about 7 arcminutes (200 kpc). The image shows

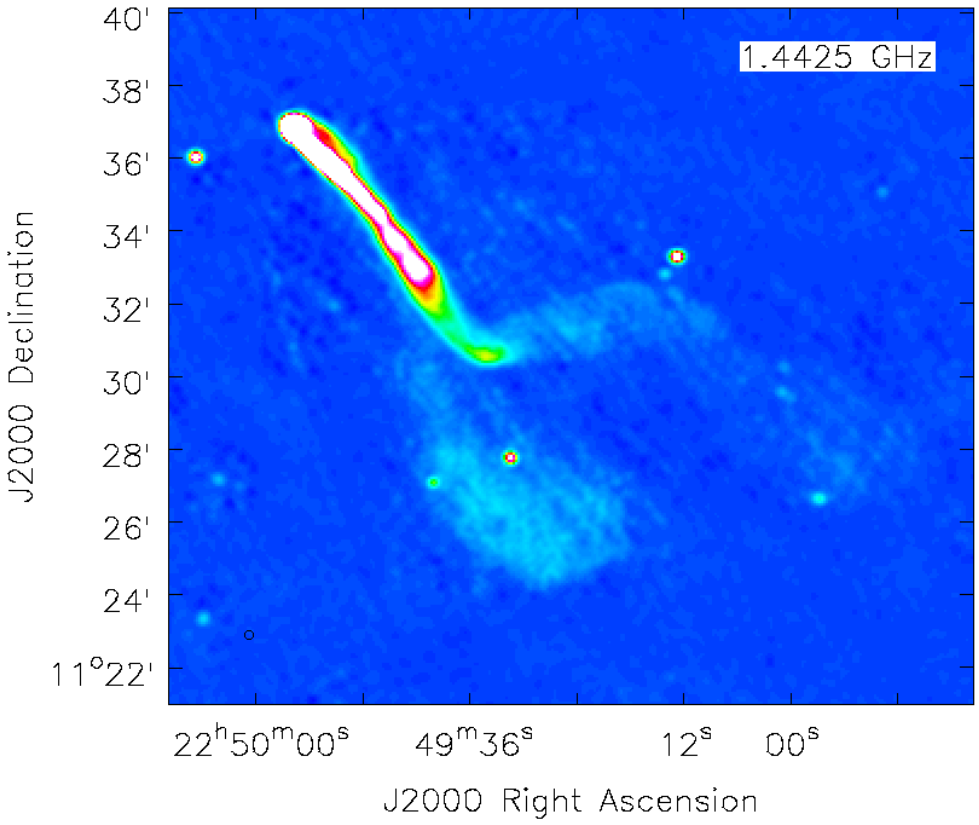

Figure 4.1: 1.44 GHz total intensity image of NGC 7385 at 14 arcsec resolution. Background sources appear superimposed onto the tail at RA 22h 49m 31.4s, Dec = +11d 27′ 45.7″ and RA = 22h 49m 12.8s, Dec = +11d 33′ 17.5″.

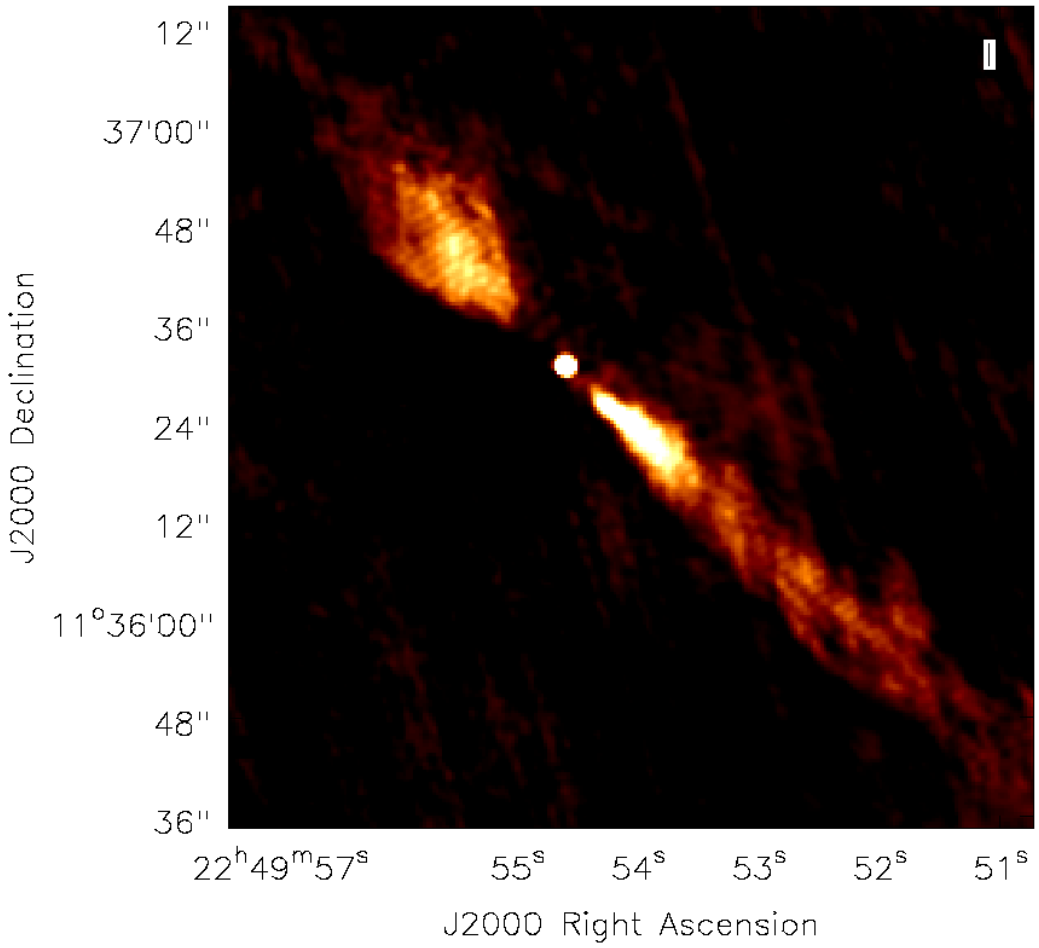

Figure 4.2: 1.49 GHz total intensity image of NGC 7385 at 1.4 arcsec resolution.

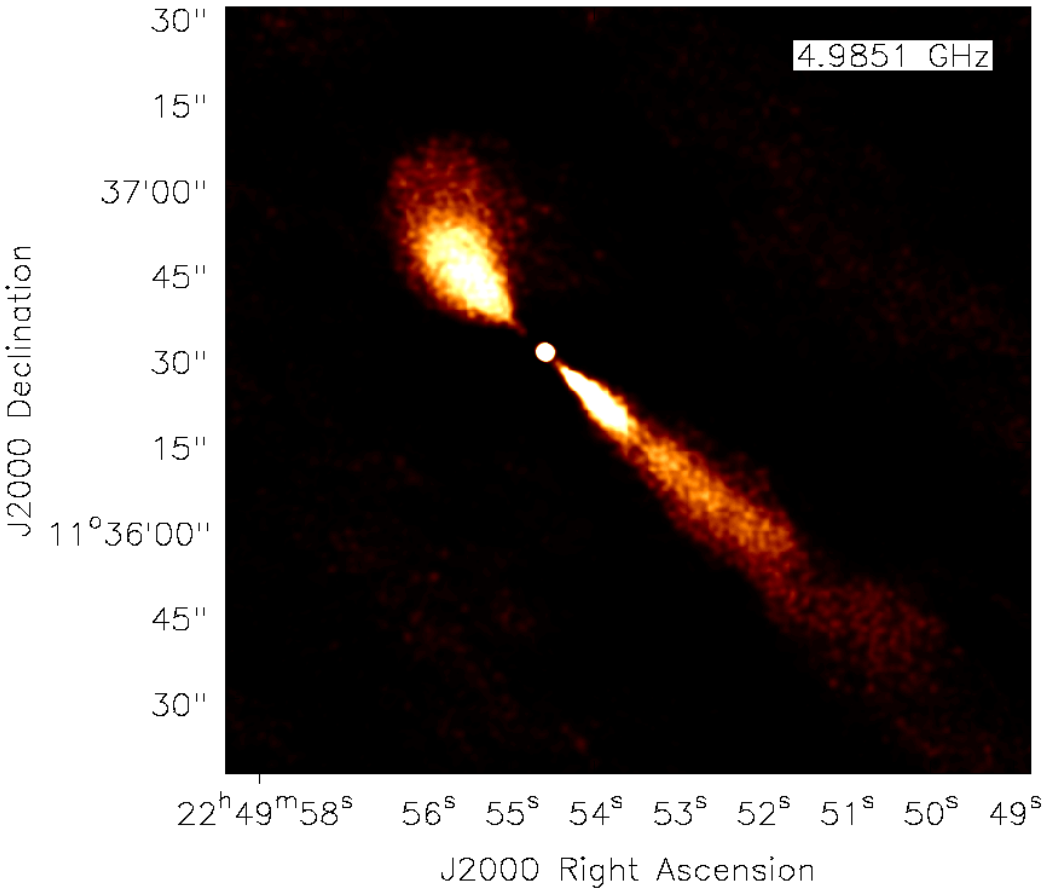

Figure 4.3: 4.89 GHz total intensity image of NGC 7385 at 1.3 arcsec resolution.

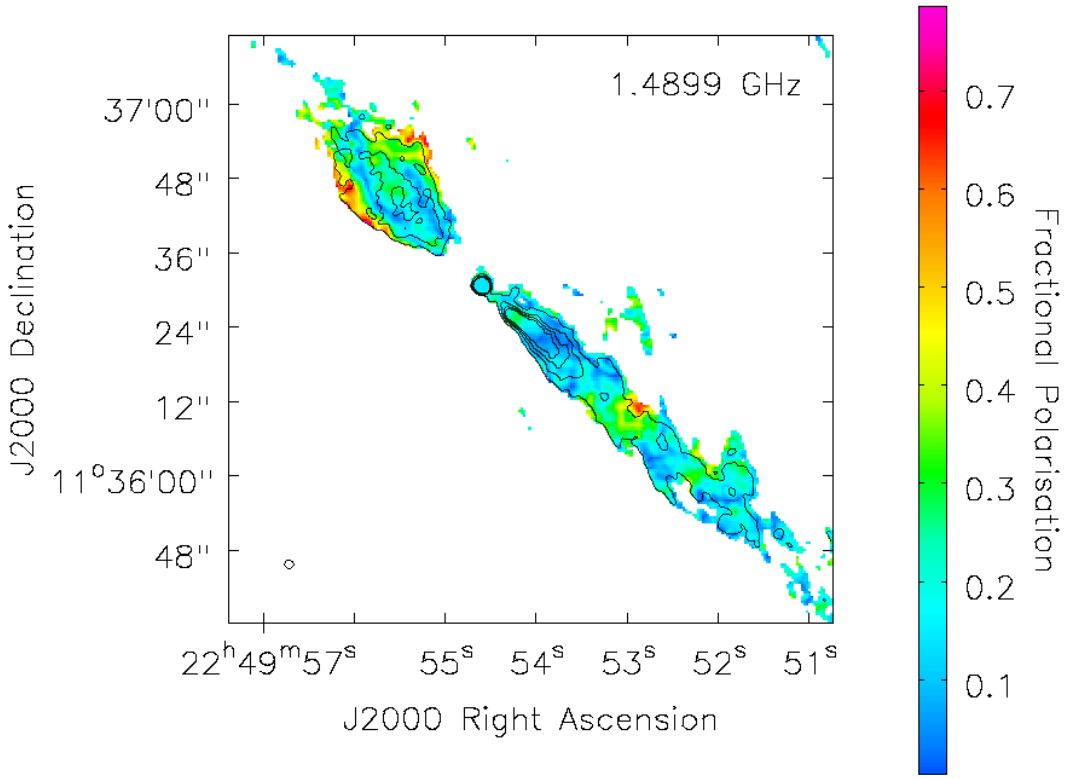

Figure 4.4: Fractional polarisation and intensity contours from the AH129 dataset showing the inner jet and counter jet at 1.49 GHz. Contour levels 2, 4, 6, 8 mJy beam^{-1}

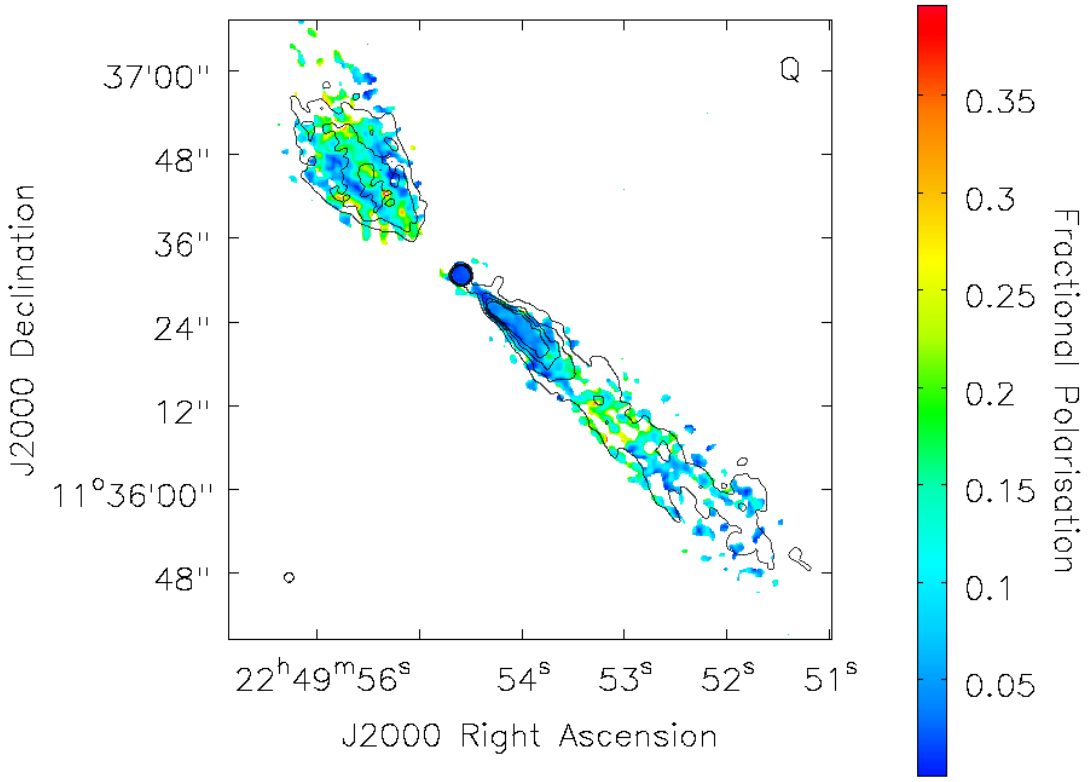

Figure 4.5: Fractional polarisation and intensity contours from the BT 18 dataset showing the inner jet and counter jet at 4.99 GHz. Contour levels 2, 4, 6, 8 mJy beam^{-1} from AH 129 are shown for ease of comparison with Figure 4.4

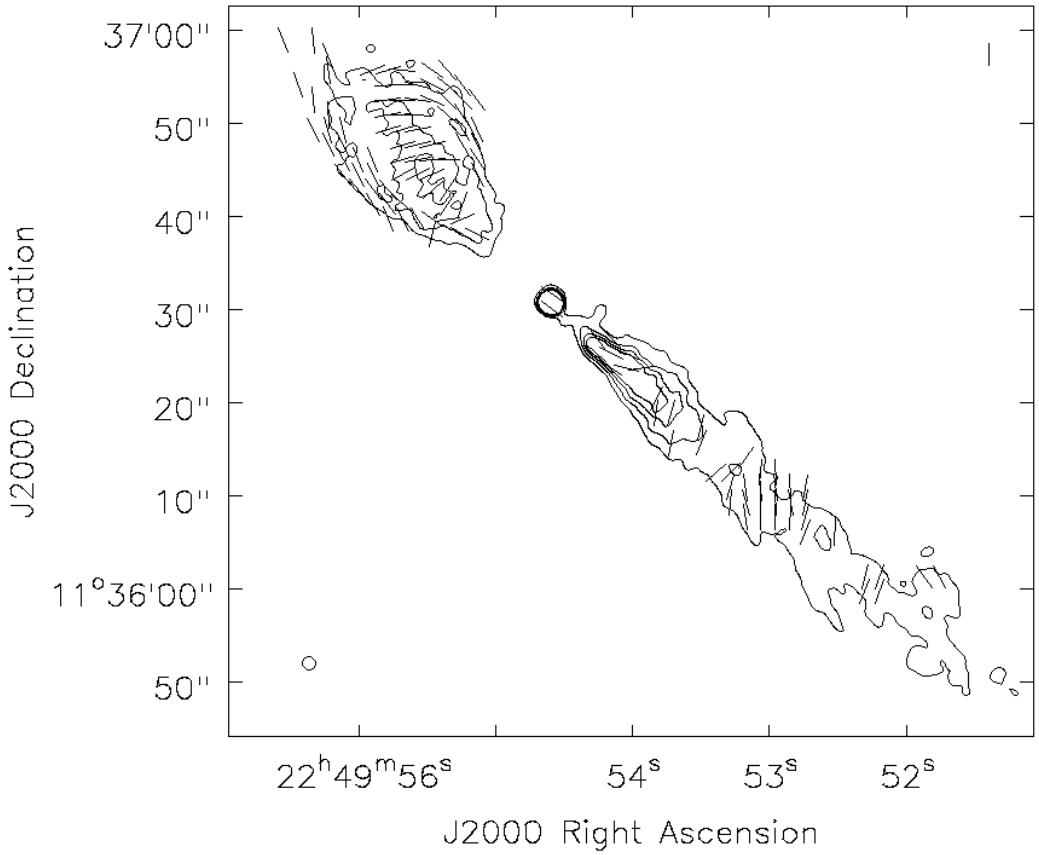

Figure 4.6: Polarisation rotated by 90° to show the apparent magnetic field direction of NGC 7385 from the AH 129 dataset at 1.49 GHz. Intensity contours at 2 mJy and 4 mJy beam^{-1} are also shown.

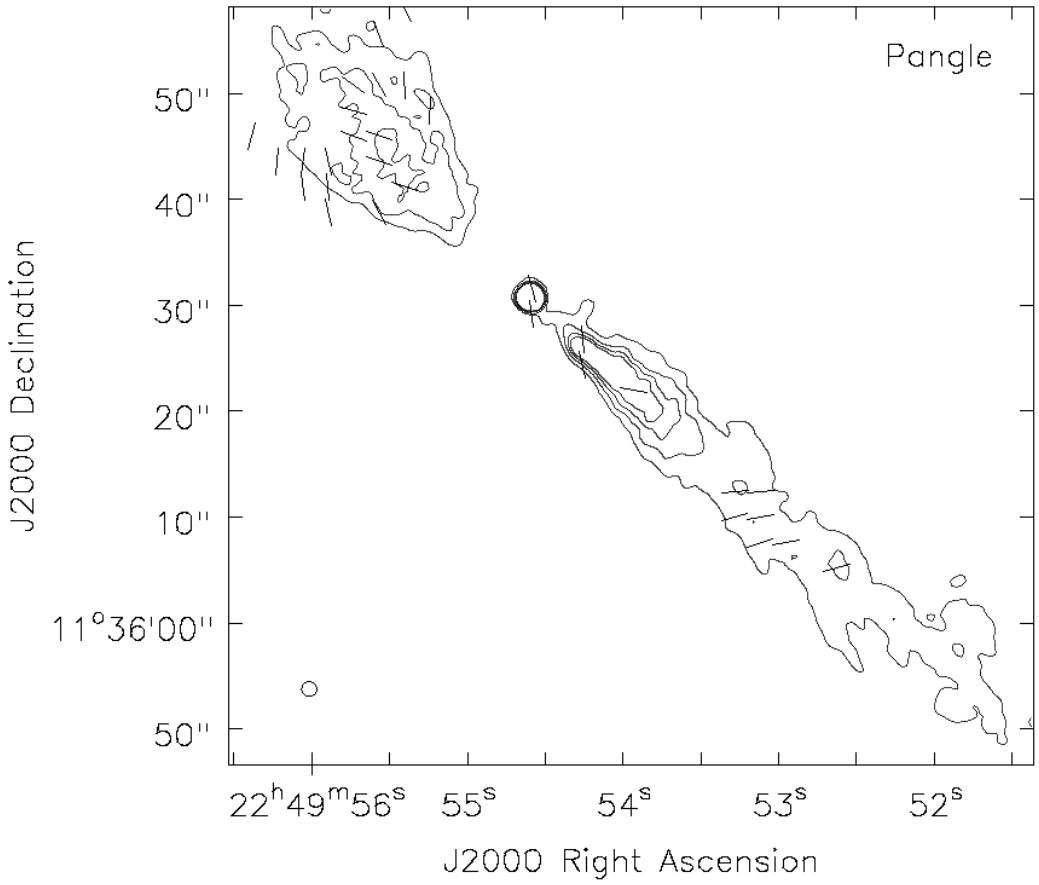

Figure 4.7: Polarisation rotated by 90° to show the apparent magnetic field direction of NGC 7385 from the BT 18 dataset at 4.99 GHz. Intensity contours at 2 mJy and 4 mJy beam^{-1} from from AH 129 are shown for ease of comparison with Figure 4.6

extended emission in which two separate tails appear SW of the core at roughly 300 kpc from the nucleus. The straight SW jet becomes diffuse and bends to the W to enter the westernmost tail. The second tail is the end of the counter-jet, produced through a series of bends and a 180° turn back towards the SW about 30″ (15 kpc) from the core. The structure of the NE component is clear from Figure 4.2. It can be interpreted as a stalled jet, and its shape suggests that the whole structure is being affected by an interaction with the external medium. The counter-jet turns to the NW and then to the SW as evident by a broadening of the radio structure. The stalled jet then crosses the main jet and emerges S of the nucleus as a plume. The intensity distribution at 4.99 GHz is given in Figure 4.3. There is clear diffuse emission to the NW of the counter-jet component, not visible in Figure 4.2. This supports the suggestion that the counter-jet is turning to the NW and then the SW.

4.2.1.3 Polarised intensity structure

Figures 4.4 and 4.5 show the fractional polarisation P of the jet at 1.41 GHz and 4.99 GHz respectively. Figures 4.6 and 4.7 display the apparent magnetic field direction at these same frequencies. At 1.41 GHz, the fractional polarisation in the counter jet appears to increase towards the edges up to a maximum of P = 0.65. In the centre of the structure the polarisation is $P \approx 0.3$, with two low polarisation ($P < 0.1$) canals on either side. The apparent magnetic field is perpendicular to the jet axis in the low polarisation region, and rotates to become parallel at the edges where they appear to track the edges of the source. The unresolved core has low fractional polarisation $P < 0.1$ and the magnetic field lies parallel to the jet direction. Further down the jet, the magnetic field direction starts to rotate and about 14″ from the core the vectors become perpendicular. Beyond this region the fractional polarisation increases steadily up to maximum values of 0.6 at 30″ before decreasing again. In this region of strong polarisation the vectors are at 50° to the jet axis. There is another region of high polarisation around 46″ from the core and here the field vectors are again perpendicular to the jet. Figure 4.8 shows the variation of fractional polarisation with distance along the centre of the jet. There is a clear region of low polarisation at 13-14″ corresponding to where the vectors rotate and the low value of P is therefore likely caused by beam depolarisation.

At 4.99 GHz, the core polarisation is $P \approx 0.02$. In the counter jet, the highest levels of polarisation occur along the component edges, N of the component and along a central channel in the NE-SW direction through the component. This agrees with Figure 4.6,

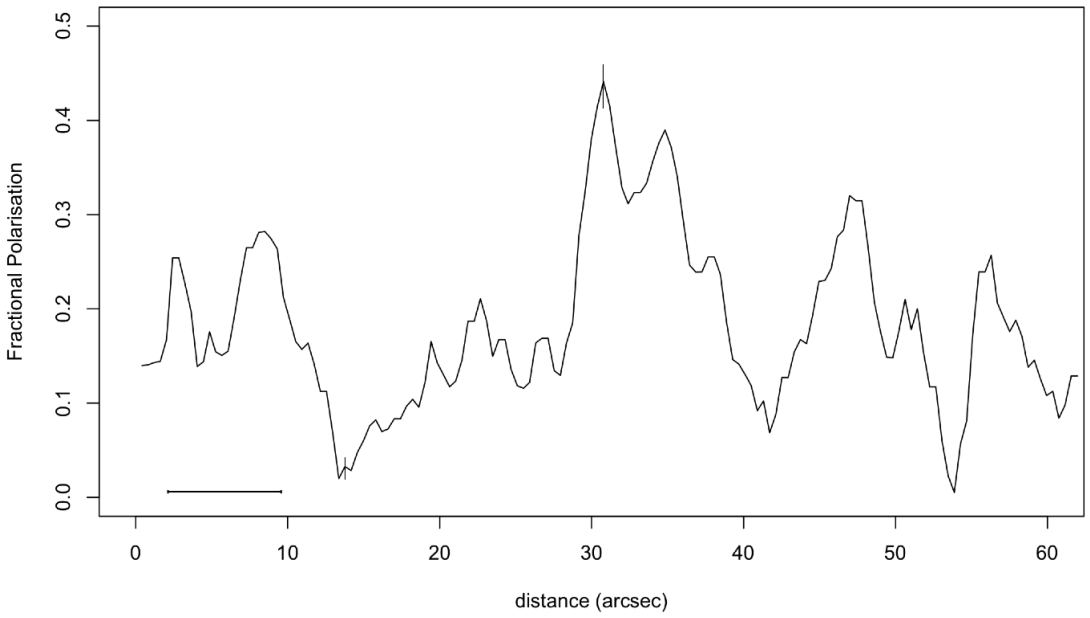

Figure 4.8: The fractional polarisation as a function of distance along the centre of the radio jet. The projection used was 1.6″ wide at an angle 319° from the nucleus. The bar marks the bright part of the optical jet.

where the regions E and W of the highly polarised central channel have a lower polarisation, at $\approx P = 0.1$. Along the main jet, the polarisation structure is similar to that at 1.41 GHz, with a region of high polarisation at 14″ from the core.

The magnetic field vectors in the core at 1.41 GHz are at 49°, compared to the vectors at 4.99 GHz which are at 21°. This implies a rotation of 28° between the L and C bands, corresponding to a rotation measure of approximately 10 rad m^{-2}. The vectors along the first 15″ of the main jet are in agreement between the two frequency bands; however beyond this region they are offset by approximately 90°. In the counter-jet component, the magnetic field is rotated by 60° along the central channel, and 30° along the SE edge. At the NE edge of the component, the angles are offset by 160°, implying a rotation measure in excess of 70 rad m^{-2} in that region. These RM values are not reliable since they use data from only two frequencies. This means that vectors could have been rotated by an additional $n\pi$ radians and this will not be detected. To resolve this ambiguity, > 3 resolution-matched observations at different frequencies are required.

4.2.1.4 VLA proposal

The lack of high-sensitivity polarisation and rotation measure maps for NGC 7385 led to a VLA proposal requesting new observations of both NGC 7385 and NGC 6109. The

Project code	Config	Date	Frequency range (GHz)	BW (MHz)	Time (s)	Resolution (arcsec)	Flux calibrator
15A-422	A	15-Aug	1.99-3.50	64	4500	0.9	3C 48
15A-422	A	15-Sept	1.03-1.99	128	1740	1.4	3C 48

Table 4.3: JVLA observational details

proposal requested 3 hours on each source in A array, with two hours at L band and one hour at S band. The key questions that it was hoped new data would answer were:

1. What are the morphologies of the radio emission in the inner jets, where existing data show strong distortions?
2. What are the spectral indices in the relativistically beamed jets, and in the heavily distorted counter-jets?
3. What is the magnetic field configuration in the jet bend regions, where complete jet reversals are observed?
4. Is there rotation measure structure near the line-emitting gas at the jet bend in NGC 7385 that can be used to help interpret the geometry of the flow?

The JVLA's L and S band receivers cover the 1-4 GHz frequency range and can provide the polarisation data needed to map the rotation measure structure near the jet deflection region and in the jets. The proposal requested full polarisation from the correlator with 2 MHz channels and 8 bit sampling at S band to cover 2 GHz of bandwidth. For the L band observations, full polarisation capability with 1 MHz channels and 8 bit sampling to cover 1 GHz of bandwidth was requested.

The sensitivity required to achieve the 4 science goals above is 15 μJy across full L band and 5 μJy across the full S band. Losses due to RFI were assumed to be 50% at L band and 25% at S band.

The L and S band observations were carried out in September 2015 and August 2015 respectively. The primary flux calibrator 3C 48 and a phase calibrator with coordinates RA 22h 32m 36.41s, Dec +11d 43′ 50.91″ (J2232+1143) were observed along with NGC 7385.

4.2.1.5 JVLA data

The observational details for the new JVLA data are given in Table 4.3.

These data were automatically passed through the VLA calibration pipeline following the completion of the observations. The VLA calibration pipeline performs basic flagging

and calibration using CASA. It is applied to Stokes I continuum data only, therefore it does not calibrate for polarisation. It generates flags in the case of shadowed data, faulty antenna and RFI, and it derives delay, bandpass and gain calibrations.

I inspected the pipeline calibration applied to NGC 7385 and deemed it to be inadequate, thus I recalibrated the data using the techniques described in chapter 2.

The L band data were severely affected by RFI. Spectral channels centred on 1.55-1.65 and 1.84GHz were flagged due to interference and I used used the RFI flagging task *aoflagger* to excise interference from other spectral channels. The first 10s of each scan were flagged and the edge channels at each spectral window were ignored when calibrating. In addition, antenna 14 was removed from all frequency bands. The S band data required less flagging, although the last three spectral windows (3.69 - 3.95 GHz) were removed. After an initial run of *clean*, the data were phase self-calibrated down to a solution interval of 20 s, and then once a strong convergence had been achieved, both the amplitude and phase were self-calibrated.

4.2.1.6 Radio morphology and spectral index

The intensity distribution of NGC 7385 at 1.51 GHz is shown in Figure 4.9 and morphological parameters determined from these observations are given in Table 4.4. Figure 4.9 shows evidence for a faint counter-jet before the emission expands into the NE component. To the N of this component, the emission appears to be deflecting towards the NW, away from the main jet axis, in agreement with Figure 4.2. The bend angle is approximately 35°. The emission along the main jet appears well collimated and straight. There are three knots of bright emission, the first extends from 0.5″ to 8″, the second from 10-11.5″ and the third and faintest from 12.5-14″. The last two knots are indistinguishable from the general run of jet diffuse emission in Figure 4.2. The S band total intensity map is given in Figure 4.10. The contours are matched to those in Figure 4.9 to show the relative faintness of the source at this frequency. The main jet remains bright for 12″, before fading completely up to 22″ from the core. The counter-jet is faint, but still displays bending towards the NW away from the main jet axis.

The spectral index ($S \propto \nu^{-\alpha}$) between 1.01 GHz and 1.99 GHz was mapped using the ratio between the first and second Taylor terms from the *clean* algorithm and is shown in Figure 4.11. The traditional method of using the ratio between the intensities of the image at different frequencies was also mapped, and is given in Figure 4.12. Only the core and 14″ along the main jet is shown, due to the faintness of the counter-jet emission in

Core flux density (mJy, 1.51 GHz)	90 $\pm$ 0.03
Core spectral index α	-0.45 $\pm$ 0.003
Core rotation measure (rad m^{-2})	-28 $\pm$ 3
NE component size (arcsec)	31 $\times$ 18
NE component flux density (Jy, 1.51 GHz)	0.44 $\pm$ 0.0001
NE component spectral index α	0.8 $\pm$ 0.06
NE component rotation measure (rad m^{-2})	-80 $\pm$ 12
SW tail projected length (arcsec)	41
SW inner jet flux (Jy, 1.51 GHz)	0.21 $\pm$ 0.004
SW jet spectral index	0.8 $\pm$ 0.05
SW jet rotation measure (rad m^{-2})	60 $\pm$ 8

Table 4.4: Morphological parameters of NGC 7385 from the JVLA observations. The spectral index α is defined as $S \propto \nu^{-\alpha}$, and the SW inner jet is taken to be up to 20″ from the core.

Component	Size (arcsec)	Total L$_{radio}$ $\times 10^{39}$erg s^{-1}	Magnetic field strength (μG	Total minimum energy density ($\times$ 10^{-5} erg m^{-3})
Nucleus	0.03	3.7		
Inner jet	0.5	8.6	23 $\pm$ 0.7	6 $\pm$ 0.02
Northern jet	0.5	15	29 $\pm$ 0.7	6.7 $\pm$ 0.02

Table 4.5: Physical parameters of the radio emission

individual frequency maps which was below the threshold required for a reliable spectral index map. I therefore use Figure 4.11 to interpret the spectral structure, although it is worth noting that the values of α in Figure 4.12 are complementary to this map.

Along the inner jet, the spectral index was found to be α = 0.81 $\pm$ 0.05, in agreement with Robertson (1981). The spectral index along the centre of the counter-jet component was also measured as α = 0.83 $\pm$ 0.08, as expected. In the core, the spectrum is inverted, with α= -0.41 $\pm$ 0.003. The core spectrum must turn over somewhere between 3.31 and 5 GHz to agree with the positive α reported by Robertson (1981). There is a clear region of inverted spectrum in the NE of the counter-jet component. Since this is spatially coincident with the optical gas cloud (as indicated by the HST contours), I interpret this as due to free-free absorption. Details of the optical astrometry are given in section 4.2.2.1.

4.2.1.7 Polarised intensity

Fractional polarisation and apparent magnetic field vector maps at 1.51 GHz are given in Figures 4.13 and 4.14. The magnetic field vectors are uncorrected for rotation measure effects, for direct comparison to the VLA map given in Figure 4.6. The core is unpolarised, with $P < 0.01$. Along the main jet P remains low until 14″. Beyond this region,

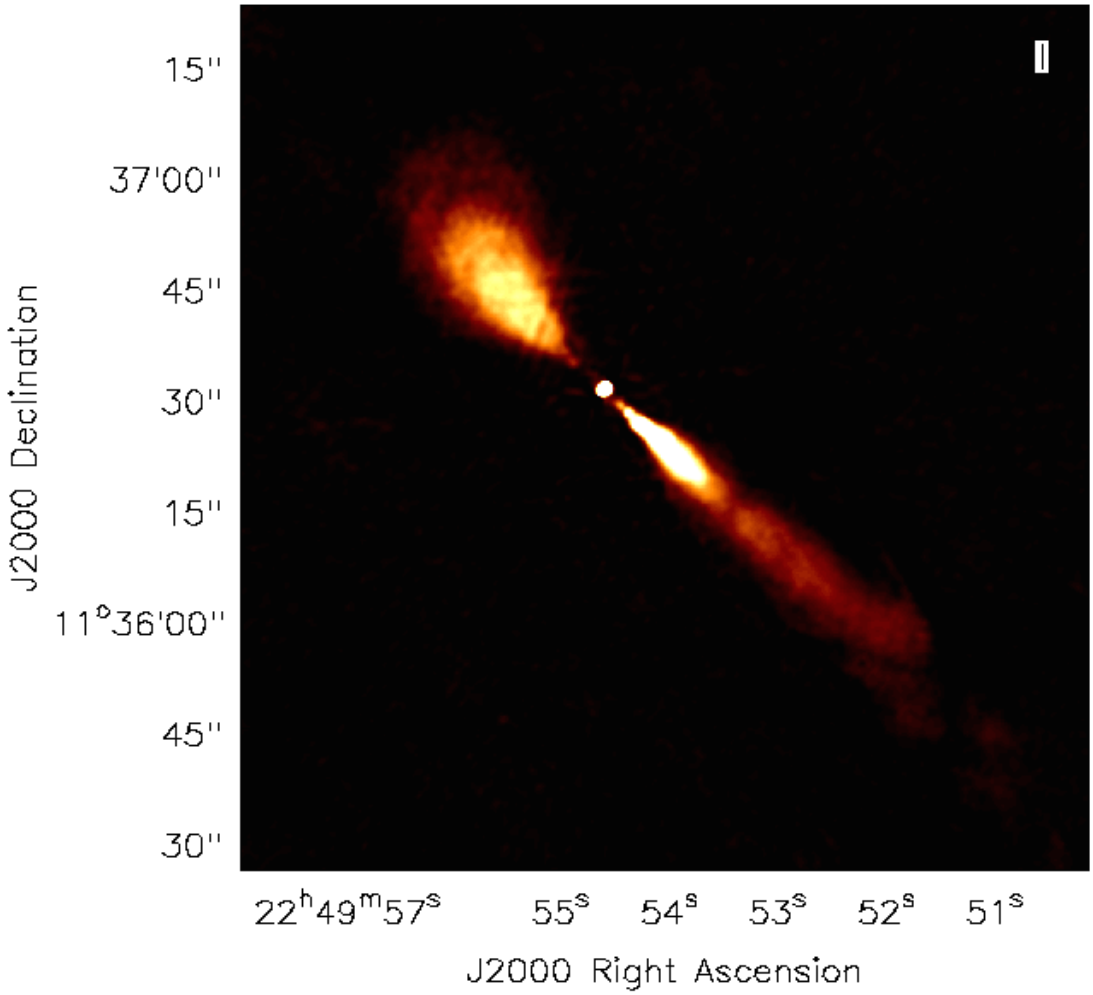

Figure 4.9: L band Stokes I image of NGC 7385 at 1.51 GHz and 1.4 arcsec resolution, showing the small scale structure and including all spectral windows. The main jet appears to extend 28 kpc to the SW.

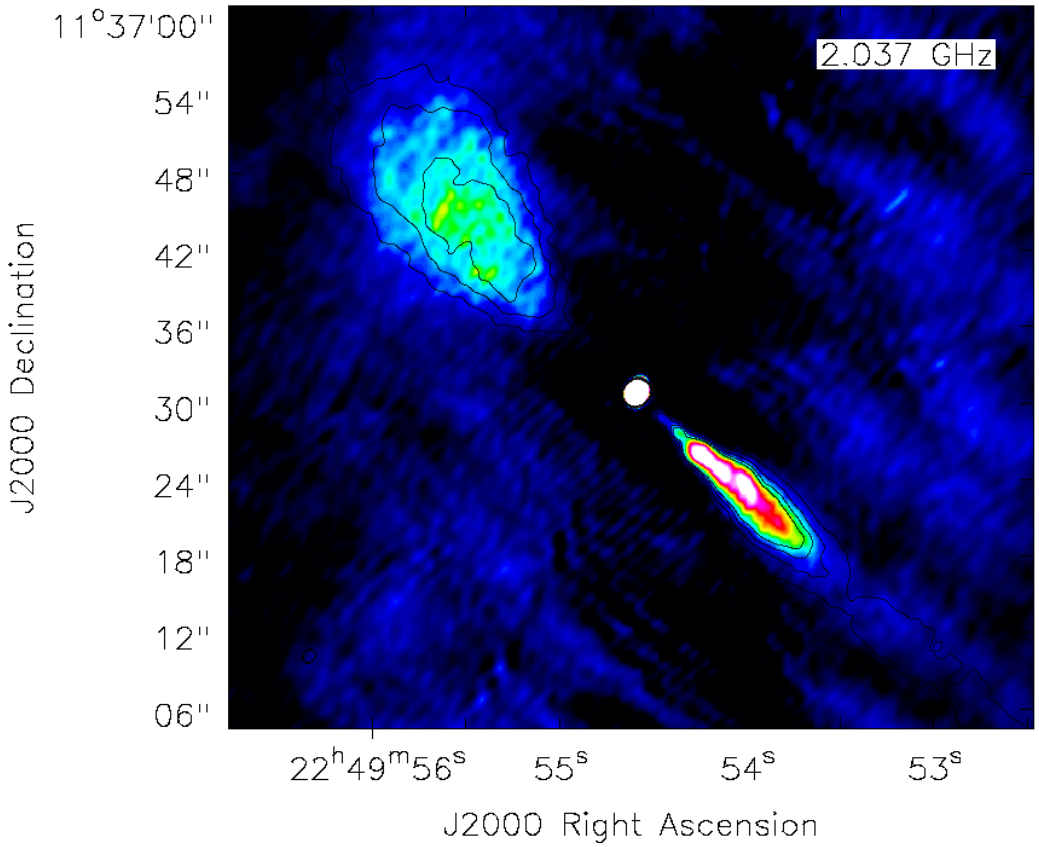

Figure 4.10: S band Stokes I image of NGC 7385 at 2.04 GHz and 0.9 arcsec resolution, showing the small scale structure. Only a few spectral windows (1.99-2.10 GHz) were included in this map. Radio contours are included at 0.8 mJy, 1.6 mJy, 2.3 mJy and 3.2 mJy beam^{-1} in a similar way to Figure 4.9 to show the relative brightness at S band compared to L band.

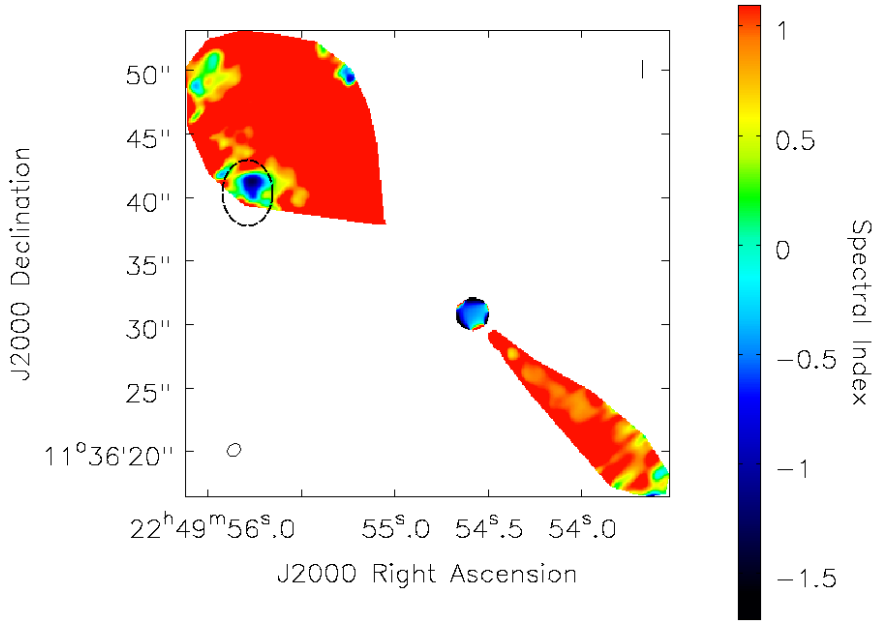

Figure 4.11: Spectral index map of NGC 7385 between 1.03 - 1.99 GHz, with a dashed region to show the position of the optical cloud.

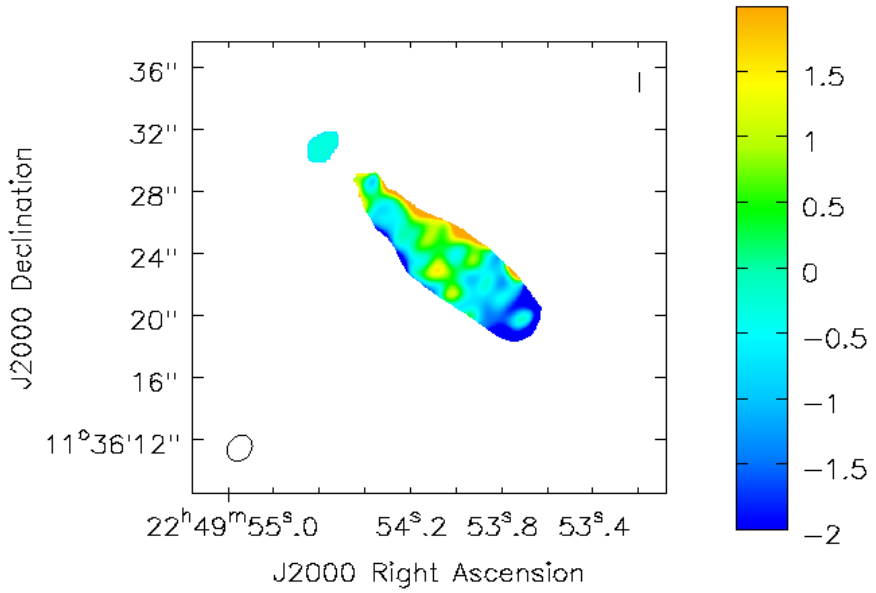

Figure 4.12: Spectral index map of NGC 7385 between 1.03 - 1.99 GHz created using the CASA task *spix*. The image shows only the core and the inner 14 arcsec of the main jet, due to the faintness of the counter-jet emission in individual spectral windows. A colour bar on the right shows the spectral index.

P increases steadily up to P = 0.35 at 30″, before decreasing again. In the counter-jet component there is a central channel in the NE direction with P = 0.2. To the E and W of this region, P = 0.12. To the N of the component P = 0.3, as seen in Figure 4.4. The apparent magnetic field vectors in the main jet displayed in Figure 4.14 show a parallel field close to the core which rotates to perpendicular about 14″ from the core. The vectors remain at 90° to the jet axis until 22″, where they rotate by a further 40°. In the counter-jet, the vectors at the centre of the component are transverse to the jet direction, whereas those at the edges are parallel to the counter-jet. The fractional polarisation results are in good agreement with maps produced in the S band at 2.8 GHz and with the VLA maps shown in Figures 4.4 and 4.5. The magnetic field vectors at L band in Figures 4.6 and 4.14 also agree.

4.2.1.8 Rotation measure structure

A rotation measure map is given in Figure 4.15, created using 6 spectral windows in the S band data (1.99 - 2.56 GHz) in CASA task *rmfit*. The image has been smoothed with a Gaussian function with FWHM of 2″ to reduce noise, and a dashed black line shows

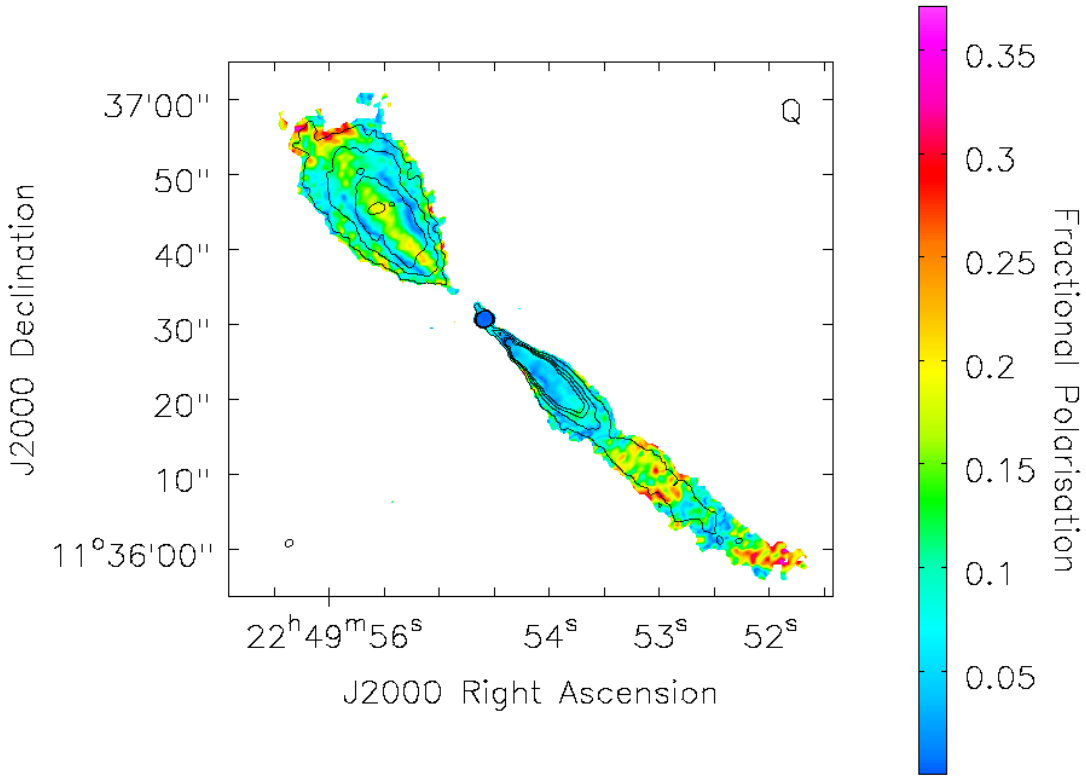

Figure 4.13: The fractional polarisation distribution in NGC 7385 at 1.51 GHz (using a single spectral window), with total intensity contours at 0.8 mJy, 1.6 mJy, 2.3 mJy and 3.2 mJy beam^{-1}.

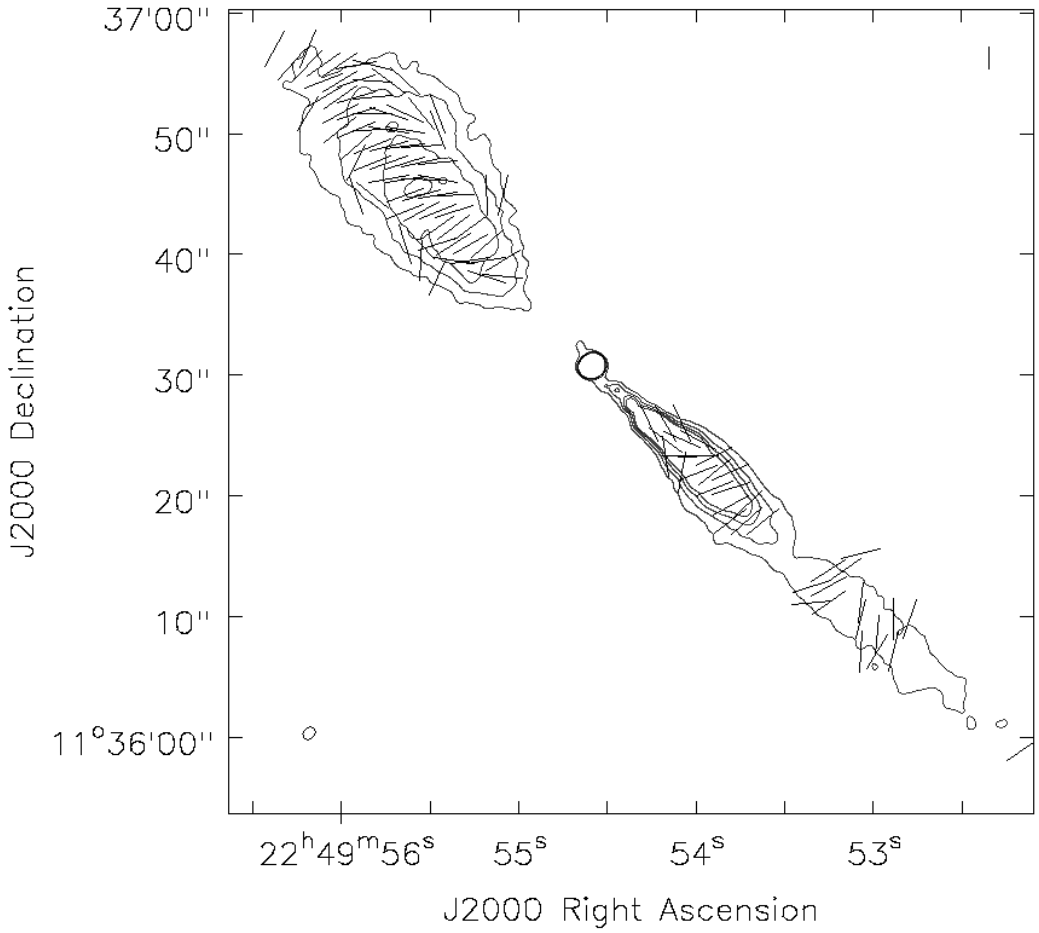

Figure 4.14: Polarisation rotated by 90° to show the apparent magnetic field direction of NGC 7385 at 1.51 GHz, with total intensity contours at 0.8 mJy, 1.6 mJy, 2.3 mJy and 3.2 mJy beam^{-1}.

the position of an optical line-emitting gas cloud. *rmfit* uses a least squares approach to determine the value of the rotation measure, based on the assumption that there is a linear relationship between ϕ and λ^2.

The map gives a core rotation measure value of -28 ± 3 rad m^{-2}, in agreement with the value measured by Taylor et al. (2009) in their rotation measure survey. There is a gradient in the rotation measure parallel to the main jet, where values decrease from 40 to -90 ± 12 rad m^{-2} over 7 arcsec from the core. Beyond this point, the rotation measure remains stable at about -30 $\pm$ 7 rad m^{-2}. In the counter-jet component, there is a clear region of high rotation measure, north east of the core and spatially coincident with the position of the optical object. This region has a high signal to noise with an average of 245 ± 16 rad m^{-2}. The rotation measure is negative on the western side of the lobe where the counter-jet is bending and also at the northern tip of the lobe, with an average value around -80 ± 13 rad m^{-2}. The rotation measure in the neighbourhood of the counter-jet as determined from other radio sources nearby is low, and can be assumed to be 0. A plot of the polarisation angle with λ^2 is given in Figure 4.16 for the region containing the optical cloud. The gradient of these points gives the rotation measure, and here it is found to be ~ 260 rad m^2.

The limitations to using a least squares approach to fitting the rotation measure are discussed in chapter 2. The *rmfit* task is limited by the $n\pi$ ambiguity problem which discards data points which do not meet the requirements of Leahy et al (1986). This significantly reduces the number of data points available to constrain the RM fit. To investigate whether *rmfit* would suffice for an accurate depiction of the RM structure within NGC 7385, I produced Q and U maps at every spectral window within the L and S band observations. At high frequencies ($\geq$ 2.5 GHz), the variation in Q and U between spectral windows was stable. At the low end of the frequency range however, sign changes between consecutive Q and U maps indicated that there is significant rotation of the polarisation vectors between each spectral window. This suggested that the polarisation structure is being averaged out by maps which combine multiple spectral windows. The maps of Stokes Q and U for each spectral window are shown in Figures 4.17, 4.18, 4.19 and 4.20. Based on these results I adopted the Fourier rotation measure synthesis approach introduced by Burn (1966) and adapted by Brentjens and de Bruyn (2005) to search for complex Faraday rotation structure within NGC 7385. This method is introduced in chapter 2 and has been used to detect complex Faraday depth structure within AGN (e.g. Law et al., 2011;

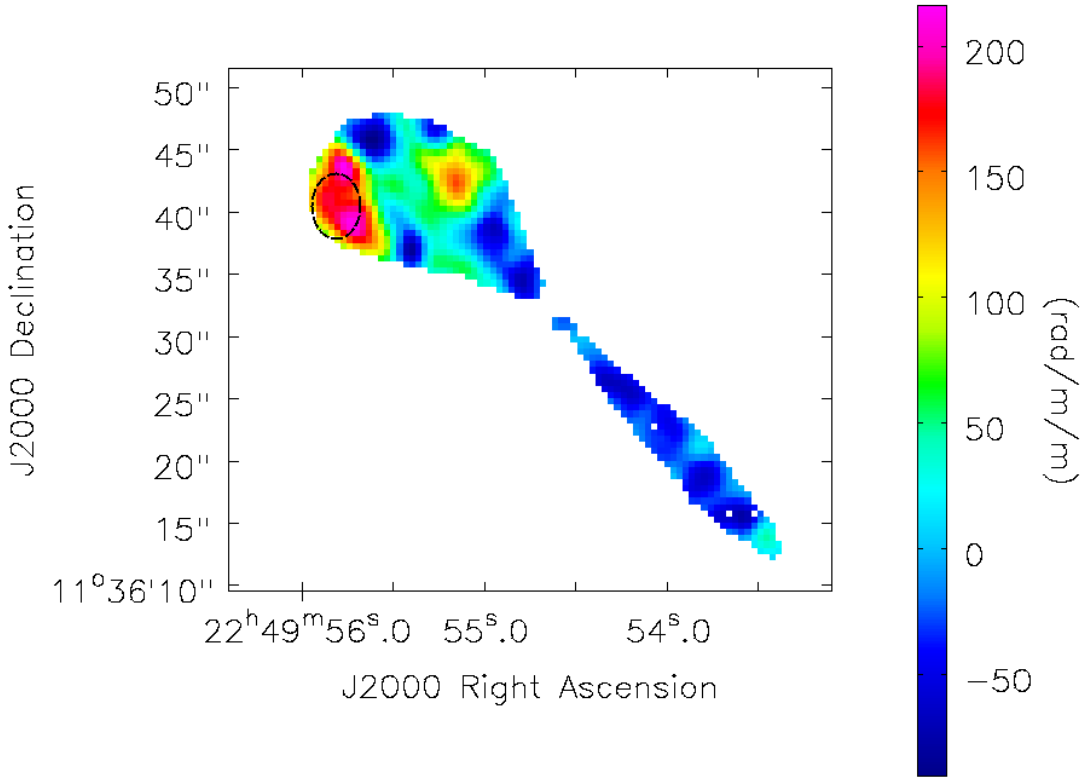

Figure 4.15: Rotation measure image created between 1.99-3.50 GHz. A dashed line shows the position of the optical cloud. This image has been smoothed with a Gaussian function with FWHM of 2 arcseconds.

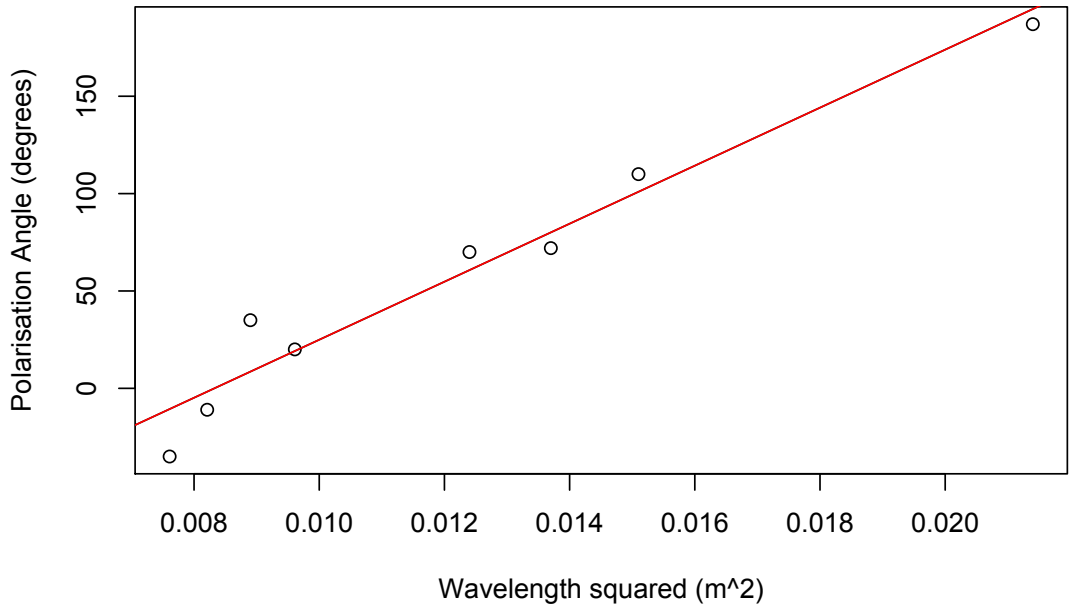

Figure 4.16: Plot of polarisation angle against λ^2 from data used in the rmfit image and in the region of the optical cloud. A linear regression line is shown and the gradient of the line is found to be $\sim$ 15000 deg m^2, equivalent to $\sim$ 260 rad m^2.

O'Sullivan et al., 2012). The RM synthesis technique overcomes the $n\pi$ ambiguity problem and allows the observer to investigate the possibility of multiple Faraday depths along the line of sight.

4.2.1.9 RM synthesis

fourier.rotationmeasure is a Fourier-based rotation measure task within CASA that allows the user to Fourier transform a multi-frequency image containing Stokes Q and U information into a image with rotation measure on the z-axis. The rotation measure axis will contain the same number of channels as the frequency axis, and the maximum rotation measure which the program solves for is defined by equation (2.61). It is essential that the input image cubes have the same synthesised beam and a regularly spaced frequency axis. Although this task proved useful in providing a basic Faraday dispersion function, it was limited in the λ^2 sampling that it could provide. Figure 4.21 shows the Fourier dispersion function produced for the core of NGC 7385 via this method for the L band dataset. Although the general shape shows a peak close to -30 rad m^{-2} as expected, the distribution is under-sampled due to the limitation on the number of pixels the rotation measure axis can contain. The resolution in ϕ space is determined by the frequency coverage λ^2, as $\delta\phi$ = $2\sqrt{3}/\Delta\lambda^2$. For the L band dataset (1.013-1.99 GHz) $\delta\phi$ = 56 rad m^{-2}. This is less than the distribution in ϕ space per pixel provided by the *fourier.rotationmeasure* task, of 71 rad m^{-2}.

A python based RM synthesis package *pyrmsynthesis*, written by Michael Bell and Henrik Junklewitz for the LOFAR configuration performs RM synthesis on multi-frequency polarised imaging data. It uses fast Fourier transforms for Fourier inversion and grids the data by convolution with a Kaiser-Bessel Window function, sampled at regular intervals (Beatty et al, 2005). The application processes the lines of sight in a 'stack' of sky images and it can be used with images provided as a set of FITS files generated by CASA. *pyrmsynthesis* creates Faraday dispersion functions either by simple Fourier transformation (to produce a 'dirty' image) or by using the RMCLEAN method as described by Heald et al (2009). A weighting parameter for each frequency can be defined by the user, or by default all channels are given an equal weight. It is also possible to define a spectral index for the emission.

I used this code to produce Faraday dispersion maps of NGC 7385. I used a combination of the individual L and S band datasets, and a concatenated dataset of the two bands to create a complete picture of the Faraday dispersion structure. Table 4.6 gives the

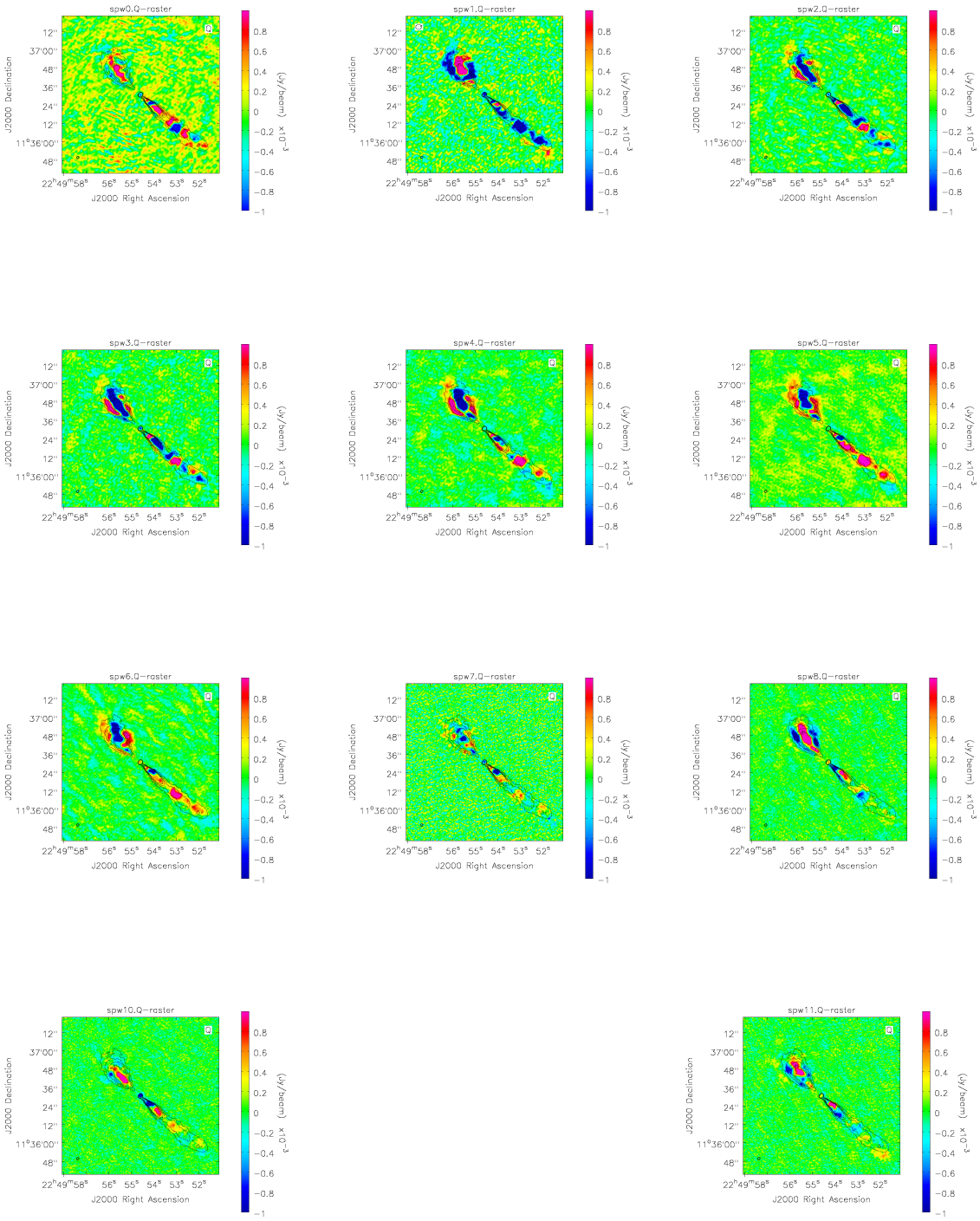

Figure 4.17: Stokes Q maps of the L band data set. The frequency of the images from left to right, top to bottom are as follows: 1.04, 1.10, 1.17, 1.23, 1.30, 1.36, 1.49, 1.62, 1.68, 1.94 and 2.00 GHz

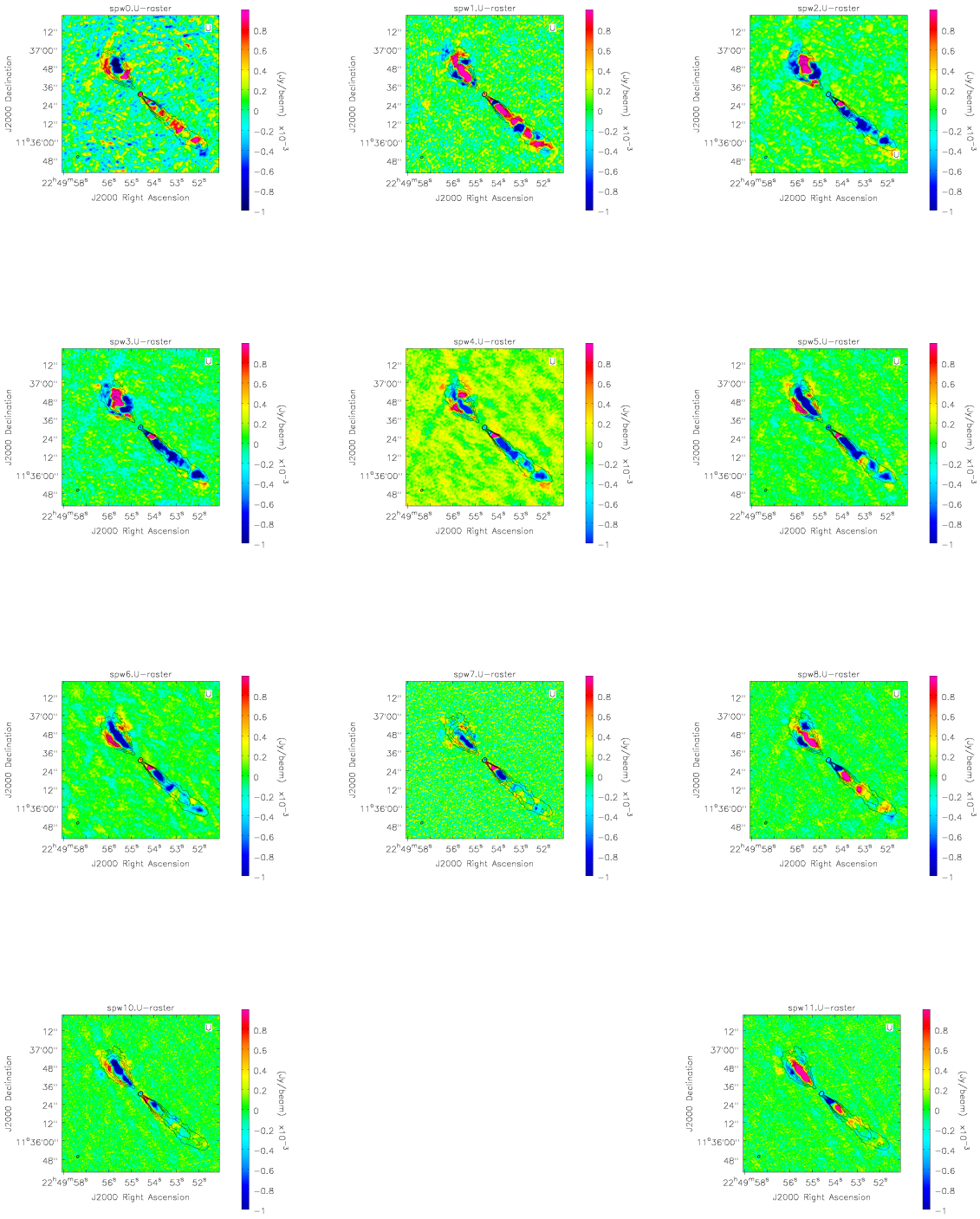

Figure 4.18: Stokes U maps of the L band data set. The frequency of the images from left to right, top to bottom are as follows: 1.04, 1.10, 1.17, 1.23, 1.30, 1.36, 1.49, 1.62, 1.68, 1.94 and 2.00 GHz

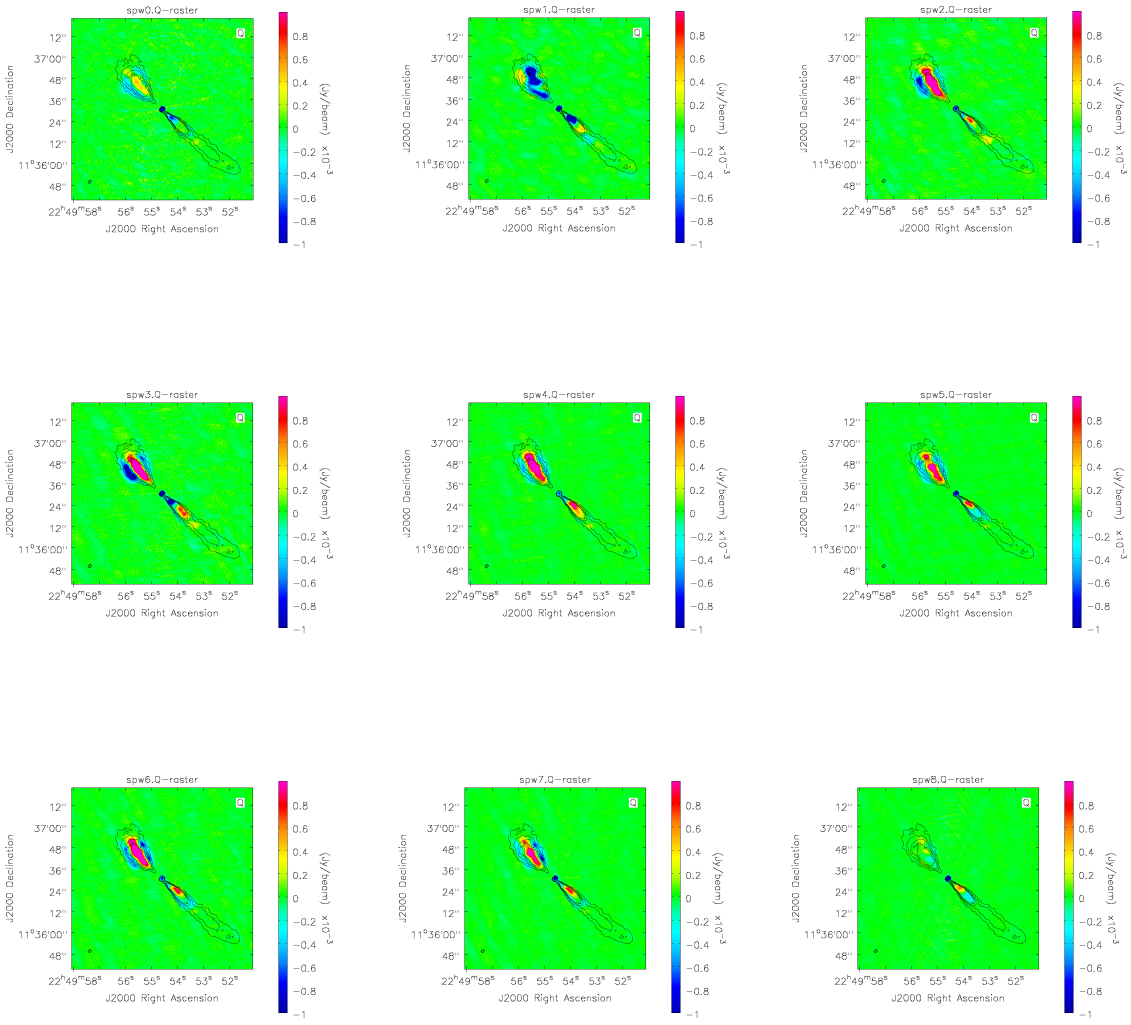

Figure 4.19: Stokes Q maps of the S band data set. The frequency of the images from left to right, top to bottom are as follows: 2.05, 2.44, 2.56, 2.69, 3.05, 3.18, 3.31, 3.44 and 3.56 GHz.

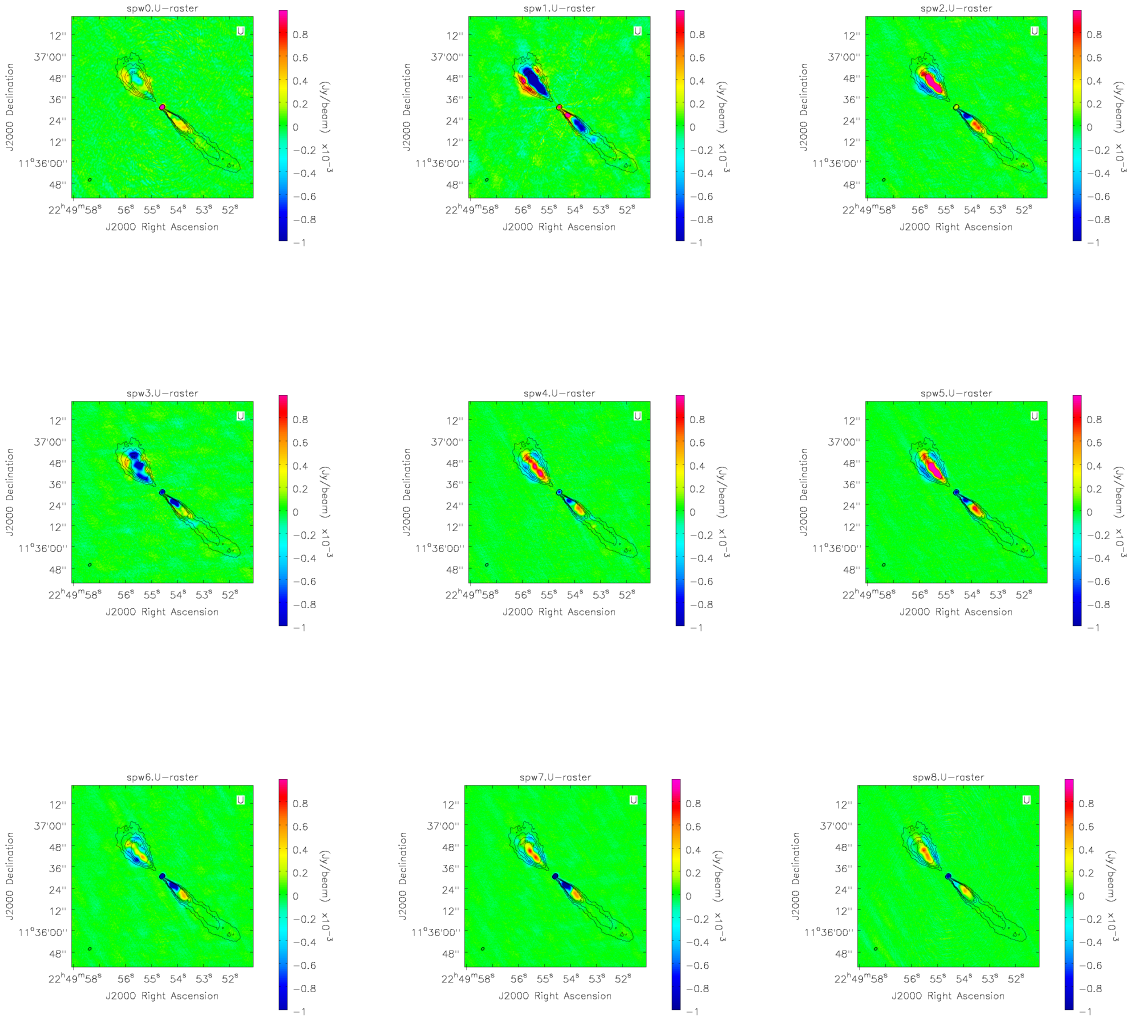

Figure 4.20: Stokes U maps of the S band data set. The frequency of the images from left to right, top to bottom are as follows: 2.05, 2.44, 2.56, 2.69, 3.05, 3.18, 3.31, 3.44 and 3.56 GHz.

Band	Freq. range (GHz)	$\delta\lambda^2$ m^2	$\lambda^2_{\rm min}$ m^2	$\phi_{\rm max}$ rad m^{-2}	$\delta\phi$ rad m^{-2}	FWHM of clean RM kernel rad m^{-2}
L	1.013-1.99	0.06	0.022	138	56	23.56
S	1.99-3.62	0.15	0.007	442	238	101
LS	1.013-3.62	0.013	0.007	443	48.0	20.14

Table 4.6: Rotation measure synthesis parameters for the JVLA data. These parameters are discussed and defined in chapter 2.

parameters of the RM synthesis fitting for these data. I split the datasets on a sub-channel basis with widths of 100 MHz per plane and each plane was resolved with the same beam to give the same image resolution.

I searched for polarised power from $\pm\phi_{\rm max}$ at Faraday depth intervals of 10 rad m^{-2} in the L and L+S bands, and 16 rad m^{-2} in the S band, corresponding to approximately 6, 5 and 15 Faraday depth intervals per $\delta\phi$ respectively. The RMTF for the L band observations is shown in Figure 4.22. The RMTF is a complex valued function, with the real part corresponding to the response of the transform parallel to the (Q, U) vector at $\lambda = \lambda_0$ and the imaginary part corresponding to the response orthogonal to it. This code takes λ_0^2 to be the mean of the sampled λ^2 values, weighted by $W(\lambda^2)$. Weighting in λ^2 space can improve the sidelobe level, at the expense of a lower ϕ resolution. I tapered with a Gaussian function using the inverse square of the noise, as in O'Sullivan et al. (2012), after testing a series of different tapers (e.g. $\sigma = \frac{1}{2}(\lambda^2_{max} - \lambda^2_{min})$ as used by Heald et al., 2009). This was deemed to be the best trade-off between sidelobe height and RMSF width.

Different frequency bands highlight different features of the Faraday dispersion function. The resolution in ϕ space of the L band data is sufficient to resolve individual peaks. The maximum observable scale however is narrow, and does not extend far enough to analyse the radio jet/optical cloud interacting region where the RM is thought to be > 200 rad m^{-2}. The S band data have a broad observable scale but lack the resolution to make an accurate representation of the RM structure. The combined L and S dataset can both resolve individual peaks and extends beyond $\pm$ 200 rad m^{-2}. Performing the RMCLEAN code within *pyrmsynthesis* significantly improves the appearance of sidelobes in the Faraday dispersion function. These structures are highlighted in Figure 4.23, which shows the Faraday dispersion function for a pixel located in the centre of the main jet, where there is not expected to be complex structure; the black line shows the uncleaned structure and the red line shows the cleaned structure. I used a CLEAN gain parameter g = 0.1, carried out 500 iterations to a cut-off value of 0.1 mJy. Figure 4.23 (a) shows a clear peak at $\approx$ -40

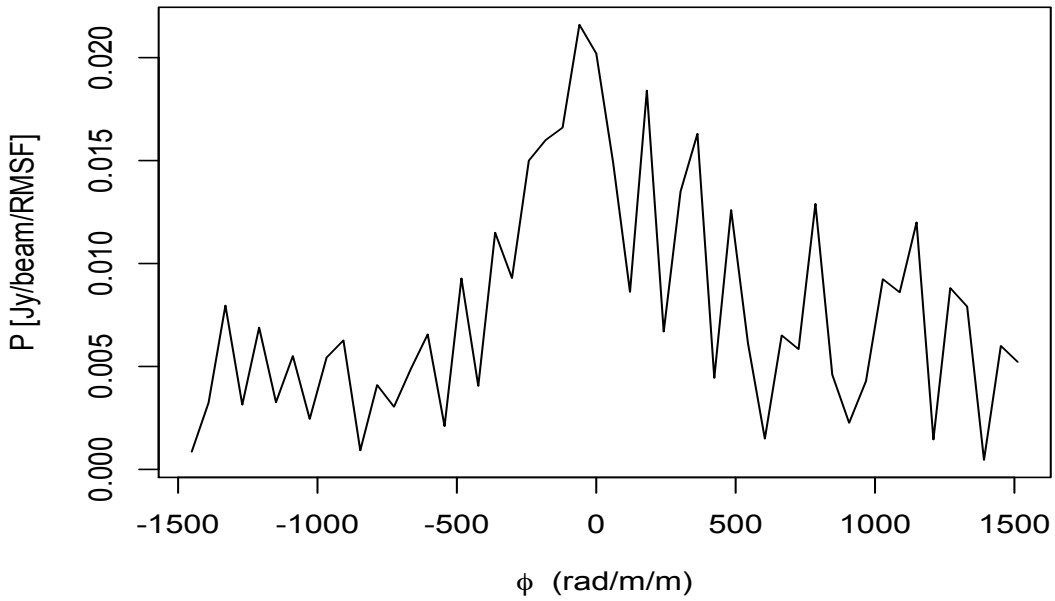

Figure 4.21: Fourier dispersion function produced using the *fourier.rotationmeasure* task within CASA for the core of NGC 7385. The distribution shows a peak close to -30 rad m^{-2}, however is under-sampled.

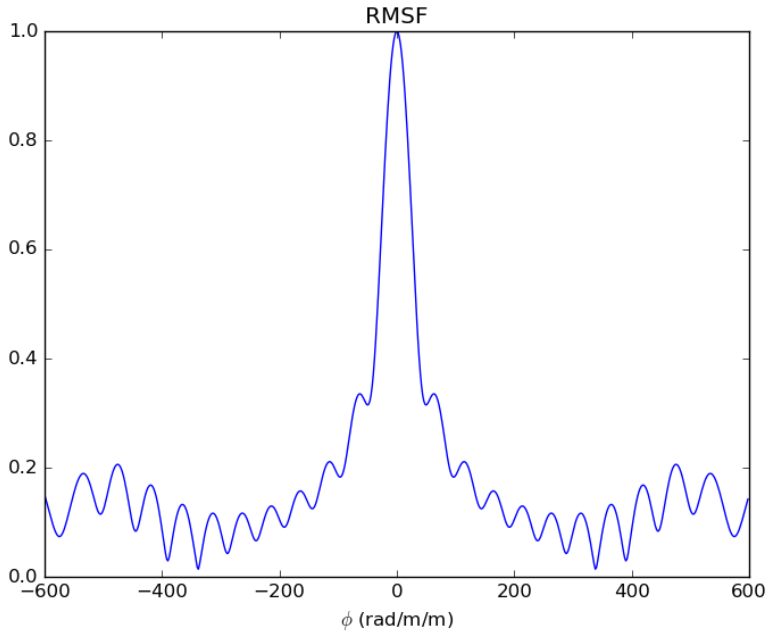

Figure 4.22: Rotation measure spread/transfer function for the JVLA L band observations, with frequency range 1.013 - 1.99 GHz and $\delta\lambda^2$ = 0.06 m^2.

rad m^{-2}. The intensity of this peak has been reduced by 25% by the cleaning process, as have the sidelobes adjacent to the main peak. In the S band, Figure 4.23 (b) shows a peak in a similar location, however the resolution in ϕ space is insufficient to give an accurate value. The combined S and L distribution given in Figure 4.23 (c) is erratic, suggesting a problem with combining the two datasets and thus will not be used further. Errors in each channel measurement were assigned using the rms noise from a small area around the source position in the clean-residual images.

The Faraday dispersion function was calculated in the NE counter-jet lobe. The profiles are shown in Figure 4.24; both datasets have been passed through the RMCLEAN algorithm and tapered in λ^2 space. The S band map shows a distinct peak, at 210 rad m^{-2}. The peak at -80 rad m^{-2} is likely a sidelobe feature. The L band map shows peaks in similar locations, but is dominated by sidelobe structure. This is likely due to gaps in the uv-coverage within the dataset where significant data were removed due to RFI. A circle with radius 3 pixels was used to determine the RM and the average value is plotted, to limit the effect of variations in RM between pixels.

The *pyrmsynthesis* code also outputs a rotation measure map. This map is given in Figure 4.25 for the S band observations. There is a clear region of high RM in the region of the optical cloud, in agreement with Figure 4.15. The core has a rotation measure value of -72 $\pm$ 2 rad m^{-2}, larger than the value reported by Taylor et al. (2009) but consistent in both the L and S band datasets. The main jet has a stable RM of approximately -80 rad m^{-2} and this is also found in the counter-jet component. The rotation measure map produced using the RM synthesis technique shows considerably less structure within the main jet and counter jet (excluding the NE edge) and lower errors than the map produced using the traditional χ / λ^2 fit. I interpret this to be due to splitting up the bandwidth into a large number of narrow frequency channels, thus only polarised emission will a high intensity will be detected above the noise level.

The rotation measure (RM) of foreground magnetised gas rotates the observed polarisation position angle PA as a function of wavelength λ according to ϕ = PA_0 + RM λ^2. Correcting for this rotation ϕ provides the polarisation position angle at zero wavelength PA_0, revealing the un-rotated structure of the magnetic field. Figure 4.26 gives maps of the magnetic field structure for the jet and counter-jet components, after the vectors have been corrected for RM.

In the main jet, the field is transverse to the jet axis close to the core, but aligns to become parallel to the jet axis further out. These angles are offset from those reported in

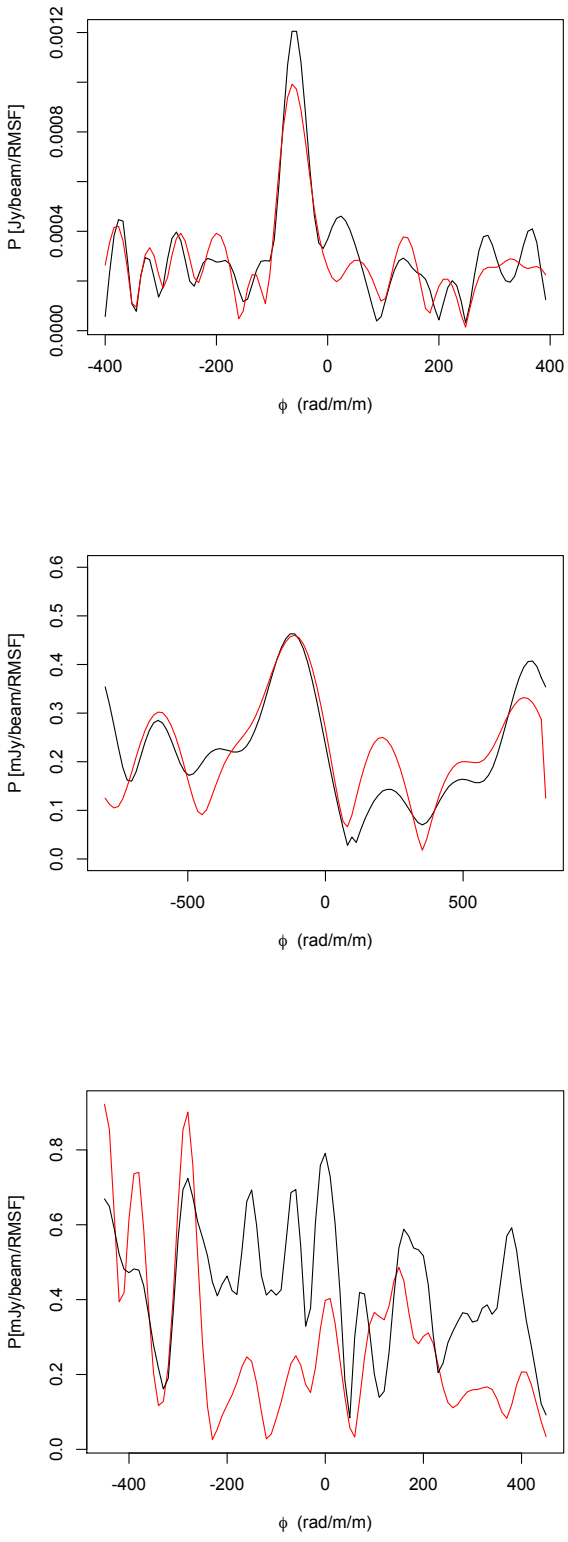

Figure 4.23: The Fourier dispersion function for a pixel along the main jet of NGC 7385 using the code *rmsynthesis* at *(a)* 1.01 - 1.99 GHz, *(b)* 1.99 - 3.62 GHz and *(c)* 1.013 - 3.62 GHz. The black line shows the behaviour of the function before it has been cleaned, and the red line shows the cleaned result.

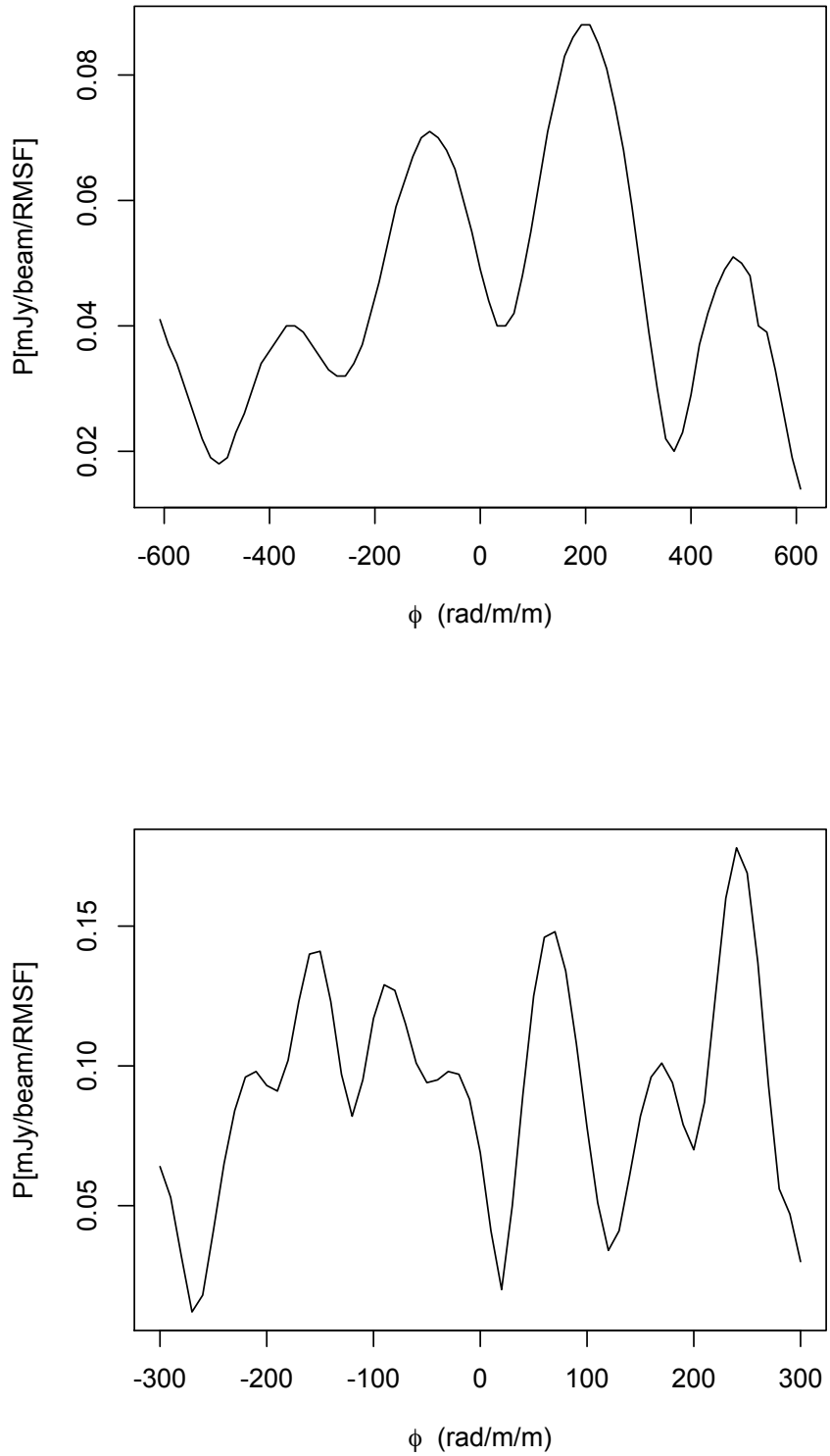

Figure 4.24: The Fourier dispersion function for a pixel in the region of the optical cloud in NGC 7385 using the code *rmsynthesis* at *(a)* 1.01 - 1.99 GHz and *(b)* 1.99 - 3.62 GHz. Both functions have been cleaned and tapered. The pixel has coordinates RA : 22 49 55.32, Dec = 11 36 43.1 (J 2000)

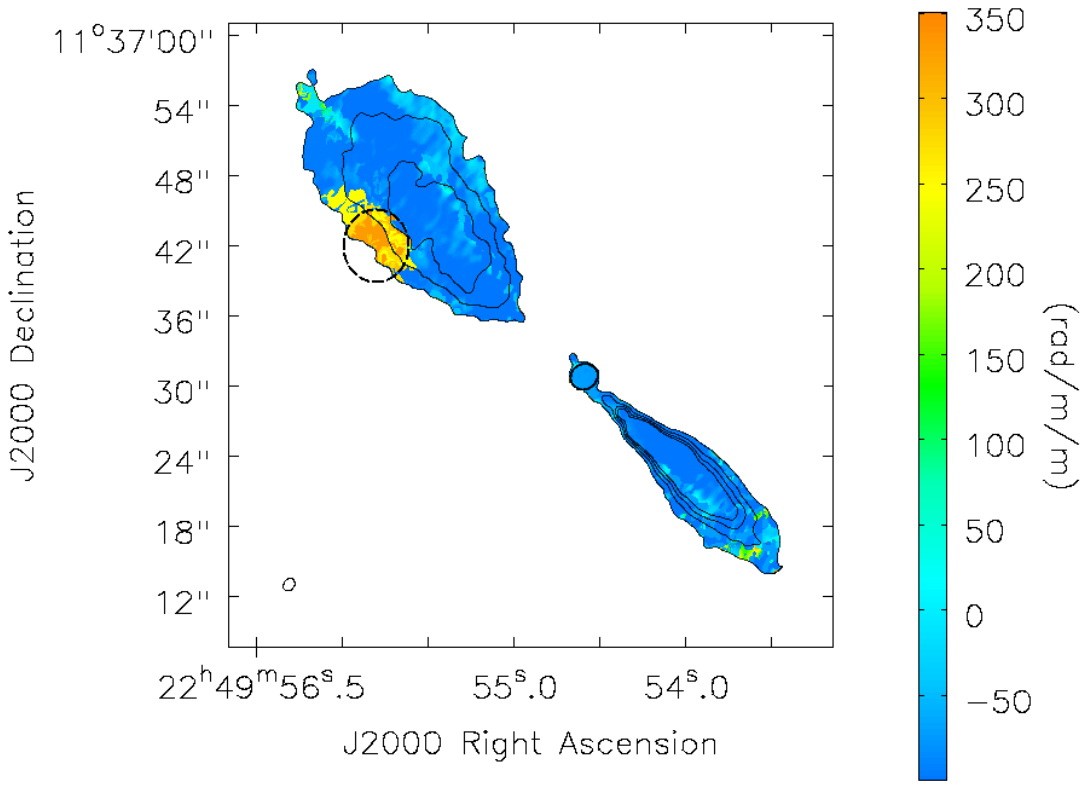

Figure 4.25: Rotation measure structure in NGC 7385 produced using the *rmsynthesis* code with radio intensity contours at 0.8, 1.6, 2.3 and 3.2 mJy beam^{-1}. A high rotation measure is seen within the dashed black line, which marks the position of the optical cloud. The typical uncertainty in the Faraday depth for a given pixel is about 7 rad m^{-2}.

Band/Filter	Exposure time (seconds)	Apertures	Central wavelength (angstroms)	Pixel size (arcsec)
F160W	2606	IR-FIX	15369	0.128
F775W	1600	UVIS	7647	0.0396
F555W	712	UVIS	5308	0.0396

Table 4.7: Observational details for HST data

Rawes et al. (2015) by about 30°, as expected for vectors corrected for a rotation measure of -60 rad m^{-2} in the L band. In the counter-jet lobe, the data show the jet deflection to be complicated. Along a central channel the magnetic field vectors appear ordered, at about 45 ° to the main jet axis. This corresponds to the location of a channel of high fractional polarisation, noted previously. To the north there is significant bending of the counter-jet component, accompanied by realignment of the magnetic field to maintain its dominant alignment along the jet. The tendency for the projected field to follow the boundaries of the source is in agreement with results on other extragalactic radio sources (e.g. 3C219, Perley et al., 1980; NGC 6251, Perley et al., 1984). At the location of the optical cloud, as indicated in Figure 4.26 by the dashed black line, the vectors rotate from parallel to the jet axis to perpendicular, marking the point at which the radio jet starts to turn.

4.2.2 Optical observations

The Hubble Space Telescope, launched into low Earth orbit in 1990, contains a 2.4m mirror and observes in the near UV, visible and near IR.

HST images of NGC 7385 were obtained on 2009 October 14 with the Wide-Field Camera (WFC3) instrument. The observation details are given in Table 4.7. The data were retrieved from the Multi-Mission Archive at Space Telescope (MAST) and all the images were flat-fielded, bias-corrected and wavelength calibrated with the standard HST pipeline routines. The Space Telescope Science Data Analysis System (STSDAS) pipeline processing software is able to produce calibrated, cosmic ray-rejected data sets in which minimal further user intervention is necessary. The HST header information was used to locate the core of NGC 7385 and these data were checked against the values provided in the literature by Simkin et al. (1984) and Simkin and Ekers (1979). Alignment of the radio and optical reference frames can be displaced due to offsets such as core shifts (e.g. Lara et al., 1994) however these are of the order 0.1-0.2 mas, significantly smaller than the scales of this study.

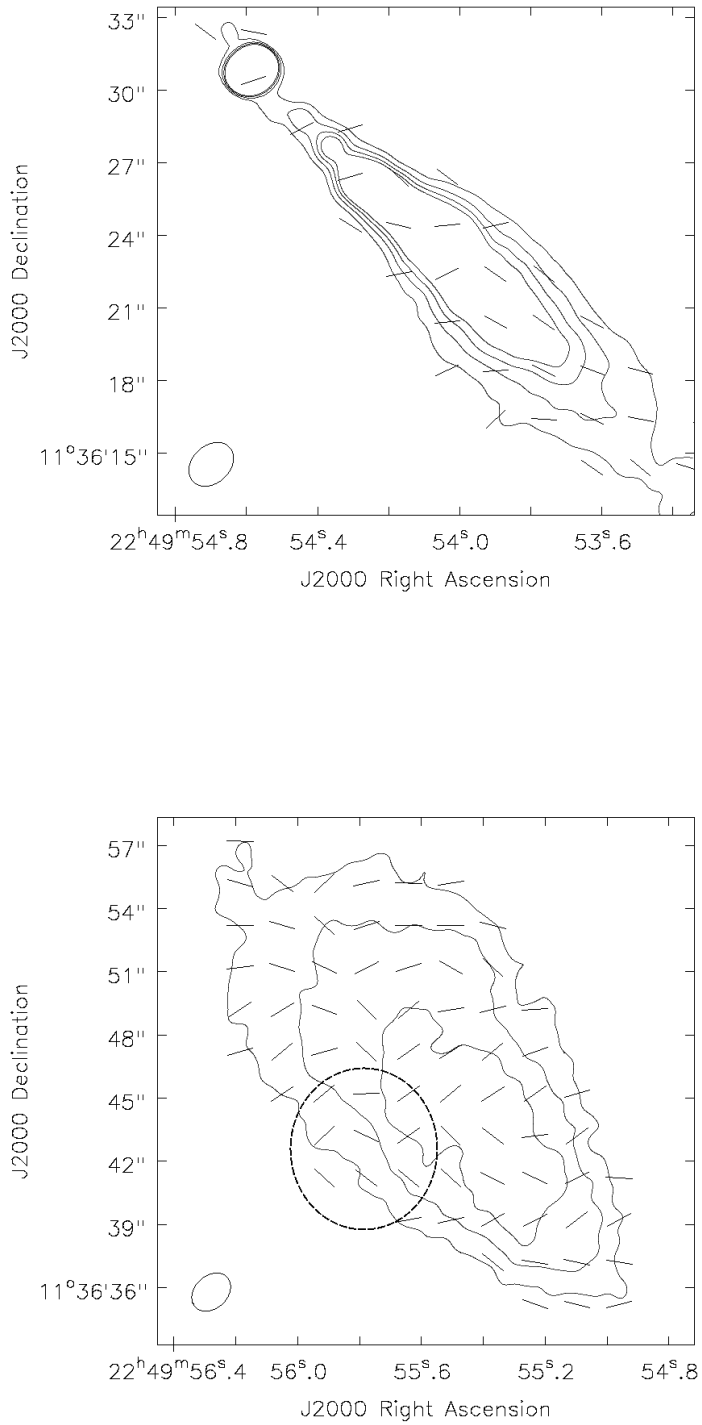

Figure 4.26: Magnetic field vectors at zero wavelength with radio intensity contours at 0.8, 1.6, 2.3 and 3.2 mJy beam^{-1}, produced using the rotation measure structure from the *rmsynthesis* code. *Top:* main jet apparent magnetic field structure. *Bottom:* counter-jet component magnetic field structure. A circular region represents the approximate position of the optical cloud.

Position of core	RA 22 49 55
	Dec 11 36 31
Position of cloud	RA 22 49 55
	Dec 11 36 43
Size of cloud (arcsec)	8.5×4.8
Flux in cloud (μJy)	2.4 ± 0.7
Length of optical jet (arcsec)	16

Table 4.8: Morphological parameters of the optical features from the HST observations.

4.2.2.1 HST data reduction

The IRAF task *ellipse* was used to fit elliptical isophotes to the galaxy images. The image is measured using an iterative method described by Jedrzejewski (1987) where each isophote is fitted at a varying semi-major axis length. The initial semi-major axis length was set at 400 pixels for the F160W filter, and 1200 pixels for the F775W and F555W filters. The position of the centre of the galaxy in terms of X and Y coordinates, the ellipticity of the galaxy and the position angle is also initialised. Using these values, the image is sampled along an elliptical path producing a 1D intensity distribution as a function of the position angle E. The harmonic content of this distribution is analysed by least-squares fitting to the function in equation (4.2), where the harmonic amplitudes A_i and B_i are related to specific ellipse geometric parameters.

$$y = y_0 + A_1 \sin(E) + B_1 \cos(E) + A_2 \sin(2E) + B_2 \cos(2E) \tag{4.2}$$

The geometric specifications can be set in the task *geompar* and the convergence and iteration parameters can be defined in *controlpar* within IRAF.

A residual image was produced by subtracting the elliptical model from the raw image, thus removing most stellar emission. Good photometry is strongly dependent on accurate knowledge of the sky value. I used sky regions clear of other sources, and took an average to determine the background for each image. The signal was then converted into Jansky, using the pipeline calibration *synphot* photometry package. Parameters of the optical features from the HST images are given in Table 4.8. The raw image of NGC 7385 with the F160W filter is shown in Figure 4.27 with the residual image produced after the subtraction of the underlying stellar emission and the removal of cosmic rays.

An optical jet can be seen extending to the SW within the radio contours. Close to the nucleus the subtraction is imperfect so I can only examine the structure and spectral distribution from 3″ onwards. The intrinsic faintness of the jet makes the edges difficult to

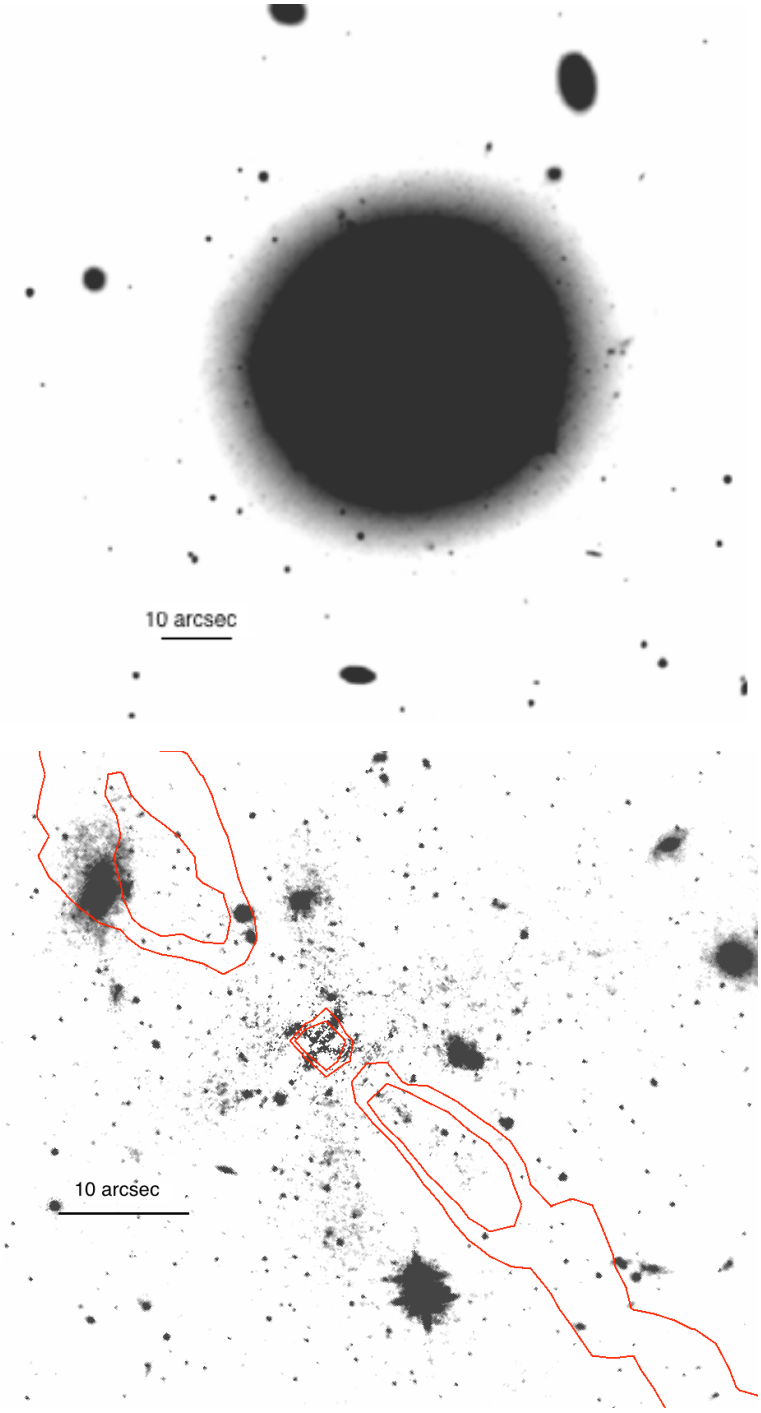

Figure 4.27: HST optical images in F160W. Both images are displayed on a logarithmic intensity scale. *Top:* HST image before galaxy subtraction. *Bottom:* zoomed view after removing cosmic rays and galaxy subtraction. Key optical features are labelled and the AH129 radio image is indicated by contours at 2 mJy and 4 mJy beam^{-1}.

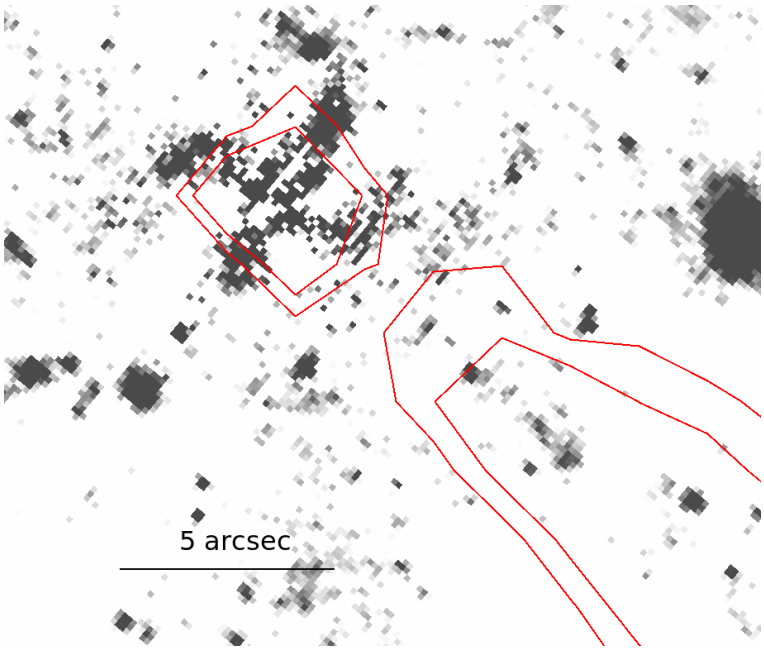

Figure 4.28: Close up of the optical jet from HST data. The radio image is indicated by contours at 2 mJy and 4 mJy beam^{-1}. The central cross pattern is an artefact of the ellipse-code.

define. Figure 4.28 shows an enlarged version of the optical jet. The flux profile along the jet was extracted and is discussed in more detail in section 4.3. The same region was used for the radio, optical and X-ray extractions. The jet is brightest and best defined between 3-10$''$ and so this region was used as the area over which to extract the flux for spectral energy calculations, although extended optical emission can be seen up to 17$''$ from the core. Errors were evaluated by combining the Poisson error in the counts in the jet with the uncertainty due to subtracting the galaxy. A noise term due to the background was also included. Although I recognise that optical emission in the region of the jet could be due to background galaxies, it is highly unlikely that such emission would exhibit a linear pattern coincident with the centre-line of the radio jet of NGC 7385.

There is an additional optical feature located within the radio counter-jet lobe. This bright optical knot has been described by Simkin and Ekers (1979). They detected faint [OII], [OIII] and Hβ emission lines with the Palomar telescope and suggested that the knot is not an optical counterpart of the process responsible for the radio emission, but arises from a secondary interaction with a relatively dense intergalactic medium. The systematic velocity of the gas relative to the stars in the galaxy strongly suggests that the knot is interacting with the radio jet. Their ground-based images from the Palomar Observatory in June 1975 show no evidence of the optical jet.

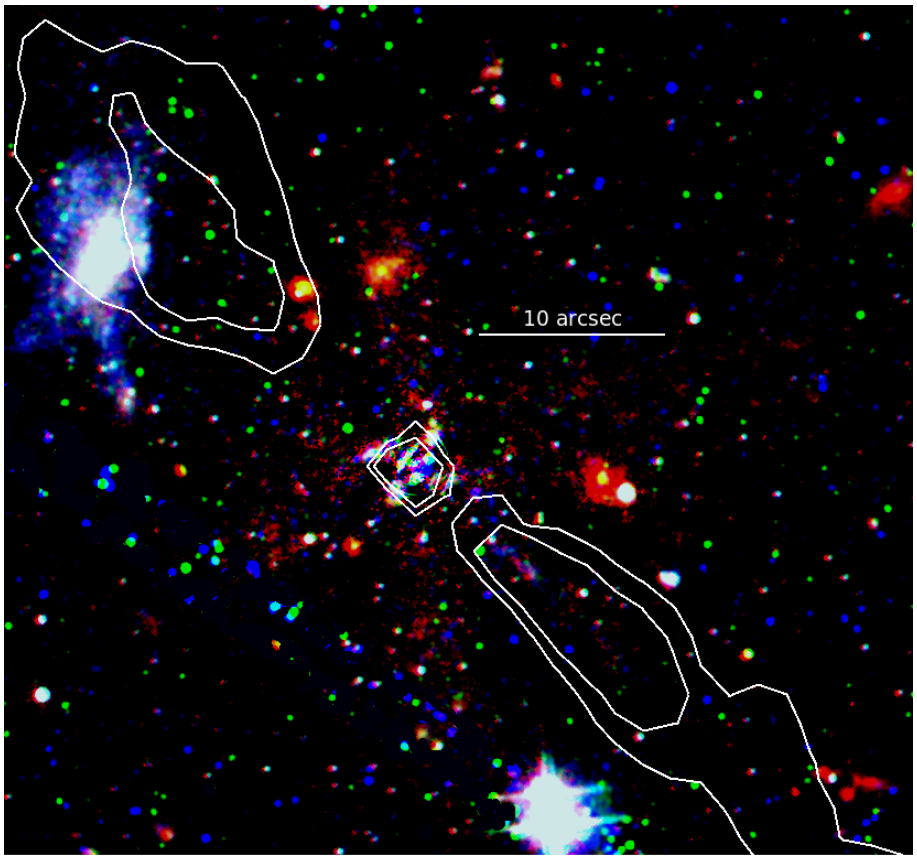

Figure 4.29: RGB cube image formed from the F160W, F775W and F555W HST images, overlayed with AH129 VLA radio contours with levels 2 mJy and 4 mJy beam^{-1}.

In the galaxy-subtracted HST image in Figure 4.27, the line-emitting cloud is bright and appears to extend beyond the radio contours. The position of the radio flux maximum as indicated by the contours is separated from the centre of this optical knot by approximately 3″ and it is also notable that the radio contours are distorted at the structure. A three-colour composite image was created using the F160W filter as the red image, F775W as green and F555W as blue. This image is shown in Figure 4.29. The optical knot is observed to be significantly bluer than the rest of the galaxy, suggesting it is gas rich and a site of strong star formation.

A dust lane becomes apparent in a three colour composite of the raw HST images (Figure 4.30). The dust lane is roughly perpendicular to the direction of the optical jet and on the counter-jet side, suggesting a disk and jet tilted so that the optical jet is moving towards us. The measured position angles of the dust lane and optical jet are $236 \pm 5°$ and $317 \pm 2°$ respectively. Dust features are observed in many radio-loud elliptical galaxies; Madrid et al. (2006) found nine galaxies out of a sample of 69 low redshift galaxies to have dust lanes (e.g. 3C 285, 3C 321, 3C 430). Capetti et al. (2000) found the fraction

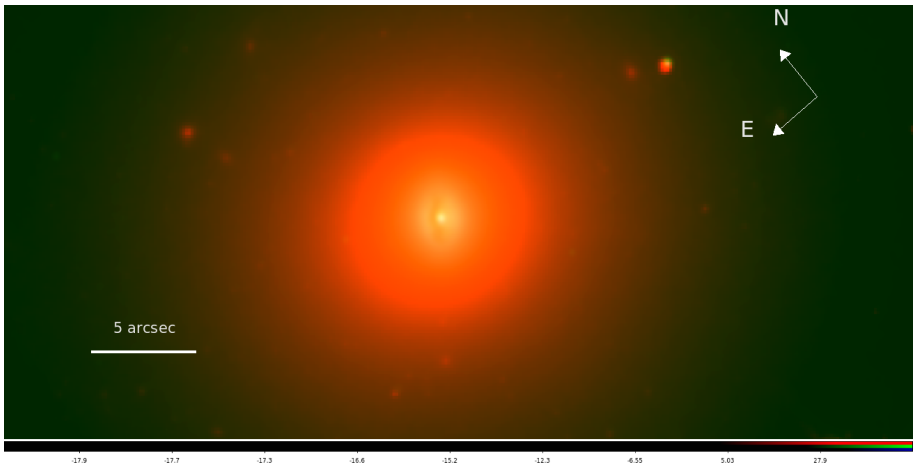

Figure 4.30: The dust lane close to the nucleus on the counter-jet side in a three colour composite image. The F160W filter was used to code the red channel, F775W the green and F555W the blue.

of host galaxies with dust lanes to be higher at low radio power, with 54% of FR I-type sources in the sample containing dust lanes. NGC 7385 should therefore be added to statistical samples for studies of the dust content of low power 3CRR radio galaxies.

4.2.3 X-ray observations

The ACIS-I instrument on *Chandra* was used to observe NGC 7385 on 2009 August 15 in VFAINT imaging mode for 40 ks, with observation ID 10233. The data were imported into CIAO and reprocessed by following the 'science threads' in CIAO version 4.6 to generate a new level 2 events file. The X-ray image in 0.5-2.0 keV is shown in Figure 4.31 with radio intensity contours overlayed. The lower image has been smoothed with a Gaussian function of σ = 3 pixels, where 1 pixel = 0.492 arcseconds, and the upper image is unsmoothed. 23 counts were found over the region of the optical jet in the 0.5-2.0 keV energy band, where the counts expected using the average over other regions symmetrically-placed relative to the X-ray core were 4. This gives a probability of detection in excess of 99%. The X-ray flux was extracted using CIAO task *srcflux*, which determines the net count rate and flux for sources in a *Chandra* observation given source and background regions and a spectral model. The background region was an annulus centered on the nucleus of the AGN with inner radius 3″ and an outer radius 9.3″. The X-ray jet and the counts in the read-out direction were excluded from the background region. This shape ensures the removal of nuclear X-ray emission spread over the jet by the point response.

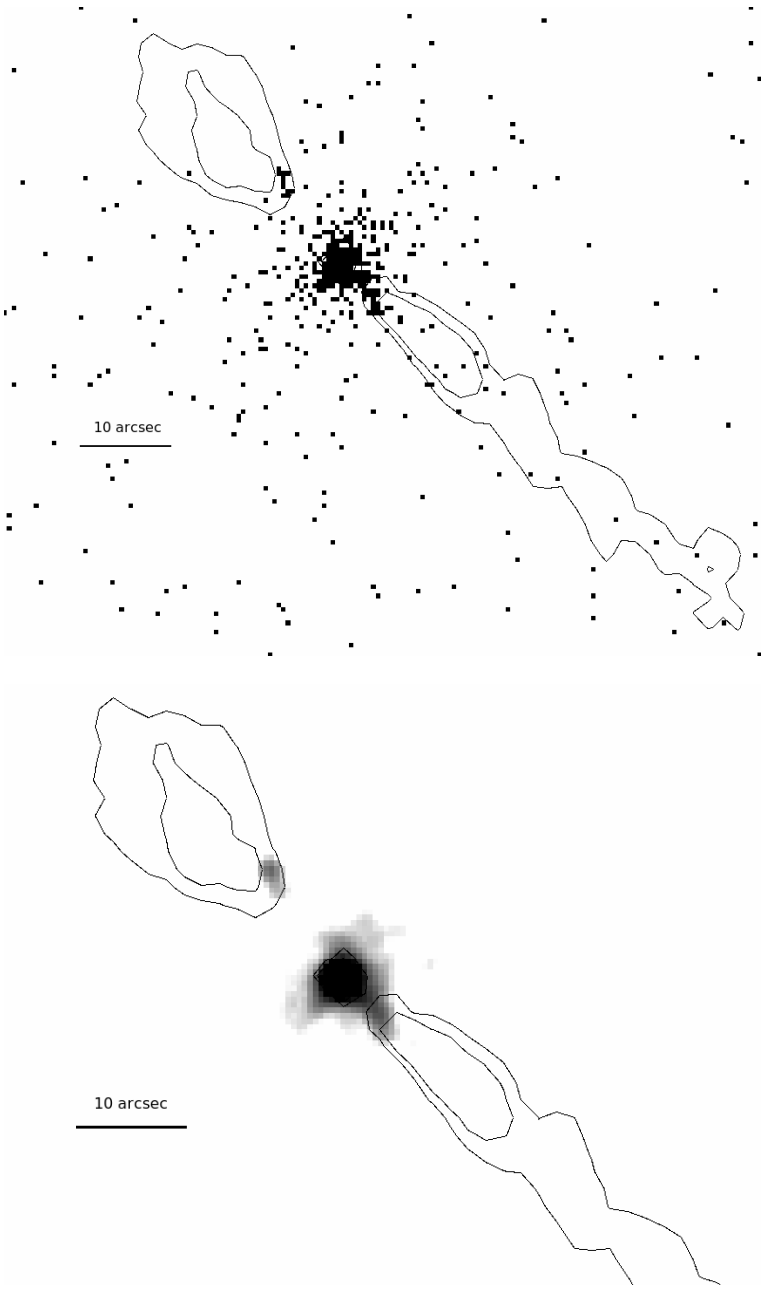

Figure 4.31: The X-ray emission of NGC 7385 produced using Chandra data and processed in CIAO with energy range 500-2000 eV. The contours are radio intensity contours from the AH129 project with contour levels 2 mJy and 4 mJy beam^{-1}. The X-ray jet can be seen extending to the south west away from the bright core. *Top:* unsmoothed image showing the raw counts in the source. *Bottom:* X-ray image smoothed with a Gaussian function σ=1.5 arcsec.

The X-ray jet is brightest in a region about 4-6″ from the core. Fainter emission is detected over a further 5″. It is difficult to determine the significance of the faint X-ray emission beyond the inner jet, although the expected background in the region of the outer jet is 3 counts. In this region, we detect 28 counts in 15 pixels along 2″ of the jet, and since the Poisson probability of detecting these counts when 3 are expected is much less than 0.1%, this implies a significant detection.

There is also a second region of X-ray emission along the W contours of the counter jet. This has no optical counterpart in the HST images. There are 26 counts within this bright X-ray structure, more than for the jet. This X-ray emitting region has been listed as CXO J224944+113640 in the *Chandra* source catalogue (Evans et al 2010).

Using a nearby region to measure the background, *xspec* was used to model the core spectrum, assuming a power law model with Galactic absorption. This gave a 1keV flux density of 20 $\pm$ 6 nJy and a photon index of 2.14 $\pm$ 0.13, with χ^2 = 26 with 25 degrees of freedom. This corresponds to a nuclear X-ray luminosity of 7 $\times$ 10^{41} ergs s^{-1} between 13.6 eV and 7 keV. There appears to be very little extended X-ray emission, although it is possible that there is some group gas to the N of NGC 7385, near NGC 7386. Duffy et al (in prep) also report the presence of a possible X-ray gas belt, seen in Figure 4.31 as asymmetrical gas NW and SE of the core.

4.3 Spectral Energy Distribution

Multi-frequency surface brightness profiles of the jet are given in Figure 4.32 up to a distance of 16″ (8 kpc) from the core. Regions have been labelled A-F in accordance with the position of peaks in intensity in the optical jet. A profile at 90° to the jet was also examined to confirm the flatness of the background, and to assess the errors associated with the surface brightness along the jet. The width of the profiles (1.1″) was chosen in accordance with the dimensions of the optical jet, so that off-axis stars would not be included.

The profiles begin at 3.5″ from the centre of the core and extend out to 16″. In regions closer to the core in the optical image, galaxy and nuclear subtraction are uncertain with bad residuals. A spectral energy distribution was extracted for regions A-D, which are bright at all frequencies, with results in all 3 bands converted into Janskys using default calibration. The optical and X-ray plots show a peak at knot A. In the radio this feature is not prominent, possibly indicating a compact knot of 1 mJy at 1.51 GHz. The optical peak

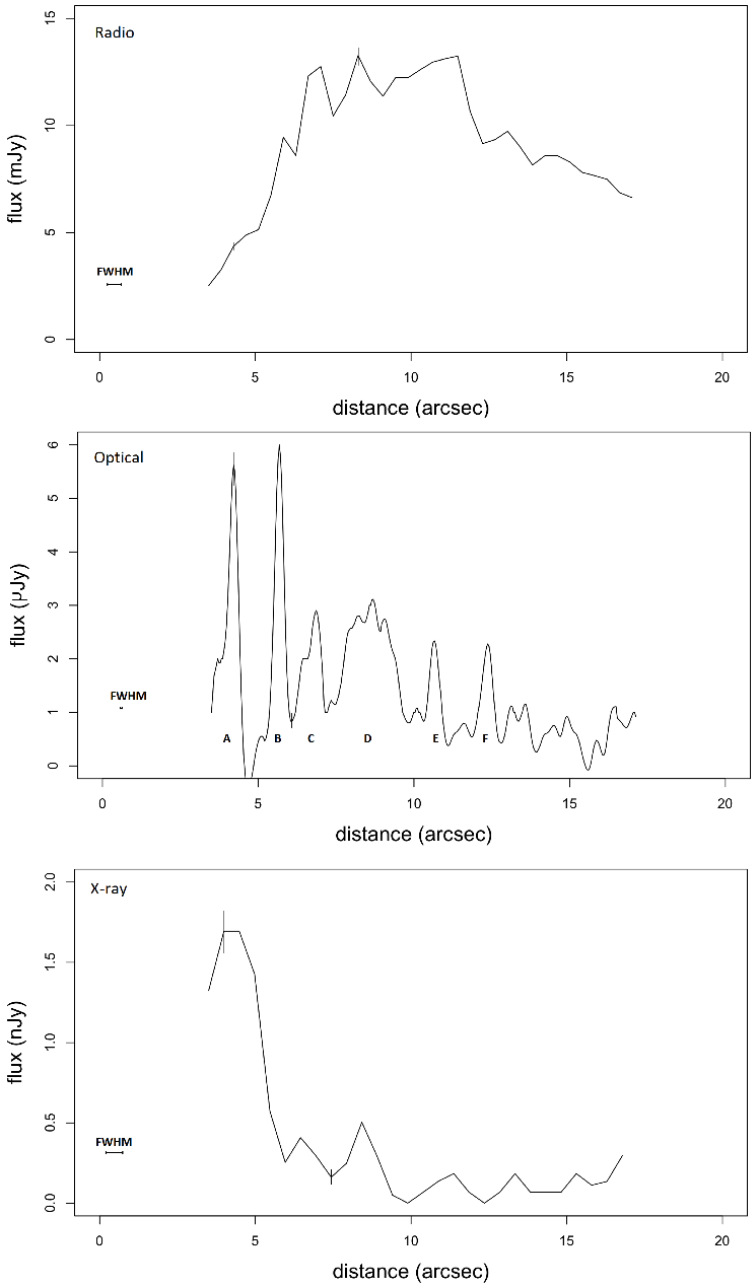

Figure 4.32: Surface brightness profiles along the centre of the radio, optical and X-ray jets. The same projection was used for each frequency, 1.1″ wide out to distance 16″ from the core. 6 peaks in the optical profile have been labelled as knot A-F. It was not possible to extract profiles closer to the core than 3.5″ due to imperfections from the ellipse subtraction. All data were background subtracted and the beam size is shown for each frequency. Representative error bars are also included.

Spectral parameter	Spectral index
α_r	0.58 ± 0.05
α_{ro}	0.48 ± 0.21
α_o	1.1 ± 0.32
α_{ox}	1.25 ± 0.15
$\Delta\alpha$	0.77 ± 0.36

Table 4.9: Spectral indices for each frequency band

region B corresponds to a decrease in X-ray intensity and a gradual intensity increase in the radio. Surface brightness was measured at each pixel along the length of the defined jet region and the high resolution of the HST image means that regions A and B can be distinguished. Due to the lower resolution of Chandra, it is possible that the large X-ray peak arises from separate unresolved components. Region C shows a peak at each frequency, as does region D. The positions of the peaks in region E and F in the X-ray image are approximately $1''$ further along the jet than in the optical. The X-ray brightness quickly drops off after region B. The radio intensity increases steadily out to $7''$ and the jet remains bright beyond the plotted X-ray and optical profiles. Optical knot F coincides with the radio polarisation rotation region where the parallel magnetic field rotates to become perpendicular to the jet direction.

The spectral index is defined as α where $S \propto \nu^{-\alpha}$, and the values obtained by extracting the flux S from the images are given in Table 4.9.

The flux in the X-ray jet was extracted using *srcflux* in CIAO. The data were analysed for uncertainties in the source and the background, and the flux at 1 keV was calculated. An adopted X-ray power law of α_X = 1.1 (based on a photon index of 2.1) and a Galactic absorption of $N_H = 5.06 \times 10^{20}$ cm^2 obtained from the COLDEN program, gave a 1 keV jet flux density of 10.6 ± 0.7 nJy. Spectral indices both within and between frequency bands are given in Table 4.9. To compute the radio-to-optical spectral index, α_{ro}, radio frequencies from both VLA and JVLA observations were used together with the lowest optical frequency. For the optical-to-X-ray index, α_{ox}, the highest optical frequency was used. The spectral range of the data from the VLA archive was too small to give a useful radio spectral index α_r , so in Rawes et al (2015), I adopted α_r = 0.5, as in Schilizzi and Ekers (1975). Schilizzi and Ekers (1975) plotted the spectral index of emission along the tail of NGC 7385 out to 14 arcminutes at 0.408 GHz and 1.415 GHz. They found the nucleus to have a flat spectrum, with α_r = 0.5, and the tail component becoming progressively steeper with distance, reaching α_r = 1. Robertson (1981) also found α =

0.5 along the first 4 arcminutes of the radio jet using WSRT data at 1.4 GHz and 5.0 GHz. A similar spectral index in the NE radio component was found in the S tail, consistent with the idea that it is a counter-jet ejected in the direction of motion of the galaxy. The new JVLA observations give α_r = 0.58 (see Figure 4.11), in agreement with the results described above.

It is difficult to find strong trends in observed features of multi-frequency radio galaxies similar in luminosity to NGC 7385 since relatively few have been detected in both optical and X-ray. For all optical jets, α_o is in the range of 1.2-1.4, similar to the value calculated for NGC 7385. If the optical slopes were steeper, the jet emission would be more difficult to detect since they would in general be fainter and of lower contrast against starlight, so jets with a steeper optical spectral index tend to be selected against. However flatter-spectrum jets would be observed, so the absence of flat optical slopes could be significant. In M87, Biretta et al. (1991) published jet SED's showing a general trend for the optical spectral index to steepen with distance from the core. We would need deeper optical data to test if this is the case in NGC 7385.

A spectral fit based on the method of Hardcastle et al. (1998) is shown in Figure 4.33. I fitted a synchrotron spectrum to a cylindrical region of length 6″ and radius 0.6″ along the inner jet. I assumed the synchrotron / energy density parameter k = 1, a spectral index α = 0.58, and an electron energy range with Lorentz factor $10 < \gamma < 100$.

I found the magnetic field strength, based on the assumption that the electrons and magnetic field are in equipartition and that relativistic beaming is negligible. The method uses the derived magnetic field strength to calculate the contribution to the X-ray emission from the synchrotron self Compton process and inverse Compton scattering of the cosmic microwave background radiation (CMB), both of which are found to be negligible. The spectrum shows the need to introduce a break $\Delta\alpha$ = 0.8 into the synchrotron spectrum. The break is constrained by the X-ray flux density and needs to be at about 9 $\times$ 10^{13} Hz, in the infrared-optical region. My derived equipartition magnetic field strength of 2.3 nT is strongly dependent on the minimum energy of the electrons, which was set at 5.11 MeV, i.e. with Lorentz factor γ_{min} = 10. With the aim of constraining the spectrum further, I extracted the flux density from a Spitzer image of NGC 7385 (see Figure 4.33) with wavelength 8.0 μm and found that the results are consistent with a near-IR position for the break frequency.

The optical knots at E and F (see Figure 4.32) are at 10.6 and 12.5″ from the nucleus respectively, corresponding to distances of 5 and 6 kpc. The synchrotron lifetime for

emission is given by $t_{\rm cool} = 0.043 B^{-\frac{3}{2}} \nu^{-\frac{1}{2}}$ in years, for an electron emitting in a B field (Tesla) with frequency ν in Hz (Worrall and Birkinshaw, 2006). For optically emitting electrons at 6.45 $\times$ 10^{14} Hz and using the estimated equipartition magnetic field strength 2.3 nT, this gives a synchrotron lifetime of the order 10^4 yrs. This is smaller than the light travel time from the nucleus, but only by a factor of two. However if we assume that the X-ray emission is also produced via the synchrotron process, the lifetime for electrons at knot D is around 800 yrs. This is over 10 times less than the light travel time to this region. This means that at some point the particles must have been accelerated or reaccelerated within the jet. The lifetime for electrons producing radiation at the break frequency is of the same order as the light travel time to the end of the optical jet. The need for the reacceleration of high energy electrons to the outer regions of jets is common in many other similar sources. The sites of reacceleration are often said to be associated with the location of shocks in the jet plasma.

4.4 Interpretation

In the preceding sections I discussed the polarisation and magnetic field structure in the radio jets of NGC 7385 and presented new images of an optical jet obtained through HST imaging. The spectral indices for the jet from the radio through to the X-ray were presented in Table 4.9 and an SED is displayed in Figure 4.33. Based on this distribution I found the synchrotron mechanism to be responsible for the observed emission in all bands. In this section I discuss the physical processes at work within the jet, and compare this to other known jets with radio and optical polarimetry. In particular I look at the relationship of the jets in M 87 (Perlman et al., 1999), 3C 66B and 3C 264 (Perlman et al., 2010), and 3C 15 (Dulwich et al., 2007) to this source.

An additional optical component was also identified which appears to be associated with the counter-jet lobe. In the subsequent sections I detail the evidence for this interaction in terms of the rotation measure structure and discuss the possible excitation mechanisms and physical origin for the optical gas.

4.4.1 Radio morphology and polarisation

The large scale structure of NGC 7385 (Figure 4.1) shows extreme jet bending on a kpc scale. The counter-jet is deflected away from the jet axis and undergoes a 180° reversal

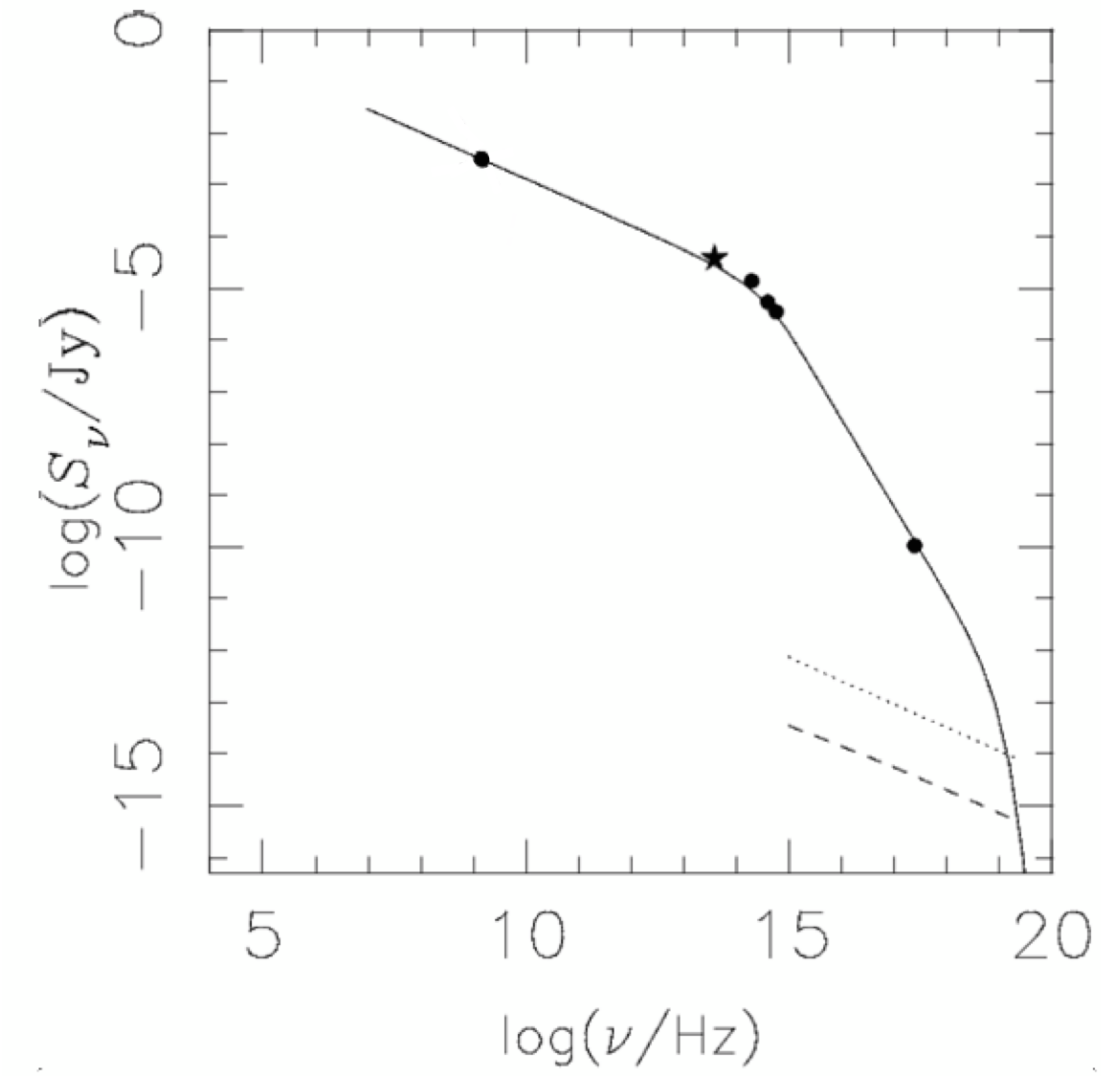

Figure 4.33: The radio to X-ray spectrum of the jet in NGC 7385. The shape is consistent with synchrotron radiation (solid black line). The contributions to the X-ray emission from synchrotron self Compton (dashed line) and inverse Compton scattering of the CMB (dotted line) are also shown. A spectral break of approximately 0.75 is needed in the optical-infrared region and the bowtie shows the error range in the radio spectral index. The black star shows the 8.0 μm flux from Spitzer data.

which sees it emerge south of the main jet as a plume of emission. Such strong curvature over just a few kpc is rare, and requires an explanation that can account for the complete change of the path of the jet without utter jet disruption. Analysing the polarisation structure within the radio emission can help to reveal the jet dynamics. Highly polarised regions of emission can indicate interactions with the external medium or the presence of shocks within the radio plasma. A high degree of polarisation also indicates an ordered magnetic field and the direction of the magnetic field vectors can shed light on the dynamics of the jet.

The fractional polarisations in the archival VLA maps and the recent JVLA observations are in agreement. The unresolved core has a low fractional polarisation, decreasing from approximately 10% at 1.41 GHz to 6% at 4.99 GHz. In the counter-jet, areas of high linear polarisation are found near the jet edges where the magnetic field appears to follow the flux contours. This suggests shearing of field lines along the edge of the counter-jet lobe. This is particularly prominent at the northern end of the counter-jet where the field appears to track the jet bends, suggesting a strong link between the local magnetic field and the dynamics that bend the jet. In the centre of the component, compression of the magnetic field by jet deceleration would cause perpendicular field lines and this magnetic field structure has been observed in many other radio lobes (Hogbom, 1979). An increase in fractional polarisation near the edges of jets could also be evidence of torsional shear. This polarisation increase is seen 14″ from the nucleus along the northern edge of the main jet. This would not be so easily observed in the centre of the jet because of the cancellation of different field directions seen in projection. Knot A in the jet of M 87 has been modelled as a torsional shock (Bicknell and Begelman, 1996, Perlman et al., 1999), and similar features are seen in Cen A (Clarke et al., 1992).

The structure in the magnetic field can also be explained in terms of velocity gradients across the jet. A sheath-like parallel field structure is shown in both the counter jet and the jet. This suggests that there could be two distinct regimes in the jet modelled by a fast moving relativistic core or 'spine', surrounded by a shear layer (the 'sheath') decelerating due to entrainment with external material. This spine-sheath model would predict the magnetic field structure observed in the counter-jet, where the slow outer sheath surrounds a core which is faint due to beaming away from the observer.

Laing (1996) uses a spine-sheath model to explain the rotation of the magnetic field vectors from parallel to a jet axis to perpendicular further out. This change in vector direction is suggested in Figure 4.32 at 13″ by a region of depolarisation. This field structure

has also been observed in many other FR I-type jets (e.g. 3C 66B, Hardcastle et al., 1996). Laing explains the pattern in terms of shear layers with a longitudinal component and a jet core without these components. Close to the nucleus the core is highly relativistic and beamed out of the line of sight, so that parallel magnetic field structure is seen by the observer. The jet decelerates as it moves away from the nucleus and the perpendicular component of the field becomes more important, causing the change in the field direction. In this model, emission from both longitudinal and transverse B fields can only be seen if it is beamed towards us. The radio polarisation vectors in 3C 15 (Dulwich et al., 2007) are consistent with this model, and it is suggested that the magnetic field is ordered with a helical structure.

Determining whether the polarisation structure observed is due to a helical magnetic field can prove difficult. A predicted consequence of strong, ordered helical fields that wrap around a jet is a gradient in the Faraday rotation measure transverse to the long axis of the jet (Blandford, 1993). Although there are a few well established cases of RM detections in bright quasars and BL Lac objects (e.g. 3C 273, Zavala and Taylor, 2005), relatively few polarisation studies have been carried out on radio galaxies due to their faintness and weak Doppler boosting. Parsec-scale RM's have been estimated for the high luminosity FR II-type galaxies 3C 111, 3C 120 and 3C 166, and the low luminosity FR I-type galaxies M 87, 3C 84, 3C 66B, 3C 78 and 3C 264 (Kharb et al., 2009). Despite the growing list of sources reported to display rotation measure gradients, Taylor and Zavala (2010) were unable to detect gradients in several of the published sources and thus proposed an objective criteria to establish what constitutes an RM gradient. They claim that many of the gradients proposed in the literature are in sources where the synthesised beam spans not much more than the width of the jet. In addition, observations at shorter wavelengths tend to probe only the brightest part of the jet base, and therefore observers run the risk of deriving RM from inconsistent part of the radio source. They report on the lack of support from simulations to corroborate the RM features described from observations, and that existing simulations of poorly resolved jets will not produce transverse RM gradients (Broderick and McKinney, 2010). Taylor and Zavala (2010) suggest two observational and two physical constraints should be met before a RM gradient is claimed. Firstly, that there are at least three resolution elements across the jet. Secondly, that there is a change in RM at least three times the typical error. Thirdly, that the spectrum is optically thin at the location of the gradient, and finally, that there is a monotonically smooth change in the RM from side to side. For the inner jet associated with

NGC 7385, the beam width is only slightly narrower than the width of the jet and there are only just sufficient resolution elements to satisfy the conditions of Taylor and Zavala (2010) and probe the RM structure transverse to the jet. These results suggest that there is no evidence for a rotation measure gradient, however higher resolution observations would be useful to probe this further.

4.4.2 Discovery of an optical jet

In this section I have focused on modelling the spectral distribution of the multi-wavelength jet in NGC 7385 using synchrotron radiation. Contributions to the X-ray emission from inverse Compton scattering of the CMB and the synchrotron self Compton process are predicted to be negligible (Figure 4.33). A broken power law electron energy distribution fits the data well, with an electron power law of energy slope 2α + 1 = 1.9 with a break at energy 9 $\times$ 10^{11} eV. The equipartion magnetic field strength B_{eq} = 2.3 nT, is lower than estimates for other sources with optical jets (e.g. 33 nT for 3C 264; Perlman et al., 2010). The minimum energy, or γ_{min} of the electrons, is the most uncertain factor with the greatest influence on the value of the magnetic field strength. B_{eq} is roughly proportional to $\gamma_{min}^{(2\alpha+1)/(\alpha+3)}$ for $\alpha > 0.5$ (Worrall and Birkinshaw, 2006). A smaller value of γ_{min} therefore would lead to an increase in the magnetic field strength. However I have already assumed a low value of γ_{min} = 10, so we could not recover a field as large as in 3C 264. The volume of the jet is also important, and it was modelled using the width of the optical jet.

The lifetime of electrons emitting optical and X-ray synchrotron radiation are shorter than the light travel time for electrons to the outer knots. Mechanisms which could permit such a situation include a highly relativistic flow, a 'low loss channel' for transporting electrons and local reacceleration (Hardcastle et al., 1996). In low loss channels, electrons might be transported in a region of low magnetic field to the outer regions of jets, and adiabatic and synchrotron losses might be negligible compared to losses due to inverse Compton scattering of the CMB photons. However in the X-ray, inverse Compton scattering on the CMB and starlight would further limit the lifetime of electrons making this mechanism an unlikely explanation for the observed emission.

Many other jets exhibit a similar energy loss problem and local reacceleration is widely believed to resolve the issue. Looking at the spectral indices of the knots individually would constrain possible sites for particle acceleration, since the optical indices would be distinguishable from interknot regions as significant losses between knots

would be observed. Hardening of indices in knots close to the nucleus could suggest that the knots are shocks at which first order Fermi acceleration is taking place (Hardcastle et al., 1996). Alternatively, particles could be accelerated by a second order Fermi process driven by turbulence through the jet (Bicknell, 1994). This process however would produce a shear sufficient to maintain a parallel magnetic field direction throughout the jet (Leahy and Perley, 1991) and this is not observed in NGC 7385.

Offsets between peaks at different frequencies could constrain the location of these privileged sites of particle acceleration. For the jet in 3C 66B, Hardcastle et al. (1996) found an offset between the radio and X-ray peaks and suggested a model in which radio knots are the sites of particle acceleration with a shock close to the X-ray peak. The shift in the position of the peak would be caused by rapid synchrotron losses of the particles emitting in the X-ray as they propagate away from the shock. Adiabatic loss as a jet expands sideways after a shock would also be important. Figure 4.32 shows an offset in the position of the optical and X-ray peaks at knots E and F, so the physical process for NGC 7385 could be similar to that described above. In addition, the low polarisation region 12″-13″ from the core and coincident with the position of the optical flux maximum in knot F, shows a rotation in the magnetic field from parallel to the jet axis to perpendicular. Perlman et al. (2010) describe this same pattern for the structure of the knot A/B region in 3C 264, and suggest that the low polarisation could be the result of field superposition and that the angle change may be due to shocks at the location of the maxima. Alternatively, the angle change in knot C in 3C 15 was modelled as the superposition of a helical strand of magnetic field on a more ordered field structure (Dulwich et al., 2007). Unfortunately we do not have optical polarimetry data to help distinguish between these two models for NGC 7385.

Theoretical and observational work from Brunetti et al. (2003) showed that low-power radio hotspots are optimum candidates for detecting an optical counterpart. They found that the shape of the synchrotron spectrum in these regions is strongly influenced by the magnetic field strength, constraining the position of the break frequency. They produced a plot of the synchrotron break frequency as a function of the equipartition magnetic field for data from the VLT and also from literature (see their Figure 4). The plot showed a clear trend which suggested that high break frequencies are likely due to the effect of the magnetic field on the cooling of the electrons. While the jet in NGC 7385 is not a hotspot, our equipartition field value of 2.3 nT predicts a value of break frequency close to 10^{15} Hz, as inferred (Figure 4.33). Since in our case we see this in a jet knot rather than a

hotspot, relativistic effects may be present.

The five jets in M 87, 3C 78, 3C 371, 3C 66B and 3C 264 show the general shape of the spectrum in Figure 4.33. For a simple energy-loss model of synchrotron radiation, the spectral break would be 0.5. We measured the break to be 0.77 (but with a large error), in accord with the jets of other low power radio galaxies where the break is in the range 0.6-0.9 (e.g. 3C 78, 3C 371, 3C 66B; Worrall, 2009). Explanations for this larger break have been offered (Pacholczyk, 1970; Wilson, 1975; Reynolds, 2009) in terms of a decrease in the magnetic field away from sites of particle acceleration, with the assumption that electrons propagate towards regions with a lower magnetic field. Another plausible explanation uses the idea of velocity gradients in the jet flow. Georganopoulos and Kazanas (2003) propose that for small angles to the line of sight, the spectral break should be 0.5 as suggested by theory. However at higher angles, when the emission of the spine is being beamed out of our line of sight, spectral breaks can be steeper. The degree of alignment affects the observed jet emission at high energies, where the optical and X-ray emission should be dominated by the spine for highly aligned jets. The orientation of the NGC 7385 jet is unknown. While HST imaging observations now exist for almost all known optical jets, HST polarimetry does not. Polarimetry across multiple frequencies can uncover differences in the magnetic field geometry encountered by different radiation populations. With this information, it is then possible to form a three dimensional picture of the energetic and field structure in the jet. Optical polarisation maps have been produced for fewer than 10 jets, and as a result very little is known about the energetic structures. It is not therefore known for the majority of sources to what extent the radio and optical emitting electron populations are cospatial and encounter a common magnetic environment.

4.4.3 A jet-cloud interaction in NGC 7385

There is clear morphological, kinematical and polarimetric evidence in NGC 7385 for an interaction between the optical gas cloud and the northern radio lobe, as originally suggested by Simkin et al. (1984). They proposed that the optical cloud is interacting with the northern lobe, leading to photoionisation of the gas and disrupting the path of the radio jet. Such a picture is supported in this thesis by the presence of Faraday rotation measures, an inverted spectral index across the interacting region and a clear deflection in the radio jet lobe. Jet-cloud interactions in nearby active galaxies are relatively rare, and few sources offer a strong enough interaction to study in detail. Because of this, the

gas acceleration mechanism within these interactions and the extent to which jet-induced shocks can ionise emission line clouds is not yet fully understood. The emission line spectra generated by gas which has been ionised in jet-cloud interactions can be used to investigate densities, velocities and temperatures for the emitting gas, and in turn these parameters can be used to constrain models of the jet-gas interactions which produce these conditions.

4.4.3.1 Morphology of the radio/optical interacting region

Our observations show that the optical cloud seen N of the nucleus in Figure 4.27, and the counter-jet radio emission are related. The northern radio structure is deflected as a result of the interaction with the optical cloud on the eastern edge and the jet no longer remains collimated downstream of this interaction. The disrupted radio jet turns through 180°, heads back towards the core and ultimately ends as a plume of emission 200 kpc south of the nucleus. Evidence for this extreme structure distortion can be seen in Rawes et al. (2015).

The cloud itself has a projected length of 7.4 kpc in the direction perpendicular to the main jet axis. Most of the bright optical emission is concentrated in an elliptical region, however fainter emission is also seen north of this area in a region of size $5.2'' \times 3.7''$, as though part of the cloud is being swept away from NGC 7385.

In other galaxies with a jet/cloud interaction, broad optical emission lines have been detected near the radio jet boundary. 3C 277.3 (van Breugel et al., 1985b) exhibits broad extranuclear lines in the regions adjacent to strong radio emission and a similar trend has been reported for 4C 26.42 (van Breugel et al., 1984) and 4C 29.30 (van Breugel et al., 1986). Large velocity gradients along the axis of the radio emission can also provide evidence for an interaction. For NGC 7385 a velocity difference of 230 ± 70 km s^{-1} between the optical object and the galaxy is reported by Simkin et al. (1984). They report no significant broadening of the optical emission lines close to the radio lobe and conclude that the emission line gas must have internal velocities between 60-90 km s^{-1}. It is therefore likely that the optical object is on the outside of the lobe, which is pushing up past it.

The rotation measure maps in produced in Figures 4.15 and 4.25 show strong Faraday rotation in the region of the optical object. This suggests that the optical cloud is on the observers' side of the radio lobe. This correlation between the presence of emission line gas and strong Faraday rotation of the radio emission is also found in 3C 277.3, 4C 26.42, Minkowski's object, and 4C 29.30 (van Breugel et al., 1985b; van Breugel et al., 1984; van

Breugel et al., 1985a; van Breugel et al., 1986). Faraday rotation seen throughout regions of emission line gas can be produced by material in the boundary layers of the radio source, acting as a Faraday screen or through near-jet gas which has taken up magnetic field leaked from the jet in a magnetosheath.

The spectral index map in Figure 4.11 shows a strong correlation between the region of negative α and the presence of the optical cloud. This suggests that the foreground cloud is causing the spectrum to turn over due to free free opacity, thus requiring a large column of absorbing material. The optical depth τ of an object is related to its emission measure EM in cm^{-6} pc by the expression:

$$\tau_\nu = 0.082[EM]T_e^{-1.35}\nu^{-2.1} \tag{4.3}$$

with electron temperature T_e in K and frequency ν in GHz. For an electron temperature T_e= 10^4K (Simkin et al., 1984), at the central frequency of the spectral map and with an optical depth τ = 1, this gives an emission measure EM = 3.2 $\times$ 10^5 cm^{-6} pc. For a path length of 10 kpc, this implies an electron density n_e = 5 cm^{-3}. These values suggest that there is a huge amount of mass in the optical cloud.

Assuming that the mass within the optical cloud is predominantly hydrogen, the mass can be estimated from

$$M(H) = \int \delta N_e m_p dV \tag{4.4}$$

where δ is a filling factor which describes how clumpy the gas is, n_e is the electron density in cm^{-3}, m_p is the mass of a proton and V is the volume of the cloud. Using a sphere with radius 5 kpc to describe the volume of the gas and a filling factor in the range 10^{-1} to 10^{-5} as deduced by Simkin et al (1984) gives a gas mass of (0.6 - 6000) $\times$ 10^6 M$_\odot$. Results published by Cedrés et al. (2013) suggest a correlation between the radius of a gas cloud and the filling factor, with larger clouds having a smaller δ. This would suggest that the value of the gas mass for the object in NGC 7385 is closer to the lower limit.

4.4.3.2 Origin of the gas

A key question when investigating these optical/radio interactions concerns the origin of the gas in the deflecting cloud. Is it gas moving with the jet-fluid which is being transported out from the nucleus, or is it local gas which is being impacted by the jet?

In the case of NGC 7385, evidence strongly favours the latter. The emission lines are far weaker in the extranuclear than in the nuclear gas (Simkin et al., 1984), suggesting that the extranuclear gas has a different metal abundance, as expected for material in the outer regions or outside of a galaxy. The spectra observed by Simkin et al. (1984) can be reproduced in a standard photoionisation model with abundances similar to those in the Magellanic clouds. Such a spectrum is also observed in Minkowski's object, where van Breugel et al. (1985a) attribute this to be conclusive evidence for local material. The morphology of the radio jet in NGC 7385 also supports the case for local gas, as the jet deflection and western expansion of the lobe can be interpreted as a result of a collision with a region of enhanced density well outside the nucleus. In addition, to power the radio emission the jet would need to be travelling at over 1000 km s^{-1}, and so any gas that it carried out would display lines of width much higher than the velocities estimated from optical spectroscopy. The optical emission lines of [NII], [OIII], [SII], Hα and Hβ can be used as empirical diagnostics to separate H II regions from AGNs (Veilleux and Osterbrock, 1987). Simkin (2001) showed that the spectra for the emission lines within the cloud of NGC 7385 differ from those of both AGN and HII regions.

4C 26.42 (van Breugel et al., 1984) is a luminous X-ray source and is immersed in a relatively cool and dense gaseous halo. The radio source is expected to entrain and compress this gas, and subsequent cooling would produce the bright optical line emission observed around the source boundary. In contrast, 4C 29.30 (van Breugel et al., 1986) shows strong evidence for a previous capture of a gas rich disk galaxy. Various loops or partial shells are visible around the object and the central region exhibits a dust lane as well as a relatively blue secondary nucleus. van Breugel et al. (1986) conclude that the emission lines are probably produced by the interaction of the radio source with debris from the merging process. The extended optical emission in Minkowski's object is also attributed to a merging process, as it is suggested that it is composed of debris related to the apparent gravitational interaction occurring between NGC 541 and NGC 545/547. In addition, 3C 305 (Heckman et al., 1982) provides evidence for the merger of a massive early-type and a gas-rich late type galaxy, triggering the ejection of radio plasma into the interstellar medium thus ionising an extended optical emission line region.

NGC 7385 shows little indication of large scale X-ray gas, nor any evidence for a recent merger with another galactic system. There is a region of X-ray emission about 5 arcmin N of NGC 7385 (see chapter 3.3), as though NGC 7385 is moving in the diffuse outer parts of gas which lies somewhat closer to NGC 7386, and it is possible that this

emission arises from a group atmosphere. NGC 7385 is not a member of a rich galaxy cluster and appears to be a fairly normal elliptical galaxy (de Vaucouleurs, 1991). There is a dust lane surrounding the optical nucleus, as presented in Rawes et al. (2015) and Figure 4.30. However if the optical object was carried up from this dust lane, then we should expect to see such objects south of the nucleus as well, and this is not observed. Additionally, since the density in the dust lane would be high, the cloud may not survive as a coherent object. There is no clear explanation for the origin of this optical object, as is the case for 3C 277.3. The distortion of the radio ridge lines around the optical cloud strongly suggests that interaction between the jet and clouds may be responsible for the emission lines and the associated continuum. Hardee et al. (1980) suggest that this spatial coincidence does not rule out the possibility that the cloud is the chance superposition of a very large isolated extragalactic H II region on the outskirts of NGC 7385. However the extreme size ($\sim 7 \times 4$ kpc^2) of the optical object strongly argues against this interpretation.

4.4.3.3 Excitation of the optical cloud

Several processes could contribute to the ionisation of the line emitting gas. The most widely accepted mechanism for the ionisation and heating of emission line gas in active galaxies is photoionisation of the gas by continuum radiation from the nucleus. This and other mechanisms are listed and discussed below.

1. The gas in the northern lobe is unlikely to be photoionised by nonstellar radiation emitted by the nucleus. The close morphological connection between the radio source and the optical object implies that the gas is somehow excited by the radio source itself. The optical emission line luminosity in the cloud is approximately 4 x 10^{40} ergs s^{-1}, assuming a type-B recombination case and the nuclear optical luminosity is estimated as 5×10^{41} ergs s^{-1}. Therefore for photoionisation to be responsible the emission line gas must intercept more than 10% of the nuclear continuum and be 100% efficient at converting it into emission lines. This is unlikely unless the radiation were somehow beamed towards the optical cloud. For $2 < n_e <$100 cm^{-3} (Simkin et al., 1984) and a cloud at a distance of 10 kpc from the core, photoionisation models (Ferland and Netzer, 1983) would require a Lyman continuum luminosity of 10^{42} erg s^{-1} for an ionisation parameter with high enough energy to sustain the degree of ionisation seen in the jet gas. This is an order of magnitude in excess of the nuclear nonthermal luminosity.

2. The gas could be photoionised by the high-energy continuation of the radio synchrotron spectrum. The width of the Hβ line from the gas in the knot is consistent with this mechanism (Simkin et al., 1984). Extrapolating the observed radio flux to UV wavelengths, and assuming a power-law synchrotron mechanism with a constant spectral index however, gives an approximate UV continuum luminosity of 10^{34} erg s^{-1}. Photoionisation is therefore unlikely since there are not enough Lyman photons to produce the observed emission line luminosity of approximately 4 x 10^{40} erg s^{-1}.
3. The optical cloud could be entrained in the jet boundary layers, subsequently forming hot massive stars and photoionising the adjacent comoving gas. This mechanism would be supported by the presence of Balmer absorption lines in an emission line spectrum, however these were not reported for NGC 7385. The strong blue continuum however, implies a significant population of young hot stars, and the relatively high [OI]/[OII] ratio measured by Simkin et al. (1984) also supports this.
4. Collisional ionisation of the gas by particles in the low energy tail of the distribution of the relativistic synchrotron emitting particles in the counter jet is a possibility in NGC 7385. Following the analysis of Ferland and Mushotzky (1984), it is possible to model the contribution to the ionisation of the gas due to cosmic rays, as well as by a power law continuum. Their plot of Hβ flux against cosmic ray density $N^*\beta$, predicts a density of $N^*\beta$ = $10^{-5.5}$ cm^{-3} for the observed Hβ flux, when ionising radiation from both the nucleus and relativistic synchrotron particles is considered. The main effect of adding cosmic rays is to increase the total luminosity of the emission lines by adding more heat and ionisation, thus creating lines with a wider range of excitation energies. There is no evidence for this in the emission line spectrum of Simkin et al. (1984).
5. The passing of a radio jet drives shock waves within the medium through which it propagates (e.g. Hartigan et al 1987). As a result, gas passing through the shock front is heated and accelerated, and its kinematics will be perturbed. Line emission is observed when the shocked gas cools to a few $\times$ 10^4 K and the [OIII] line luminosity is dominated by emission between 2-3 $\times$ 10^4 K. The broad component of line emission can therefore reveal gas which has been passed through the shock front. Radiation is emitted as the gas cools and this radiation then photoionises the gas cloud. Simkin et al. (1984) did not recover the ratios expected for a shocked medium with a low velocity (60-90 km s^{-1}). This model requires a power law synchrotron continuum, and the width of the Hβ line is consistent with photoionisation by a source with a spectral

index similar to that observed by Simkin et al. (1984). A radio knot embedded in the diffuse northern lobe may be evidence for a shock which has heated and expanded the jet fluid, arising as a result of the interaction of the jet and cloud. This knot is evident in the radio contours in Figure 4.9. This shock could also be due to effects internal to the jet and lobe, or reconfinement of a jet as it responds to changing external pressure.

An optical-radio jet interaction is reported for the low redshift galaxy PKS 2152-699 (Fosbury et al., 1998). Here the continuum emission is reported to be red where the optical object overlaps with the radio emission, implying that the emission in that region is synchrotron radiation from the radio jet (Worrall and Birkinshaw, 2014). A large, adjacent region does appear to be the same sort of thing as in NGC 7385, but with much larger line widths (Smith et al 2017; submitted). In NGC 7385, the continuum is observed to be blue throughout the interacting region. This blue continuum, observed by Simkin et al. (1984) and also shown by our three colour composite HST image (Figure 4.29) suggests that the cloud contains a population of young stars. Although Simkin et al. (1984) conclude that their results are mostly consistent with photoionisation by a power-law continuum, their observations do not rule out the possibility of photoionisation by a population of early-type stars. Jet induced star formation is proposed as the ionisation mechanism in Minkowski's object and it was suggested by van Breugel et al. (1985a) that star formation may only occur in jets with low power, where the momentum carried by the jet is not sufficient to completely disrupt the optical cloud. A similar photoionisation mechanism however, was proposed for the high power radio galaxy 3C 285 (van Breugel and Dey, 1993), supporting the process proposed by De Young (1981) in which the lobes of powerful FRII type galaxies can trigger star formation.

It is possible to estimate the number of stars required to photoionise the optical cloud. The flux of the Hβ line measured by Simkin et al. (1984) gives a total Hβ luminosity of $L_\beta = 9 \times 10^{37}$ erg s^{-1} and a corresponding Hα luminosity of $L_\alpha = 2.5 \times 10^{38}$ erg s^{-1}. Assuming that the gas is optically thin in the Balmer lines and collisional ionisation is negligible, this requires the production of 4×10^{50} photons per second by hot stars. Referring to Table 2.3 in Osterbrock (1974), it is found that about 6×10^3 $B_{0.5}$ type stars are necessary to produce this many photons. An estimate of the total mass can be calculated using the initial mass function given by Kroupa (2001) as

$$\xi(m) \propto m^{-\alpha} \tag{4.5}$$

$$\alpha = \begin{cases} 0.3, & m < 0.08 \\ 1.3 & 0.08 < m < 0.5 \\ 2.3 & m > 0.5 \end{cases}$$

Integrating over the mass function to find the total stellar mass required to excite the gas, gives approximately 7×10^5 $M_\odot$. This is within the gas mass range calculated by Simkin et al. (1984) and in agreement with the mass calculated from the emission measure of the cloud. If photoionisation by stars is the mechanism for exciting the emission line gas however, traces of supernova explosions should be detectable at radio wavelengths and in infrared images as point-like objects . Using the radio luminosity expression for supernova remnants given by van der Laan (1962) at 1.5 GHz this gives a flux density of 50 mJy. In addition, the spectral index from supernova remnants is represented by a power-law, reflecting the synchrotron radiation from the supernova remnant shell, and for strong shocks α is approximately 0.5 (Bell, 1978). In the case of shocks with a low mach number, steeper spectra ($\alpha > 0.5$) are expected. It is therefore unlikely, although not impossible, that the gas has been photoionised by a population of young stars.

Simkin (2001) highlight that the optical line ratios within NGC 7385 cannot be reproduced by shock or radiation dominated models, and suggest that the line ratios may be an optical diagnostic for the narrow interface between the plasma in the radio jet and the external gas. Two possibilities are presented to reproduced the observed line ratios: firstly, a mixture of shocks and secondary UV ionisation, with mixing at the interface between the jet and the gas. Secondly, an electron/positron pair plasma with a component of low-energy particles not present in electron/proton jets. If these low-energy particles mix with the optical gas at the interface, they may excite the gas with an input energy spectrum different to those derived from either radiative or shock excitation. In this case however, X-ray emission lines may be expected.

4.4.3.4 Jet deflection

It is possible to evalulate whether the mass of the optical cloud, M_c is sufficient to deflect the radio counter-jet component with mass M_j, using the following equation:

$$M_c \sim \frac{\dot{M}_j V_j t_c}{V_c} \tag{4.6}$$

If the jet thrust ($\sim \dot{M}_j V_j$) is assumed to be equal to the integral of the ram pressure

over the counter-jet (assuming minimum energy and a jet diameter of about 10 kpc), then $\dot{M}_j V_j \sim 4 \times 10^{25}$ N. If this cloud has been accelerated by the jet, then it can have moved no further than its projected distance from the nucleus ($\sim$ 11 kpc). This gives the condition that $t_c \leq 7 \times 10^7$ yr, assuming the speed of the optical cloud with respect to the surrounding galaxy to be 230 km s^{-1} (Simkin et al., 1984). This in turn constrains M_c: $M_c \leq 5 \times 10^6$ $M_\odot$, for moderate projection effects. Since this falls within the range obtained by Simkin et al. (1984) using spectroscopic line widths, it lends support to the conclusion that the radio counter-jet component can be deflected by the cloud.

A more sophisticated analysis of bent jets involves theories of oblique internal shocks. A model for a jet-cloud ricochet interaction, incorporating hydrodynamical simulations uses a strong shock with adjacent oblique shocks developing at the cloud collision site. Shocked jet material at the side of the cloud may heat and accelerate the cloud while on the other side it may escape at a certain angle relative to the incident jet (e.g. Canto and Raga, 1996). The speed of such shocks can't be too high to avoid overheating of the gas cloud. A full numerical simulation is needed to test this for our particular case.

4.4.4 The possible jet-cloud interaction scenarios

I propose 3 distinct scenarios to explain the radio and optical observations of the jet-cloud region in NGC 7385. Firstly, the cloud is in front of the radio jet and there is no interaction between the two. Secondly, the jet glances off the cloud, deflecting the path of the jet and leaving the optical cloud intact. Thirdly, the jet collides with the cloud and gas from the cloud is mixed into the downstream radio plasma. An illustration of the jet path for each case is given in Figures 4.34, 4.35 and 4.37. I test the scenarios by requiring them to explain: the deflection of the radio jet, the morphology of the optical gas cloud, the lack of X-ray emitting gas, the high rotation measure, the disordered magnetic field configuration, the observed fractional polarisation and the ionised optical emission in that region.

4.4.4.1 Scenario 1 : no interaction

Figure 4.34 shows a jet which propagates behind the optical gas cloud. There is no interaction between the two, and the RM results purely from the cloud being a foreground Faraday screen along the line of sight between the jet and the observer. In this case, the optical cloud must be photoionised by non-stellar radiation from the nucleus, explaining

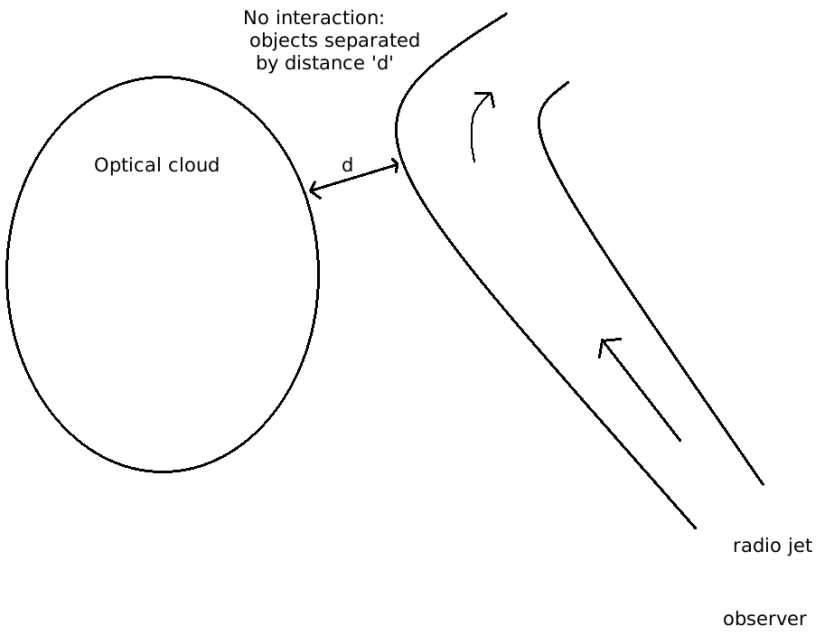

Figure 4.34: Scenario 1 for the jet-cloud interaction: the cloud is separated from the jet by distance d, and there is no interaction.

the lack of X-ray emission. A significant number of the parameters listed above however, cannot be explained via this mechanism. The morphology of the radio jet strongly suggests the path of the plasma is being deflected by an interaction with the external medium. The position of the optical cloud at the location of the jet bend is too much of a coincidence to be ignored. In addition, the magnetic field structure of a radio jet propagating freely through the ISM would be more coherent, possibly with the spine-sheath structure observed in the lobes of other low-power radio galaxies. Instead, there is clear evidence for the magnetic field vectors tracking the bending of the jet.

It is therefore unlikely, although not impossible, that there is no jet-cloud interaction.

4.4.4.2 Scenario 2: a glancing blow

In this scenario, the jet propagates through the ISM and encounters the optical cloud. There is an edge-on collision, which causes the jet to deflect towards the NW. This is illustrated in Figure 4.35. Gas within the optical cloud is ionised as a result of the collision, possibility as a result of shock compression passing across the gas. It is not known from optical spectroscopic studies (Simkin et al., 1984) how much of the cloud is ionised by the presence of the jet, thus neutral and molecular gas studies would be useful in that region.

As the optical gas is sheared along the boundaries of the radio source, Kelvin Helmholtz

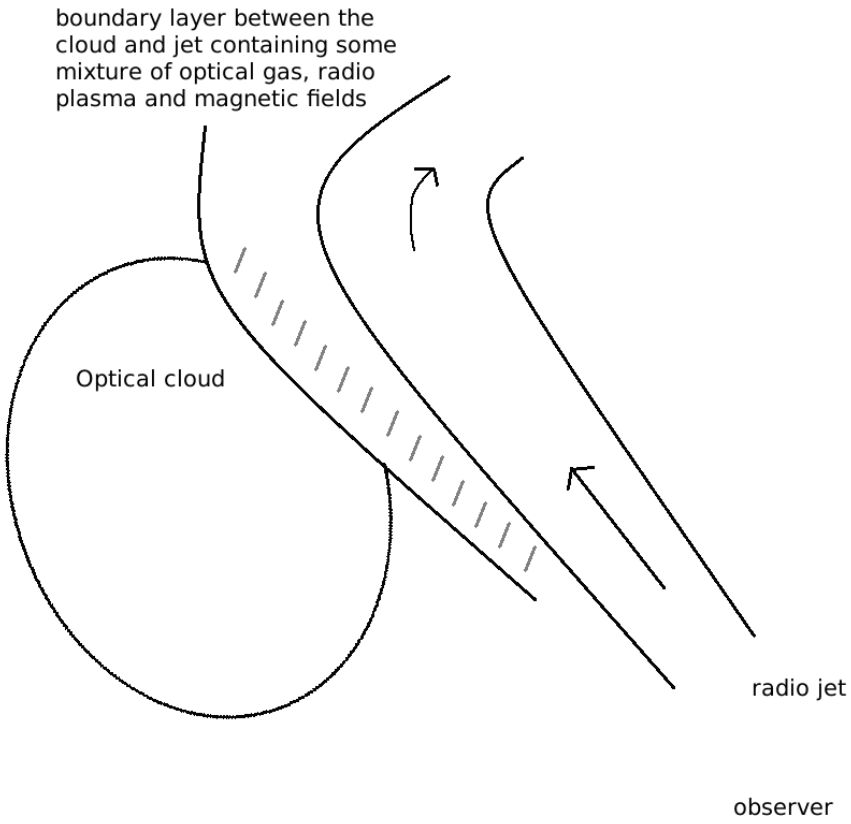

Figure 4.35: Scenario 2 for the jet-cloud interaction: the jet glances off the cloud, and there may be some entrainment of the optical gas into a boundary layer between the two media.

instabilities can form. These instabilities can result in the entrainment of clumps of gas into the outer layers of the radio source, creating a mixing layer between the cloud and the lobe consisting of both relativistic and thermal plasma. An observational signature of entrainment of the gas is the detection of beam depolarisation. Although the fractional polarisation in this region is not low, it is lower than expected for the edges of a radio lobe where $P \approx 0.4$ is often observed due to shearing against the external medium (Bridle and Perley, 1984). The high rotation measure can then be produced by either:

1. Rotation by the foreground optical cloud (no entrainment).

2. Rotation by an irregular Faraday screen in the boundary layers of the radio component (i.e. the cloud is being entrained).

A key indicator for whether the optical gas is entrained or whether it acts purely as a foreground screen is how the polarisation position angle ϕ changes with λ^2. If the gas were mixed in with the radio source, we would expect to see a disruption in the linear ϕ / λ^2 relationship. Unfortunately, the data are inadequate to test this relation at high resolution. Strong depolarisation of the radio emission between frequencies is detected in almost all other sources with an optical/radio jet interaction. There is evidence for depolarisation in NGC 7385; however the small frequency range at matched angular resolution between the spectral windows means that it is difficult to draw any conclusions from the depolarisation map due to large errors.

Pressure equilibrium between the ionised gas and the radio emitting plasma can also indicate entrainment of the optical gas. Comparable pressures in the radio emission and the ionised gas would suggest that the region of high ionisation has been compressed by the interaction with the radio plasma. The pressure in the northern lobe was calculated from minimum energy arguments, using values of the flux obtained at different frequencies from the VLA observations. Assuming a synchrotron emitting plasma, the equipartition magnetic field strength and energy density were calculated using the code of Hardcastle et al. (1998). These values are given in Table 4.5 and agree with the results of Robertson (1981) for the energy density in NGC 7385, and are typical of other head tail sources (Jaffe, 1977). These values give a pressure of $P = 1.6 \times 10^5$ K cm^{-3} in the radio lobe. Assuming pressure equilibrium with a gas with temperature 10^4 K, this gives an electron density $n_e = 16$ cm^{-3}, in agreement with the range 2-100 cm^{-3} calculated by Simkin et al. (1984) from the optical line emission ratios and consistent with the electron

density calculated from emission measure arguments. Thus it is reasonable to assume that the cloud and the radio counter-jet component are in pressure equilibrium. The pressure in the component is comparable to that found in the radio emission near Minkowski's object, and the electron density is of the same order as the optical line emitting region in 4C 26.42.

It is possible to use this value for n_e in the equation relating the RM to the line of sight magnetic field, $B_{//}$:

$$RM = 812 \int n_e B_{//} dl \tag{4.7}$$

where the rotation measure is measured in rad m^{-2}, n_e is the electron density in cm^{-3}, $B_{//}$ is the line of sight magnetic field in mG, and dl is the path length, in parsec. An RM of 270 rad m^{-2} as indicated by the Faraday dispersion distribution and RM maps gives $B_{//}$ = 6.6 nG. This is orders of magnitude smaller than what one might expect, even if the magnetic field were undergoing field reversals.

This suggests that the Faraday screen is not created purely by the emission line gas, or that the ionised and magnetised material are not evenly distributed throughout the cloud. If the ionised material along the line of sight contains clumps of n_e threaded by the same $B_{//}$, then a filling factor δ must be included on the right hand side of equation 4.8. As noted previously, this filling factor has been constrained by Simkin et al. (1984) to be between 10^{-1} and 10^{-5}. A value of δ of less than 10^{-2} would increase $B_{//}$ to a more typical value for such clouds.

Alternatively, the magnetic field could be concentrated in a narrow layer in the gas, and not throughout. This layer would need to be much narrower than the size of the cloud to give the low average magnetic field estimate above, and could lie at the interface of the radio/optical interaction. A narrow magnetosheath near the jet could act as a mixing layer into which magnetic field field from the radio jet leaks and the optical cloud is entrained. If there were no field reversals, and assuming a 1 nT field, the layer would be 1% of the diameter of the cloud. Lyutikov (2006) discusses 'magnetic draping'; the formation of a thin, magnetised boundary layer between two media, and finds that the magnetic field should be directed along the contact point separating the fluids. This interpretation for NGC 7385 is therefore supported by Figure 4.26 and highlighted in Figure 4.36, which shows the polarisation position angle as a function of distance through a region transverse to the jet direction where the optical cloud and radio plasma are throughout to overlap. The change in fractional polarisation is also shown. The polarisation vectors start to

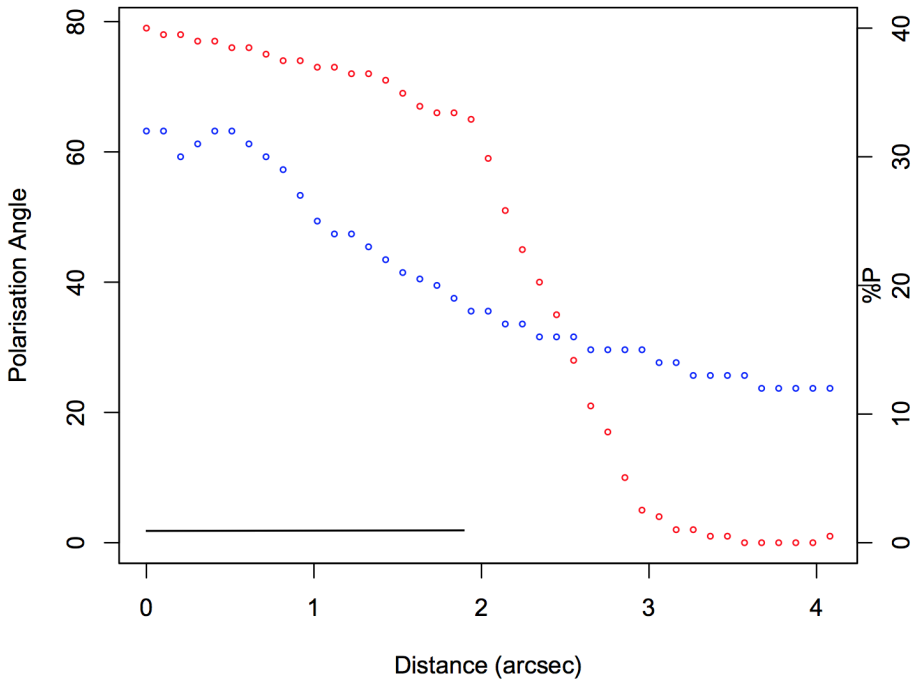

Figure 4.36: The change in polarisation position angle (red) with distance for a slice taken transverse to the direction of the counter-jet in the region of the optical cloud at 1.51 GHz from Figure 4.13. The fractional polarisation is also shown in blue. The black line indicates the extent of the optical cloud.

change direction about 2″ inside the radio counter-lobe, where the cloud culminates. The fractional polarisation decreases from $\sim$ 30% at the edge of counter-jet to $\sim$ 17% within the region containing the cloud. Beyond this point, the level of fractional polarisation remains approximately constant.

Irregularities in the intercloud medium could also decrease the observed $B_{//}$, and a plausible origin for these irregularities would be turbulence associated by the entrainment of ambient gas by the radio source. This turbulence would have to be small however, to avoid the RM vanishing along the line of sight.

The lack of X-ray emission in the cloud region means that the gas cannot be excited to energies high enough to produce X-ray radiation, or that the volume of the excited gas is small. For the jet-cloud interaction in PKS 2250-41 (Villar-Martin et al., 1999), line widths of up to 900 km s^{-1} within the cloud are measured. This is significantly higher than the gas velocities measured by Simkin et al. (1984). Villar-Martin et al. (1999) find that shock acceleration alone cannot explain the large line widths in PKS 2250-41, and that some form of entrainment must be acting. They suggest entrainment in the hot wind detected behind the shock; instabilities arise at the interface between the shocked gas

and the slower moving cloud, leading to entrainment and acceleration (e.g. Klein et al., 1994). They also propose that entrainment of the cloud in the boundary layers of the jet and the ISM could produce large line widths and accelerate the clouds to a significant fraction of the jet speed. For NGC 7385, the low velocity (60-90 km s^{-1}) in the cloud suggests that the acceleration of the gas could be caused purely by the passing of a shock front. Entrainment of the optical cloud into the boundary layers of the jet would produce significantly higher velocities than those observed.

This interpretation of the jet-cloud interaction for NGC 7385 is successful in explaining radio and optical morphologies, the polarisation observations, and the rotation measure structure. The magnetic field strength determined from the RM strongly indicates that the Faraday screen is not created purely by the emission line gas, thus the gas may be entrained into the boundary layer of the radio lobe to some extent. This boundary layer could consist of a mix of optical gas, magnetic fields and both relativistic and thermal plasma.

4.4.4.3 Scenario 3: mixing of the optical cloud and the radio jet

The third scenario which could explain the observed jet-cloud morphology involves a collision in which the optical cloud is disrupted by the radio jet and the gas mixes in with the radio plasma. The jet then deflects and turns through 180°. An illustration of this is shown in Figure 4.37. In a similar way to scenario 2, the gas is ionised by shock and collisional excitation, but on a larger scale.

For the radio jet to turn through 180° implies a significant interaction with an obstacle in its path. This lends support to a picture in which the radio jet fully interacts with the optical gas, to the extent that the path of the jet is completely disrupted. The optical gas however, does not show evidence for being swept along by the radio jet or broken up as a result of a collision. The polarisation of the radio jet can be described in terms of turbulence within the magnetic field due to mixing of the optical gas, providing a low fractional polarisation in that region.

In this interpretation, the rotation measure structure can be explained as due to rotation by ionised gas, which was entrained by the jet and deposited in the northern lobe. A signature of mixing of the cloud with the radio plasma can be found by investigating the Faraday depth of the rotating screen. The Faraday dispersion function shown in Figure 4.24 shows a peak at approximately 210 rad m^{-2}. If the peak at -70 rad m^{-2} is assumed to be a sidelobe, which is a reasonable assumption to make since there are adjacent

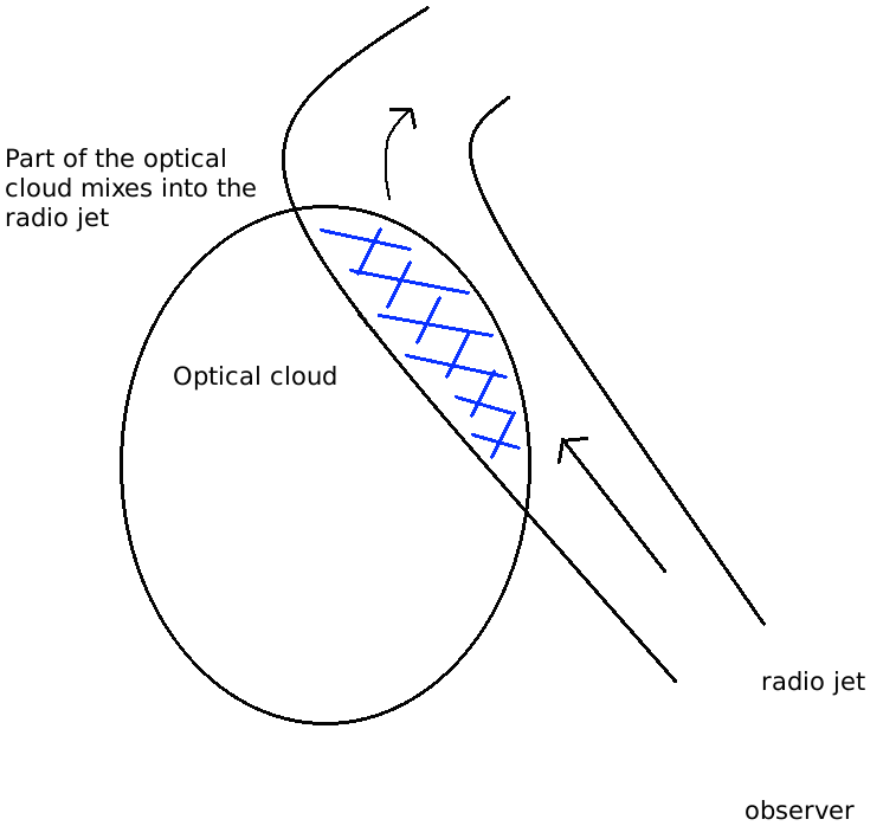

Figure 4.37: Scenario 3 for the jet-cloud interaction: the jet collides with the optical cloud and gas mixes in with the radio plasma

peaks either side of the main feature, then the presence of the optical cloud has shifted the RM by ≈ 270 rad m^{-2}. Whether or not the optical cloud is mixed in with the radio plasma is dependent on whether the feature can be viewed as 'Faraday thick'. For a Faraday thick medium, the plane of polarisation at the back of the structure is rotated more than that at the front, so in Figure 4.24 we should see a constant level of signal to be distributed over a wide range of Faraday depth (Burn 1966). The resolution in Faraday depth space $\Delta\phi$ for the S band data is 238 rad m^{-2}, thus it should be possible to resolve a Faraday thick structure in ϕ space. There is no evidence for such a structure from Figure 4.24. If the peak at -70 rad m^{-2} is not taken to be a sidelobe, then this indicates that there is polarised emission with two distinct rotation measures along the line of sight.

Additionally, if the degree of polarisation decreases with λ^2 for the NGC 7385 observations then this depolarisation could be explained by mixing of the emitting and rotating media, as well as by the finite spatial resolution of the observations. Unfortunately as mentioned above, it was difficult to draw any firm conclusions from depolarisation maps due to large errors.

Although a strong interaction is implied by the extreme jet bend in NGC 7385, there is insufficient evidence to suggest that the optical gas is mixed in with the radio plasma. For a light jet, entrainment of gas would cause rapid slowing of jet motion making it easier for the jet to be bent by external influences. I find the most likely interpretation to be scenario 2, where the jet deflects off the cloud and although there is no mixing of the gas and the radio plasma in the radio lobe, a small mixing layer between the two media can explain the rotation measure and estimated magnetic field strength. A narrow magnetosheath near the jet could produce the rotation measure, consisting of a combination of both relativistic and thermal plasma. Leakage of the magnetic field from the radio plasma can help explain the low magnetic field estimate found for the optical cloud. In addition, Simkin (2001) suggest that the optical line ratios detected by Simkin et al. (1984) may be consistent with a model in which mixing at the interface between the radio jet and the gas cloud causes a mixture of shocks and secondary UV ionisation capable of exciting the cloud.

In the following section I will outline some future observations which could help to distinguish between these scenarios further.

4.4.5 Future work

High spatial resolution studies of the optical line emission within the cloud would help to distinguish between the three scenarios described above. Disturbed kinematics and

high velocity motions (e.g. Axon et al 1998) revealed by emission line profiles provide evidence for interactions between radio emitting plasma and emission line gas. From these observations, it will be possible to determine how much of the optical cloud has been ionised due to interaction with the radio jet, and how much is ambient gas. If gas ionised by the jet is found to be spatially extended, then this will infer whether it is being entrained by the jet boundary layer. A relatively compact region however, would suggest that the cloud is being ionised purely by a shock front.

3C 171 (Clark et al., 1998), PKS 1932-46 (Villar-Martin et al., 1998) and PKS 2250-41 (Villar-Martin et al., 1999) are jet-cloud interaction candidates that have been studied in depth using optical spectroscopy. All sources show similar kinematic/ionisation properties despite a wide range in the emission line morphologies of the individual sources. In addition, (Sutherland et al., 1993) provided a theoretical framework for understanding the emission line spectra produced by clouds. New observations of NGC 7385 could therefore provide valuable information on whether jet-cloud interactions have constant effects on the physics and kinematic properties of the emission line gas and in understanding the role played by interactions between the radio and optical emitting structures in active galaxies.

Further radio observations of NGC 7385 would also help to constrain the jet dynamics and the magnetic field configuration within the bends. LOFAR would be able to provide excellent RM spectra, and next generation instruments such as the SKA will provide high resolution observations of nearby galaxies, enabling the investigation of these properties with unprecedented sensitivity. The capability and science goals of these telescopes are discussed further in chapters 6 and 7.

4.5 Summary

NGC 7385 is a highly unusual radio source due to the presence of a jet that appears to bend through 180°. Other jet-cloud interactions have been observed, but none have produced such a dramatic deflection and disruption of the jet path. Further studies of the optical line emission and radio polarisation are needed to constrain the kinematic properties of the cloud and the dynamics of the jet. In the next chapter, I shall provide an in-depth study of another radio galaxy which displays a jet bend $> 180°$. This source will provide further insight into the environmental conditions capable of producing such unusual jet morphologies.

Chapter 5

Multi-frequency Observations of the Radio Galaxy NGC 6109

In this chapter I present multi-frequency observations of the radio galaxy NGC 6109, with archival VLA and recent JVLA observations. I also use optical data from *Spitzer*, KPNT and CFHT in conjunction with *Chandra* X-ray observations, taken as part of a survey to look at the X-ray activity of low redshift 3CRR galaxies. The radio emission associated with NGC 6109 is seen to extend for over 250 kpc into the ICM and at high resolution a bright swirl region SE of the core is observed. This component marks where the SE jet undergoes a dramatic ($> 180°$) rotation, as a possible consequence of jet precession or an interaction with the external environment. Such extreme jet deflection is rare, and I present polarisation and rotation measure distributions in order to probe the physical mechanisms responsible for the observed morphology.

5.1 Introduction

How radio jets interact with their environment has been investigated increasingly vigorously over the last few decades. The intergalactic medium can modify the structure of a radio source via ram-pressure or confinement. Such effects can cause bends and deflections in the jets and tails of radio galaxies, producing dramatic and unusual structures spanning hundreds of kpc across the sky. In turn, the radio sources can heat and move the IGM.

Although gas motions are the most popular explanation, jet bends have also been attributed to helical jet trajectories (Conway and Murphy, 1993). A number of these

have been identified with VLBI observations (e.g. 1156+295, Hong et al., 2004; 3C 345, Steffen et al., 1995), but few have been reported on kpc scales. Helical signatures include the projected spatial structure, the kinematics of the jet and for sinusoidal trajectories, the variability of the object. Jets with a density much greater than that of the external medium propagate almost without resistance through the interstellar medium and are not deflected from a straight path. 'Light' jets however, can display sinusoidal trajectories of individual knots (e.g. NGC 315, Worrall et al., 2007) bent by interaction with the external medium. Theoretical models for such oscillating, bent structures include helical modes in hydrodynamic jets (Hardee, 1987; Birkinshaw, 1991) or in magnetised jets (Königl and Choudhuri, 1985). The collision of a jet with a dense or magnetised medium is capable of producing strong jet deflections, as seen in chapter 4 for NGC 7385.

Bends and wiggles in jets on a parsec scale are often attributed to jet precession (e.g. Gower et al., 1982; Linfield, 1981). Precession in general describes a change in the direction of the instantaneous spin axis. Jet precession models are two sided and involve an emerging jet and counter-jet precessing equally and at the same time in the rest frame of the core. Precession parameters which vary due to changes in the angular momentum of the system at the jet launching point (e.g. due to a change in the fuelling process) are described as precession and are distinctly different from Scheuers Dentist's Drill phenomenon (Scheuer, 1982). The Dentists Drill mechanism is the distortion of a jet on one side due to local conditions (e.g., buoyancy effects). This phenomenon therefore does not produce a symmetric pattern for the jet and counter-jet.

The sustained periodic precession exhibited by jet axis of the Galactic micro quasar SS 433 has been studied in depth (e.g. Bell et al., 2011; Marshall et al., 2014). A geometric model describing this, and other similar objects, is described by Hjellming and Johnston (1981). In this model, symmetric jets are launched at speed β along an axis which traces a cone throughout a precession period P, of opening angle ϕ inclined to our line of sight at angle i, in terms of a precession phase ψ. The jet material, once launched, is assumed to move ballistically, thus undergoing no acceleration or deceleration.

VLBA images of Mkn 501 (Conway and Wrobel, 1995) showed a misalignment of the jet close to the core and this was inferred as the projection of a helical pattern, possibly generated by Kelvin-Helmholtz instabilities driven at the origin through orbital motion of the central engine in a binary black hole system. This link between jet helical distortion and binary systems has been investigated further (e.g. Villata and Ferrari, 1995; Hardee, 2000; Tateyama et al., 1998) and helical paths in the radio structure of other objects have

been confirmed (e.g. blazar OJ 287, Vicente et al., 1996; 3C 345, Zensus et al., 1995; M 87, Reid et al., 1989, 3C 120, Walker et al., 2001).

The mechanisms invoked to cause jet precession all require a misalignment between the accretion disk and a black hole. Some of the most common explanations for jet precession include gas flow onto the accretion disk (e.g Scheuer and Feiler, 1996), a binary black hole system (e.g. 4C 73.18, Roos et al., 1993; Cygnus A, Canalizo et al., 2003; OJ 287, Lehto and Valtonen, 1996) and an offset in the angular momentum in the disk and of the gas in the host galaxy. Helical jets could also result due to fluid-dynamical instabilities in the interface between the jet material and the surrounding medium (Hardee, 1987).

NGC 6109 is an FR I-type head-tail radio galaxy located in a poor cluster with redshift z = 0.029 (Wegner et al., 1999). It was mapped with the WSRT and the extended radio structure was reported by Ekers (1978). The radio tail extends for 250 kpc to the NW and a leading component was observed SE of the core, in alignment with the main jet axis. New JVLA observations have revealed a counter-jet component with a highly unusual doughnut-like structure. Such a morphology has not been observed for any other low power radio galaxies, thus the focus of this chapter is to discuss what mechanisms or environmental factors could produce this unique structure.

Throughout this section I adopt the cosmological parameters H_0= 70 kms^{-1} Mpc^{-1}, $\Omega_{\Lambda 0}$ = 0.7, Ω_{m0} = 0.3. The redshift of NGC 6109 corresponds to a luminosity distance of 123 Mpc and a projected linear scale of 0.59 kpc arcsec^{-1}.

5.2 Observations and Analysis

5.2.1 Radio observations: calibration and data reduction

NGC 6109 has been observed with the VLA for 7 different science projects since 1985. I initially used data from the NRAO archive to map the intensity distribution and polarisation structure of its radio features. The unusual jet morphology discerned from these maps prompted a proposal to the VLA to request further observations with the upgraded JVLA telescope. The enhanced capabilities of this telescope would allow me to probe the polarised emission of this source with higher sensitivity and to investigate the RM structure. Details of this proposal which also included NGC 7385, are given in chapter 4.

5.2.1.1 Archival data

The NRAO archive contains nearly all VLA data since observing started in 1976, and all contents are available through the Archive Access Tool (AAT). I selected datasets which had observed NGC 6109 for more than 500 s, had used more than 26 antennas, and had all four correlations available. Table 5.1 gives details of the VLA observations I calibrated and imaged from the archive. The data reduction and imaging was carried out as described in chapter 2 and section 4.2.1.1. Although I processed all these data, not all measurement sets had sufficient quality to produce useful radio maps.

The BT 7 projects at 1.67 GHz (44 arcsec resolution) and 4.98 GHz (14 arcsec resolution) were used to map the extended structure of the radio emission associated with NGC 6109 and these are displayed in Figures 5.1 and 5.2 respectively. The small scale structure of NGC 6109 was mapped with the BT 7 project at 1 arcsec resolution at 4.98 GHz, and the AH 766 project at 0.4 arcsec resolution at 4.86 GHz. The latter project was also used to investigate the polarised intensity. Total intensity images at 4.98 GHz and 4.86 GHz are shown in Figures 5.3 and 5.4 respectively.

The final deconvolved Stokes I, Q and U images at each frequency had rms noise levels within a factor of 2 of the expected limiting noise level estimated from the noise temperature of the VLA receivers. The Stokes Q and U images generally had lower rms noise levels than the Stokes I images, because of the smaller dynamic range. Stokes V images were checked to ensure that they showed no structure; any visible structure could indicate an error in the calibration tables, or unflagged RFI. A fractional polarisation map is given in Figure 5.5, at 4.86 GHz, produced by combining the Stokes I, Q and U images in the form

$$P = \sqrt{\frac{Q^2 + U^2}{I^2}} \tag{5.1}$$

The apparent magnetic field direction can be determined by rotating the polarisation position angle by 90° and these vectors are shown alongside the fractional polarisation in Figure 5.5. The rotation measure structure cannot be determined from these data due to inadequate frequency coverage with insufficient signal to noise at matched angular resolutions; thus the vectors are uncorrected for Faraday rotation effects.

Table 5.2 lists some fundamental parameters and measured quantities for the radio galaxy NGC 6109 from the AH 766 (4.86 GHz), and BT 7 (1.67, 4.98 GHz) observations.

Project code	Configuration	Date	Frequency (GHz)	Bandwidth (MHz)	Time (s)	Resolution (arcsec)	Flux calibrator
AF 0106	B	85-May	1.41-1.64	50	2320	3.9	3C 286
AW 112	C	84-Jun	4.83-4.89	50	1020	3.9	3C 48, 3C 286
BT 18	B	95-Oct	4.99	50	940	1.2	3C 48
AH 766	A	02-Apr	4.84-4.89	50	8160	0.4	3C 48, 3C 286
BT 0007	D	93-Oct	1.67-4.98	50	11220	44/14	3C 286
BT 0012	CD	95-Jan	4.99	50	3920	1.2	3C 48, 3C 286

Table 5.1: VLA observations used to calibrate and produce images of NGC 6109 from the NRAO data archive.

5.2.1.2 Radio Morphology

The large-scale radio emission associated with NGC 6109 is displayed in Figure 5.1 and shows a tail extending to the NW for a projected distance of 250 kpc. On large scales this head-tail structure looks similar to NGC 7385 except that there is no bifurcation of the tail visible in the data. A discrete background source at RA= 16h 17m 20s, Dec= 35d 09′ is superimposed on the tail itself, and a weaker background source lies at the end of the tail. A radio source associated with NGC 6107 is visible SW of the core at RA = 16h 17m 20s, Dec = 34d 54′. Emission along the tail remains bright for about 50 kpc, beyond which it rapidly drops off. The emission remains largely collimated to the N out to 100 kpc, and beyond this point the tail bends to the W and then again to the N. The total flux density for this source is 1.9 Jy at 1.67 GHz.

The radio emission at 14 arcsec resolution in C band is shown in Figure 5.2. Multiple bright emission regions are seen along the NW jet, as highlighted by the surface brightness distribution in Figure 5.6. The first and second bright regions are separated by a projected distance of approximately 61 kpc, and the second and third by 42 kpc.

It was noted by Ekers (1978) that there may be a small component SE of the core of NGC 6109. A high resolution map was not published until 1985 in a sample of 57 high resolution VLA maps looking at narrow angle tailed sources (O'Dea and Owen, 1985). The map showed a circular component SE of the core, with no obvious counter-jet. O'Dea and Owen (1985) suggested that this structure might be produced if the beams were ejected parallel and antiparallel to the direction of motion of the galaxy, in a similar way to NGC 7385 (Schilizzi and Ekers, 1975). They proposed that the counter-jet beam ejected into the direction of motion would interact with the ICM in a manner more typical of double radio sources and might form the observed edge-brightened lobe.

A high resolution image of NGC 6109 is shown in Figure 5.4. A bright core is visible at RA = 16h 17m 20s, Dec = 34d 54′. NW of the core the jet is collimated along the tail. The jet remains bright for 3 kpc before fading and emission extends out to approximately 30 kpc. SE of the core no counter-jet is visible but radio emission is seen 5 kpc from the bright core. This radio component has a swirl-like structure and appears to be brightest along the SE edge. In Figure 5.3, a faint counter-jet is visible extending towards the SE although the emission is too faint to extract a flux density. The NW jet remains bright for 3.5″ before rapidly fading. Extended emission is seen to the NW for 20″ at which point the radio emission is too faint to distinguish from the background noise. The SE component does not show the same swirl-like structure as seen in Figure 5.4, and looks

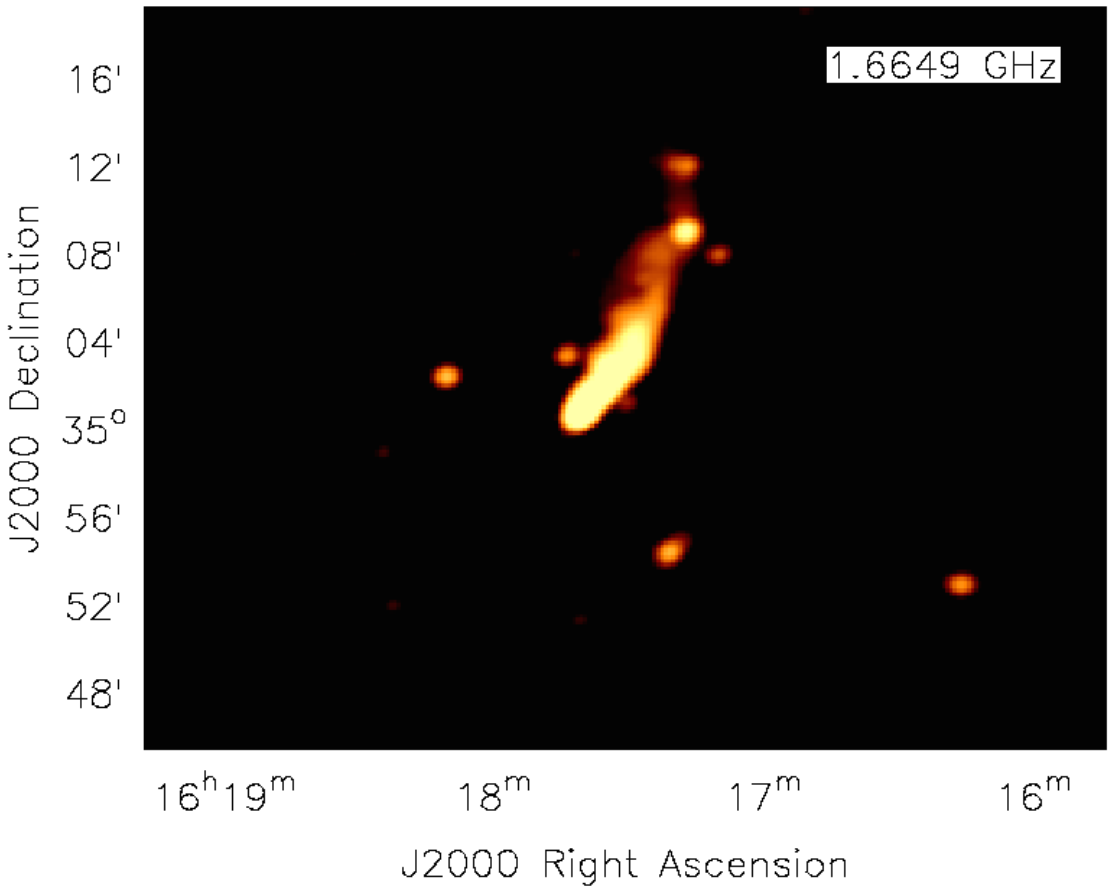

Figure 5.1: Extended radio emission from NGC 6109 at 44 arcsec resolution at 1.67 GHz from BT 7 archival data. A discrete background source at RA= 16h 17m 20s, Dec= 35d 09′ is superimposed on the tail itself, and a weaker background source lies at the end of the tail. A radio source associated with NGC 6107 is visible SW of the core at RA = 16h 17m 20s, Dec = 34d 54′.

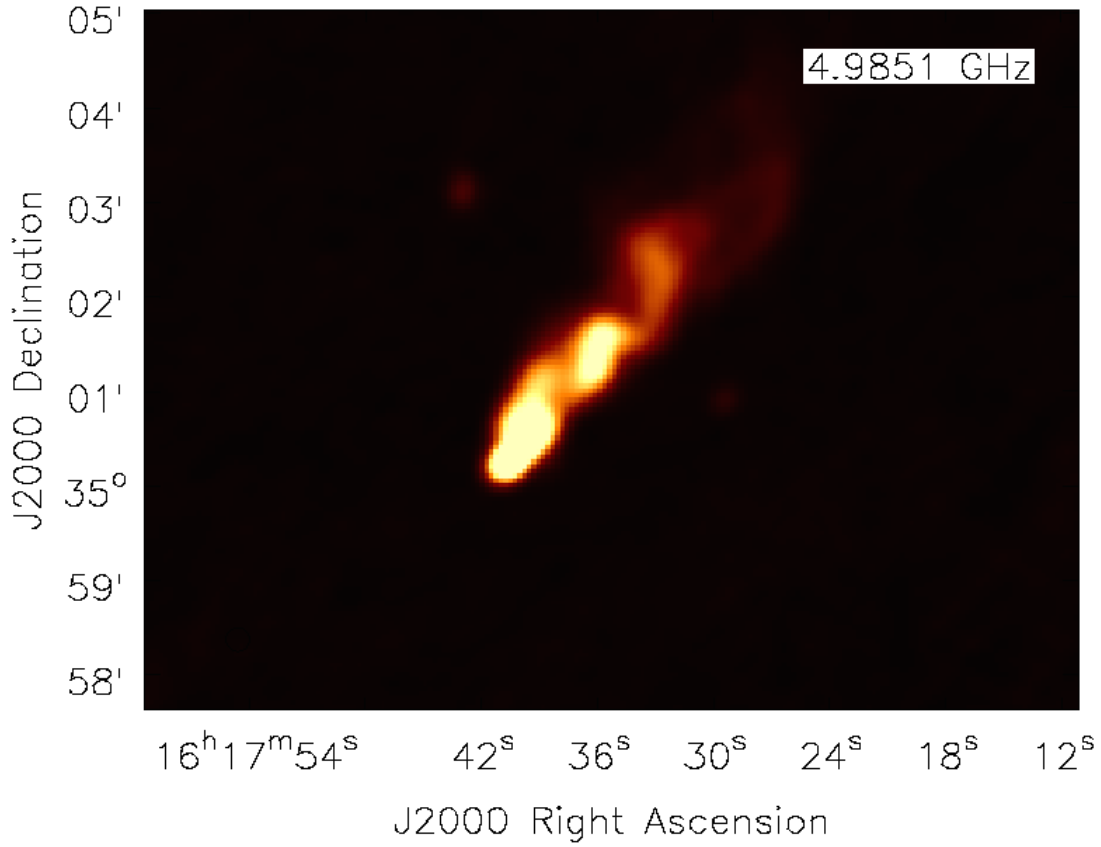

Figure 5.2: Extended radio emission from NGC 6109 at 14 arcsec resolution at 4.98 GHz from BT 7 archival data. Multiple bright knots are seen along the NW jet.

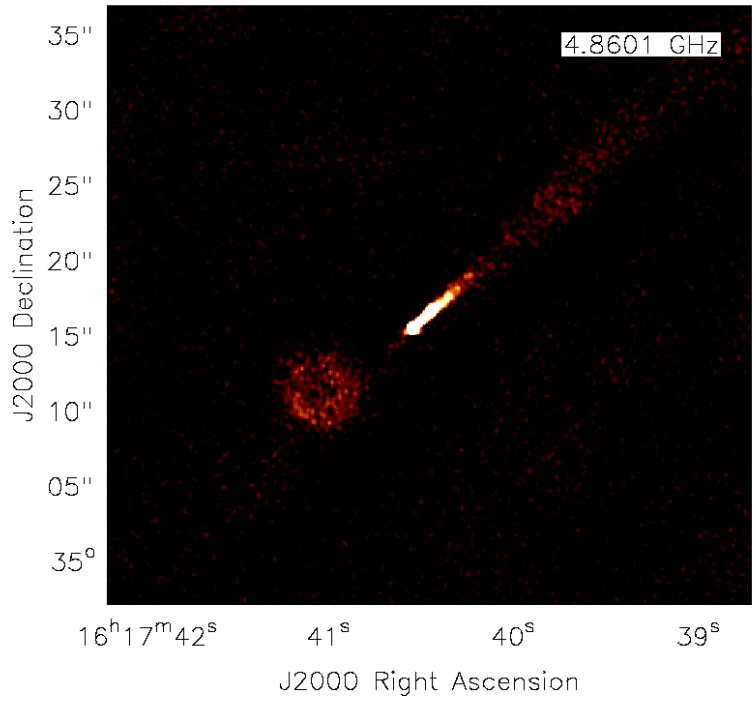

Figure 5.3: Small scale radio emission from NGC 6109 at 1.2 arcsec resolution at 4.86 GHz from BT 18 archival data. A bright straight jet extends to the NW for 3.5″ before fading, and emission is detected up to 20″ from the core. Diffuse emission is visible SE of the core

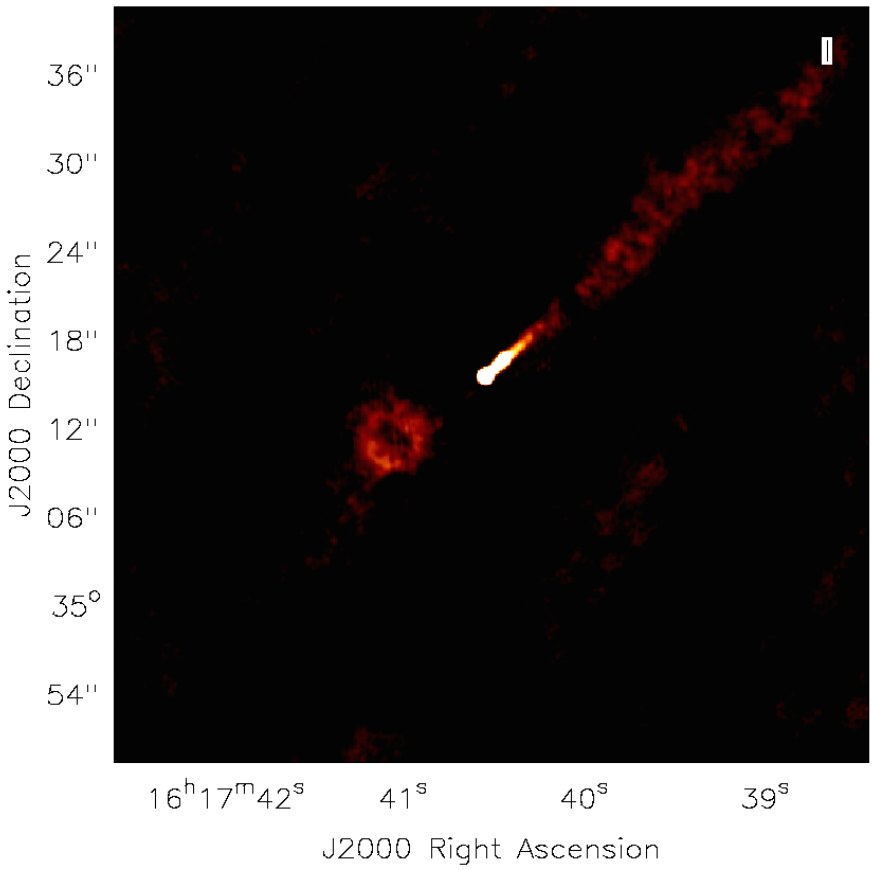

Figure 5.4: Small scale radio emission from NGC 6109 at 0.4 arcsec resolution at 4.86 GHz from AH 766 archival data. A bright knot is detected 1″ from the core along the NW jet, and the jet remains bright for 3″ before fading. Circular diffuse emission is visible SE of the core, with slightly more structure than seen in Figure 5.3.

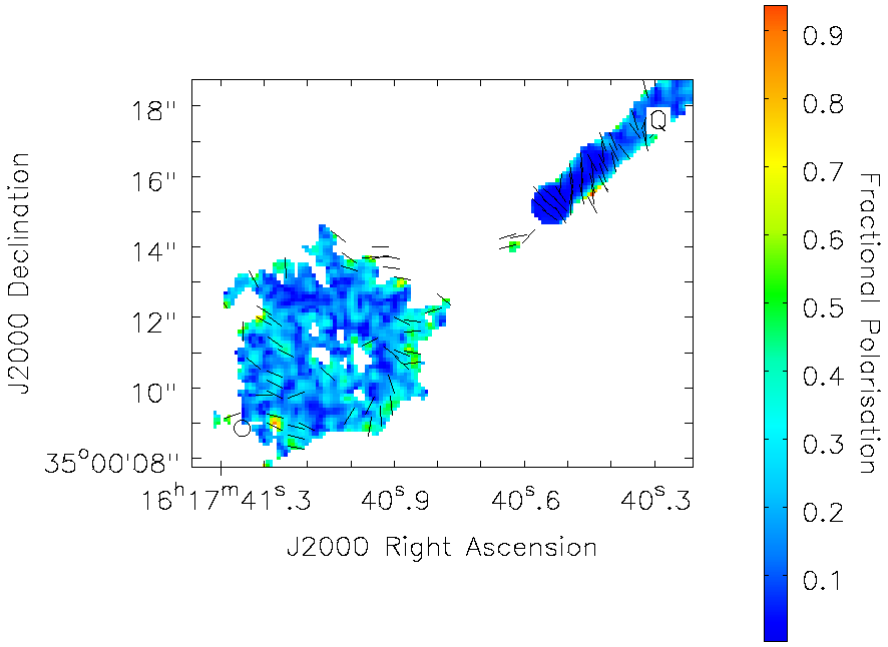

Figure 5.5: Fractional polarisation of the radio emission in NGC 6109 at 4.86 GHz from AH 766 archival data, with apparent magnetic field vectors overlayed

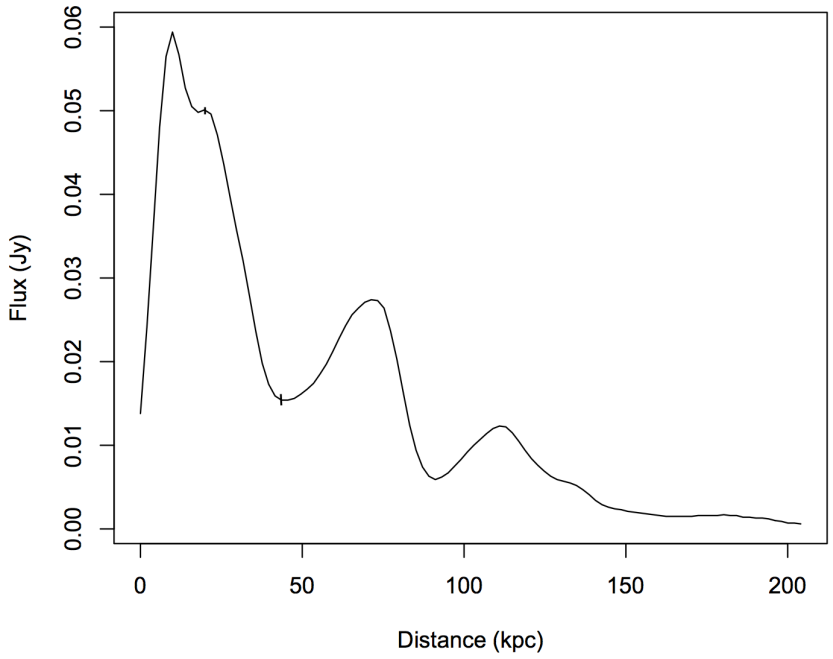

Figure 5.6: A surface brightness profile along the radio jet at 14 arcsec at 4.98 GHz. This profile highlights the bright knots seen along the jet at projected distance of approximately 60 and 100 kpc from the core. I used a projection 2″ wide and representative error bars are shown.

Total Flux Density (Jy, 1.67 GHz)	1.9
Total Power (W Hz^{-1}, 1.67 GHz)	$\sim 10^{24}$
Core Position (J 2000)	RA 16 17 40.05
	Dec 35 00 25.8
Core Flux Density (mJy, 4.86 GHz)	28 ± 0.4
Core Power (W Hz^{-1}, 4.86 GHz)	$\sim 10^{22}$
SE Component Position (J 2000)	RA 16 17 41.03
	Dec 35 00 10.96
SE Component Size (arcsec, 4.86 GHz)	6.5×5.8
SE Component Flux Density (mJy, 4.86 GHz)	17 ± 1
Core - SE Component Distance (arcsec)	4.7
NW jet projected length (arcsec, 4.86 GHz)	3.8
NW Jet Flux (mJy, 4.86 GHz)	11 ± 1
Tail Length (arcsec, 4.86 GHz)	34.1

Table 5.2: Morphological parameters of NGC 6109 from the archival observations

more like a circular lobe.

5.2.1.3 Polarised intensity

The fractional polarisation of NGC 6109 at 4.86 GHz is given in Figure 5.5. The unresolved core has a low fractional polarisation $P < 0.05$ and this remains constant until approximately $3''$ from the core, where it increases to $P = 0.1$. The apparent magnetic field vectors in the core are perpendicular to the jet direction, and do not begin to rotate until the polarisation increases $3''$ from the core. Further along the main jet, the fractional polarisation remains $0.1 < P < 0.2$ until $7''$ from the core where the polarised intensity is too low to provide a reliable result. The magnetic field vectors in this region are parallel to the direction of the jet axis. In the swirl region, the polarisation shows no significant structure: the highest regions are at the edges of the component, as found in other low power radio sources (e.g. Bridle and Perley, 1984). The apparent magnetic field vectors show little ordering. E and W of the component the vectors are radial to the jet direction. N and S they appear circumferential, tracking the bending of the jet.

5.2.1.4 JVLA observations

Further interpretation of the jets within NGC 6109 was limited by the lack of high sensitivity, high resolution observations and the need for several observational quantities, such as polarisation and rotation measure distributions. Much of the structure of the source is of low surface brightness, requiring high sensitivity to reveal the full extent of the source.

Project code	Config	Date	Frequency (GHz)	BW (MHz)	Time (s)	Resolution (arcsec)	Flux calibrator
15A-422	A	15-Aug	1.99-3.50	128	4500	0.9	3C 286

Table 5.3: JVLA details of NGC 6109 observations

At the same time, the dynamics of the inner regions are revealed by small scale structure, which dictates the need for high resolution observations. Finally, both total intensity and polarisation observations at multiple frequencies are required to examine the total intensity, spectral index, polarisation, rotation measure and magnetic field structures within the source.

NGC 6109 was observed with the JVLA as part of the proposal described in chapter 4. Both L and S band observations were requested, however only the S band observations were carried out. Details of the observations are given in Table 5.3. These data were automatically passed through the VLA calibration pipeline following the completion of the observations. The VLA calibration pipeline performs basic flagging and calibration using CASA. It is applied to Stokes I continuum data only, therefore it does not calibrate for polarisation. It generates flags in the case of shadowed data, faulty antenna and RFI, and it derives delay, bandpass and gain calibrations. I inspected the pipeline calibration applied to NGC 6109 and deemed it to be inadequate, thus I recalibrated the data using the techniques described in chapter 2. All data were self-calibrated after an initial run of CLEAN, repeating the procedure down to a solution interval of 20 seconds. A final self-calibration cycle was carried out on both the amplitude and phase of the source when I observed a strong convergence of the phase-only solutions.

The S band observations were not severely affected by RFI, however were still passed through the data flagging algorithm *rflag* in CASA. The polarisation properties of the flux calibrator 3C 286 are stable at S band frequencies, thus this source was used to calibrate for polarisation. The source J1635+3808 (4C 38.41) with RA = 16h 35m 15.5s and Dec = 38d 08′ 04″ was used as the phase calibrator.

5.2.1.5 Radio morphology and Spectral Index

The intensity distribution of NGC 6109 at 2.99 GHz is shown in Figure 5.7 and morphological parameters determined from these observations are given in Table 5.4. NW of the core the jet is collimated along the tail. The jet remains bright for 5″ before fading. The opening angle of the jet appears to increase within this dim, well-collimated region and then brightness flaring is observed approximately 12″ from the core. The jet remains

Core flux density (mJy, 2.99 GHz)	38.9 ± 0.04
Core spectral index α	0.05 ± 0.01
Core rotation measure (rad m^{-2})	24 ± 1
Core - SE component projected distance (arcsec)	5.3
SE component size (arcsec)	5.3×5.6
SE component flux density (mJy, 2.99 GHz)	21.0 ± 0.5
SE component spectral index α	0.5 ± 0.02
NW tail projected length (arcsec)	43
NW jet projected length (arcsec)	5.9
NW jet flux (mJy, 2.99 GHz)	16.3 ± 0.4
NW jet spectral index	0.5 ± 0.02
NW jet rotation measure (rad m^{-2})	32 ± 2
Core - NW knot projected distance (arcsec)	12
NW knot projected length (arcsec)	13
NW knot flux (mJy, 2.99 GHz)	24.7 ± 0.4

Table 5.4: Morphological parameters of NGC 6109 from the JVLA observations. The spectral index α is defined as $S \propto \nu^{-\alpha}$.

bright for approximately $12''$. Within this high-emissivity region, the emission bends up to the N and then to the W and bright non-axisymmetric substructures are observed. A surface brightness profile of the main jet is given in Figure 5.9 to highlight the position of the bright knot and the subsequent decrease of the flux linearly with distance out to 20 kpc. The core has a flux density of 37 mJy at 2.99 GHz and there is a second bright peak about 2 kpc from the core.

SE of the core, a faint counter-jet is visible (see Figure 5.8). The jet extends $5''$ in length before entering a tight swirl of radio emission. This swirl has a radius of $5''$, and the emission at the centre of the component is noticeably fainter, giving it a doughnut-like shape. The highest surface brightness is detected along the SE of the component, and there is broader low-surface brightness radio emission to the NE. The flux density enclosed within the swirl region is 19 mJy at 2.99 GHz. A surface brightness profile is given in Figure 5.10 to show the intensity distribution through the doughnut component and highlight the hole at the centre of the structure. This indicates that the radio emission is sweeping around through $>180^\circ$ rather than just expanding into the IGM like a radio lobe.

A plot of how the spectral index α (S $\propto \nu^{-\alpha}$) changes along the length of the jet is given in Figure 5.11. The points were taken from a map created using two Taylor terms in the CLEAN algorithm. The spectral index is given by the ratio of the first two coefficients of the Taylor expansion, between the upper and lower S band frequencies. A projection

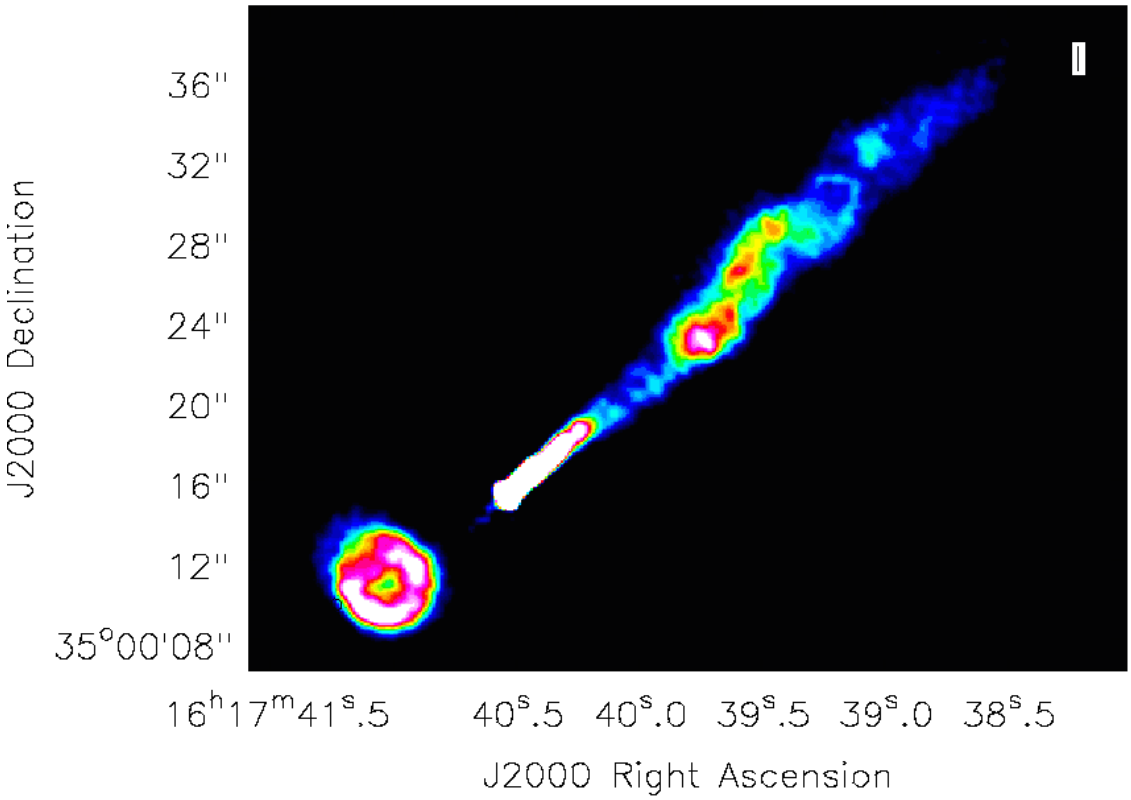

Figure 5.7: Small scale radio emission from NGC 6109 at 0.9 arcsec resolution at 2.99 GHz. A straight jet is seen extending to the NW for 5″ before it fades. At 12″ a bright knot is visible for 20″ before emission decreases. SE of the core, a striking feature is observed. This component has a doughnut-like structure with a radius of 5″.

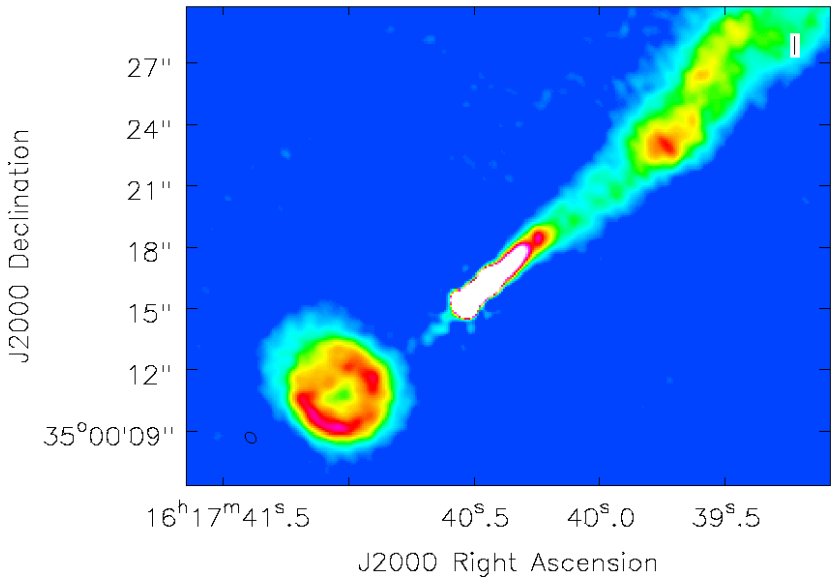

Figure 5.8: Small scale radio emission from NGC 6109 at 0.9 arcsec resolution at 2.99 GHz. The image highlights the counter-jet and the diffuse emission NE of the doughnut component.

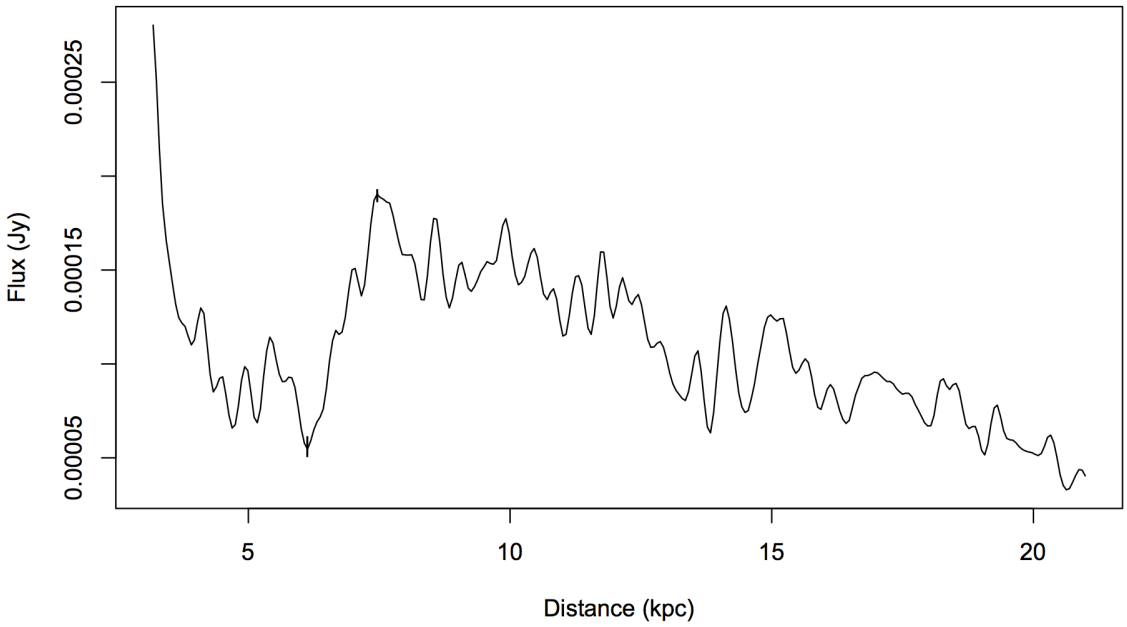

Figure 5.9: Surface brightness profile highlighting the knot region within the main jet by excluding the bright emission from the core. The brightness drops approximately linearly with distance from the leading edge. I used profiles with width 0.2″ and representative error bars are shown.

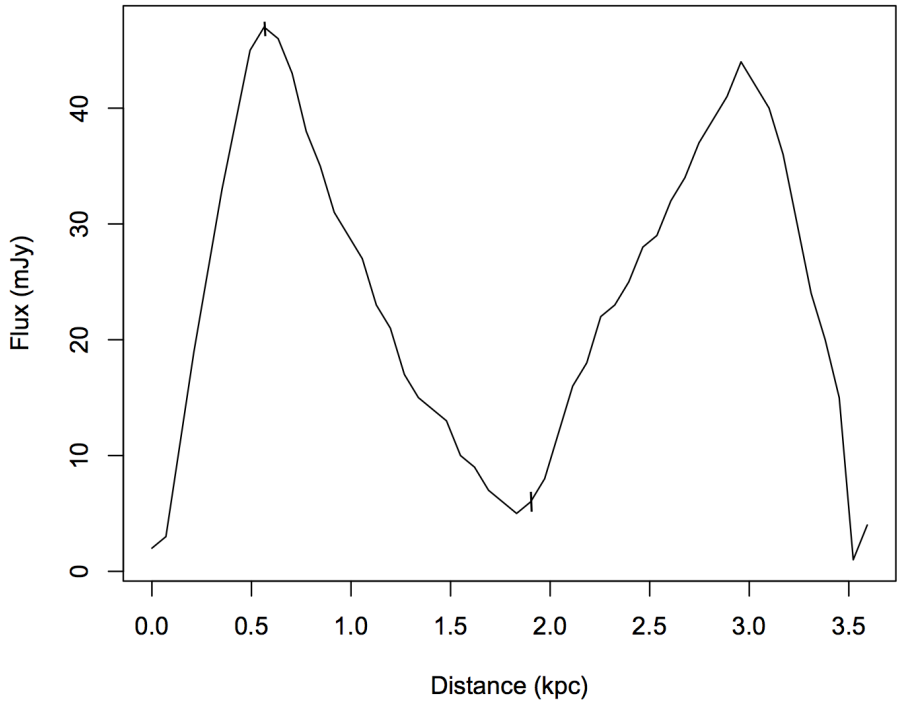

Figure 5.10: Surface brightness profile highlighting the lack of emission in the centre of the doughnut component. The projection measures from W to E horizontally across the component, with width 0.2″. The profile shows a higher slightly flux on the W side of the feature, otherwise the peaks are roughly symmetric. Representative error bars are shown.

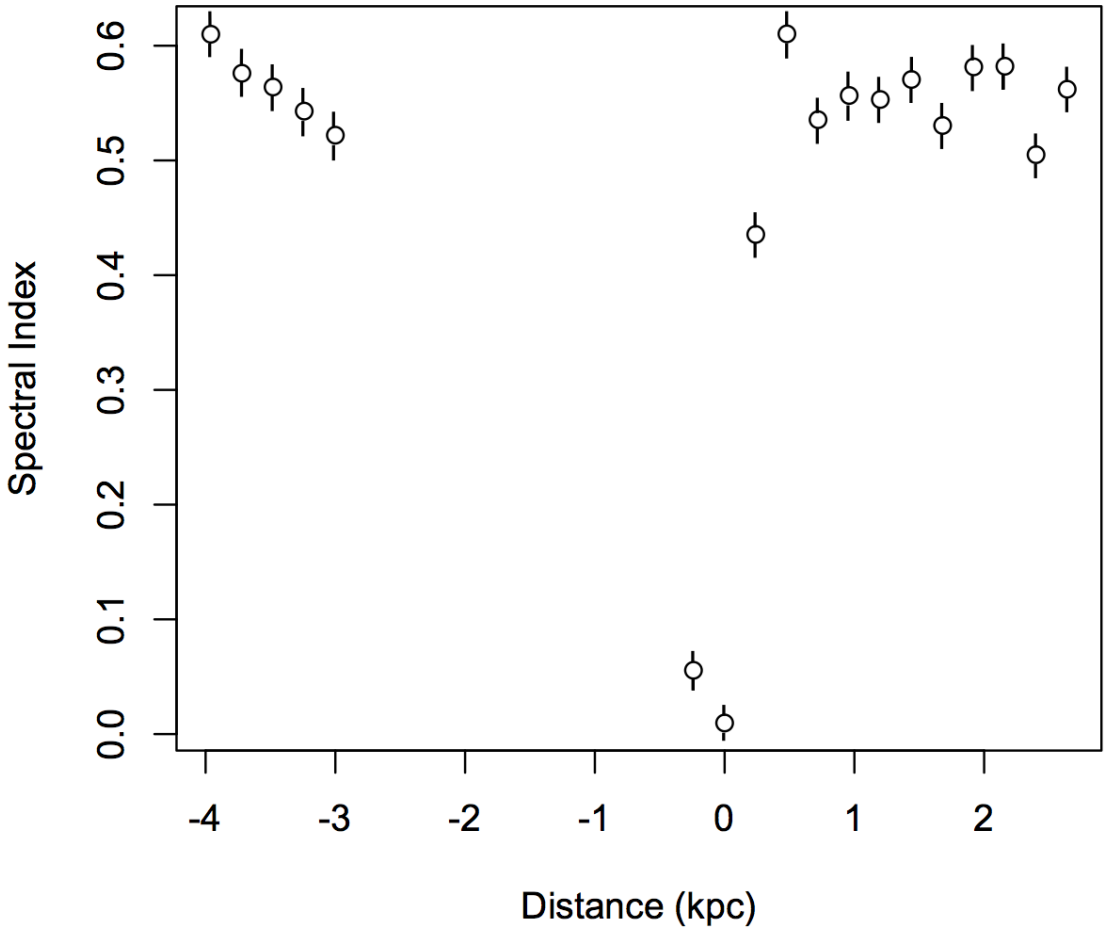

Figure 5.11: Spectral index α with distance to the NW, where 0 corresponds to the position of the core, thus a negative distance refers to points SE of the core. The spectral index was measured every 0.2 arcsec and transverse profiles 0.6 arcsec wide were averaged. Measurements were not taken between -3 and 0 kpc because the emission was too faint to give reliable results.

with width 0.6″ was used to map the spectral index at 0.2″ increments along the jet, and the core is located at 0 kpc. The core has α = 0.05 $\pm$ 0.01 and the spectral index along the main jet is $\alpha \approx 0.56 \pm 0.02$ along the first 6″. Beyond this point, the radio emission is too faint to give good spectral index results. In the counter-jet, the spectral index is 0.5-0.7, in agreement with the emission along the main jet. These values agree with the results of Ekers (1978), who found α = 0.5 along the inner NW jet. They also reported α = 1 along the tail out to 50 kpc and more pronounced steepening of the spectral index at higher frequencies, suggesting the existence of a break in the radio spectrum.

5.2.1.6 Polarised intensity

The frequency coverage of the new JVLA observations is sufficient to reveal the polarisation structure at high resolution and to probe the magnetic field configuration within the radio emission. I used Stokes I, Q and U images at 1.4 arcsec resolution to derive the distributions of degree of polarisation and polarisation position angle at 2.99 GHz. The degree of polarisation was corrected to first order for Ricean bias (Wardle and Kronberg, 1974).

A fractional polarisation map is given in Figure 5.12. To minimise the likelihood of possible errors in measurements of P caused by residual sidelobe structure in the total intensity data, all pixels with errors $>$ 0.01 in fractional polarisation are blanked. The peak fractional polarisation in the image is 51%, similar to the peak values found in other radio sources (Bridle and Perley, 1984) and comparable to the theoretical maximum for a source with a uniform magnetic field (Pacholczyk, 1970). In the core, the polarisation is P = 0.1 $\pm$ 0.02. Along the bright part of the main jet P = 0.15 $\pm$ 0.02. In the SE doughnut component, the SW and NE sides have fractional polarisation P = 0.31 $\pm$ 0.03, whereas the SE and NW sides display lower polarisation P = 0.09 $\pm$ 0.02. The source shows an increased fractional polarisation around the edges of the doughnut component, as found in radio source lobes (Laing, 1996). The component shows more structure in the polarisation than the archival 1.51 GHz map (see Figure 5.5). In the core and along the NW jet, the maps are in agreement.

5.2.1.7 Rotation measure structure

Rotation measure synthesis was used to investigate the rotation measure structure in the doughnut component and along the main jet. Based on the results in chapter 4, this was carried out using the *rmsynthesis* code designed by Michael Bell and detailed in chapter 2. I CLEANed the data using MFS imaging and averaged 50 channels per frame, to produce an image with 20 different frequency planes ranging from 2.05 GHz to 3.95 GHz at 100 MHz intervals. The RM synthesis was carried out with a weighting function of 1 / σ^2_{rms} and 500 clean iterations. The RMTF for the model is given in Figure 5.13. The fitted FWHM of the clean response is 94 rad m^{-2}.

In the core, the RM is found to be 24 $\pm$ 1 rad m^{-2} in agreement with Taylor et al. (2009). Along the main jet, the rotation measure is constant, at 32 $\pm$ 2 rad m^{-2} for 5$''$. Beyond this region the RM is unavailable due to low signal to noise, until the bright knot

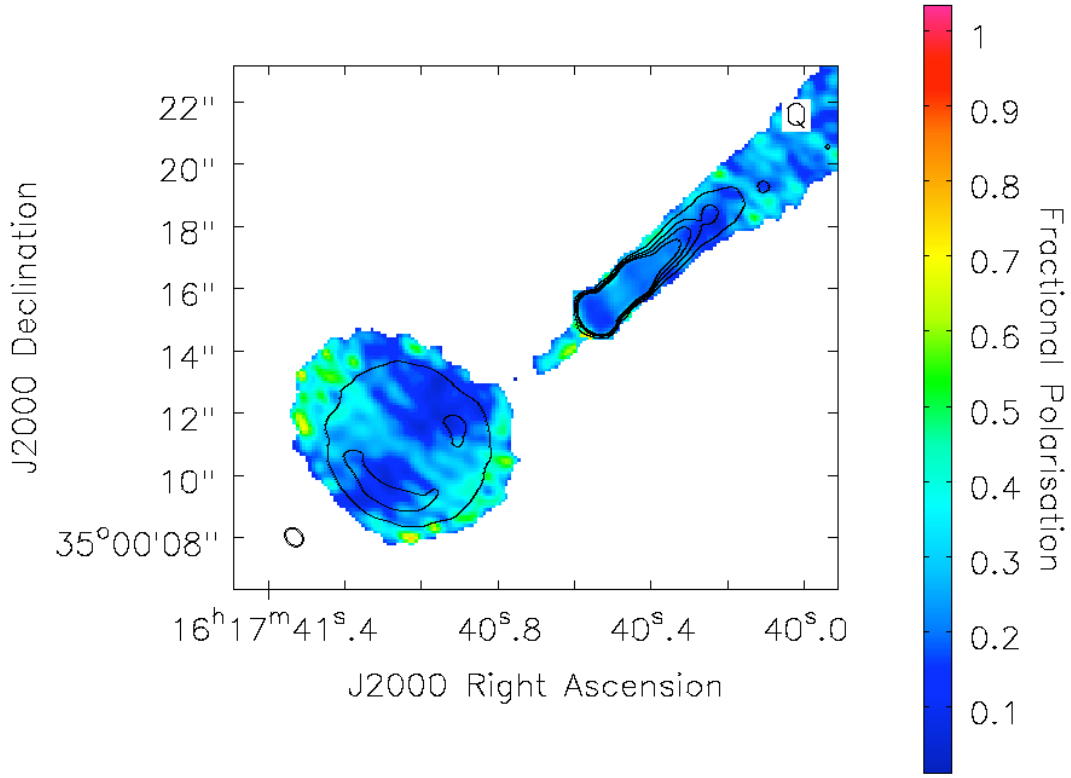

Figure 5.12: Fractional polarisation structure of NGC 6109 at 2.99 GHz, with JVLA contours overlayed at 0.8, 1.6, 3.2 and 6.4 mJy. Any pixels with errors $> 1\%$ have been blanked.

at 12″ from the core. Within the knot, the rotation measure is 40 ± 8 rad m^{-2}.

Figure 5.14 shows the RM synthesis distribution in the doughnut component, overlayed with 2.99 GHz JVLA total intensity contours. I also used the CASA program *rmfit* to produce a rotation map and this is given in Figure 5.15. Both maps give a similar rotation measure for the core, however the *rmfit* map shows a lower rotation measure in other regions. I will use the map produced via rotation measure synthesis for interpretation of the structure in NGC 6109, for the reasons discussed in chapter 1 and chapter 4.

The regions of high RM appear to correspond with regions of high radio flux. This is highlighted further in Figure 5.16, which shows the intensity of the polarised flux at a rotation measure of 200 rad m^{-2}. The regions of strongest polarised intensity clearly lie within the total flux contours. The distribution of the rotation measure at 32 rad m^{-2} is shown in Figure 5.17. Here the strongest polarised intensity is found to lie across the component, almost perpendicular to the axis of the main jet. I find no significant polarised structure below 0 rad m^{-2}. Faraday dispersion spectra were produced in ± 400 rad m^{-2} in the core, 5″ along the main jet and in the highest flux regions of the doughnut. These spectra are given in Figures 5.18 and 5.19. The sidelobes on these spectra are low, and the observed flux peaks are sensible.

The regions of high RM correspond to areas of low fractional polarisation. It is possible that the emission has been depolarised by the Faraday screen responsible for the RM structure, or that beam depolarisation is affecting the observed levels of polarisation. These two mechanisms can be distinguished by investigating the RM structure on sub-beam scales. Substructure in the screen density or magnetic field could be studied further with lower frequency JVLA or LOFAR observations. A higher fractional polarisation is detected in the NE-SW direction where the RM is lower, at 32 rad m^{-2}. The RM along the main jet and across the doughnut component has a uniform structure, suggesting that this RM is associated with a foreground screen outside the cluster.

The rotation measure (RM) of foreground magnetised gas rotates the observed polarisation position angle PA as a function of wavelength λ according to $\phi = PA_0 + \mathrm{RM}\ \lambda^2$. Using the calculated RM values, I produced maps of the magnetic field direction at zero wavelength. These maps are given in Figures 5.20, 5.21 and 5.22 for the core, the bright knot at 12″ and the doughnut component respectively, with 2.99 GHz JVLA total intensity contours. In the core, the magnetic field is as expected for a low power FRI type jet; the vectors rotate from parallel to the jet direction to perpendicular further out. In the knot and doughnut component however, the magnetic field is complex. Figure 5.21 shows a

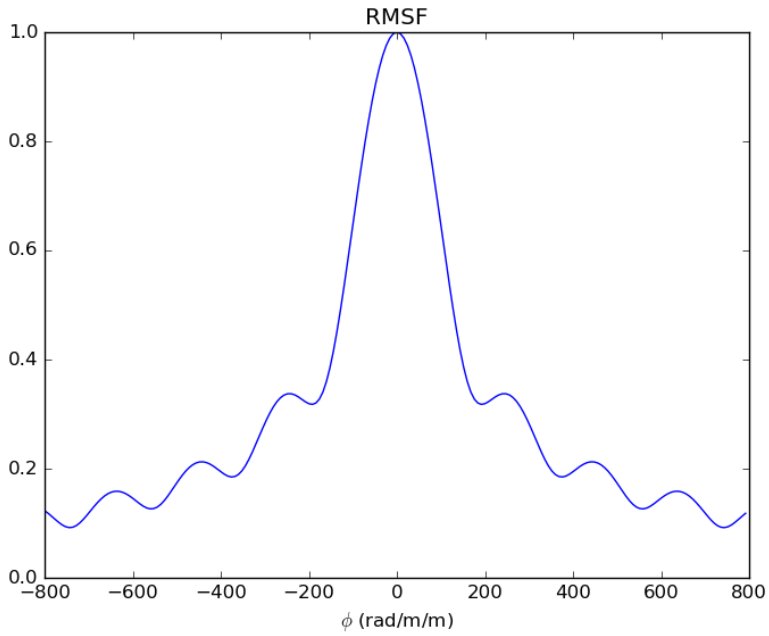

Figure 5.13: The RMSF for the *rmsynthesis* code as applied to NGC 6109 for frequency range 2.05 - 3.95 GHz with 100 MHz intervals

combination of transverse and parallel magnetic field components, and I suggest that such disorder is due to recollimation shocks and jet distortion. In the doughnut component, the magnetic field vectors also show a combination of transverse and parallel magnetic field components. S of the component, along the high flux contours, the field is longitudinal with respect to the jet direction and appears to track the bending of the source. This field could be produced by shearing of the field into a direction tangential to the source boundary (Blandford and Rees, 1978) and is a structure commonly observed in other sources where jet bending is evident. Along the centre of the component, where a channel of RM of magnitude 32 rad m^{-2} is located, the vectors are transverse to the direction of the main jet. Magnetic field structure is also detected to the NE, where diffuse emission is thought to expand into the environment. This diffuse emission has a transverse magnetic field structure, although longitudinal emission is seen on the E side possibly at the boundary between the radio emission and the external medium. The complex magnetic field structure within this component suggests that shocks and compression of the radio structure may play a significant role in affecting this part of the flow.

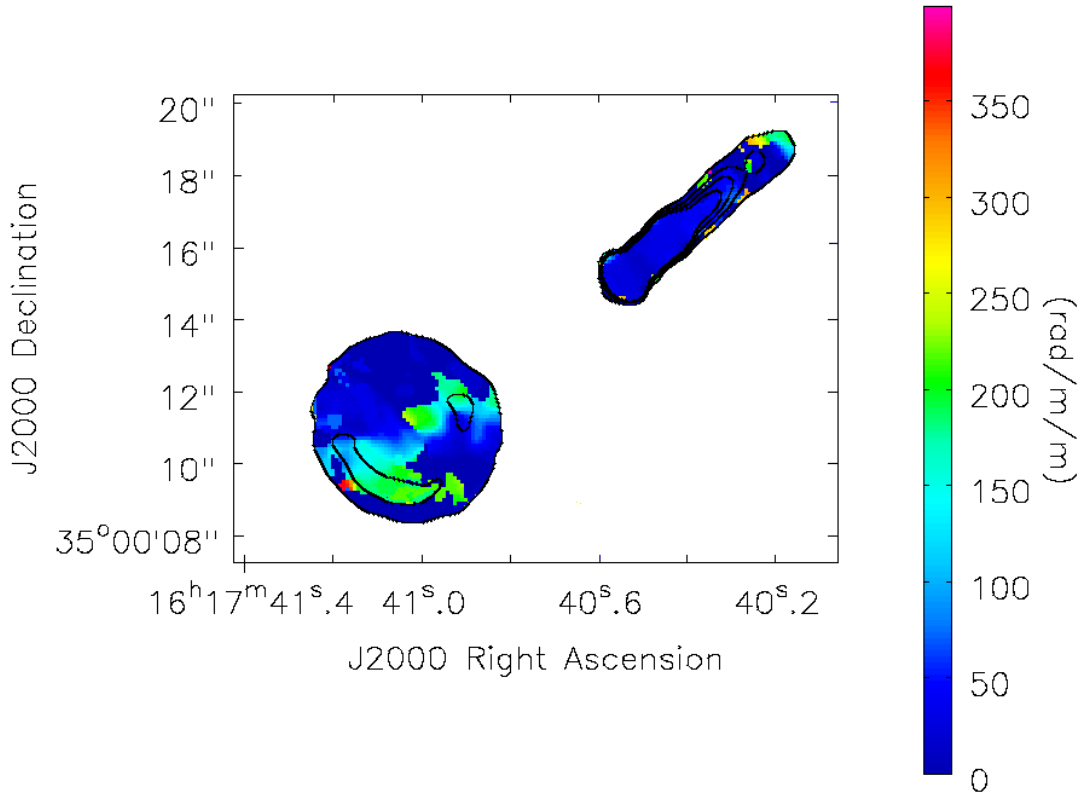

Figure 5.14: Rotation measure structure produced using the *rmsynthesis* code for NGC 6109 at 2.99 GHz with JVLA contours overlayed at 0.8, 1.6, 3.2 and 6.4 mJy beam^{-1}.

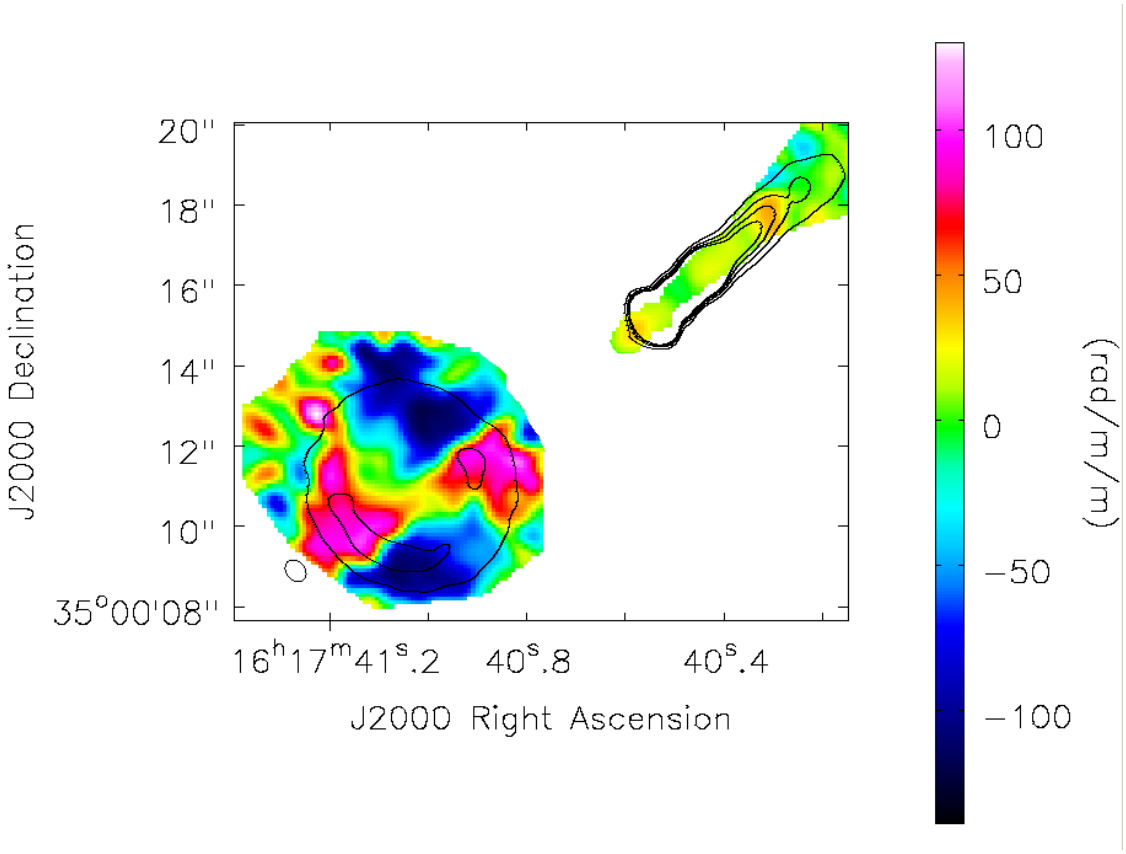

Figure 5.15: Rotation measure structure produced using the *rmfit* code in CASA for NGC 6109 at 2.99 GHz with JVLA contours overlayed at 0.8, 1.6, 3.2 and 6.4 mJy beam^{-1} and a colour bar to the right.

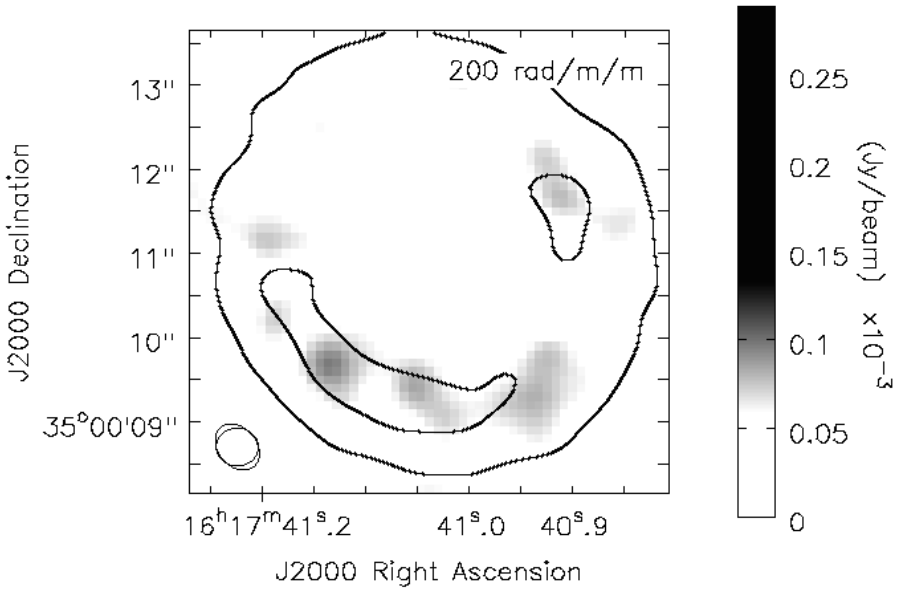

Figure 5.16: Polarised intensity structure at RM = 200 rad m^{-2}, with JVLA contours overlayed at 0.8, 1.6, 3.2 and 6.4 mJy beam^{-1}. A clear region of high RM is seen along the SE edge of the component, within the contours.

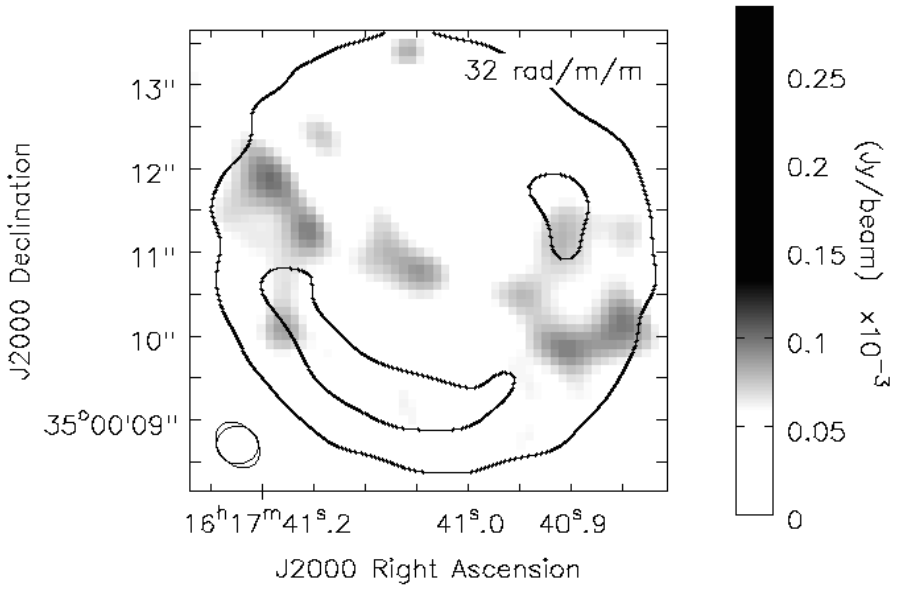

Figure 5.17: Polarised intensity structure at RM = 32 rad m^{-2}, with JVLA contours overlayed at 0.8, 1.6, 3.2 and 6.4 mJy beam^{-1}. A clear channel of polarised emission at this rotation measure runs perpendicular to the axis of the main NW jet across the doughnut component.

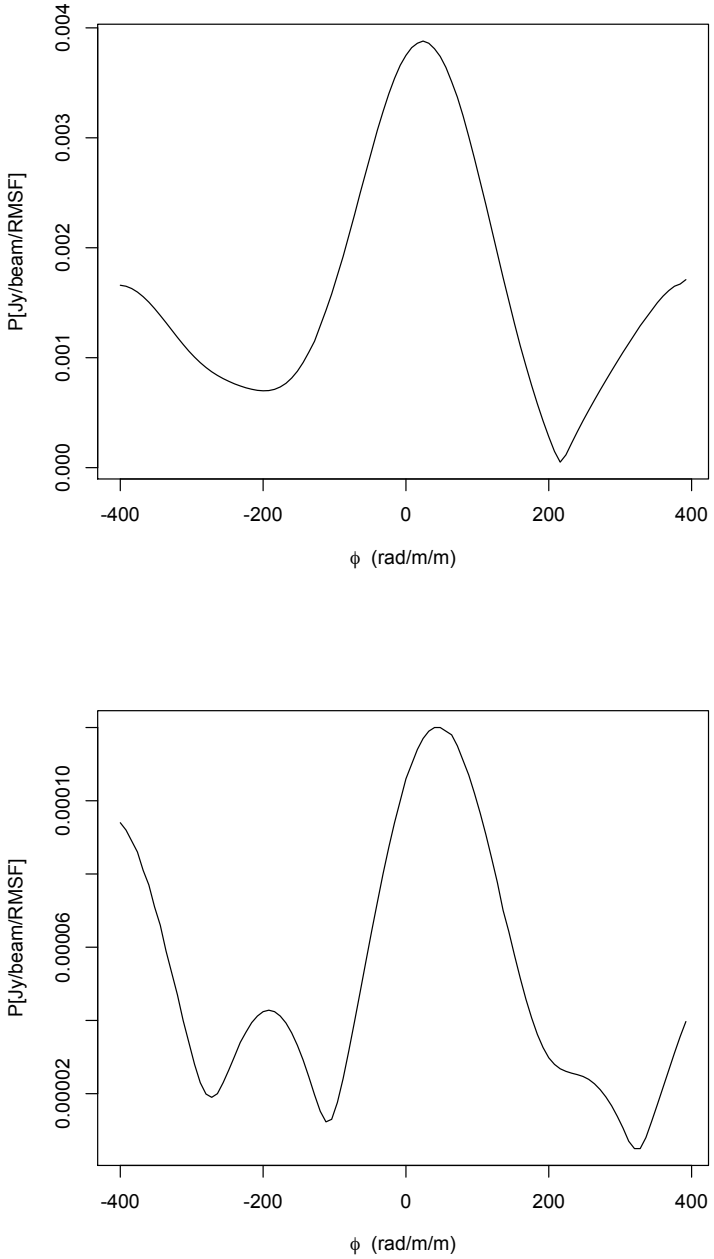

Figure 5.18: The Faraday dispersion distribution in *(top)*:the core and *(bottom)*: the jet of NGC 6109. The RM synthesis was carried out with a weighting function of 1 / σ^2_{rms} and 500 clean iterations to reduce the appearance of sidelobes.

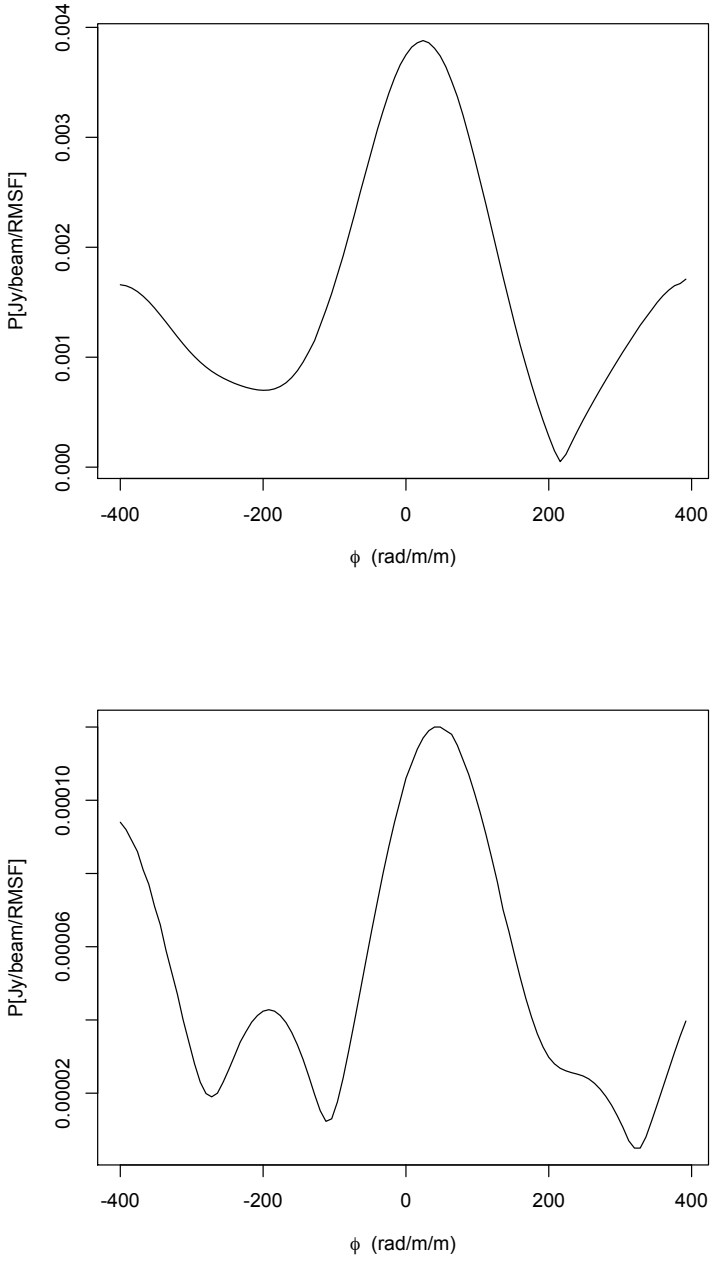

Figure 5.19: The Faraday dispersion distribution in *top*: S of the doughnut and *bottom*: NW of the doughnut in NGC 6109. The RM synthesis was carried out with a weighting function of 1 / σ^2_{rms} and 500 clean iterations to reduce the appearance of sidelobes.

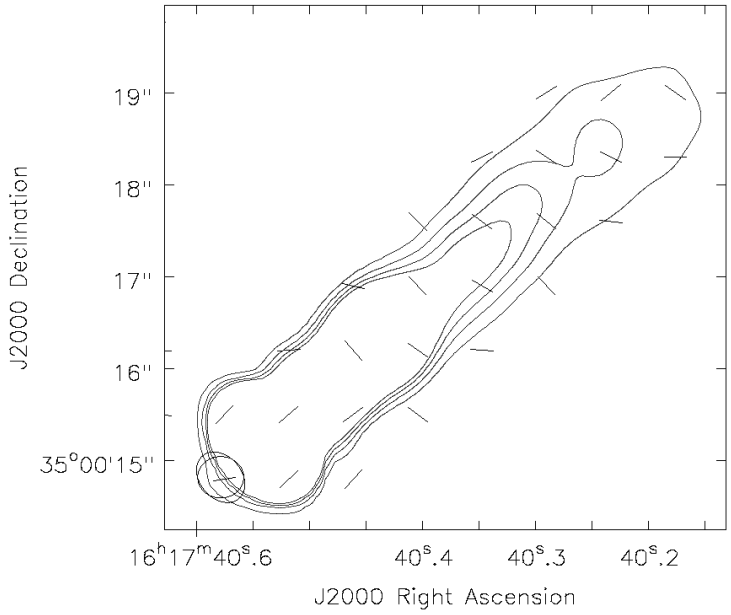

Figure 5.20: The magnetic field direction in the core and along the first 5 kpc of the main jet, corrected for Faraday rotation and shown with JVLA total intensity contours at 0.8, 1.6, 3.2 and 6.4 mJy beam^{-1}.

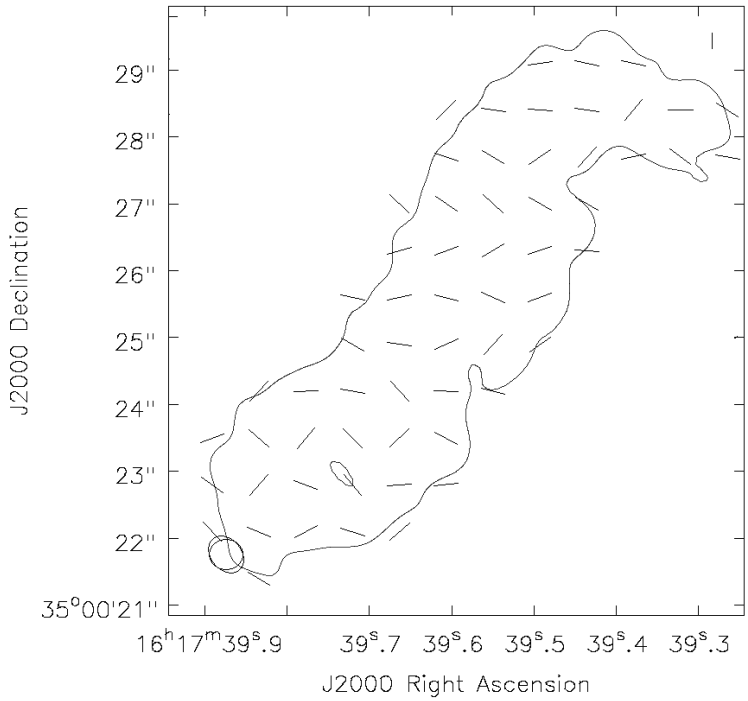

Figure 5.21: The magnetic field direction in the bright knot 12″ along the main jet, corrected for Faraday rotation and with JVLA total intensity contours at 0.8, 1.6, 3.2 and 6.4 mJy beam^{-1}.

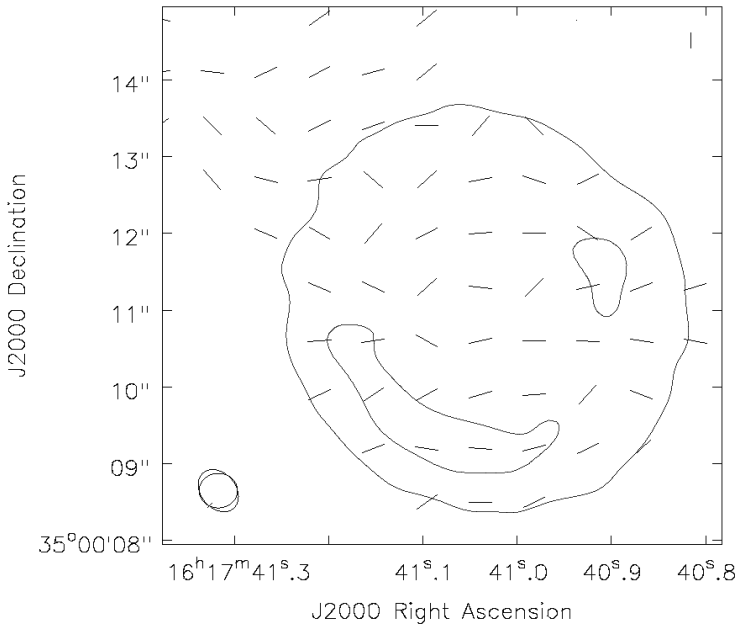

Figure 5.22: The magnetic field directions in the doughnut component, corrected for Faraday rotation and with JVLA total intensity contours at 0.8, 1.6, 3.2 and 6.4 mJy beam^{-1}.

5.2.1.8 A model of the doughnut region

I used the CASA tasks *simobserve* and *simanalyze* to investigate the doughnut structure in NGC 6109. These tasks allow the user to simulate an interferometric measurement set and then grid, invert and deconvolve the measurement set into an output image. These tasks were used to model different shapes to attempt to reproduce the doughnut-like structure.

The analysis used both a two-Gaussian model and a two disk model to interpret whether the intensity of the jet varies radially outwards from the centre of the component or has an approximately uniform distribution around the structure. The Gaussian model used a 5″ FWHM circular component centred at RA = 16h 17m 41s and Dec = 35d 00′ 11″ to replicate the outer edge. A second Gaussian profile with a 1″ FHWM and a negative flux was added to the first model, to give a low emission region at the centre. The disk model used two separate disks with the same circular geometry as the Gaussian model but a uniform radial intensity distribution. The images produced were compared to the real data and χ square test gave a goodness of fit χ^2 =156 for the Gaussian model and χ^2 =134 for the disk model.

The Gaussian and disk models are shown with the corresponding (real - model) images in Figure 5.23. The disk model in particular highlights the bright edge SE of the centre and the extended emission to the NE. The faint counter-jet is prominent NW of the image and

Telescope	Instrument	Date	Wavelength (μm)	Time (s)
Spitzer	IRAC	05-Mar	3.6	863
Spitzer	IRAC	05-Mar	4.5	863
Spitzer	IRAC	05-Mar	5.8	863
Spitzer	IRAC	05-Mar	8.0	863
CFHT	MOS	04-Apr	0.35	300
KPNT	RCA3	85-Feb	0.8	150

Table 5.5: Details of the optical observations available for NGC 6109

rest of the structure appears well modelled. This suggests that the doughnut component is better modelled by disk-like structure where the emission is largely uniform at all points around the component.

5.2.2 Optical observations

At optical wavelengths, NGC 6109 has been observed with *Spitzer*, the Canada France Hawaii Telescope (CFHT) and the Kitt Peak National Telescope (KPNT). I used IRAF to examine all the available data and search for evidence of optical features coincident with the radio emission. The resolution of the KPNT and CFHT data exceeds that of *Spitzer*, however all are poor compared to HST. Unfortunately, NGC 6109 has not been observed with HST at this time. Table 5.5 gives the details for the optical observations of NGC 6109.

5.2.2.1 *Spitzer* observations

NGC 6109 was observed with the Spitzer Space Telescope as part of a program of IRAC and MIPS imaging and photometry of the complete sample of $z < 0.1$ 3CRR radio galaxies (Birkinshaw et al., 2005). The project aimed to construct wide-band spectra for the radio jets and to measure the energy output of the nuclei. The 3.6 μm IRAC image is shown in Figure 5.24 with 1.51 GHz VLA radio contours in order to visualise the extent of the radio emission in terms of the optical AGN emission. The NW tail extends out to the edge of the optical emission and the radius of the optical emission is found to be approximately $33''$ (20 kpc). The IRAC images were cosmic-ray corrected within IRAF and the task *ellipse* was used to fit elliptical isophotes to the galaxy images. This method is described in section 4.2.2.1. The result of this fitting for the 4.5 μm image is shown in Figure 5.25 with 1.51 GHz VLA radio contours. This image shows multiple optical features coincident with the radio emission, so I subtracted this 4.5 μm image from the

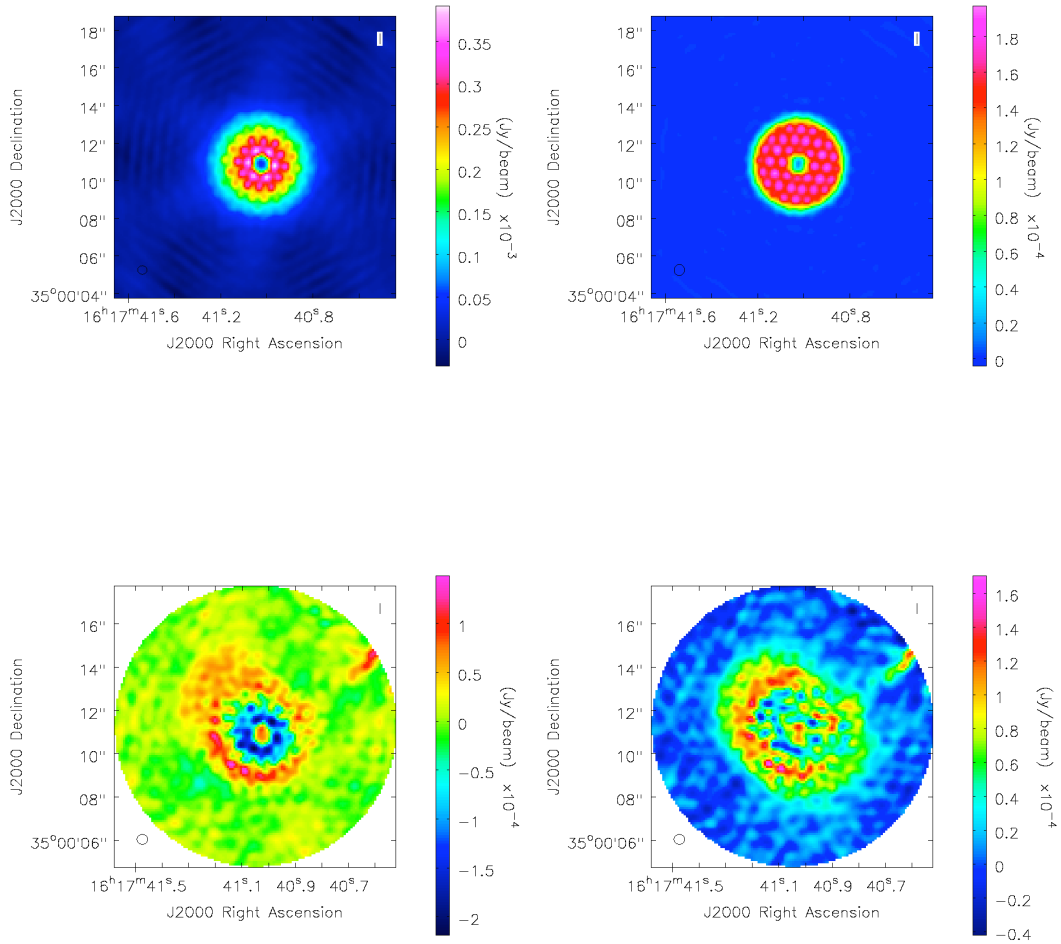

Figure 5.23: *Top:* Gaussian (left) and disk (right) models from CASA task *simobserve* created to model the doughnut structure. *Bottom:* the difference between the model image and the real image for the Gaussian *(left)* and disk *(right)* fit, computed using the *immath* task in CASA. The counter-jet is clearly visible to the NW and diffuse emission is seen to the NE.

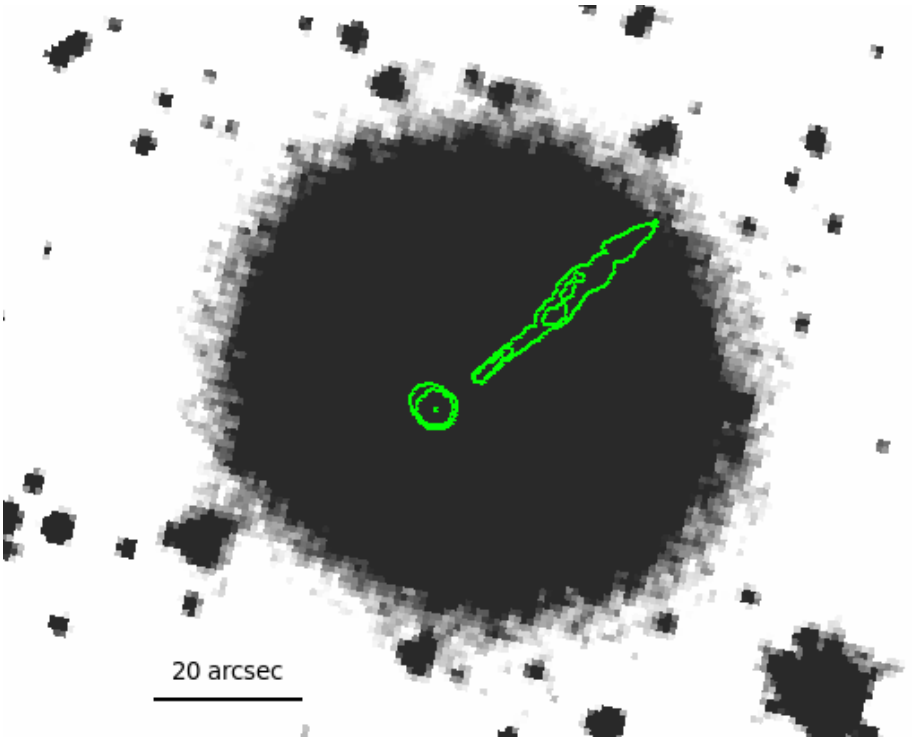

Figure 5.24: *Spitzer* IRAC image at 3.6 μm with VLA total intensity contours at 0.1, 0.2 and 0.4 mJy beam^{-1}.

8 μm image to look for residual features. This subtraction removed most of the optical emission, suggesting that there are no prominent optical features associated with the radio components.

5.2.2.2 CFHT observations

CFHT observations of NGC 6109 taken in 2002 were used to map the optical emission. Unlike HST, few ground-based optical observatories add information to their image headers to translate pixel coordinates to sky coordinates. The program SETWCS (Downey and Mutel, 1996) was designed to automatically add world coordinate system information to the header of images by matching the spatial distribution of observed stars with reference catalogues. The sequence of processes used in SETWCS was retained in the revised program, IMWCS.

I used IMWCS to assign a world coordinate axis to the CFHT data. I used the program IMSTAR to catalog stars with positions from images with a known WCS, such as those from the Digitised Sky Survey (DSS). This data is then used by IMWCS to fit a standard WCS function to the matches and add the information to the image header. I checked the resulting coordinate system by comparing it to the *Spitzer* images and the radio flux

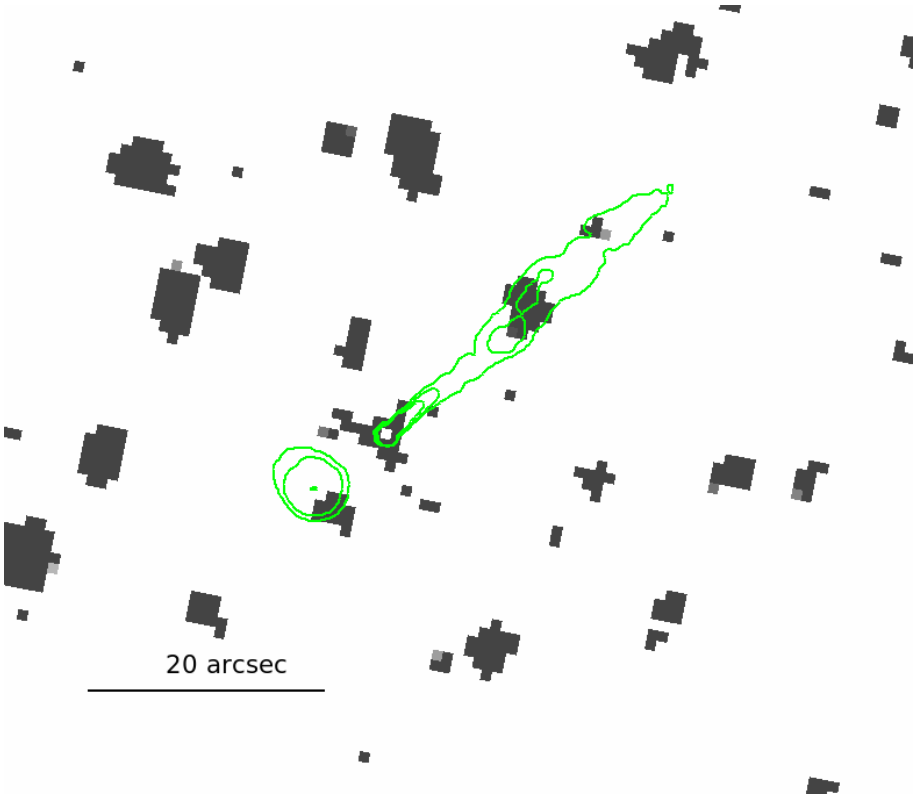

Figure 5.25: *Spitzer* IRAC image at 4.5 μm after ellipse subtraction, with VLA total intensity contours at 0.1, 0.2 and 0.4 mJy beam^{-1}.

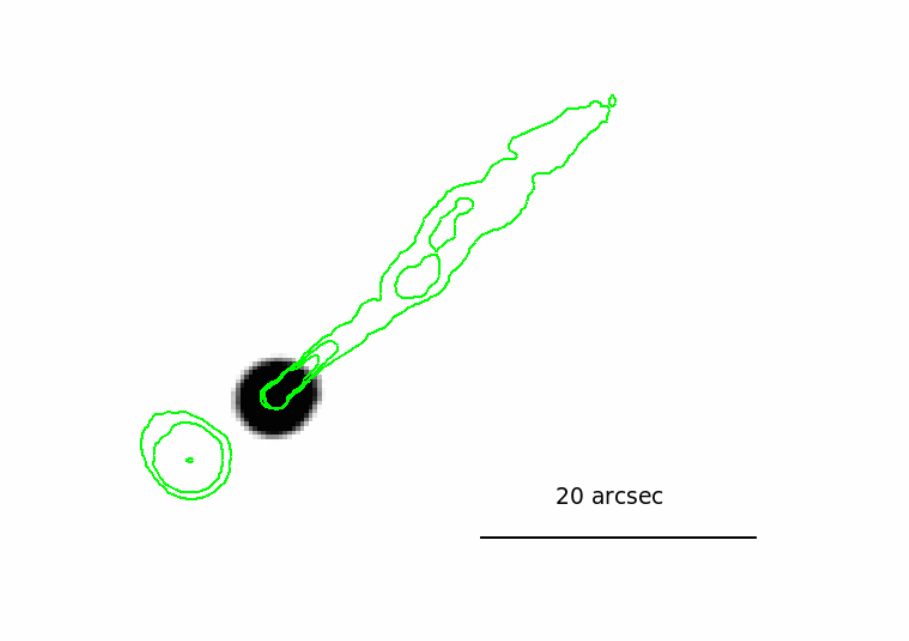

Figure 5.26: CFHT MOS image at 0.35 μm with VLA total intensity contours at 0.1, 0.2 and 0.4 mJy beam^{-1}.

contours, and the final image is shown in Figure 5.26. There is no evidence for optical features coincident with the radio emission, although there is a slight broadening of the optical image to the W.

5.2.2.3 KPNT observations

I used archived data from KPNT of NGC 6109 to confirm that there is no obvious optical emission coincident with the radio features. I assigned a world coordinate axis to the data as described above and removed cosmic rays. The images were passed through the IRAF task *ellipse* in order to remove stellar emission. Images of the optical emission before and after ellipse subtraction are given in Figures 5.27 and 5.28 respectively. There is no evidence in Figure 5.28 for optical features beyond the core.

5.2.3 X-ray observations

The ACIS-S instrument on *Chandra* was used to observe NGC 6109 on 2003 September 28 in VFAINT imaging mode for 19.39 ks, with observation ID 3985. The data were imported into CIAO and reprocessed by following the 'science threads' in CIAO version 4.6 to generate a new level 2 events file. These procedures apply the energy-dependent sub-pixel event repositioning algorithm. Unrelated sources were masked using output

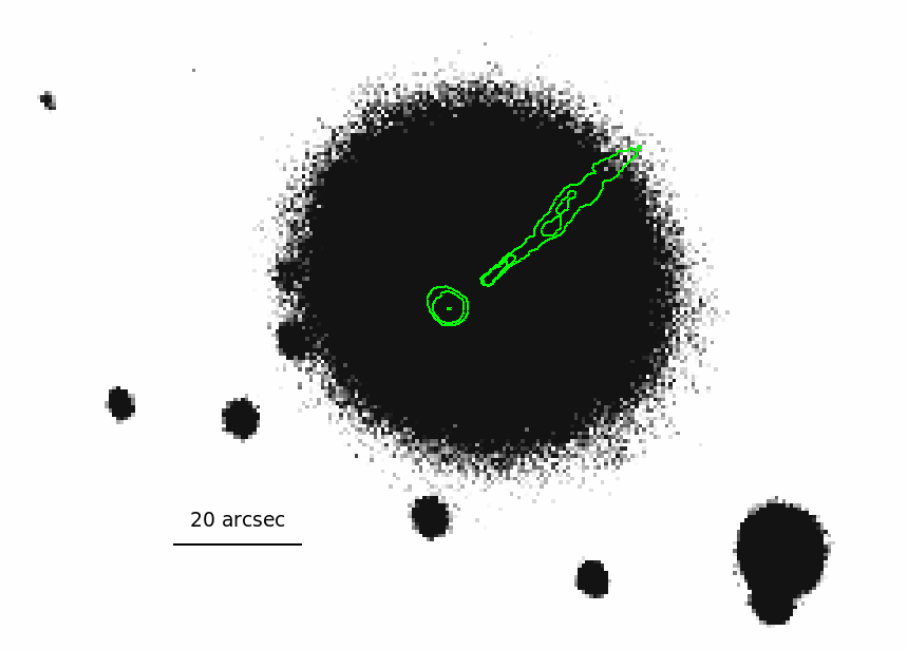

Figure 5.27: KPNT RCA3 image at 0.8 μm with VLA total intensity contours at 0.1, 0.2 and 0.4 mJy beam^{-1}.

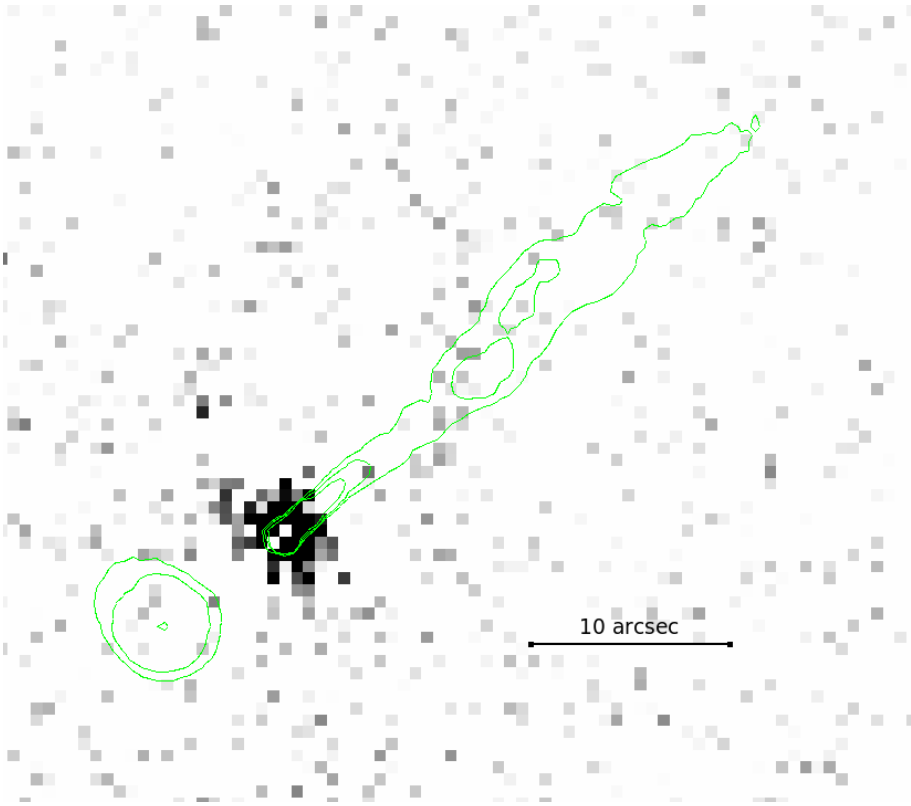

Figure 5.28: KPNT RCA3 image in R band after ellipse subtraction, with VLA total intensity contours at 0.1, 0.2 and 0.4 mJy beam^{-1}.

from the CIAO WAVDETECT task. An X-ray image at 0.5-2.0 keV is shown in Figure 5.29 with 1.51 GHz VLA total intensity intensity contours overlayed. The image has been smoothed with a Gaussian function of σ = 3 pixels, where 1 pixel = 0.492 arcseconds. There is no evidence in the X-ray emission for significant structure beyond the core.

The following X-ray analyses were carried out by Diana Worrall, to aid the understanding of the physics behind the radio structure in NGC 6109. The ISM can affect jet propagation via pressure gradients and buoyancy forces (e.g. Bicknell, 1994; Worrall et al., 1995) so a knowledge of the density and pressure within the ISM, which can be determined directly from X-ray observations, is essential to an understanding of jet dynamics.

As originally discovered by Feretti et al. (1995) using *ROSAT* data, the X-ray environment is complex, with NGC 6109 embedded in a relatively poor cluster environment. With the improved point spread function (PSF) of *Chandra* the emission from NGC 6109 itself is separable into an AGN component and galaxy atmosphere (Evans, 2005). Because cluster emission covers the S3 chip, blank-sky fields were used to sample background for spatial analysis, filtering the source data for times of flaring using the same criteria as applied to the background fields, and re-normalizing to match rates at 9.5-12 keV where the particle component of the background dominates. This cleaning shows the *Chandra* data for NGC 6109 to have been subject to more background flaring than is usual, resulting in just 10.5 ks of data acceptable for using with the blank-sky data. A local (cluster) background was used for fitting spectral models to the galaxy-scale gas, and the flare screening criteria was relaxed to to 3σ clipping and used 19.0 ks of data. All spectral fitting fixes absorption from gas along the line of sight in our Galaxy with $N_{\rm H} = 1.47 \times 10^{20}$ cm^{-2}.

From *ROSAT* it was known that cluster X-ray gas encompasses the two brightest cluster galaxies NGC 6109 and NGC 6107, with an envelope of major axis oriented in a roughly NE-SW direction (Feretti et al., 1995). With *Chandra* data we find that the galaxy atmosphere of NGC 6109 has a similar orientation to the cluster gas; its long axis is orthogonal to the general line of the radio features, as found in a significant fraction of nearby radio galaxies (Duffy et al. 2017, in preparation). While there may be a few excess counts associated with the NW radio jet within about 3 arcsec of the core, there are no obvious X-ray features associated with the counter-jet 'swirl'. In this work a spherical approximation is used to describe the gas distribution as this allows straightforward estimates of pressure, and because the extent of the emission along the line of sight is uncertain.

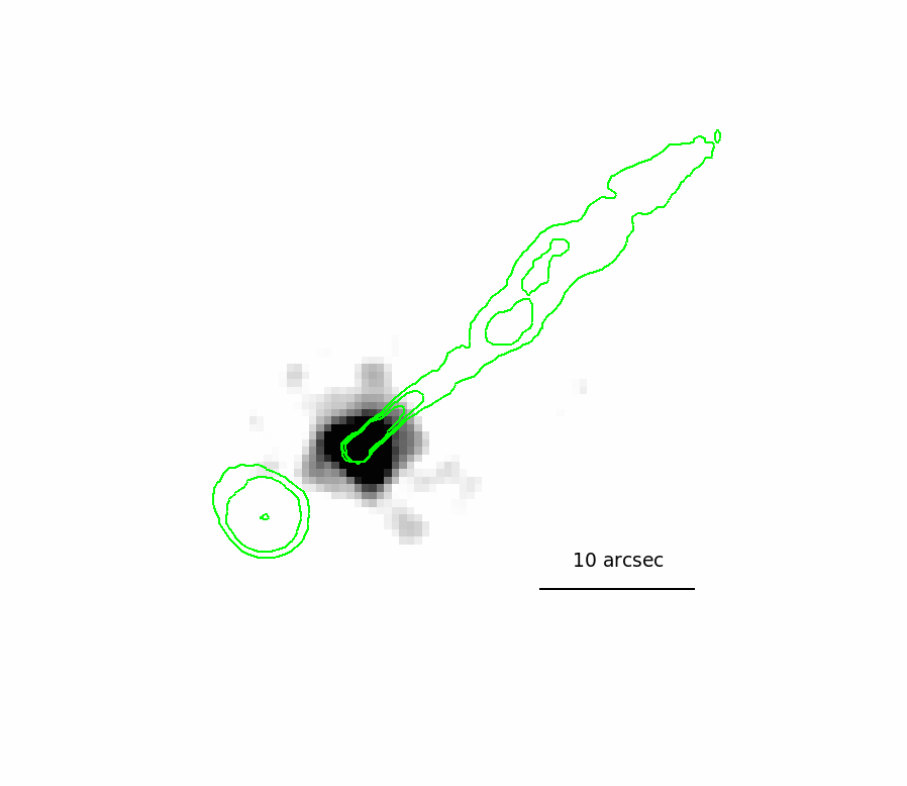

Figure 5.29: *Chandra* X-ray image of NGC 6109 smoothed with a Gaussian function σ = 1.5 arcsec, and with an energy range 500-2000 eV. The image shows JVLA radio contours at 0.1, 0.2 and 0.4 mJy beam^{-1}.

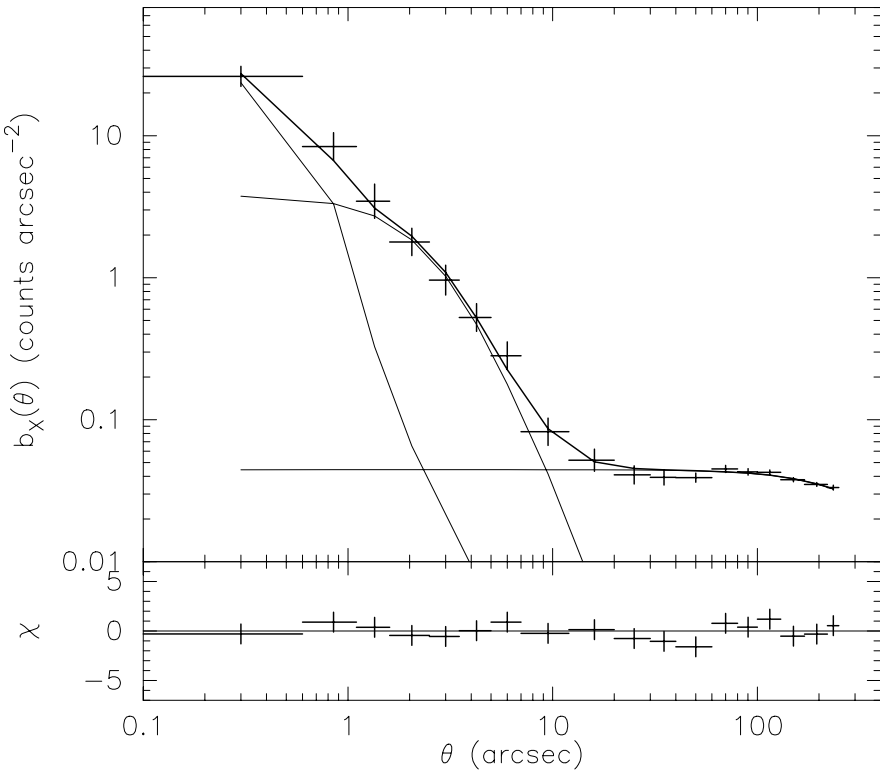

Figure 5.30: Background-subtracted exposure-corrected 0.4-5 keV radial profile. The broadest model component describes the group gas. The narrowest component is the PSF, representing the AGN core, and the their component is a β-model convolved with the PSF, representing the galaxy-scale gas. The galaxy component is best fitted with parameters $\beta = 0.8$, $\theta_{\rm c} = 2.8$ arcsec (χ^2/dof = 9.4/15).

Figure 5.30 shows the radial profile. Within a radius of 10 arcsec of the galaxy nucleus the number of counts in the resolved galaxy emission is roughly twice that in the AGN. Guided by the radial profile, we extracted counts from a core-centred annulus of radii 1.3 and 10 arcsec to sample the galaxy spectrum, with background from a core-centred annulus of radii 20 and 70 arcsec, and the results were fitted to a thermal (APEC) model. Similar results for the temperature were found by fitting all the emission in a circle of radius 10 arcsec to the combination of a power law and thermal emission. Abundances were poorly constrained but showed a preference for low values and were subsequently fixed at 20 per cent of Solar. The fit gives $kT = 0.76^{+0.10}_{-0.12}$ keV (90% uncertainties). This is consistent within uncertainties with the temperature found by Evans (2005) who made the first attempt to separate AGN and gas emission using the *Chandra* data.

Parameters of the gas were measured, including density and pressure as a function of radius using the spatial and spectral results and methodology presented in Birkinshaw and Worrall (1993) and Worrall and Birkinshaw (2006). A total bolometric luminosity is found for the galaxy component of $(1.4^{+0.3}_{-0.2}) \times 10^{41}$ ergs s^{-1}, in excellent agreement with Sun et al. (2007).

5.3 Interpretation

NGC 6109 was originally classified as a 'head-tail' type galaxy by Colla et al. (1975), based on radio observations from WSRT at 50 cm. O'Dea and Owen (1985) re-classified it as a narrow angle tailed (NAT) source, following a VLA snapshot survey of 57 radio sources in clusters. NAT morphology is attributed predominantly to the interaction of radio emission ejecta by a moving galaxy with the intracluster medium (e.g. Jones and Owen, 1979; Christiansen et al., 1981). The bending of the radio jets in NAT's provides important constraints on the physical conditions within the jets and the immediate environment in the galaxy and intracluster medium.

5.3.1 Brightness flaring

The brightness flaring within the NW jet occurs following an extended region in which the radio emission is weak. There is a small amount of geometrical flaring, i.e. an increase in the jet opening angle and the two phenomena are related in that the brightness flaring point occurs just after the jet opening angle begins to increase with distance. The term 'flaring'

has been used elsewhere (e.g. Bridle, 1982; Krause et al., 2012; Laing and Bridle, 2014) to describe both phenomena. Laing and Bridle (2014) investigated the systematic properties of 10 decelerating jets in low luminosity FR I-type radio galaxies from the 3CRR catalogue, in order to infer magnetic field structures and emissivities within the flaring regions. Some of these sources (e.g. NGC 315, 3C 31) display similar morphologies to the bright region in NGC 6109 and at high resolution have been found to contain complex, non-axisymmetric, high brightness structures (e.g. Worrall et al., 2007). Evidence for deceleration accompanied by evolution of transverse velocity profiles within 6/10 of the sources in the sample of Laing and Bridle (2014) supports an interpretation where deceleration in the flaring region is dominated by interactions with the external environment and entrainment of surrounding galactic material. Mass loading due to mass-loss from stars within the jet volume (Phinney, 1983) can also contribute, however it cannot explain the evolution of the velocity profiles. Three distinct mechanisms have been suggested for the sudden brightening within FR I-type jets. Firstly, if the jet is under-pressured with respect to the ambient medium, a stationary recollimation shock can form (Sanders, 1983). The recollimation shock signifies the start of flaring and the high brightness region consists of a series of shocks which form due to oscillation of the jet around pressure equilibrium. The shocks give rise to high emissivity regions through both compression and first-order Fermi acceleration. Secondly, an external pressure gradient can result in the formation of a standing shock (Bicknell, 1984). Thirdly, jets are likely to be unstable to the formation of Kelvin-Helmholtz instabilities (Perucho et al., 2012). Brightness enhancements can be caused by the pressure maxima associated with these instabilities. For NGC 6109, there is no evidence for a jet over-density close to the core, and the external pressure derived from isothermal beta-model fits to *Chandra* observations gives $P = 9.2^{3.1}_{4.8} \times 10^{-13}$ J m^{-3} at 12$''$ from the core (where the brightness flaring is observed). The fits give no strong pressure gradient with distance from the core, however the combination of a small drop in external pressure and Kelvin Helmholtz instabilities could cause flaring (as for 3C 31, Perucho and Martí, 2007). Laing and Bridle (2014) find that in general, the dominant magnetic-field component is longitudinal close to the AGN and toroidal after recollimation for the decelerating jets. I find no specific alignment of the magnetic field vectors within the high emissivity region of the NW jet associated with NGC 6109.

5.3.2 Pressure and energy considerations

A faint radio counter-jet is visible in Figure 5.8, SE of the core. The expression

$$R = \left(\frac{1 + \beta \cos\theta}{1 - \beta \cos\theta} \right)^{3-\alpha} \tag{5.2}$$

gives R, the ratio of the brightness between the jet and the counter-jet where α is the spectral index and θ is the angle between the line of sight and the jet. At 1.8″ from the core, I find R = 17.0 $\pm$ 0.3, constraining βcosθ to 0.51. The equation D = (1 + β cosθ)/(1 - β cosθ) is the corresponding Doppler distance ratio, D and I find D = 3.1. The SE component at a projected distance of 4″ from the core, if moving relativistically with the same speed as the jet, would be associated with a two-sided ejection event that would produce a matching feature 12.4″ along the main jet. Looking at Figure 5.7 and the surface brightness profile in Figure 5.9, the bright knot along the main jet lies 12″ from the core, suggesting that the flaring region could be an outflow emitted at the same time as the SE component, in the opposite direction. Therefore whatever causes the brightness enhancement along the NW jet, could also be responsible for the unusual jet morphology observed to the SE. The constraint on β implies that jets have decelerated to sub-relativistic speeds on the scale of the JVLA maps, but are still moving at a high enough speed for relativistic Doppler terms to be important.

I calculated the equipartition energy density within a cylindrical region using the synchrotron code of Hardcastle et al. (1998), given the flux density at multiple frequencies and the redshift of the radio galaxy. I assumed equipartition between the electrons and the magnetic field and negligible relativistic beaming. For the doughnut region with radius 5″ and an estimated length 3″, U_{eq} = 9.1 $\times$ 10^{-12} J m^{-3}. The NW knot on the main jet side was modelled with a length 20″ and radius 1″, to include the full extent of the flaring region as indicated by Figure 5.9. This gave U_{eq} = 9.5 $\times$ 10^{-12} J m^{-3}. The similarity of these energy densities supports the idea that the knot is the counterpart of the swirl, ejected in the opposite direction. The magnetic field strength in the SW component was calculated as B = 3.2 nT and the minimum pressure P = 2.3 $\times$ 10^{-12} J m^{-3}. The X-ray gas density and pressure out to 20 arcsec (to include the full doughnut component) from the core are found to be $\rho = 1.05^{+0.6}_{-0.6} \times 10^{-3}$ cm^{-3} and $P = 2.8^{+2.0}_{-2.0} \times 10^{-13}$ J m^{-3}, suggesting that the radio component may be slightly over-pressured with respect to the external environment at the furthest point from the core. If the jet lies close to the line of sight, the jet volume may be larger since I have measured only the projected volume. This would decrease the internal pressure slightly, but not by enough to pressure match the radio and X-ray gas. The X-ray pressure out to 10″ from the core (where the counter-jet

enters the radio swirl) is found to be $P = 1.4^{+0.5}_{-0.5} \times 10^{-12}$ J m^{-3}, in approximate equilibrium with the radio emission and the gas density is calculated as $\rho = 5.05^{+0.95}_{-1.4} \times 10^{-3}$ cm^{-3}. The corresponding gas temperature of $kT = 0.76^{+0.10}_{-0.12}$ keV is significantly lower than the temperature deduced by Feretti et al (1995) who fitted an optically thin plasma model to the gas detected by the ROSAT satellite ($kT = 2.4 \pm 1.2$ keV).

Pressure equilibrium between ambient gas and the radio emission in the main jet is reported by Feretti et al. (1995). However they find that further along the tail, about 100 kpc from the core, there is a larger apparent imbalance towards the external pressure dominating. This is consistent with the findings of Killeen et al. (1988) and Feretti et al. (1992). They argue that it is likely that assumptions used for the calculation of equipartition parameters cause the imbalance and that the entire tail is confined by the intergalactic medium. They suggest that the energy ratio between relativistic protons and electrons may be between 20-60, rather than unity, and that the electrons may radiate below the low frequency cut off of 10 MHz.

The unique shape and extreme distortion of the radio emission require an interpretation that can account for the morphology, polarisation structure and rotation measure presented in the previous sections. Helical motion within jets on a parsec and kpc scale has been modelled in both magnetohydrodynamic and force-free jet models (De Villiers et al., 2005; McKinney, 2006; McKinney and Blandford (2009)) and these models have sufficient resolution to compare structure with features observed in AGN jets (e.g. Hardee et al., 2001, Hughes et al., 2002). Hardee (2003) note that the polarisation in helically modelled jets is typically well below the maximum value of 70% for synchrotron radiation. They attribute this to mean that the magnetic field in jets beyond the acceleration region is not well organised.

5.3.3 Signatures of helical jets

Observational signatures of helical jets have been found in X-ray binaries (e.g. Hjellming and Rupen, 1995), planetary nebulae (e.g. López et al., 1993) and the jets of AGN. The term 'helical jet' can describe three distinct jet morphologies, as illustrated in Figure 5.31. Firstly, ballistic helical jets describe jets in which each jet fluid element flows along a straight line but the overall structure is helical due to the periodic change in the ejection direction of the elements. Secondly, the fluid elements within helically bent jets all propagate along a distorted path, delineated by a curved jet axis. Finally, jets with an internally helical structure are straight on a large scale, but individual fluid elements flow

along helical trajectories within the jet.

An important property of helical jet structures is that the observed properties are not always symmetric with respect to the axis of the helix. The proper motion and magnetic field vectors on one side of the helix always point in a direction closer to the line of sight than those on the opposite side. This means that quantities such as the flux, optical depth, polarisation and rotation measure can be asymmetric, especially if the speed of the jet is relativistic. For example the brightness of the jet on the side of the helix where the velocity flow is more aligned to the observer will be enhanced in comparison to emission from the other side. Signatures of helical jets can be revealed by observations of the projected spatial structure, the kinematics of the jet and the variability of the central object.

Relativistic effects can cause apparent superluminal motion and differential Doppler-boosting of the emission. These effects are strongly influenced by the angle between the line of sight and the jet, and are more relevant for helicity observed on a parsec scale.

Some of the observable structural and kinematic signatures are summarised in Figure 5.31. The top example shows a standard straight jet with fluid elements propagating along straight lines in a direction approximately parallel to the jet axis. All the fluid elements point in the same direction and the overall structure shows no bending or distortion. One key parameter of a helical jet is the ratio between the density in the jet and in the external medium. Jet components with a high density can propagate through the ISM without resistance and remain on a straight path in a homogenous medium, thus observations of an oscillating trajectory provides strong evidence for a low density helically bent jet.

5.3.3.1 Ballistic helical jets

For a ballistic helical jet the direction of ejection varies between two limits that define a precession cone with opening angle ψ. The amplitude of the oscillations increases with distance away from the core and the wavelength of the oscillating trajectory remains unchanged. However in practice, the wavelength tends to decrease with distance due to the deceleration of the jet elements as they interact with the external medium. Observations of radially moving jet knots with a decreasing or constant wavelength is a strong indicator for a jet undergoing precession. The proper motion of the observed fluid elements is directed radially away from the core in straight lines.

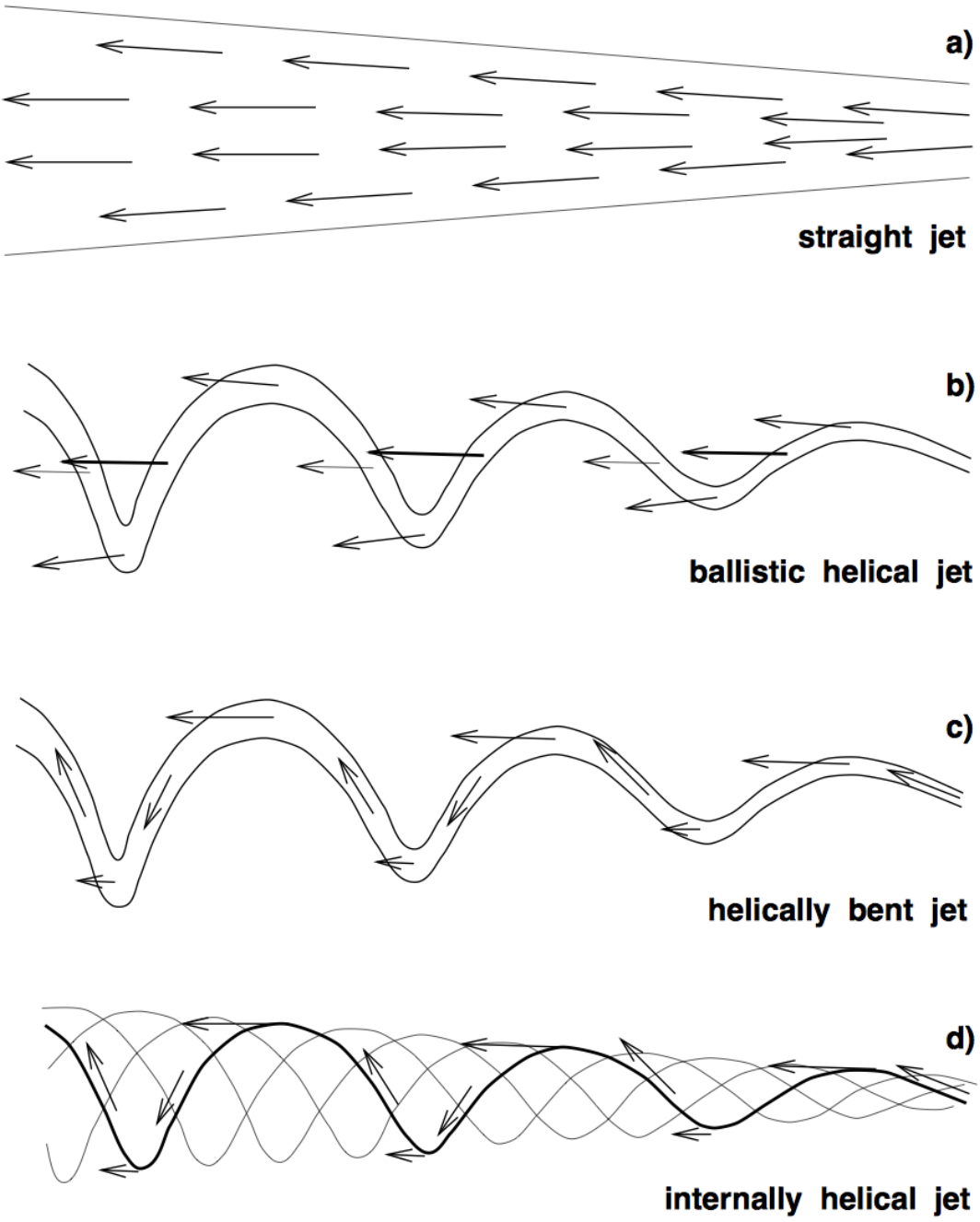

Figure 5.31: The proper motion vectors for a straight jet *(a)* and different kinds of helical jet *(b, c* and *d)* are shown schematically. Reproduced from Steffen (1997).

5.3.3.2 Helical bending

If the jet structure as a whole appears to be helically bent, then the jet elements flow along the helix. If inhomogeneities are present within the jet flow, the direction and magnitude of the proper motion can vary as they flow along the deflected path. In a similar way, the radial velocity is modified since the direction of the velocity vector also changes. These changes are most noticeable on the side of the jet pointing closest to the line of sight. An observational signature of the jet structure being helically bent is that the internal components all move along the same path. In the same way as in the case of jet precession, the overall motion of the helical pattern is directed radially outwards at a roughly uniform speed. The amplitude and wavelength of the oscillations however may vary in a different way.

Several mechanisms can cause jets to bend, such as transverse winds, collisions of the jet with gas clouds, or density gradients in the external medium. Hydrodynamical or magneto-hydrodynamical instabilities can also lead to helical distortions on the surface of a jet (e.g. Appl and Camenzind, 1992; Hardee and Clarke, 1992).

5.3.3.3 Internal helix

For the internal helix structure, the jets are straight on a large scale but the jet fluid elements flow along helical paths within the jet. Doppler effects cause the side of the jet closest to the line of sight to appear brighter than the other, and the degree of observed asymmetry is dependent on the Lorentz factor and degree of twisting within the helix. The path of jet elements flowing along separate helical field lines will differ, so there may be evidence for changes in the oscillating pattern of the emission for consecutive jet features. The internal helix model can be directly associated with the 'sling-shot' model for the formation of jets (e.g. Camenzind, 1986) in which jet plasma is accelerated along magnetic field lines anchored in the black hole and accretion disk. This mechanism produces both a helical magnetic field and a helical flow configuration.

There does not appear to be a straightforward interpretation of the radio morphology in NGC 6109. There is no evidence in the optical or X-ray images for collisions with gas clouds or significant density variations in the IGM. The existence of a high RM along the S edge of the doughnut however, suggests the presence of magnetised plasma interacting with or in front of the radio object. The low fractional polarisation in this region suggests

that the external gas is structured on scales $< 1''$, or causes fine-scale internal structure in the jet, or both. This magnetised plasma could be the remnants of a radio trail from a galaxy that has passed close to NGC 6109. The bright regions in the radio flux could suggest sites of shock compression, where the radio emission has encountered magnetised gas and been compressed, resulting in a dramatic jet deflection. Although viable, this hypothesis does not clearly account for a $>180^\circ$ jet loop.

Although the situation is not clear NGC 6109, provides a fascinating example of a radio morphology not seen in any other known radio source. In the following sections I will discuss the possible mechanisms listed above along with further observations that are needed in order to create a more complete picture of the processes at work.

5.3.4 Ballistic model

A ballistic model of the helical jet, whereby the jet is thought to precess, can explain the doughnut like feature if the angle to the line of sight is taken to be small. The component can then be interpreted as a helical outflow, viewed almost front on so that the emission appears circular. This scenario however, offers no clear explanation of the high regions of rotation measure detected to the S of the component. The large scale structure of NGC 6109 is also suggestive of helical jet morphology. Figure 5.32 shows the 14 arcsec resolution C band observation of the main jet, overlayed with an approximate helical path. The morphology of the jet traces the path well, with the helix expanding out into the external medium as the jet slows down.

Steenbrugge and Blundell (2008) use a ballistic model to interpret the radio emission in Cygnus A. They find that the radio knots that delineate the jet and deviate from a straight line can be satisfactorily fitted with the precession model of Hjellming and Johnston (1981). In this model, symmetric jets are launched at speed β along an axis which traces a cone throughout a precession period P, with opening angle ϕ, inclined to our line of sight at angle θ, in terms of a precession phase ψ. I used a similar ballistic model to see whether I could replicate the observed structure of NGC 6109. I adopted a jet speed of β = 0.5, based on the jet/counter-jet ratio calculations and the angle to the line of sight θ was taken to be small. The simulations model the jet trajectory over approximately 1.9 $\times$ 10^4 years and the parameters used to reproduce the models shown in Figures 5.33 and 5.34 are given in Table 5.6.

I judged the best fit model to be L, which successfully produces the doughnut component sufficiently far from the core. Most of these models all assume a single precession

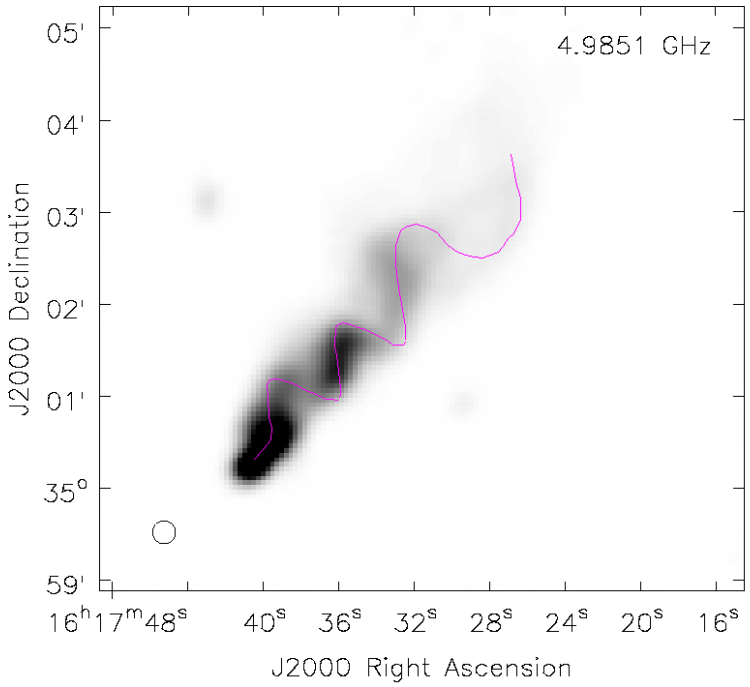

Figure 5.32: VLA image of NGC 6109 at 4.99 GHz and14 arcsec from the BT 7 VLA project. A helical path is traced along the emission to highlight a possible jet trajectory.

Precession cone half angle	precession rate deg/yr	opening angle ϕ	viewing angle θ	Figure label
10	0.02	20	0	A
15	0.02	20	0	B
20	0.02	20	0	C
25	0.02	20	0	D
15	0.04	20	0	E
15	0.01	20	0	F
15	0.02	40	0	G
15	0.02	30	0	H
15	0.02	10	0	I
15	0.02	20	10	J
15	0.02	20	40	K
10	0.02	20	10	L

Table 5.6: The parameters for the ballistic jet models shown in Figure 5.33 and Figure 5.34.

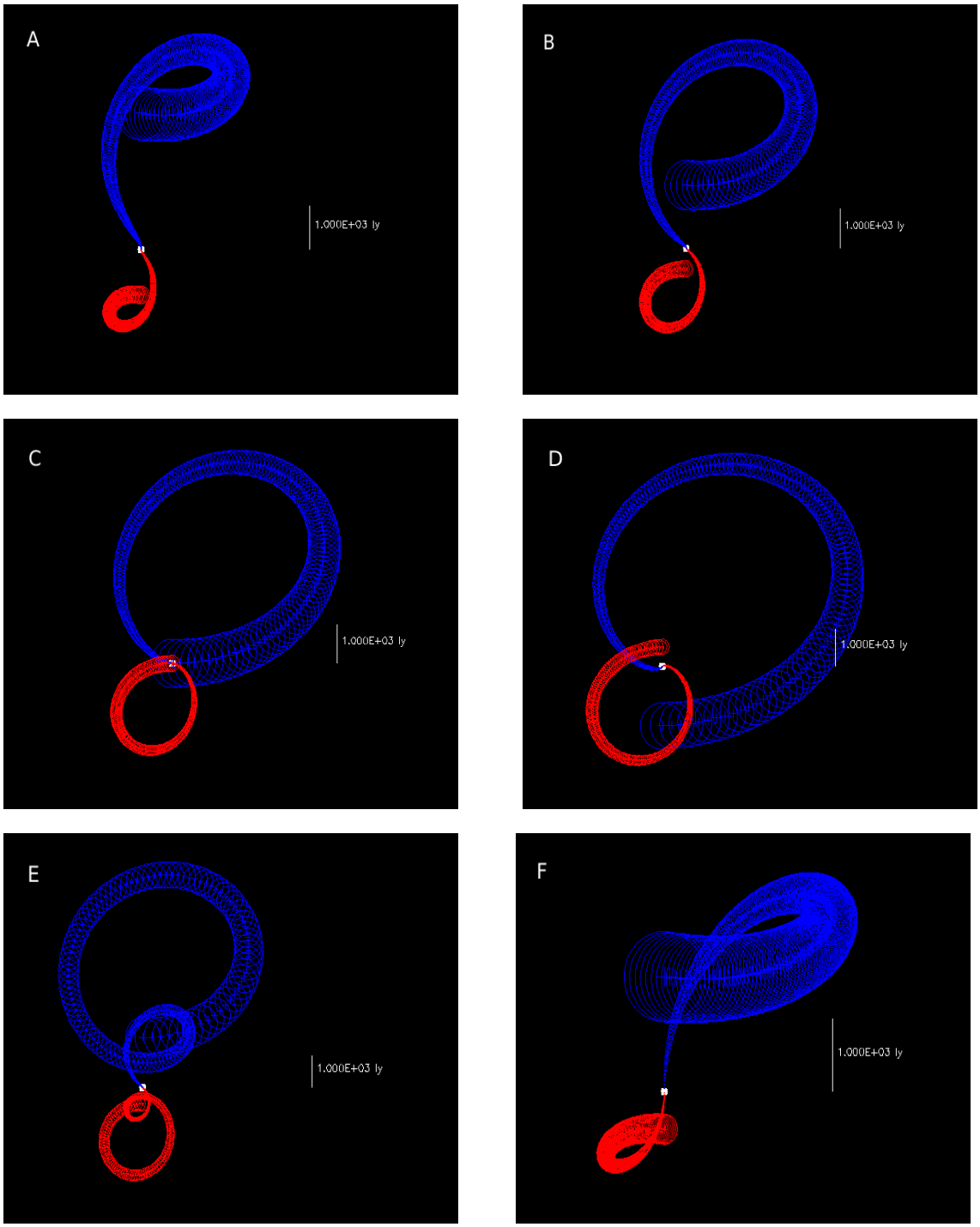

Figure 5.33: Ballistic simulations of the precessing jets in NGC 6109. Different models are labelled and the parameters for each model are given in Table 5.6.

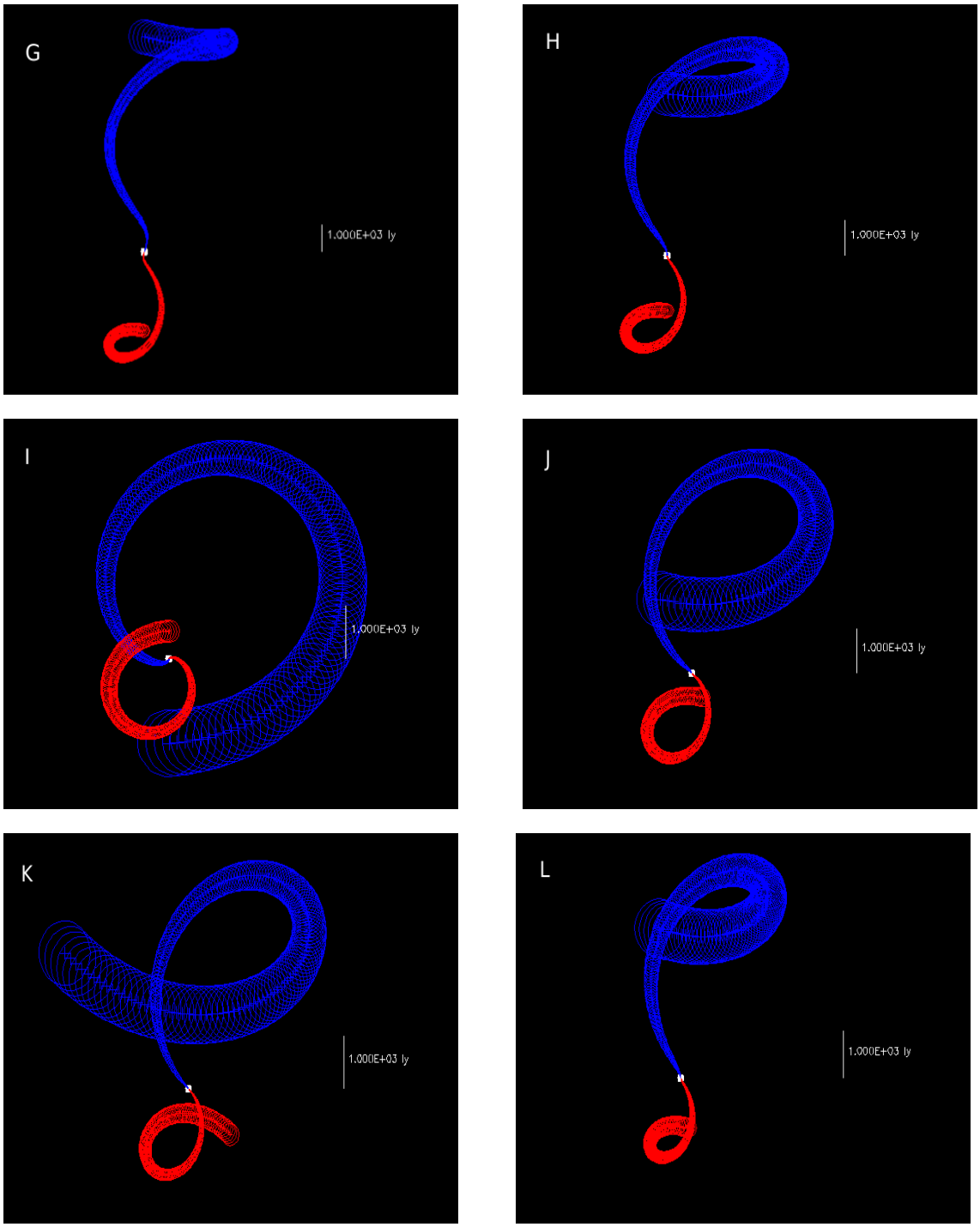

Figure 5.34: Ballistic simulations of the precessing jets in NGC 6109. Different models are labelled and the parameters for each model are given in Table 5.6.

period, with the exception of E, where the precession rate of 0.04 deg/year means that multiple helical turns can be observed over 1.9×10^4 years. The symmetric structure of the component in NGC 6109 suggests that either only one complete turn is observed, or that successive turns are aligned perfectly behind the first turn. If the turns were not perfectly aligned we would expect to see spatially translated ellipses. In contrast, the low precession rate model in D does not form a sufficiently symmetric ellipse to replicate NGC 6109. For models with the precession cone half angle $> 15°$, the circular component is produced too close to the core, overlapping both the core and the opposing jet. The model in L estimates a jet precession period of $T_j = 1.8 \times 10^4$ years.

The ballistic model however, doesn't include deceleration of the jet as it propagates beyond a few kpc, thus can only be used as a guide to whether such extreme jet features can be produced ballistically. Precession models by Gower et al. (1982) highlight how the beam velocity can cause significant geometry changes in twin relativistic jets. As the speed increases from a non-relativistic model with $\beta = 0.001$ up to a relativistic model with $\beta = 0.99$, the approaching beam is stretched and the intensity contrast between increasing and receding beams increases. Therefore a stretch factor between the jets may be a useful diagnostic for β. In addition, Gower et al. (1982) present models of the geometries expected due to precession for different cone angles ϕ and values of β, for all angles of inclination. Their results suggest that tighter swirls and a more symmetric structure can be achieved for lower values of β.

5.3.5 Jet precession

Although a precessing jet model is a possible explanation for the observed structure of NGC 6109, is it not clear why the black hole would be precessing. A few mechanisms have been suggested for such a movement; a binary black hole causing the disc of the primary black hole to precess (Katz, 1997; Caproni and Abraham, 2004), an instability in the disk caused by radiation pressure forces or magnetic fields (Pringle, 1997; Liu and Melia, 2002) and the Lense-Thirring dragging of inertial frames (Roos, 1988; Caproni et al., 2006b).

The passage of a secondary black hole through the primary accretion disk can produce density waves and induce shocks in a jet (Romero et al., 2000). Evidence for central engines of AGN formed by massive binary systems includes double nuclei (NGC 4486B, Lauer et al., 1996), wiggly jets (e.g. Kaastra and Roos, 1992) and periodic optical light curves (OJ 287, Villata et al., 1998). Radio structure associated with the AGN, built up

over many precession periods, will be aligned with the orbital angular momentum. On scales observed by the VLA however, precession related curvature could be discernable.

In this mechanism, the spin axes will undergo geodetic precession about the total angular momentum, and for the more massive black hole the precession period $P_{\rm prec}$ in years is given by Begelman et al. (1980) as

$$P_{\rm prec} = 600 r_{16}^{5/2} \left(\frac{M}{m} \right) M_8 \tag{5.3}$$

where r_{16} is the distance in cm ($\times$ 10^{16}), M is the mass of the larger black hole and m is the mass of the smaller black hole.

If the radio plasma is sufficiently collimated near a black hole then the Lense Thirring effect aligns the jets with the black hole axis, and the beams will then precess with a period $\rm P_{prec}$.

Using the jet precession period of 1.8×10^4 years, as suggested by the ballistic model, a black hole mass M_8 = 1 and binary mass ratio M/m = 10, gives an orbital radius of the order 5 pc. This corresponds to a wide binary system, where the precession time scale should be comparable with the inferred lifetime of extended radio components.

The orbital time period for the binary system is given by

$$P_{\rm orb} = 1.6 r_{16}^{3/2} M_8^{-1/2} yr \tag{5.4}$$

assuming Keplerian motion. For r = 5 pc this gives $P_{\rm orb}$ = 600 yrs.

Evidence for a binary system could be provided from the detection of double or displaced emission lines. Broad emission lines may originate in a region around the larger black hole, whereas narrow line emission could come from a system enveloping the binary. The broad lines may then peak at a different velocity from that of the galaxy as determined by the narrow lines (Begelman et al., 1980). These lines however would be hard to distinguish from outflow.

Radiation driven instabilities can lead to warping and precession in accretion disk systems. Petterson (1977) showed that if an accretion disk is optically thick, the radiation pressure will produce nonaxisymmetric torques that will change the initial configuration of the disk. This instability has been used to explain anomalies in the morphology in a number of astrophysical sources. Such sources include X-ray binary systems (Ogilvie and Dubus, 2001) and the maser disk of NGC 4258 (Maloney et al., 1996). Caproni et al. (2006b) however, find that in the case of an AGN, the critical radius at which the disk

becomes unstable to irradiation warping is larger than the outer disk radius for all AGN within their sample. This suggests that for these objects, and therefore also for NGC 6109, the disk is stable against radiation torques.

The influence of magnetic fields on accretion disks has been investigated for magnetised central objects such as neutron stars and white dwarfs, where the stellar magnetic field can induce disk warping and precession (e.g. Lipunov, 1980; Terquem and Papaloizou, 2000). Lai (2003) has extended these results for non magnetised central sources, and showed that a large scale magnetic field threading the disk can also induce a warping instability and precession due to an interaction with the induced electric current in the disk. This was supported by non-linear simulations carried out by Pfeiffer and Lai (2004) in which warped accretion disks driven by magnetic torques undergo rigid-body precession. However it is not yet know what could provide the large scale magnetic field.

Finally, the Lense-Thirring effect can cause jet precession. The Lense-Thirring effect is the frame dragging produced by a rotating compact body that causes precession of a particle if its orbital plane is inclined in relation to the equatorial plane of the rotating object (Lense and Thirring, 1918). The precession angular velocity $\Omega_{\rm LT}$ is given by (e.g. Wilkins, 1972)

$$\Omega_{\rm LT}(R) = \frac{2G}{c^2}\frac{J}{R^3} \tag{5.5}$$

where $J = aGM^2/c$ is the black hole angular momentum and a is the black hole spin parameter. For a precession period T_{prec} = 1.8 $\times$ 10^4 years, a black hole mass in the range $10^8 \leq M \leq 10^{10} M_\odot$ and a spin parameter a = 0.1 - 0.9, the orbital radius R is constrained to $1 \leq R \leq 40$ parsec.

Nixon and King (2013) argue that the Lense Thirring effect alone is not a promising mechanism for explaining jet precessions, because the accretion disc generally has total angular momentum small compared with that of the spinning black hole, strongly restricting the motion of any jet across the sky. They suggest that rapid precessions could occur if the disc plane is broken into distinct planes by large disc tilts. This would happen when the Lense-Thirring torque is strong enough to overcome the viscous torques holding the disc together (Nixon and King, 2013). As a result, they propose that additional disk physics is needed to explain observations of jet precession, and offer alternative mechanisms that although largely unexplored, may offer more promising techniques for moving jets.

The combined action of the Lense-Thirring effect and the internal viscosity of the accretion disk forces the alignment between the angular momenta of the black hole and the accretion disk, and this is known as the Bardeen-Petterson effect (Bardeen and Petterson, 1975). This effect only concerns the innermost part of the disk due to the short range of the Lense-Thirring effect, while the outer part of the disk remains in its original configuration. Thus the structure of an accretion disk around a rapidly rotating black hole has a warped structure that could be divided into three distinct regions: inner region, transition regions and outer region. This effect induces a precession around the rotation axis of the black hole and Scheuer and Feiler (1996) showed that the disk alignment and precession time scales are identical. This mechanism has been invoked to explain precession and a progressive change in the jet direction in NGC 1097 (Caproni et al., 2004) NGC 1068 (Caproni et al., 2006a), and NGC 4258 (Caproni et al., 2007).

The Bardeen Petterson transition radius for a thin disk, based on the hydrodynamic simulations of Nelson and Papaloizou (2000), can be expressed as

$$R_{\rm BP} = Aa^{2/3}R_g \tag{5.6}$$

where the scaling parameter A is a function of the viscosity of the radial accretion (Shakura and Sunyaev, 1973) and the aspect ratio of the disk, with $10 \leq A \leq 300$. This suggests $R_{BP} > 1$ parsec for the NGC 6109 system.

The Bardeen Petterson effect is a viable mechanism for causing precession that could explain the structure of doughnut component and apparent helical jet trajectory on a large scale in NGC 6109. Jet precession however cannot account for the observed magnetic field and rotation measure structure. In the precessing system SS 433, the magnetic field is found to track the helical trajectory of the jet on a parsec scale (Hjellming and Johnston, 1981, Stirling et al., 2004). If this magnetic field structure remains stable out to kpc scales during jet precession, then we would expect to see a circumferential field within the doughnut component. Although this field is observed S of the component, the majority of the field structure in the component is radial. SS 433 also shows evidence for high fractional polarisation at the leading edges of the helices (Roberts et al., 2008) produced as the jet material flows into an ambient medium containing a tangled magnetic field. The resulting compression orders the field in two dimensions (Bridle and Perley, 1984). NGC 6109 is not significantly polarised at the edges of the doughnut, highlighting the lack of large scale ordering of the magnetic field in this region. The presence of a non-uniform rotation measure within the component supports the hypothesis that some

external magnetic material may be contributing to, or causing the large jet bending.

5.3.6 Helical jet bending

A significant number of radio galaxies have been reported to display jet bending on kpc scales. Parallels between NGC 6109 and NGC 7385 can be drawn, as both have been categorised as low redshift 'head-tail' galaxies by the 3CRR survey (Laing et al., 1983) and exhibit $\geq$180° jet deflections. In the case of NGC 7385 however, our Hubble Space Telescope (HST) data revealed a large optical cloud in the path of the counter-jet, and the interaction between the jet and the cloud is believed to cause the strong jet bending (Rawes et al, in prep). Unfortunately NGC 6109 has not been observed with HST, however multiple optical observations from *Spitzer*, CFHT and KPNT show no similar diffuse gas clouds in the vicinity of the counter-jet component. Therefore although both objects exhibit significant jet bending, different mechanisms are required to explain the deflections.

Less extreme jet bending has been observed in other FR I-type galaxies (e.g. 3C 66B, Hardcastle et al., 1996; 3C 321, Evans et al., 2008), and it is possible that the mechanisms which produce these deflections could also apply to NGC 6109. Various proposals for bending jets include buoyancy or ram pressure in a dense ICM (Miley et al., 1972), orbital motion (Blandford and Icke, 1978; Roos et al., 1993) and precessing jet models (Condon and Mitchell, 1984).

Eilek et al. (1984), studying the wide-angle tail source 3C 465, modelled the C-symmetric source in several bending scenarios. Since the jets within the host galaxy are straight, all models ascribe the effect to the ICM. They conclude that the most likely model is bending due to the large-scale velocity of magnetised plasma in the ICM. This is because the source is at the centre of a cluster and thus has no large scale velocity of its own to explain the bending. NGC 6109 belongs to a small concentration of galaxies at one edge of the cluster Zw 1611+3717 (Ulrich, 1978), which itself lies in a supercluster extending over 60 Mpc. If large scale velocity structures from the ICM were responsible for the jet bends, then the main jet would also be significantly bent once it reached beyond the galaxy's ISM (a few kpc), and this is not observed.

A high fractional polarisation and well ordered magnetic field are often observed in bent jets and indicate shearing or compression of the radio source as it propagates through the intercluster medium. Miley et al. (1975) attribute the curved path of the radio trail in NGC 1265 to the orbit of the galaxy through the cluster and differential motions of the

cluster medium. They report fractional polarisation as high as 60% and well ordered magnetic field vectors along the radio emission. This is not the case for NGC 6109, the fractional polarisation reaches only 30% in the highest regions and is around 10% everywhere else.

The effect of galactic ram pressure and pressure gradients on jet deflection have been investigated (e.g. Jones and Owen, 1979; Begelman et al., 1979; De Young, 1991) in terms of the bending equation:

$$\frac{\rho_j v_j^2}{R_{\text{bend}}} = \frac{\rho_{\text{icm}} v_g^2}{R_p} \tag{5.7}$$

where ρ_j and v_j are the density and velocity of the jet, R_{bend} is the radius of curvature of the jet deflection, ρ_{icm} is the density of the ICM and v_g is the velocity of the parent galaxy. The term R_p is the scale over which the ram pressure acting on the beam changes, and I set this equal to the width of the jet (e.g. Begelman et al., 1979; Jones and Owen, 1979) (i.e. $R_p \sim 1$ kpc). Adopting $\rho_{\text{icm}} = 5.1 \times 10^{-3}$ cm^{-3} (see section 5.3), $v_g = 8.9 \times 10^6$ ms^{-1} (Ulrich, 1978), $\rho_j = 6 \times 10^{-4}$ cm^{-3} and $v_j = 1.5 \times 10^8$ ms^{-1} gives a radius of curvature $R_{\text{bend}} = 29$ kpc. Galactic ram pressure is therefore not strong enough to cause the tight jet bending within NGC 6109.

The strong rotation measure in the S region of the doughnut component is suggestive of some external magnetic medium being responsible for, or contributing to the large scale bending seen in NGC 6109. Although the precession model can replicate the observed structure, it cannot explain the complex RM and magnetic field configurations observed. An alternative explanation is therefore required which can combine both the morphological and polarisation observations. Such a model involves an interaction between the radio plasma and some unknown magnetic plasma, causing a major deflection of the path of the radio jet. A diagram of such a trajectory is given in Figure 5.35. As the counter-jet turns, compression of the jet leads to the formation of shocks, which are evident as a brightening of the radio emission. At the S the magnetic field is circumferential, and appears to track the bending of the radio jet. Evidence for this magnetic gas is seen in the rotation measure and fractional polarisation maps, where the emission has been depolarised by the presence of structured Faraday rotating material. The radio jet continues to deflect around a helical path, and high flux is seen to the NW of the structure, as a result of possible superposition of the jet with itself. This deflecting gas then slows down and is observed as diffuse emission to the NE. Here the magnetic field is radial as it spreads out into the

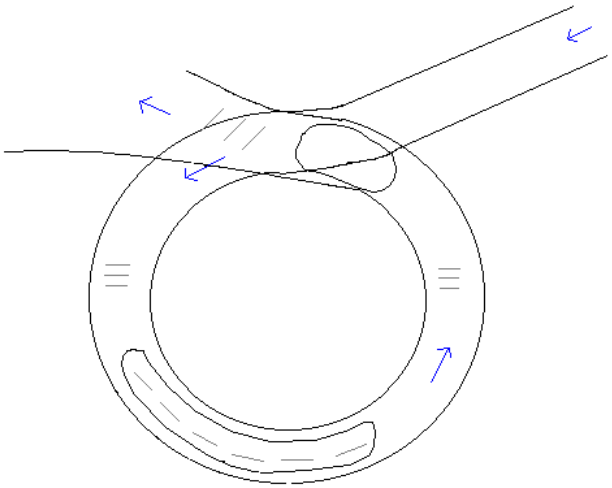

Figure 5.35: A diagram of the possible jet trajectory. Blue arrows show the path of the jet, and grey lines show the magnetic field direction in that region. Regions of high flux and high RM are indicated to the SE and NW of the structure.

external medium. Along the E edge of the diffuse emission, the magnetic field is longitudinal, possibly tracking the edge of the diffuse emission. The radial field lines observed through the centre of the structure require an explanation, and could possibly be the result of compression due to the action of the external magnetic field.

The gas density of n_e = 10^{-3} cm^{-3} at 10″ from the core, as determined from the X-ray analysis can be used to provide an estimate for the magnetic field strength causing the high RM observations. The line of sight magnetic field B$_{//}$ is calculated using the equation

$$RM = 0.81 \int n_e B_{//} dl \tag{5.8}$$

where the rotation measure is measured in rad m^{-2}, n_e is the electron density, in cm^{-3}, $B_{//}$ is the line of sight magnetic field, in μG, and dl is the path length, in parsec.

For RM = 200 rad m^{-2} and assuming a path length of approximately 1 kpc, $B_{//}$ = 25 μG, or 2.5 nT.

This magnetic field strength is of the same order as that observed in the lobes of AGN, but lower than the value of B_{eq} calculated in section 5.3.2. This lends support to the

idea that the magnetic plasma could be remnants from a radio galaxy that passed close to NGC 6109, leaving behind a faint magnetised trail. This trail would not be observed by the VLA, but could possibly be probed with X-ray spectroscopy or a low-frequency, high resolution map of the field by (e.g.) LOFAR. An elliptical trajectory caused by the wake of another galaxy has been observed before, in the low power FR I-type galaxy NGC 7016. Similarities and parallels between these two galaxies will be drawn in the next section, along with a discussion on the prevalence of galaxies with extreme jet deflections.

One difficulty this model faces is why an interaction with magnetised gas would cause the jet to continuously bend, rather than deflect and then continue on a linear path. A 180° jet reversal is observed in NGC 7385, but this source requires a further push to complete a the observed loop.

5.4 Summary

The radio structure in NGC 6109 shows a jet bending through $> 180°$. The remarkable morphology can be explained by a helically bent jet deflected due to an interaction with magnetised plasma. It is also possible that precession of the jet on a kpc scale could be responsible for the helical structure, however this interpretation cannot account for the polarisation properties of the radio components. Low-frequency observations are needed to probe the magnetised plasma further; these studies would be able to map weak magnetic fields and trace the path of the counter-jet as it slows down and emerges from the loop.

Chapter 6

The prevalence of large scale bending in radio sources

In this chapter I discuss a few other sources which show large scale bends comparable to those in observed NGC 7385 and NGC 6109. I give details of VLA observations of NGC 7016 and NGC 7018 that I use to map the radio intensity and polarisation, in order to compare the features with NGC 6109. Finally, I discuss the surveys which have catalogued nearby radio galaxies and the future surveys which will be used in order to extend this sample in the search for more kpc scale jet bends.

6.1 Large Jet Bends in Other Sources

QSO 0800+608 (z = 0.689, Hewitt and Burbidge, 1989) provides an interesting comparison with NGC 6109 because it shows a strongly curved radio feature emitted in the opposite direction to a straight collimated jet (Sivakoff, 2001). 8.44 and 1.56 GHz VLA maps for the object provided by Mark Birkinshaw are shown in Figure 6.1. At 8.44 GHz, a straight collimated jet is seen extending to the NE of an unresolved core. Multiple bright knots are seen within the jet, out to a projected distance of 18″. To the S, a faint counter jet is visible, with bright curved emission seen 8″ from the core. At 1.56 GHz, the S component is more prominent, and shows a strongly curved trajectory that draws resemblance to the feature within NGC 6109. Based on the detection by Jackson et al. (1990) of a diffuse optical source located 4″ SW of the core, Sivakoff (2001) used simulations of a counter-jet that collides into a diffuse optical cloud to attempt to explain the observed structure. Jackson et al. (1990) postulate that the outgoing counter-jet suffers a

collision which deflects and slows it, in a similar way to the mechanism proposed for 3C 275.1 (Stocke et al., 1985). The simulated maps produced by Sivakoff (2001) exhibit an extended spherical structure; where the highest flux is found at the centre of the extended emission (at the location of the cloud) rather than at the edges as is seen in Figure 6.1. The simulated emission also extends beyond the location of the collision, not maintaining a roughly symmetric shape. A collision hypothesis is therefore rejected for explaining the morphology of this object.

Sivakoff (2001) also dismisses a bent jet scenario, suggesting that such a geometry which requires the jet to bend through $> 90^{\circ}$ is contrived. No significant rotation measure is found for this source by Sivakoff (2001) with VLA data, however depolarisation maps produced by Jackson et al. (1990) show a rise in the degree of depolarisation towards the SW part of the counter-lobe structure, approximately $6''$ from the core. These results also show a projected magnetic field circumferential at 6 cm, but a large rotation in position angle between 6 and 20 cm, indicating Faraday rotation due to thermal material either outside or inside the lobe. High-resolution and sensitive JVLA observations of this quasar may reveal rotation measure structure undetectable by the narrow bandwidth receivers of the VLA. Further observations would be useful for comparison to NGC 6109 and for constraining the parameters of both the jets and external environment involved in producing such distorted radio structures.

MRC B1221-423 is a member of a sample of southern radio sources similar in power to the 3CRR sources (Burgess and Hunstead, 2006, see section 6.3). Optical emission within the host galaxy is distorted; clear signatures of interaction including tidal tails and shells are observed (Safouris et al., 2003). The source has a redshift of $z = 0.1706$ (Simpson et al., 1993) and is classified as a compact steep-spectrum (CSS) source. These sources are bright but compact, and radio emission from these sources lies well within its host galaxy. Radio contours of the jets in MRC B1221-423 produced by Johnston et al. (2010) are shown in Figure 6.2. The S jet undergoes an interaction with the host galaxy, and is bent through 180°. The projected length of the S jet from the optical nucleus to knot F (see Figure 6.2) is 8.6 kpc. The N jet is shorter, with a projected core-jet distance of only 2.5 kpc.

A high fractional polarisation (> 50 %) is observed at the E and S edges of the source. The orientation of the magnetic field with respect to the jet direction varies significantly across the source. The magnetic field is perpendicular to the jet path at knot D, before rotating to become circumferential to the jet direction along the component edge between

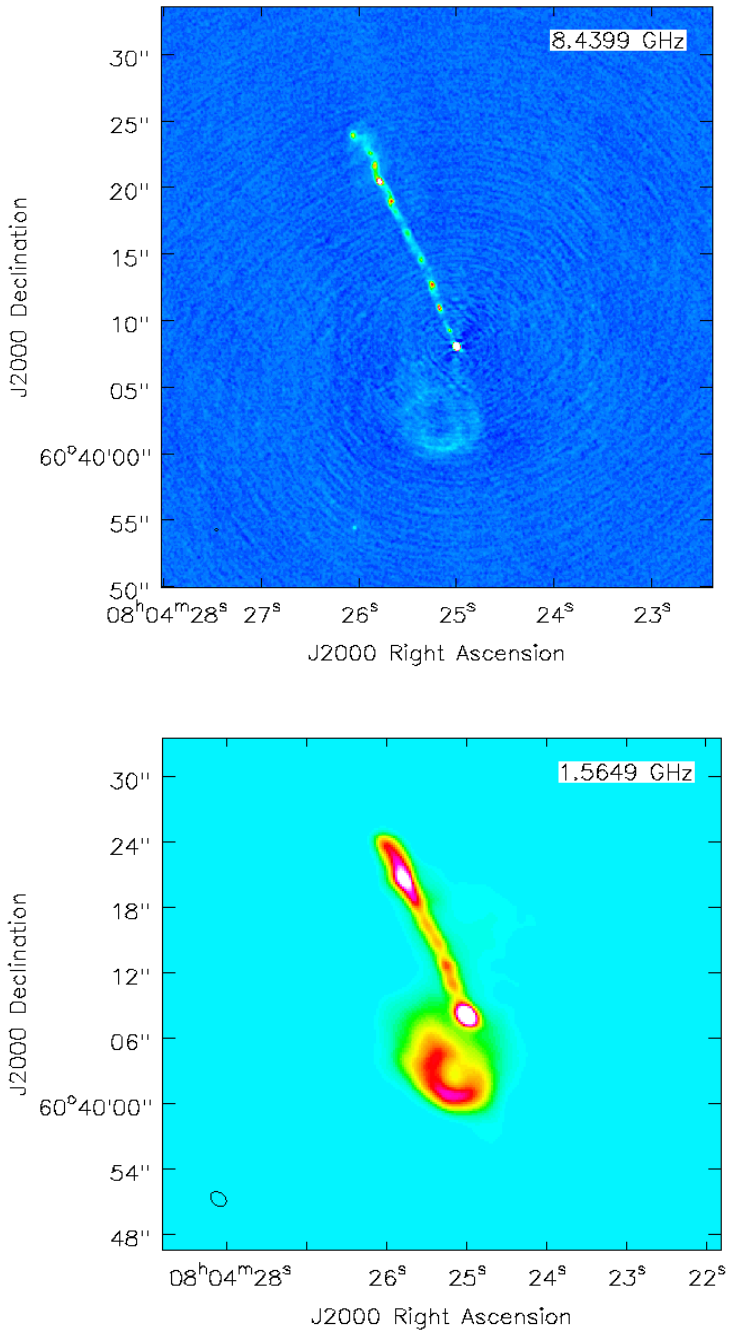

Figure 6.1: VLA radio maps at *(top)* 8.44 GHz and *(bottom)* 1.56 GHz.

knot D and F, where the extreme bending occurs. The field then rotates once again to perpendicular to the jet axis, beyond knot F.

The N half of the source is found to have a Faraday depth of approximately -800 rad m^{-2}, while the S half is approximately -30 rad m^{-2}. The latter value is close to that of the Galactic foreground RM, however Johnston et al. (2010) suggest that the large Faraday depths associated with the N lobe are a consequence of a magnetoionic screen local to the source. This N lobe is found to be significantly depolarised with decreasing frequency, implying small-scale inhomogeneities in the Faraday screen. There is no significant depolarisation in the S jet.

Johnston et al. (2010) also detect HI in absorption, with a narrow component with a velocity difference of 250 km s^{-1} compared to the velocity of the galaxy determined from the stellar component. The combination of this absorption and the radio continuum observations suggest that the source is in a gas rich environment. The location of the absorbing gas is not clear from the observations. The narrow absorption components could represent a discrete cloud at some distance from the galaxy, however higher resolution HI observations are required to investigate this further.

The morphology of the S jet can be interpreted as due to an interaction between the jet and gas in the host galaxy. The alignment of the magnetic field along the jet supports the interpretation of the S component as a single connected structure. This field could be produced by shearing of the field into a direction tangential to the source boundary (Blandford and Rees, 1978) and is a structure commonly observed in other sources where jet bending is evident. Interestingly there is no evidence in the RM structure for a dense ISM in the jet bending region. Johnston et al. (2010) describe two possible scenarios to explain the jet bending. Firstly, that the extreme change in projected jet direction can be explained by a helical jet viewed almost head on. The lack of evidence for a dense ISM at the jet bend is consistent with this interpretation. Secondly, that infalling gas could be interacting with the jet, producing a significant jet deflection and an asymmetric polarisation structure in the lobes. Saikia and Gupta (2003), also attribute a high degree of polarisation asymmetry in CSS sources to an interaction between jets and infalling material.

This source therefore provides another example of extreme jet bending caused by a possible interaction with the external environment. The scale of the bending is similar to that in NGC 7385, despite all the radio emission being confined within the host galaxy. Both sources show a similar polarisation structure, where the magnetic field vectors track

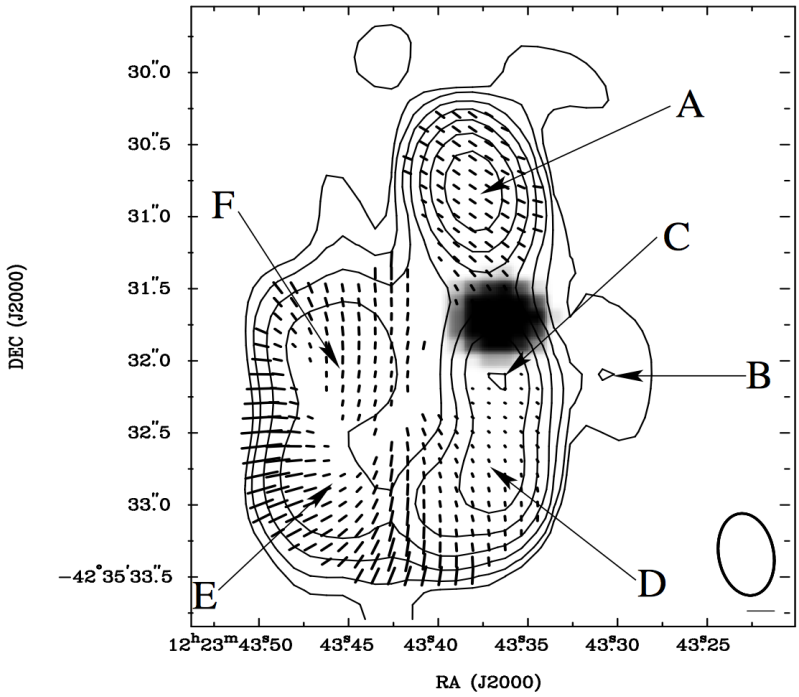

Figure 6.2: Total intensity contour map of MRC B1221-423 at 19.3 GHz, with the position of the optical nucleus shown in greyscale. Vectors show the projected electric field at each pixel location, uncorrected for Faraday rotation. The scale bar in the bottom right hand corner corresponds to 50% fractional polarisation. Reproduced from Johnston et al. (2010).

the bending of the jet and the ordering of the field increases towards the jet edges.

Significant jet bends are often observed on VLBI scales, where large angle misalignments are often attributed to projection effects. In particular, some core dominated radio sources (e.g. 3C 309.1, Wilkinson et al., 1986) have been observed with large angle misalignments and the distribution of these angles has been extensively studied (e.g. Pearson and Readhead, 1988; Conway and Murphy, 1993). These studies found peaks of misalignment angles at 0° and 90°, and angles $> 180°$ to be rare. The bent jets of NGC 7385 and NGC 6109 are not moving with large (≥ 2) bulk Lorentz factor γ, and are assumed to have jet speeds of around $\beta = 0.5$, in accordance with other FR I-type jets observed on arcsecond scales and based on calculations of the jet to counter-jet ratio R. Projection effects are not likely to play a significant role in the interpretation of these objects, however it is interesting to note that even on milliarcsecond scales, jet bends of this order are not expected, or observed.

6.2 NGC 7016 and NGC 7018

A loop-like structure is also observed in the FR I-type radio source associated with the galaxy NGC 7016. The galaxies NGC 7016 and NGC 7018 reside in the central regions of cluster A3744 at $z = 0.0381$ (Mazure et al., 1996). The structure of the radio emission associated with these galaxies is remarkable, with both exhibiting 'tendril' like features which extend into the external medium for hundreds of kpc. The sources show very different morphologies and structures, despite having similar luminosities. This provides a unique opportunity to examine and understand the intrinsic differences related to different source morphologies for two sources in the same cluster of galaxies and hence with very similar environments. Furthermore, the two sources have luminosities close to the characteristic break point between the classification of FR I and FR II-type sources thus this complex radio system also provides a chance to examine the transition between these classes and hence a better understanding of the physical mechanisms responsible for governing radio source morphology.

For the present study, I used observations of NGC 7018 and NGC 7016 from the VLA archive at 1.26-1.39 GHz. These are the same observations used by Worrall and Birkinshaw (2014) however I have built upon this work by including polarisation studies and rotation measure fitting of the data. These observations have a bandwidth of 128 MHz, allowing observations at different frequencies but with the same resolution to be

Project code	Config	Date	Frequency range (GHz)	BW (MHz)	Time (s)	Resolution (arcsec)	Flux calibrator
11A-199	A	11-June	4.83-4.96	128	27360	0.4	3C 48
11A-199	A	11-June	1.26-1.39	128	15700	1.4	3C 48

Table 6.1: VLA observational details of NGC 7016 and NGC 7018.

produced. An absolute flux density scale for the observations was obtained using the primary flux calibrator 3C 48. Phase calibration of the VLA antennas and the atmosphere was based on the calibration source J2129-1821, which was observed at approximately two minute intervals. Calibration of the observations used the standard VLA calibration programs, and followed the methods described in chapter 2. The observational details are given in Table 6.1. The large scale radio structure of the two sources is given in Figure 6.3, at 1.39 GHz with a resolution of 1.4 arcsec.

NGC 7018 (N source displayed in Figure 6.3) shows a double-lobed structure with hotspots at the outer edges of the lobes and a low flux jet associated with the N lobe. The NE hotspot is a double hotspot, oriented in the E-W direction and the jet cannot be traced all the way to the hotspots. The flux density of NGC 7018 is found to be 4.6 Jy at 1.39 GHz, corresponding to a power of approximately 10^{25} W Hz^{-1}. This is on the lower end of the limit for the power of an FR II-type source (Bridle and Perley, 1984). The projected distance of the hotspots from the core is 37 kpc. The flux density of the E hotspot is 45 mJy at 1.39 GHz and that of the W component is 51 mJy. W of the hotspots the lobe shows a distinct edge in the NW-SE direction.

There is a single hotspot in the SW lobe, with a flux density of 30 mJy at 1.39 GHz at a projected distance of 55 kpc from the core. There is no evidence for a counter-jet between the core and the SW hotspot. The surface brightness in the SW lobe decreases smoothly away from the hotspot, while the surface brightness of the N lobe is more irregular.

A long tail is seen to extend from the SW lobe towards the W, and the surface brightness along this tail is irregular, suggesting discrete features. The tail extends W for approximately 48 kpc, bends to the NW for 25 kpc and then deflects through 90° towards the SW. Faint diffuse emission is detected up to 160 kpc from the core. Cameron (1988) and Worrall and Birkinshaw (2014) report a second tail trailing the N lobe in the NW direction. This second tail is not visible at 1.39 GHz in Figure 6.3 but diffuse emission is detected N of the W edge of the lobe.

Cameron (1988) find the spectral index along the tails to steepen with distance from the lobes, indicative of outwards motion. They compared NGC 7018 with the sample of

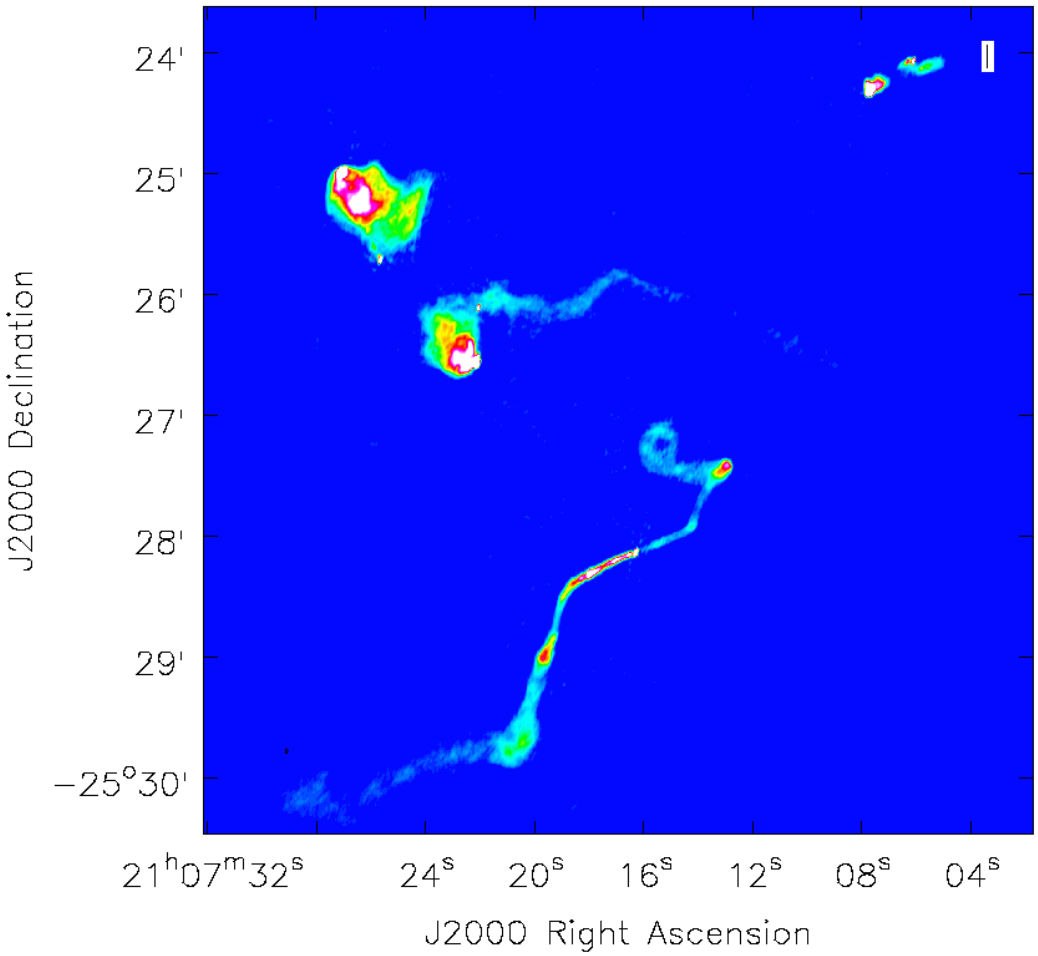

Figure 6.3: VLA total intensity image of the two radio sources associated with NGC 7018 (upper source) and NGC 7016 (lower source), at 1.4 arcsec resolution and 1.39 GHz. A small background source showing a double structure lies NW of NGC 7018.

Leahy and Williams (1984) and showed with lower-resolution maps that the tails could be an extreme example of distorted back flow from the lobes. Buoyant tendrils extend out to the cluster's extremities, potentially a result of the galaxy's motion and consequent drag. The bends in the W tendril could be caused by atmospheric winds.

A small background source showing a double structure lies NW of NGC 7018, and a background point source is superimposed on the base of the W tail. The opening angle of the tails is approximately 56°, measured between the core and the start of the tails. The surface brightness distribution along the tails is given by Cameron (1988). The NW tail shows fluctuations in both surface brightness and FWHM, in terms of bright emission separated by regions of lower surface brightness. Cameron (1988) interprets this as evidence for the presence of separate blobs of plasma within the tail. Within the W tail, the surface brightness shows a smoother decrease along its length, but also displays fluctuations in the FWHM.

NGC 7016 shows an FR I-type jet structure, in which the jets emanating from the core change into plumes which gradually decrease in surface brightness and disappear. This source is seen in Figure 6.3 to the S of NGC 7018. Close to the core, the SE jet and NW counter-jet are straight, however at 30-35″ sharp asymmetric jet bends are observed. The main jet extends SE before bending towards the S by approximately 50° and shows an overall gradual decrease in surface brightness along its length. The jet shows a region of enhanced surface brightness where it undergoes a 70° bend to the E about 115″ from the core . Beyond this point the jet develops a cocoon of emission, possibly marking the transition of the SE jet to a plume. Plumes can be identified by a continuous steepening of the spectral index and observations of a magnetic field aligned with the surface brightness ridgeline (Bridle, 1988). The feature culminates with a drop in surface brightness, with a total projected length of 300 kpc.

On the counter-jet side, the NW jet bends to the N approximately 18 kpc from the core. The jet continues to the N for 8 kpc until the surface brightness increases and the jet appears to end abruptly with an edge brightened hotspot. The jet re-emerges from this hotspot with a lower surface brightness, and propagates to the E for 19 kpc where it enters the southern edge of an apparent loop in the jet. This loop has a semi-major axis of about 5 kpc. There is no visible exit point within the loop structure, although diffuse emission is observed to the S. The emission is likely to complete one, perhaps two loops before entering a plume in a direction parallel to the main jet. This structure provides evidence for a helical trajectory. The swirl coincides with an X-ray cavity (Worrall and

Birkinshaw, 2014), so it is possible that the swirl was produced due to a collision with the radio plasma from NGC 7018, or in the wake of its motion.

The total flux density of NGC 7016 is found to be 4.31 Jy at 1.39 GHz, corresponding to a power of $10^{24.9}$ W Hz^{-1}, slightly below the transition power between FR I and FR II-type sources, and almost as bright as NGC 7018.

Polarisation observations show the fractional polarisation and magnetic field structure in the two sources to exhibit many of the characteristics found in other radio sources. These include edge brightening of the fractional polarisation and alignment of the magnetic field with the edges of the sources produced by shearing of the field at the boundaries of the sources. A fractional polarisation map is given in Figure 6.4; the peak fractional polarisation is observed to be 58% (E of the NE lobe in NGC 7018), comparable to peak values found in other sources (Bridle and Perley, 1984) and close to the theoretical maximum for a source with a uniform magnetic field (Pacholczyk, 1970). A high fractional polarisation is also found to the N of the swirl component, as it bends towards the W.

Cameron (1988) found only slight evidence for internal depolarisation in the sources, but stronger evidence for depolarisation due to unresolved foreground Faraday rotation. I looked at the rotation measure structure within the two sources and found a significantly higher RM in the N lobe (up to 150 rad m^{-2}) of NGC 7018 than in the S lobe (up to 50 rad m^{-2}). In NGC 7016 the emission is fainter and therefore the RM structure obtained is less reliable. This map is given in Figure 6.5. I find an RM of about 20 rad m^{-2} along both of the inner jets. The RM within the source peaks at 85 rad m^{-2}, at the position of the bright hotspot W of the swirl feature.

The depolarisation structure within NGC 7018 does not follow the pattern expected for AGN jets, where the lobe containing the brighter jet is almost always less depolarised than the lobe on the counter-jet side (Laing, 1988; Garrington et al., 1988). Bicknell et al. (1990) suggest that the range in amplitude of the RM structure found in each lobe of NGC 7018 is an indication of Kelvin Helmholtz instabilities of various scales in the boundary between the radio lobes and the surrounding medium. The lack of large RM structure in NGC 7016 compared to NGC 7018 then indicates that the jets of the FR I-type source lack the large-scale K-H instabilities exhibited by the FR II-type sources, a possible result of the different physical processes governing the propagation of FR I and FR II-type jets.

The centre of cluster A 3744 lies between the two radio galaxies, and one core radius from the centre encompasses the W tail of NGC 7018 and the northern half of NGC 7016. Cameron (1988) suggest that the central ICM may be responsible for RM fluctuations

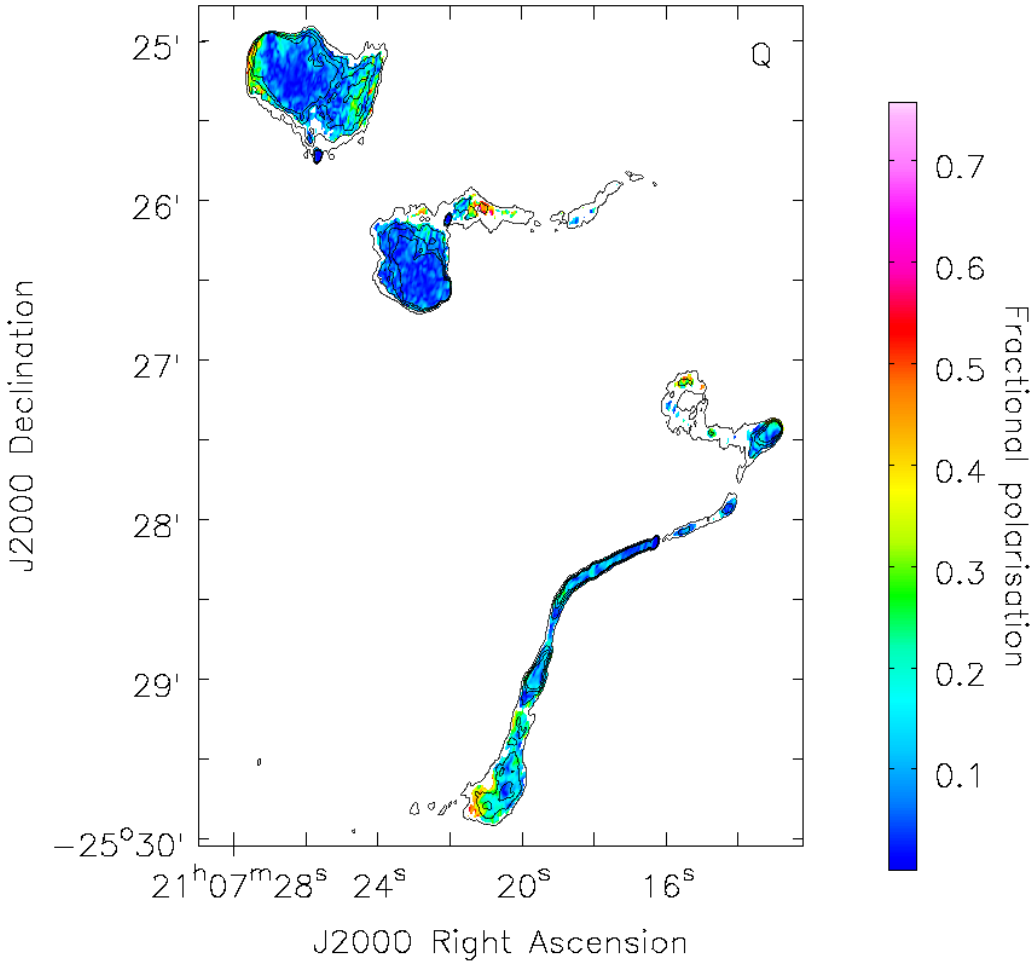

Figure 6.4: Fractional polarisation at 1.39 GHz within the radio sources NGC 7018 and NGC 7016, shown with total intensity contours at 2, 4, 8, and 16 mJy beam^{-1}.

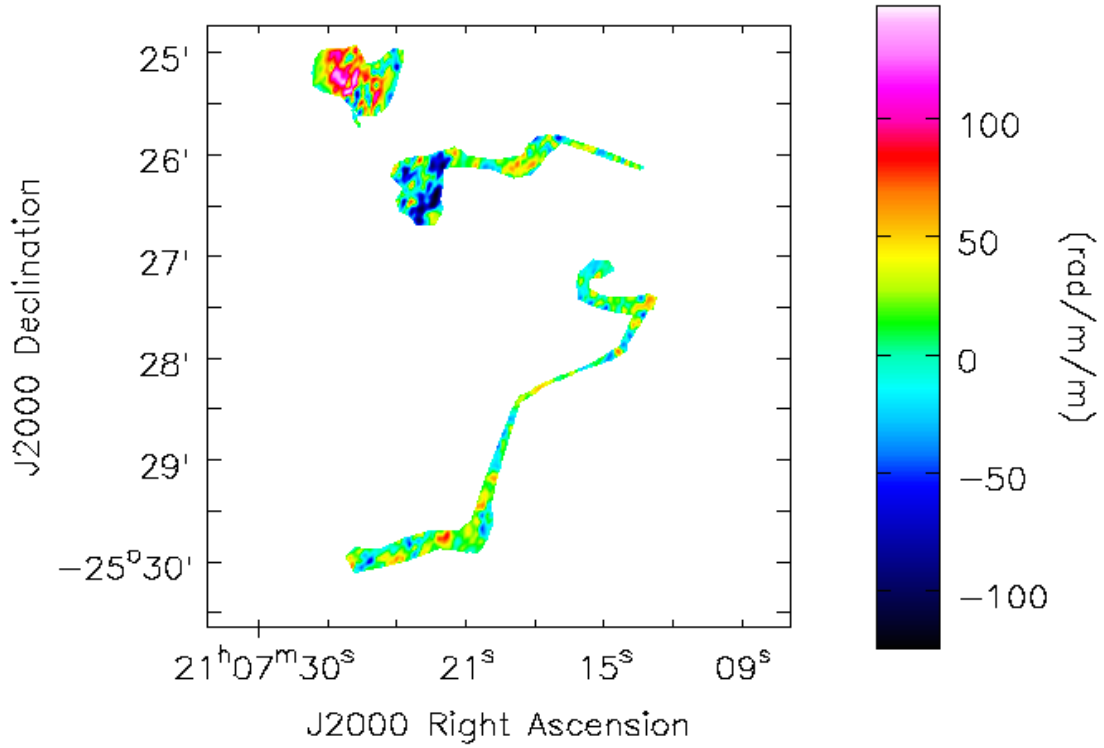

Figure 6.5: Rotation measure structure at 1.39 GHz within the radio sources NGC 7018 and NGC 7016

observed in these regions. The minimum pressure within the tails of NGC 7018 is found (Cameron, 1988) to be smaller than the expected ICM pressure for a given position. Entrainment of thermal material into the tails will reduce the pressure contrast, but there is evidence for buoyancy in the tails, so that the tails are lighter than the ICM. The tails may be pressure confined by the ICM which, when combined with buoyant acceleration of the tails by the pressure gradient in the ICM, may account for their jet-like appearance.

The outer regions of both NGC 7016 and NGC 7018 show an overall alignment of the magnetic field vectors in the direction of elongation of features in the sources, as found in the diffuse outer regions of other large sources (e.g. Miley et al., 1975). The field lines along the tails in NGC 7018 are aligned along the jet flow, evidence for flow along the tails away from the lobes, in which alignment of the magnetic field is reduced by strong turbulence-induced shear in the tails (Bicknell, 1984). The magnetic field vectors in the lobes are circumferential around the outer edges, as seen in other FRII sources (e.g. Cygnus A, Dreher et al., 1987). This circumferential field is produced by effects such as shearing of the field into a direction tangential to the lobe boundary, compression of the lobe by the ICM and backflow (Blandford and Rees, 1978).

Figure 6.6 shows that the swirl is clearly defined by the B vectors, which are aligned around the loop. In the bright hotspot W of the swirl, the magnetic field is radial and the RM is higher than the rest of the jet, suggesting that shocks or compression of the jet may be responsible for the observed brightness. Alternatively, this bright hotspot could be a very tight swirl, produced as a result of a collision with magnetised plasma (possibly a radio trail associated with NGC 7018). The swirl to the W would then be a secondary swirl with a larger radius.

6.2.1 A comparison with NGC 6109

Both NGC 6109 and NGC 7016 show evidence for helical jet motion in the form of 'swirls' projected onto the sky. The structures are thought to do at most two complete loops before culminating in diffuse emission, barely detectable in L band maps. Despite showing a similar overall swirl morphology, the intensity distribution, magnetic field and rotation measure structure within these components are noticeably different. Additionally, NGC 7016 and NGC 6109 are located in significantly different environments, thus it is interesting to note that a similar loop-like structure can be produced for sources in the centre of both rich and poor clusters. Both sources are classified as FR I-type jets; however the luminosity of NGC 7016 is significantly larger than that of NGC 6109.

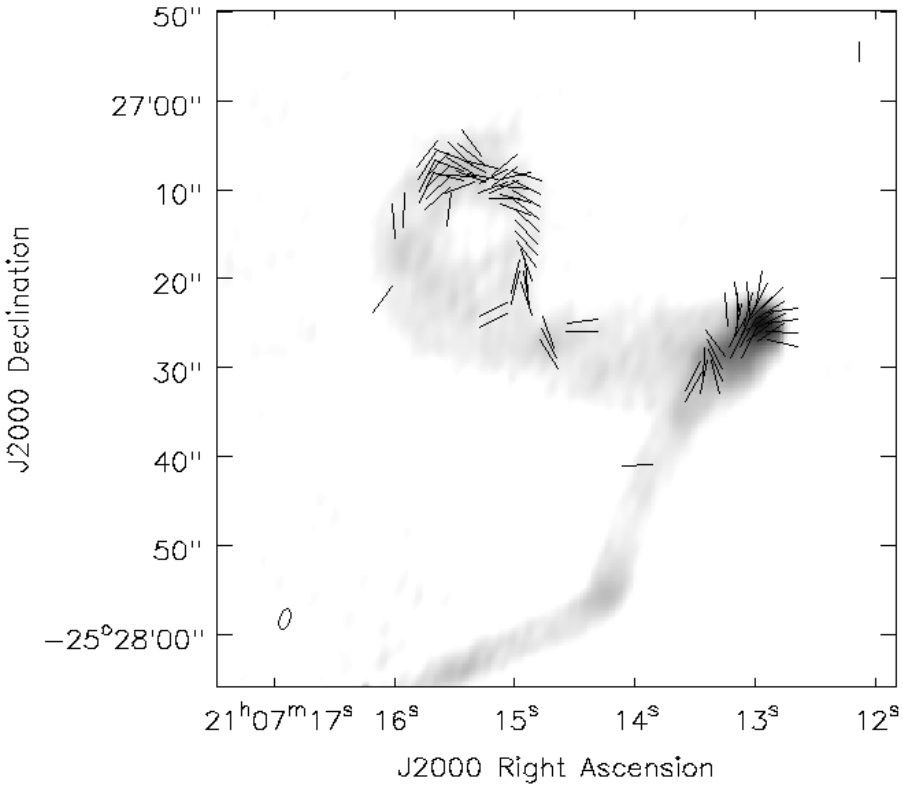

Figure 6.6: Magnetic field direction within the swirl feature of NGC 7016, shows with a grey-scale total intensity image at 1.39 GHz.

In NGC 7016, the counter-jet undergoes a series of bends before the swirl component is produced. The jet appears to stall at an edge brightened hotspot, before turning through 90° and entering the swirl of emission. The complex source morphology suggests an interaction with the cluster atmosphere, and the swirl feature lies within or at the edge of an X-ray cavity (Worrall and Birkinshaw, 2014) where the extended radio emission from NGC 7018 and NGC 7016 are thought to overlap. Measurements of the sound speed within the local X-ray gas suggest that radio plasma should have been developing and filling the cavity for at least 10^8 years to produce the observed structure, and this is comparable with the crossing time for NGC 7018 at a speed characteristic of the cluster velocity dispersion. It is likely therefore that NGC 7018 is responsible for carving out the cavity, and that the swirl observed in NGC 7016 results from an interaction with a wake left by the motion, or with a trail of radio plasma from NGC 7018. Jet bending for the S jet in NGC 7016 also supports the interpretation that the source is being shaped and pushed around by the cluster atmosphere.

The observation of a second radio source displaying a swirl of emission as a possible result of a collision with old radio plasma from a passing galaxy, supports the hypothesis presented for NGC 6109 that the doughnut component is interacting with magnetised gas from a radio trail. The edge brightened hotspot in NGC 7016 could be evidence for the collision site, with the flux increase a result of shocks where the radio plasma is compressed against some external medium. The jet then decelerates significantly, and is swept about by ICM winds. Both sources show a lack of X-ray emission in the swirl regions, indicating that a low density ICM offers less resistance (e.g. viscosity) to extreme states of motion.

In both radio galaxies, an increase in flux is observed at the most extreme point of the bend (i.e. the SW edge of the doughnut in NGC 6109 and the N edge of the swirl in NGC 6109). Flux variations can be caused by shocks propagating through the jet as it deflects against the external medium, or Doppler effects if part of the flow is still moderately relativistic. The swirl in NGC 7016 is larger in size than that in NGC 6109, with a projected radius of 8.12 kpc and the total flux enclosed within the loop is found to be 0.56 Jy at 1.39 GHz. The fractional polarisation around the edges of both components reaches as high as 56%. In NGC 7016 the polarisation maximum coincides with the highest flux regions, unlike NGC 6109 where the high flux regions are associated with strong rotation measures. Interestingly, where the radio emission is thought to slow down and emerge from the swirl as diffuse emission in NGC 7016, the fractional polarisation remains low,

at approximately 15%. In NGC 6109 however, the diffuse emission is associated with a high level of fractional polarisation, up to 56%. No significant RM is found within the swirl region in NGC 7016, although the bright hotspot to the W shows a high RM.

The lack of other sources showing these extreme jet loops means that NGC 6109 and NGC 7016 must share some common characteristics. If the swirls are simply the result of an interaction between nearby galaxies, then why have more not been observed? If FR I-type jets are capable of producing these loops as a result of interactions with magnetised media, then why did the jet in NGC 7385 not loop around, after it collided with the optical gas cloud? Having a sample of just a few low power radio galaxies makes it difficult to answer these questions. In the next section, I will look at the potential for new distorted source features to be observed, and address why these sources are important to understanding and interpreting the evolution of galaxies.

6.3 The Potential For More 180° Jet Bends

The 3CRR catalogue (Laing et al., 1983) is a second revision to the 3C catalogue published by the University of Cambridge (Edge et al., 1959) as an astronomical catalogue of celestial radio sources detected at originally 159 MHz, and subsequently 178 MHz. The 3CRR catalogue includes all galaxies not originally detected but meet the flux and declination limits. All sources are detected in the Northern Hemisphere with 178 MHz flux density $>$ 10.9 Jy, have a declination $\delta > 10^{\circ}$ and a Galactic latitude b, -10° $< b <$10°. The nearest 85 radio galaxies in this catalogue are presented by Leahy et al. (1996) in their 'Atlas of DRAGN's', found at *www.jb.man.ac.uk/atlas*. This atlas shows the extended morphology of all 85 radio galaxies and provides information about the source properties. I used this atlas to examine the morphology of all the sources listed alongside NGC 7385 and NGC 6109, in order to see whether any other sources show evidence for strong jet bending. Details of the FR I-type sources within the 3CRR catalogue is given in Table 6.2. This table gives the redshift of the source, the morphology, and whether it is listed as a DRAGN. The emission from source 3C 231 is due to a starburst, and the other source not listed as a DRAGN, 3C 380 is a compact steep spectrum source with a high redshift.

NGC 7385 and NGC 6109 are both low power FR I-type jets with an apparent 'head-tail' morphology. This means that they have been observed to display only one significant jet, either because twin jets are not clearly resolved, or because one jet is quickly

destroyed. It may be however, that some sources classified as displaying a head-tail structure may contain two jets, one of which has turned through 180° and is directed back along the same direction as the main jet. This is the case for NGC 7385, and the doughnut component in NGC 6109 was previously missed because it is small compared to the extended jet tail thus is not seen at low resolution. FR I-type sources have lower velocities than FR-II type sources, thus their jets are more susceptible to being pushed around by external media. Both QSO 0800+608 and MRC B1221-423 (described above) however, are powerful radio sources thus the jet dynamics required for large scale bending cannot be limited to low-power, low-velocity sources alone.

Within the 3CRR sample, only 3 radio galaxies have been classified as head-tail galaxies. These are NGC 7385, NGC 6109, and 3C 264. High resolution images of 3C 264 have been examined (Baum et al., 1997; Lara et al., 1997) and show no evidence for a counter-jet component. The fact that 2 out of 3 of the head-tail galaxies within the 84 nearest 3CRR sources display $\geq$180° jet deflections implies that they may be more common that we realise.

The 3CRR catalogue only covers the Northern Hemisphere for sources with a declination greater than 10°. The Molonglo Southern 4 Jy sample (MS4) was compiled by Burgess and Hunstead (2006) in order to provide an equivalent survey of the Southern sky for comparison with the well-studied 3CRR sample. A selection frequency of 408 MHz (as opposed to 178 MHz used for 3CRR) was used to allow sources to be selected from the Molonglo Reference Catalogue (MRC; Large et al., 1981). The selection criteria for the sample required a declination -85° $< \delta <$ -30°, a flux density $>$ 4.0 Jy and a galactic latitude $|b| > 10°$. Galactic sources and sources within the Magellanic Cloud regions were also excluded. 228 sources were obtained for the sample, and more than 90% of the MS4 sample had been optically identified, either with the UK Schmidt Southern Sky Survey or on R-band CCD images made with the Anglo-Australian Telescope. A subsample of 137 sources, the SMS4, was defined to have $S_{178\mathrm{MHz}} > 10.9$ Jy, making it a southern equivalent of the northern 3CRR sample. These sources were imaged at 5 GHz at 2-4″ resolution with the Australian Telescope Compact Array, and in general the sample was found to have mostly properties consistent with those in 3CRR. The source density and angular sizes with the SMS4 however, were found to be slightly higher than 3CRR.

Within the 3CRR sample, 28 sources are classified as FR I-type objects. This corresponds to 16.3% of the overall sample and only 1.7% of the sample are unclassified. In the MS4 sample, 34 FR I-type sources are identified, corresponding to 14% of the overall

Source	redshift z	DRAGN?	Morphology
3C 31	0.0173	yes	TTJ
3C 66B	0.0215	yes	TTJ
3C 76.1*	0.0324	yes	BTJ
3C 83.1B	0.0179	yes	NAT
3C 84	0.0179	yes	RD
3C 231	0.0013	no	-
3C 264	0.0214	yes	HT
3C 272.1	0.004	yes	BTJ
A 1552	0.0843	yes	TTJ
3C 274	0.004	yes	RD
3C 288	0.246	yes	-
3C 293	0.04503	yes	CD
3C 296	0.0237	yes	BTJ
3C 305*	0.0410	yes	PD
3C 310*	0.0540	yes	RD
3C 314.1	0.1197	yes	RD
3C 315	0.01083	yes	RD
NGC 6109	0.0301	yes	HT
3C 338*	0.0299	yes	RDp
NGC 6251*	0.024	yes	-
3C 346	0.161	yes	CD
3C 380	0.691	no	CSS
3C 386	0.0170	yes	RD
3C 442A*	0.0263	yes	RDp
3C 449	0.0171	yes	TTJ
NGC 7385	0.025	yes	HT
3C 465*	0.0313	yes	WAT

Table 6.2: FRI-type sources in the 3CRR catalogue. Morphologies correspond to : TTJ - twin tailed jet; BTJ - bridged tail jet; NAT - narrow angle tail; RD - relaxed double (p - peculiar); HT - head tail; CD - compact double; CSS - compact steep spectrum. Sources listed with * have been re-classified by Birkinshaw et al (in prep) as FRI/FRII boundary sources (see chapter 1 for details).

sample, with 22.8% of objects unclassified. In the SMS4 sample, 16.1% of sources (22 in total) are classified as FRI-type objects, with 17.5% of the total sources unclassified in jet morphology. These statistics suggest that a few of the sources in the Southern sky should exhibit structures similar to those of NGC 7385 and NGC 6109.

Several of the radio sources listed in the SMS4 catalogue have been studied in depth (e.g. Fornax A, McKinley et al., 2015; Cen A, O'Sullivan et al., 2013). The radio source B1221-423 discussed in section 6.1 formed part of the SMS4 sample, thus we know that interesting jet morphologies are contained within the sources. The sample has not however, been analysed in as much depth as the 3CRR catalogue, and many sources remain to be thoroughly investigated.

Whilst these surveys have revealed the complexity of the radio source sky, the samples are limited to a small number of sources and are susceptible to observational bias effects such as beaming. The Murchison Widefield Array (MWA, Tingay et al., 2013; Ord et al., 2015) is located in Western Australia at the Murchison Radio-Astronomy Observatory. The low observing frequency of the MWA means that non-thermal sources will be very bright, and Faraday rotation and depolarisation will be strong. One of the key science goals of the MWA is the new GaLactic and Extragalactic All-sky MWA Survey (GLEAM, Wayth et al., 2015) covering the frequency range 72 - 231 MHz; this survey allows identification of a complete sample of a large number of bright extragalactic radio sources selected at 151 MHz. The flux density limit of 4 Jy means that this sample is significantly larger than 3CRR and MS4. The GLEAM survey covers the sky in the declination range -80° $< \delta <$25° and the survey catalogue is constructed from a series of 120 s drift scan observations, each set covering a 30.72 MHz-wide instantaneous frequency band between 72-231 MHz. Hurley-Walker et al. (2017) published the catalogue after the first year of observations, containing 307,456 radio sources with 20 separate flux density measurements across the observing frequency band. The $>$ 4 Jy subset of this catalogue will significantly augment the information obtained from 3CRR, and work is ongoing to cross-match the source sample with SUMSS (Bock et al., 1999) and NVSS surveys (Condon and Kaplan, 1998) to derive robust positions for the origin of the radio emission (Jackson et al., 2016). The wide fractional bandwidth and high sensitivity of the GLEAM survey is a significant step forward in the mapping of the radio sky, and will produce maps of both compact and large diffuse radio sources. As a result of this, sources such as NGC 7385 and NGC 6109 may become a much more common occurrence and we may be able to see other remarkable shapes in the radio sky.

Bent-tailed radio sources are often used as probes to locate high density environments (Mao et al., 2010; Wing and Blanton, 2011) and to study the local magnetic field within these regions. The curved structure of these sources is usually attributed to ram pressure due to the relative movement of the host galaxy within the ICM. The coexistence of bent tailed sources and clusters at redshift $z < 0.1$ is at a rate of 1-2 per cluster (Mao et al., 2009) and there is growing evidence that such associations carry on as far as $z = 2$, at the limit of cluster detection (Dehghan and Johnston-Hollitt, 2014). This correlation between bent tailed radio sources and galaxy clusters presents a powerful tool to investigate the physical characteristics of rich environments. A main observational goal of the SKA is to detect these bent tailed sources in large quantities in order to investigate the dynamical state of clusters and probe conditions within the local environment.

Phase 1 of the SKA (SKA1: Norris et al., 2013) plans to undertake a series of tiered surveys with increasing sensitivity over smaller and smaller areas of the sky. Dehghan et al. (2014) evaluated the ability of SKA1 surveys to identify bent tailed radio sources by investigating the 4 deg^{2}area of the Australia Telescope Large Area Survey of the Chandra Deep Field-South field (ATLAS-CDFS) and out of 3000 radio sources in the field, 45 bent tailed sources were identified. Extrapolating these detections to the 1.4 GHz continuum surveys to be undertaken on pathfinder instruments such as the EMU survey on ASKAP (Norris et al., 2011), should see the detection of at least 470,000 bent tailed radio galaxies. The SKA1 level surveys are expected to double this number, giving of order 1 million bent tailed radio sources.

The structure of NGC 7385 and NGC 6109 have been shown in this thesis to be noticeably altered by deviations in the density of the external medium, whether that be by a large optical gas cloud or the presence of some unknown magnetised media. Other bent tailed galaxies have provided evidence for cluster winds and mergers (e.g. Pratley et al., 2013; Dehghan and Johnston-Hollitt, 2014), shedding light on the dynamics within the parent cluster. Importantly however, all studies on these sources have focused only on individual objects, and statistical studies have yet to be carried out. It is hoped that the wealth of information to be obtained by bent tailed sources will be uncovered by the SKA surveys, and that models of different environmental effects will be able to simulate both the most common bent tailed shapes and the extreme jet bends that we see in NGC 7385 and NGC 6109.

Chapter 7

Conclusions

In this thesis, I have examined the morphology and polarisation structure of radio galaxies which show evidence for large jet bends on a kpc scale. I have complemented the radio data with optical and X-ray observations in order to investigate the properties of the external environment and interpret the jet structure. I now review the key findings of this work, together with concluding remarks on the three main aims that I set out in the introductory chapter. I finish by suggesting further work that could be carried out to advance this field of research.

In chapter 2, I outlined the synthesis imaging techniques I used to calibrate and image radio datasets from the VLA. These techniques were used to create maps of the total intensity, polarisation and rotation measure structure within radio galaxies that show unusual jet distortions. An overview of these sources is given in chapter 3, before new observations were presented in chapters 4, 5 and 6.

7.0.1 NGC 7385

Observations of the low-power FR I-type radio galaxy NGC 7385 are given in chapter 4. I have presented results from new JVLA observations, together with optical and X-ray data from HST and *Chandra* in order to produce a multi-wavelength picture of the local environment of the radio source. My key findings are presented below.

1. Emission from the brighter radio jet is visible at optical and X-ray wavelengths. The optical jet has a projected length of 5 kpc and a similar morphology to other known optical jets in low-power radio galaxies. The shape of the radio to X-ray electron spectrum along the jet is consistent with synchrotron radiation, with a low magnetic field strength ~ 2 nT. NGC 7385 can now be placed on the short list of radio sources

with synchrotron jets detected in both the optical and X-ray, in the hope that more extensive investigations (such as optical polarimetry) could reveal the sites for particle reacceleration along these jets.

2. The radio counter-jet shows evidence for 180° bending on a kpc scale. This NW jet is detected up to 15 kpc from the core, at which point it bends towards the W and then towards the SW, as evident by a broadening of the radio structure on large scales. The jet then crosses the main SW jet and emerges S of the core as a plume. I used both archival VLA and new JVLA observations to map the intensity distribution, spectral index and magnetic field structure at the site of the bend.

3. I used HST data to reveal the presence of a large gas cloud, coincident with the counter-jet component. I investigated the magnetic field and rotation measure structure in this region with radio observations in order to determine whether the jet deflection described above is the consequence of a jet-cloud interaction. I found strong rotation measures coinciding with the position of the optical object, providing evidence for the cloud being at the very least, in front of the radio lobe. I discussed the origin of the cloud and suggest that it is most likely to be gas local to the host galaxy. I reviewed the possible processes which could contribute to the ionisation of the optical gas cloud, and find it unlikely that the gas has been photoionised by a population of young stars, as is found to be the case for other similar jet-cloud interactions. I estimated the magnetic field in the interacting region, and suggest that the field lies in a mixing layer produced as a consequence of entrainment of the cloud by the boundary layers of the jet.

7.0.2 NGC 6109

Observations of the radio galaxy NGC 6109 also show evidence for large scale jet bends, and in this case the jet rotates through $> 180°$. Multi-wavelength observations show no evidence for optical or X-ray features, thus the jet rotation cannot be explained in terms of a jet-cloud interaction similar to NGC 7385. My key findings are:

1. A remarkable jet structure is observed S of the radio core. I discuss the various mechanisms that can produce this helical jet structure and conclude that both helical jet

precession and a helically bent jet are viable possibilities. The almost perfectly circular appearance of the counter-jet component supports the former, whereas the latter is suggested by the presence of rotation measure structure along the bottom of the component.

2. Rotation measure structure is detected along the S edge of the helical feature, suggesting that some external magnetised gas is interacting with the jet plasma. I found no evidence in *Spitzer*, CFHT or KPNO optical observations for any features coincident with the radio emission. *Chandra* X-ray observations also show no significant structure beyond the core.

3. I carried out ballistic simulations to prove that the observed structure can be reproduced by a precessing jet and discuss the various mechanisms that can cause precession. I conclude that although jet precession on a kpc scale is a viable mechanism for the observed radio morphology, a helically bent jet due to an interaction with magnetised plasma is the most plausible explanation.

In chapter 7, I present VLA images of the radio galaxy NGC 7016, which show a similar swirl-like feature to NGC 6109. I conclude that the swirl structure is likely to have been produced by an interaction with radio plasma from the nearby FR II-type galaxy NGC 7018. Although both bent components show a similar morphology, the polarisation and rotation measure structure is found to be different.

The maps of NGC 7385 and NGC 6109 within this thesis make use of new JVLA observations. These observations successfully allowed sensitive, high resolution images of the total intensity, polarised intensity and the rotation measure to be produced, one of the main goals of this work. The rotation measure synthesis techniques I used allowed me to investigate interactions between the jets and the external environment, which when complemented by optical and X-ray observations, helped me to create a detailed profile of the conditions within the host environment. I conclude that it is likely that the jet bends within both these sources are produced as a result of a collision with magnetised plasma and that such extreme distortions should be observable in other low-power radio galaxies as sample sizes increase.

7.1 Future work

Further observations will help to constrain the jet dynamics within the radio sources studied in this thesis. For NGC 7385, improved optical spectroscopy of the line-emitting gas cloud could give valuable information on the chemical abundances and constrain the internal gas velocities. This would help to interpret whether the cloud is being entrained by the radio jet and probe the gas excitation mechanisms further. For NGC 6109, observations of the host galaxy with HST would provide conclusive evidence of whether there is any optical emission at the location of the doughnut component, helping to distinguish between jet precession and helical jet bending. Any magnetised radio trails that may be interacting with the doughnut component would be observable with low-frequency radio observations (e.g. LOFAR) and these data would also be able to track weak magnetic fields. In addition, VLBI observations of the inner jets of NGC 6109 would be useful in searching for further evidence of jet precession and constraining the jet/counter-jet ratio.

Most importantly however, in order to thoroughly understand and interpret these large scale jet bends in the context of the external environment, a larger sample is required. In chapter 7, I presented an overview of the 3CRR and MS4 surveys which map extragalactic radio sources in the Northern and Southern hemisphere respectively, and I outlined the future surveys which will map radio galaxies with unparalleled sensitivity and in huge numbers. These surveys will pave the way for the SKA.

7.1.1 Future instrumentation

One of the key scientific and technological pathfinder telescopes for the SKA project is the Low Frequency Array (LOFAR). LOFAR uses an array of simple omni-directional antennas instead of a large mechanical dish antenna. The electronic signals from the antennas are digitised, transported to a central digital processor and combined in software to emulate a conventional dish antenna. The array spans across Europe, consisting of over 7000 individual antenna and provides the sensitivity in observations at frequencies below 250 MHz needed to probe the physical processes in the centre of AGN. The high sensitivity and broad bandwidth of LOFAR means that a single polarimetric observation at a single IF can simultaneously provide accurate estimates of both the rotation measure and the polarisation position angle. In addition, the low observing frequency means that even weak magnetic fields can be investigated. For sources such as NGC 7385 and NGC 6109, this means that it may be possible to trace the magnetic field of the bent jets from

the core out to hundreds of kpc.

Details of the next generation radio telescopes are given in Table 7.1. The combination of the observations from these instruments should ensure a breakthrough in our understanding of the role of radio galaxies in galaxy evolution. These telescopes will be able to probe the physical conditions in the low-energy tail of outflowing plasma, and investigate both mildly relativistic and sub-relativistic components of outflows. From these observations it will be possible to explore the kinetic feedback between the radio galaxy and the ambient medium and look for further evidence for interactions. 3D Faraday tomography, made possible by the sensitivity and multichannel polarimetric capability of both LOFAR and SKA, will constrain parameters of these interactions further. In addition, SKA is expected to yield hugely improved statistics for the use of extragalactic background source rotation measures (Govoni et al., 2014), making the investigation into the rotation measure structure within strongly bent sources much more robust. The kinetic output of AGN in the form of large scale jets is thought to be a prime contributor to AGN feedback (Heinz and Grimm, 2005). The feedback from AGN strongly influences black hole growth (Di Matteo et al., 2004) and it has been shown that AGN can cause shocks and ripples in the IGM (e.g. Perseus A, Fabian et al., 2003). A combination of X-ray data and observations with LOFAR and $\mathrm{SKA_{low}}$ will create a complete picture of the dynamics and energetics of interactions between extragalactic outflows and IGM.

Telescope	Frequency range (MHz)	Number of stations	B_{max} km	Resolution arcsec	Science drivers
LOFAR	30-240	55+	600	0.4-3.4	extended outflows, feedback, relics
$MeerKAT_{low}$	580-2500	87	60	0.4-1.8	BH, extended flows, lobes
$MeerKAT_{high}$	8000-14500	87	60	0.07-0.12	outflows, lobes, BH
ASKAP	30-240	45	8	5.0-11.0	extended outflows, lobes
SKA_{low}	70-700	550	300	0.7-6.8	extended flows, lobes, relics
SKA_{mid}	700-3000	550	300	0.1-0.7	outflows, BH
SKA_{high}	3000+	550	3000	0.001-0.004	relativistic flows, BH, non-thermal continuum

Table 7.1: Future radio instrumentation and their observational details

Bibliography

Appl, S. and Camenzind, M.: 1992, A&A **256**, 354

Attridge, J. M., Roberts, D. H., and Wardle, J. F.: 1999, ApJ **518(2)**, L87

Baars, J. W. M., Genzel, R., Pauliny-Toth, I. I. K., and Witzel, A.: 1977, A&A **61**, 99

Bardeen, J. M. and Petterson, J. A.: 1975, ApJ **195**, L65

Baum, S. A., O'Dea, C. P., Giovannini, G., Cotton, W. B., de Koff, S., Feretti, L., Golombek, D., Lara, L., Macchetto, F. D., Miley, G., et al.: 1997, ApJ **483(1)**, 178

Begelman, M. C., Blandford, R. D., and Rees, M. J.: 1980, Nature **287**, 307

Begelman, M. C., Rees, M. J., and Blandford, R. D.: 1979, Nature **279**, 770

Bell, A. R.: 1978, MNRAS **182**, 443

Bell, M. R., Roberts, D. H., and Wardle, J. F. C.: 2011, ApJ **736**, 118

Bennett, A.: 1962, MmRAS **68**, 163

Berkhuijsen, E. M., Horellou, C., Krause, M., Neininger, N., Poezd, A. D., Shukurov, A., and Sokoloff, D. D.: 1997, A&A **318**, 700

Bicknell, G., Cameron, R., and Gingold, R.: 1990, ApJ **357**, 373

Bicknell, G. V.: 1984, ApJ **286**, 68

Bicknell, G. V.: 1994, *Australian Journal of Physics* **47**, 669

Bicknell, G. V.: 1995, ApJS **101**, 29

Bicknell, G. V. and Begelman, M. C.: 1996, ApJ **467**, 597

Biretta, J., Sparks, W., and Macchetto, F.: 1999, ApJ **520(2)**, 621

Biretta, J. A., Stern, C. P., and Harris, D. E.: 1991, AJ **101**, 1632

Birkinshaw, M.: 1991, *The stability of jets*, p. 278, UCP, Cambridge

Birkinshaw, M., Barthel, P., Green, P., Hines, D., Hooper, E., Lawrence, C., Smith, H., Wilkes, B., Willner, S., Worrall, D., and van Bemmel, I.: 2005, *The low-redshift 3CRR sources: missing data*, Spitzer Proposal

Birkinshaw, M. and Worrall, D.: 1993, ApJ **412**, 568

Birkinshaw, M. and Worrall, D.: 2013, *PKS B2152-699: jet deflection and boosted X-ray emission*, ATNF Proposal

Blandford, R. and Icke, V.: 1978, MNRAS **185(3)**, 527

Blandford, R. and Payne, D.: 1982, MNRAS **199(4)**, 883

Blandford, R. D. and Rees, M. J.: 1978, Phys. Scr **17(3)**, 265

Blandford, R. D. and Znajek, R. L.: 1977, MNRAS **179(3)**, 433

Blanton, E. L., Gregg, M. D., Helfand, D. J., Becker, R. H., and Leighly, K. M.: 2001, AJ **121**, 2915

Bock, D.-J., Large, M., and Sadler, E. M.: 1999, AJ **117(3)**, 1578

Böhringer, H., Chon, G., and Collins, C. A.: 2014, A&A **570**, A31

Bolton, J. G., Gardner, F. F., and Mackey, M. B.: 1964, *Australian Journal of Physics* **17**, 340

Bracewell, R.: 1986, *The fourier transform and its applications*, Vol. 5, McGraw-Hill, New York

Brentjens, M. A. and de Bruyn, A. G.: 2005, A&A **441**, 1217

Bridle, A. H.: 1982, in *Extragalactic radio sources*, pp 121–128, Springer

Bridle, A. H.: 1988, in *Active Galactic Nuclei*, pp 329–343, Springer

Bridle, A. H., Hough, D. H., Lonsdale, C. J., Burns, J. O., and Laing, R. A.: 1994, AJ **108**, 766

Bridle, A. H. and Perley, R. A.: 1984, ARA&A **22(1)**, 319

Briggs, D. S.: 1995, BAAS **27**, 1444

Brocksopp, C., Kaiser, C., Schoenmakers, A., and De Bruyn, A.: 2007, MNRAS **382(3)**, 1019

Broderick, A. E. and McKinney, J. C.: 2010, ApJ **725**, 750

Brouw, W. N.: 1971, *Ph.D. thesis*, Leiden Observatory, Leiden University

Brunetti, G., Bondi, M., Comastri, A., and Setti, G.: 2002, A&A **381(3)**, 795

Brunetti, G., Mack, K.-H., Prieto, M. A., and Varano, S.: 2003, MNRAS **345**, L40

Burbidge, G. R.: 1959, ApJ **129**, 849

Burgess, A. and Hunstead, R.: 2006, AJ **131(1)**, 100

Burn, B. J.: 1966, MNRAS **133**, 67

Burns, J. O. and Gregory, S. A.: 1982, AJ **87**, 1245

Butcher, H. R., van Breugel, W., and Miley, G. K.: 1980, ApJ **235**, 749

Camenzind, M.: 1986, A&A **162**, 32

Cameron, R. A.: 1988, *Ph.D. thesis*, Australian National University

Canalizo, G., Max, C., Whysong, D., Antonucci, R., and Dahm, S. E.: 2003, ApJ **597(2)**, 823

Canto, J. and Raga, A. C.: 1996, MNRAS **280**, 559

Capetti, A., de Ruiter, H. R., Fanti, R., Morganti, R., Parma, P., and Ulrich, M.-H.: 2000, A&A **362**, 871

Caproni, A. and Abraham, Z.: 2004, ApJ **602(2)**, 625

Caproni, A., Abraham, Z., Livio, M., and Mosquera Cuesta, H. J.: 2007, MNRAS **379**, 135

Caproni, A., Abraham, Z., and Mosquera Cuesta, H. J.: 2006a, ApJ **638**, 120

Caproni, A., Livio, M., Abraham, Z., and Mosquera Cuesta, H. J.: 2006b, ApJ **653**, 112

Caproni, A., Mosquera Cuesta, H. J., and Abraham, Z.: 2004, ApJ **616**, L99

Cedrés, B., Beckman, J. E., Bongiovanni, Á., Cepa, J., Asensio Ramos, A., Giammanco,

C., Cabrera-Lavers, A., and Alfaro, E. J.: 2013, ApJ **765**, L24

Christiansen, W., Pacholczyk, A., and Scott, J.: 1981, ApJ **251**, 518

Clark, B. G.: 1973, *Proceedings of the IEEE* **61(9)**, 1242

Clark, N., Axon, D., Tadhunter, C., Robinson, A., and O'brien, P.: 1998, ApJ **494(2)**, 546

Clarke, B.: 1980, A&A **89**, 377

Clarke, D. A., Burns, J. O., and Norman, M. L.: 1992, ApJ **395**, 444

Colla, G., Fanti, C., Fanti, R., Gioia, I., Lari, C., Lequeux, J., Lucas, R., and Ulrich, M.: 1975, A&AS **20**, 1

Collett, E.: 2005, *Field guide to polarization*, SPIE

Collin-Souffrin, S.: 1987, A&A **179**, 60

Collin-Souffrin, S. and Dumont, A.: 1990, A&A **229**, 292

Condon, J. and Kaplan, D.: 1998, A&AS **117(2)**, 361

Condon, J. and Mitchell, K.: 1984, ApJ **276**, 472

Conway, J., Cornwell, T., and Wilkinson, P.: 1990, MNRAS **246**, 490

Conway, J. and Murphy, D.: 1993, ApJ **411**, 89

Conway, J. and Wrobel, J.: 1995, ApJ **439**, 98

Cooke, B. A.: 1976, Nature **261**, 564

Cornwell, T. and Fomalont, E. B.: 1989, in *Synthesis Imaging in Radio Astronomy*, Vol. 6, p. 185

Cornwell, T., Golap, K., and Bhatnagar, S.: 2005, in *Astronomical Data Analysis Software and Systems XIV*, Vol. 347, p. 86

Cornwell, T., Voronkov, M., and Humphreys, B.: 2012, in *SPIE Optical Engineering+ Applications*, p. 85, International Society for Optics and Photonics

Crane, P., Peletier, R., Baxter, D., Sparks, W., Albrecht, R., Barbieri, C., Blades, J., Boksenberg, A., Deharveng, J., Disney, M., et al.: 1993, ApJ **402**, L37

Crane, P. C. and Napier, P. J.: 1989, in R. A. Perley, F. R. Schwab, and A. H. Bridle

(eds.), *Synthesis Imaging in Radio Astronomy*, Vol. 6 of *Astronomical Society of the Pacific Conference Series*, p. 139

Croft, S., van Breugel, W., de Vries, W., Dopita, M., Martin, C., Morganti, R., Neff, S., Oosterloo, T., Schiminovich, D., Stanford, S. A., and van Gorkom, J.: 2006, ApJ **647**, 1040

Croton, D. J.: 2006, MNRAS **369**, 1808

de Vaucouleurs, G.: 1991, *Science* **254**, 1667

De Villiers, J.-P., Staff, J., and Ouyed, R.: 2005, *ArXiv Astrophysics e-prints*

De Young, D. S.: 1981, Nature **293**, 43

De Young, D. S.: 1991, ApJ **371**, 69

Dehghan, S. and Johnston-Hollitt, M.: 2014, AJ **147(3)**, 52

Dehghan, S., Johnston-Hollitt, M., Franzen, T. M. O., Norris, R. P., and Miller, N. A.: 2014, AJ **148**, 75

Di Matteo, T., Croft, R. A. C., Springel, V., and Henrquist, L.: 2004, in T. Storchi-Bergmann, L. C. Ho, and H. R. Schmitt (eds.), *The Interplay Among Black Holes, Stars and ISM in Galactic Nuclei*, Vol. 222 of *IAU Symposium*, pp 471–476

Downey, E. and Mutel, R.: 1996, in *Astronomical Data Analysis Software and Systems V*, Vol. 101, p. 380

Dreher, J. W., Carilli, C. L., and Perley, R. A.: 1987, ApJ **316**, 611

Dulwich, F., Worrall, D. M., Birkinshaw, M., Padgett, C. A., and Perlman, E. S.: 2007, MNRAS **374**, 1216

Edge, D. O., Shakeshaft, J. R., McAdam, W. B., Baldwin, J. E., and Archer, S.: 1959, MmRAS **68**, 37

Eilek, J., Burns, J., O'Dea, C., and Owen, F.: 1984, ApJ **278**, 37

Eisenhauer, F., Perrin, G., Brandner, W., Straubmeier, C., Böhm, A., Baumeister, H., Cassaing, F., Clénet, Y., Dodds-Eden, K., Eckart, A., et al.: 2009, in *Science with the*

VLT in the ELT Era, pp 361–365, Springer

Ekers, R. D.: 1969, *Australian Journal of Physics* **6**, 3

Ekers, R. D.: 1978, A&A **69**, 253

Ekers, R. D., Wall, J. V., Shaver, P. A., Goss, W. M., Fosbury, R. A. E., Danziger, I. J., Moorwood, A. F. M., Malin, D. F., Monk, A. S., and Ekers, J. A.: 1989, MNRAS **236**, 737

Emmering, R. T., Blandford, R. D., and Shlosman, I.: 1992, ApJ **385**, 460

Erickson, W. C.: 1999, in G. B. Taylor, C. L. Carilli, and R. A. Perley (eds.), *Synthesis Imaging in Radio Astronomy II*, Vol. 180 of *Astronomical Society of the Pacific Conference Series*, p. 601

Evans, D.: 2005, *Ph.D. thesis*, University of Bristol

Evans, D., Hardcastle, M., Croston, J., Worrall, D., and Birkinshaw, M.: 2005, MNRAS **359(1)**, 363

Evans, D. A., Fong, W.-F., Hardcastle, M. J., Kraft, R. P., Lee, J. C., Worrall, D. M., Birkinshaw, M., Croston, J. H., and Muxlow, T. W.: 2008, ApJ **675(2)**, 1057

Everett, J. E.: 2003, *Ph.D. thesis*, University of Chicago

Fabian, A. C., Sanders, J. S., Allen, S. W., Crawford, C. S., Iwasawa, K., Johnstone, R. M., Schmidt, R. W., and Taylor, G. B.: 2003, MNRAS **344**, L43

Fanaroff, B. and Riley, J.: 1974, MNRAS **167(1)**, 31P

Fanidakis, N., Baugh, C., Benson, A., Bower, R., Cole, S., Done, C., and Frenk, C.: 2011, MNRAS **410(1)**, 53

Fanti, R., Lari, C., Parma, P., and Ekers, R. D.: 1981, A&A **94**, 61

Feretti, L., Fanti, R., Parma, P., Massaglia, S., Trussoni, E., and Brinkmann, W.: 1995, A&A **298**, 699

Feretti, L., Perola, G. C., and Fanti, R.: 1992, A&A **265**, 9

Ferland, G. J. and Mushotzky, R. F.: 1984, ApJ **286**, 42

Ferland, G. J. and Netzer, H.: 1983, ApJ **264**, 105

Finlay, E. A. and Jones, B. B.: 1973, *Australian Journal of Physics* **26**, 389

Fomalont, E. B. and Perley, R. A.: 1999, in G. B. Taylor, C. L. Carilli, and R. A. Perley (eds.), *Synthesis Imaging in Radio Astronomy II*, Vol. 180 of *Astronomical Society of the Pacific Conference Series*, p. 79

Fosbury, R. A. E., Morganti, R., Wilson, W., Ekers, R. D., di Serego Alighieri, S., and Tadhunter, C. N.: 1998, MNRAS **296**, 701

Freeland, E., Cardoso, R., and Wilcots, E.: 2008, ApJ **685(2)**, 858

Gabuzda, D., Christodoulou, D., Contopoulos, I., and Kazanas, D.: 2012, in *Journal of Physics: Conference Series*, Vol. 355, IOP Publishing

Gabuzda, D. C., Murray, É., and Cronin, P.: 2004, MNRAS **351(4)**, L89

Gardner, F. F. and Davies, R. D.: 1966, *Australian Journal of Physics* **19**, 441

Garrington, S. T., Leahy, J. P., Conway, R. G., and Laing, R. A.: 1988, Nature **331**, 147

Georganopoulos, M. and Kazanas, D.: 2003, ApJ **589**, L5

Gibbs, J. W.: 1899, Nature **59**, 606

Govoni, F., Johnston-Hollitt, M., Agudo, I., Akahori, T., Beck, R., Bonafede, A., Carozzi, T. D., Colafrancesco, S., Feretti, L., Ferriere, K., Gaensler, B. M., Harvey-Smith, L., Haverkorn, M., Heald, G. H., Mao, S. A., Rudnick, L., Schnitzeler, D., Scaife, A., Stil, J. M., Takahashi, K., Taylor, A. R., and Wucknitz, O.: 2014, *Cosmic Magnetism Science in the SKA1 Era*, Technical report

Gower, A. C., Gregory, P., Unruh, W., and Hutchings, J.: 1982, ApJ **262**, 478

Gower, J. F. R., Scott, P. F., and Wills, D.: 1967, MmRAS **71**, 49

Hamaker, J. P., Bregman, J. D., and Sault, R. J.: 1996, A&AS **117**, 137

Hardcastle, M., Birkinshaw, M., and Worrall, D.: 2001, MNRAS **323(2)**, L17

Hardcastle, M. and Croston, J.: 2005, MNRAS **363(2)**, 649

Hardcastle, M., Massaro, F., Harris, D., Baum, S., Bianchi, S., Chiaberge, M., Morganti,

R., O'Dea, C., and Siemiginowska, A.: 2012, MNRAS **424(3)**, 1774

Hardcastle, M., Worrall, D., Birkinshaw, M., Laing, R., and Bridle, A.: 2002, MNRAS **334(1)**, 182

Hardcastle, M. J., Alexander, P., Pooley, G. G., and Riley, J. M.: 1996, MNRAS **278**, 273

Hardcastle, M. J., Birkinshaw, M., and Worrall, D. M.: 1998, MNRAS **294**, 615

Hardcastle, M. J. and Worrall, D. M.: 1999, MNRAS **309**, 969

Hardee, P. E.: 1987, ApJ **318**, 78

Hardee, P. E.: 2000, ApJ **533(1)**, 176

Hardee, P. E.: 2003, ApJ **597**, 798

Hardee, P. E. and Clarke, D. A.: 1992, ApJ **400**, L9

Hardee, P. E., Eilek, J. A., and Owen, F. N.: 1980, ApJ **242**, 502

Hardee, P. E., Hughes, P. A., Rosen, A., and Gomez, E. A.: 2001, ApJ **555**, 744

Hawley, J. F. and Krolik, J. H.: 2006, ApJ **641(1)**, 103

Heald, G., Braun, R., and Edmonds, R.: 2009, A&A **503**, 409

Heckman, T. M., Miley, G. K., Balick, B., van Breugel, W. J. M., and Butcher, H. R.: 1982, ApJ **262**, 529

Heckman, T. M., Smith, E. P., Baum, S. A., van Breugel, W. J. M., Miley, G. K., Illingworth, G. D., Bothun, G. D., and Balick, B.: 1986, ApJ **311**, 526

Heinz, S. and Grimm, H. J.: 2005, ApJ **633**, 384

Hewitt, A. and Burbidge, G.: 1989, in *A new optical catalog of QSO (1989)*

Hill, J. M. and Longair, M. S.: 1971, MNRAS **154**, 125

Hjellming, R. and Rupen, M.: 1995, Nature **375(6531)**, 464

Hjellming, R. M. and Johnston, K. J.: 1981, ApJ **246**, L141

Högbom, J.: 1974, A&AS **15**, 417

Hogbom, J. A.: 1979, A&AS **36**, 173

Hong, X.-Y., Jiang, D., Gurvits, L., Garrett, M., Garrington, S., Schilizzi, R., Nan, R., Hirabayashi, H., Wang, W., and Nicolson, G.: 2004, A&A **417(3)**, 887

Hopkins, P. F. and Hernquist, L.: 2006, ApJS **166**, 1

Hoyle, F. and Fowler, W. A.: 1967, Nature 213(373)

Hughes, P., Aller, H., and Aller, M.: 1989, ApJ **341**, 68

Hughes, P. A., Miller, M. A., and Duncan, G. C.: 2002, ApJ **572(2)**, 713

Hurley-Walker, N., Callingham, J. R., Hancock, P. J., Franzen, T. M., Hindson, L., Kapińska, A., Morgan, J., Offringa, A. R., Wayth, R. B., Wu, C., et al.: 2017, MNRAS **464(1)**, 1146

Jackson, C., Franzen, T. O., Seymour, N., White, S., Murphy, T., Sadler, E., Callingham, J., Hunstead, R., Hughes, J., Wall, J., Bell, M., Dwarakanath, K., For, B., Gaensler, B., Hancock, P., Hindson, L., Hurley-Walker, N., Johnston-Hollitt, M., Kapinska, A., Lenc, E., McKinley, B., Morgan, J., Offringa, A., Procopio, P., Staveley-Smith, L., Wayth, R., Wu, C., and Zheng, Q.: 2016, *ArXiv e-prints*

Jackson, N., Browne, I. W. A., Shone, D. L., and Lind, K. R.: 1990, MNRAS **244**, 750

Jaffe, W.: 1977, in D. L. Jauncey (ed.), *Radio Astronomy and Cosmology*, Vol. 74 of *IAU Symposium*, p. 305

Jedrzejewski, R. I.: 1987, MNRAS **226**, 747

Johnston, H. M., Broderick, J. W., Cotter, G., Morganti, R., and Hunstead, R. W.: 2010, MNRAS **407(2)**, 721

Jones, T. and Owen, F.: 1979, ApJ **234**, 818

Kaastra, J. S. and Roos, N.: 1992, A&A **254**, 96

Katz, J.: 1997, ApJ **478(2)**, 527

Kauffmann, G. and Haehnelt, M.: 2000, MNRAS **311**, 576

Khachikian, E. Y. and Weedman, D. W.: 1974, ApJ **192**, 581

Kharb, P., Gabuzda, D. C., O'Dea, C. P., Shastri, P., and Baum, S. A.: 2009, ApJ **694**,

1485

Killeen, N. E. B., Bicknell, G. V., and Ekers, R. D.: 1988, ApJ **325**, 180

Klein, R. I., McKee, C. F., and Colella, P.: 1994, ApJ **420**, 213

Königl, A. and Choudhuri, A. R.: 1985, ApJ **289**, 173

Kraft, R., Birkinshaw, M., Nulsen, P., Worrall, D., Croston, J., Forman, W., Hardcastle, M., Jones, C., and Murray, S.: 2012, ApJ **749(1)**, 19

Krause, M., Alexander, P., Riley, J., and Hopton, D.: 2012, MNRAS **427**, 3196

Kroupa, P.: 2001, MNRAS **322**, 231

Lai, D.: 2003, ApJ **591(2)**, L119

Laing, R., Bridle, A., Parma, P., and Murgia, M.: 2008, MNRAS **391(2)**, 521

Laing, R. A.: 1988, Nature **331**, 149

Laing, R. A.: 1996, in R. D. Ekers, C. Fanti, and L. Padrielli (eds.), *Extragalactic Radio Sources*, Vol. 175 of *IAU Symposium*, p. 147

Laing, R. A. and Bridle, A. H.: 2014, MNRAS **437**, 3405

Laing, R. A., Riley, J. M., and Longair, M. S.: 1983, MNRAS **204**, 151

Lara, L., Alberdi, A., Marcaide, J. M., and Muxlow, T. W. B.: 1994, A&A **285**, 393

Lara, L., Cotton, W., Feretti, L., Giovannini, G., Venturi, T., and Marcaide, J.: 1997, ApJ **474(1)**, 179

Large, M., Mills, B., Little, A., Crawford, D., and Sutton, J.: 1981, MNRAS **194(3)**, 693

Lauer, T. R., Tremaine, S., Ajhar, E. A., Bender, R., Dressler, A., Faber, S., Gebhardt, K., Grillmair, C. J., Kormendy, J., and Richstone, D.: 1996, ApJ **471(2)**, L79

Law, C. J., Gaensler, B. M., Bower, G. C., Backer, D. C., Bauermeister, A., Croft, S., Forster, R., Gutierrez-Kraybill, C., Harvey-Smith, L., Heiles, C., Hull, C., Keating, G., MacMahon, D., Whysong, D., Williams, P. K. G., and Wright, M.: 2011, ApJ **728**, 57

Leahy, J. P., Bridle, A. H., and Strom, R. G.: 1996, in R. D. Ekers, C. Fanti, and L. Padrielli (eds.), *Extragalactic Radio Sources*, Vol. 175 of *IAU Symposium*, p. 157

Leahy, J. P. and Perley, R. A.: 1991, AJ **102**, 537

Leahy, J. P., Pooley, G. G., and Jagers, W. J.: 1986, A&A **156**, 234

Leahy, J. P. and Williams, A. G.: 1984, MNRAS **210**, 929

Ledlow, M. J. and Owen, F. N.: 1996, AJ **112**, 9

Lehto, H. J. and Valtonen, M. J.: 1996, ApJ **460**, 207

Lense, J. and Thirring, H.: 1918, *Physikalische Zeitschrift* 19

Linfield, R.: 1981, ApJ **250**, 464

Lipunov, V. M.: 1980, AZh **57**, 1253

Liu, S. and Melia, F.: 2002, ApJ **573(1)**, L23

Longair, M. S.: 2011, *High Energy Astrophysics*, Cambridge Univ Press

López, J., Meaburn, J., and Palmer, J.: 1993, ApJ **415**, L135

Lyutikov, M.: 2006, MNRAS **373**, 73

Lyutikov, M., Pariev, V. I., and Gabuzda, D. C.: 2005, MNRAS **360(3)**, 869

Madrid, J. P., Chiaberge, M., Floyd, D., Sparks, W. B., Macchetto, D., Miley, G. K., Axon, D., Capetti, A., O'Dea, C. P., Baum, S., Perlman, E., and Quillen, A.: 2006, ApJS **164**, 307

Maloney, P. R., Begelman, M. C., and Pringle, J.: 1996, ApJ **472(2)**, 582

Mannering, E.: 2013, *Ph.D. thesis*, University of Bristol

Mannering, E., Worrall, D. M., and Birkinshaw, M.: 2013, MNRAS **431(1)**, 858

Mao, M. Y., Johnston-Hollitt, M., Stevens, J. B., and Wotherspoon, S. J.: 2009, MNRAS **392(3)**, 1070

Mao, M. Y., Sharp, R., Saikia, D., Norris, R. P., Johnston-Hollitt, M., Middelberg, E., and Lovell, J. E.: 2010, MNRAS **406(4)**, 2578

Marshall, H. L., Heinz, S., and Schulz, N. S.: 2014, in *American Astronomical Society Meeting Abstracts*, Vol. 223, p. 323.07

Martel, A. R., Sparks, W. B., Macchetto, D., Biretta, J. A., Baum, S. A., Golombek, D.,

McCarthy, P. J., de Koff, S., and Miley, G. K.: 1998, ApJ **496(1)**, 203

Mazure, A., Katgert, P., den Hartog, R., Biviano, A., Dubath, P., Escalera, E., Focardi, P., Gerbal, D., Giuricin, G., Jones, B., Le Fevre, O., Moles, M., Perea, J., and Rhee, G.: 1996, A&A **310**, 31

McBride, J. and McCourt, M.: 2014, MNRAS **442(1)**, 838

McKinley, B., Yang, R., López-Caniego, M., Briggs, F., Hurley-Walker, N., Wayth, R. B., Offringa, A. R., Crocker, R., Bernardi, G., Procopio, P., Gaensler, B. M., Tingay, S. J., Johnston-Hollitt, M., McDonald, M., Bell, M., Bhat, N. D. R., Bowman, J. D., Cappallo, R. J., Corey, B. E., Deshpande, A. A., Emrich, D., Ewall-Wice, A., Feng, L., Goeke, R., Greenhill, L. J., Hazelton, B. J., Hewitt, J. N., Hindson, L., Jacobs, D., Kaplan, D. L., Kasper, J. C., Kratzenberg, E., Kudryavtseva, N., Lenc, E., Lonsdale, C. J., Lynch, M. J., McWhirter, S. R., Mitchell, D. A., Morales, M. F., Morgan, E., Oberoi, D., Ord, S. M., Pindor, B., Prabu, T., Riding, J., Rogers, A. E. E., Roshi, D. A., Udaya Shankar, N., Srivani, K. S., Subrahmanyan, R., Waterson, M., Webster, R. L., Whitney, A. R., Williams, A., and Williams, C. L.: 2015, MNRAS **446**, 3478

McKinney, J. C.: 2006, MNRAS **368(4)**, 1561

McKinney, J. C. and Blandford, R. D.: 2009, MNRAS **394(1)**, L126

Middelberg, E. and Bach, U.: 2008, *Reports on Progress in Physics* **71(6)**, 066901

Migliori, G., Grandi, P., Palumbo, G. G., Brunetti, G., and Stanghellini, C.: 2007, ApJ **668(1)**, 203

Miley, G., van der Laan, H., and Wellington, K.: 1975, A&A **38**, 381

Miley, G. K., Perola, G. C., van der Kruit, P. C., and van der Laan, H.: 1972, Nature **237**, 269

Miller, N. A., Owen, F. N., Burns, J. O., Ledlow, M. J., and Voges, W.: 1999, AJ **118**, 1988

Mills, B. Y., Little, A. G., and Joss, G. H.: 1976, *Australian Journal of Physics* **3**, 33

Mills, B. Y., Slee, O. B., and Hill, E. R.: 1960, *Australian Journal of Physics* **13**, 676

Murray, N. and Chiang, J.: 1997, ApJ **474(1)**, 91

Napier, P.: 1982, *National Radio Astronomy Observatory Newsletter* **6**, 2

Napier, P. J., Thompson, A. R., and Ekers, R. D.: 1983, *IEEE Proceedings* **71**, 1295

Narayan, R. and Nityananda, R.: 1986, ARA&A **24**, 127

Nelson, R. P. and Papaloizou, J. C.: 2000, MNRAS **315(3)**, 570

Nixon, C. and King, A.: 2013, ApJ **765(1)**, L7

Norris, R. P., Afonso, J., Bacon, D., Beck, R., Bell, M., Beswick, R. J., Best, P., Bhatnagar, S., Bonafede, A., Brunetti, G., Budavári, T., Cassano, R., Condon, J. J., Cress, C., Dabbech, A., Feain, I., Fender, R., Ferrari, C., Gaensler, B. M., Giovannini, G., Haverkorn, M., Heald, G., Van der Heyden, K., Hopkins, A. M., Jarvis, M., Johnston-Hollitt, M., Kothes, R., Van Langevelde, H., Lazio, J., Mao, M. Y., Martínez-Sansigre, A., Mary, D., Mcalpine, K., Middelberg, E., Murphy, E., Padovani, P., Paragi, Z., Prandoni, I., Raccanelli, A., Rigby, E., Roseboom, I. G., Röttgering, H., Sabater, J., Salvato, M., Scaife, A. M. M., Schilizzi, R., Seymour, N., Smith, D. J. B., Umana, G., Zhao, G.-B., and Zinn, P.-C.: 2013, *PASA* **30**, e020

Norris, R. P., Hopkins, A. M., Afonso, J., Brown, S., Condon, J. J., Dunne, L., Feain, I., Hollow, R., Jarvis, M., Johnston-Hollitt, M., Lenc, E., Middelberg, E., Padovani, P., Prandoni, I., Rudnick, L., Seymour, N., Umana, G., Andernach, H., Alexander, D. M., Appleton, P. N., Bacon, D., Banfield, J., Becker, W., Brown, M. J. I., Ciliegi, P., Jackson, C., Eales, S., Edge, A. C., Gaensler, B. M., Giovannini, G., Hales, C. A., Hancock, P., Huynh, M. T., Ibar, E., Ivison, R. J., Kennicutt, R., Kimball, A. E., Koekemoer, A. M., Koribalski, B. S., López-Sánchez, Á. R., Mao, M. Y., Murphy, T., Messias, H., Pimbblet, K. A., Raccanelli, A., Randall, K. E., Reiprich, T. H., Roseboom, I. G., Röttgering, H., Saikia, D. J., Sharp, R. G., Slee, O. B., Smail, I., Thompson, M. A., Urquhart, J. S., Wall, J. V., and Zhao, G.-B.: 2011, *PASA* **28**, 215

O'Dea, C. and Owen, F.: 1985, AJ **90**, 927

Offringa, A. R., de Bruyn, A. G., Biehl, M., Zaroubi, S., Bernardi, G., and Pandey, V. N.: 2010, MNRAS **405**, 155

Ogilvie, G. and Dubus, G.: 2001, MNRAS **320(4)**, 485

Ord, S. M., Crosse, B., Emrich, D., Pallot, D., Wayth, R. B., Clark, M. A., Tremblay, S. E., Arcus, W., Barnes, D., Bell, M., Bernardi, G., Bhat, N. D. R., Bowman, J. D., Briggs, F., Bunton, J. D., Cappallo, R. J., Corey, B. E., Deshpande, A. A., deSouza, L., Ewell-Wice, A., Feng, L., Goeke, R., Greenhill, L. J., Hazelton, B. J., Herne, D., Hewitt, J. N., Hindson, L., Hurley-Walker, N., Jacobs, D., Johnston-Hollitt, M., Kaplan, D. L., Kasper, J. C., Kincaid, B. B., Koenig, R., Kratzenberg, E., Kudryavtseva, N., Lenc, E., Lonsdale, C. J., Lynch, M. J., McKinley, B., McWhirter, S. R., Mitchell, D. A., Morales, M. F., Morgan, E., Oberoi, D., Offringa, A., Pathikulangara, J., Pindor, B., Prabu, T., Procopio, P., Remillard, R. A., Riding, J., Rogers, A. E. E., Roshi, A., Salah, J. E., Sault, R. J., Udaya Shankar, N., Srivani, K. S., Stevens, J., Subrahmanyan, R., Tingay, S. J., Waterson, M., Webster, R. L., Whitney, A. R., Williams, A., Williams, C. L., and Wyithe, J. S. B.: 2015, *PASA* **32**, e006

Osterbrock, D. E.: 1974, *Astrophysics of gaseous nebulae*, Freeman, San Francisco

O'Sullivan, S. P., Brown, S., Robishaw, T., Schnitzeler, D. H. F. M., McClure-Griffiths, N. M., Feain, I. J., Taylor, A. R., Gaensler, B. M., Landecker, T. L., Harvey-Smith, L., and Carretti, E.: 2012, MNRAS **421**, 3300

O'Sullivan, S. P., Feain, I. J., McClure-Griffiths, N. M., Ekers, R. D., Carretti, E., Robishaw, T., Mao, S. A., Gaensler, B. M., Bland-Hawthorn, J., and Stawarz, Ł.: 2013, ApJ **764**, 162

Owen, F. and Ledlow, M.: 1994, in *The Physics of Active Galaxies*, Vol. 54, p. 319

Owen, F. N. and Laing, R. A.: 1989, MNRAS **238(2)**, 357

Pacholczyk, A. G.: 1970, *Radio astrophysics. Nonthermal processes in galactic and*

extragalactic sources, Freeman, San Francisco

Pacholczyk, A. G. and Scott, J. S.: 1976, ApJ **210**, 311

Parma, P. and Weiler, K. W.: 1981, A&A **96**, 412

Pearson, T. and Readhead, A.: 1988, ApJ **328**, 114

Pearson, T. J. and Readhead, A. C. S.: 1984, ARA&A **22**, 97

Perley, R. A., Bridle, A. H., and Willis, A. G.: 1984, ApJS **54**, 291

Perley, R. A., Bridle, A. H., Willis, A. G., and Fomalont, E. B.: 1980, AJ **85**, 499

Perley, R. A. and Butler, B. J.: 2013, ApJS **204**, 19

Perlicki, K. and Yasin, M.: 2015, in *Advances in Optical Fiber Technology: Fundamental Optical Phenomena and Applications*

Perlman, E. S., Biretta, J. A., Zhou, F., Sparks, W. B., and Macchetto, F. D.: 1999, AJ **117**, 2185

Perlman, E. S., Padgett, C. A., Georganopoulos, M., Sparks, W. B., Biretta, J. A., O'Dea, C. P., Baum, S. A., Birkinshaw, M., Worrall, D. M., Dulwich, F., Jester, S., Martel, A., Capetti, A., and Leahy, J. P.: 2006, ApJ **651**, 735

Perlman, E. S., Padgett, C. A., Georganopoulos, M., Worrall, D. M., Kastner, J. H., Franz, G., Birkinshaw, M., Dulwich, F., O'Dea, C. P., Baum, S. A., Sparks, W. B., Biretta, J. A., Lara, L., Jester, S., and Martel, A.: 2010, ApJ **708**, 171

Perucho, M. and Martí, J.: 2007, MNRAS **382(2)**, 526

Perucho, M., Martí-Vidal, I., Lobanov, A. P., and Hardee, P. E.: 2012, A&A **545**, A65

Petterson, J.: 1977, ApJ **214**, 550

Pfeiffer, H. P. and Lai, D.: 2004, ApJ **604(2)**, 766

Phinney, E.: 1983, *Ph.D. thesis*, University of Cambridge

Pratley, L., Johnston-Hollitt, M., Dehghan, S., and Sun, M.: 2013, MNRAS p. 448

Price, R., Burns, J. O., Duric, N., and Newberry, M. V.: 1990, BAAS **22**, 881

Pringle, J. E.: 1997, MNRAS **292**, 136

Pudritz, R. E., Ouyed, R., Fendt, C., and Brandenburg, A.: 2007, *Protostars and Planets V* pp 277–294

Rand, R. J. and Lyne, A. G.: 1994, MNRAS **268**, 497

Rau, U. and Cornwell, T. J.: 2011, A&A **532**, A71

Rawes, J., Worrall, D. M., and Birkinshaw, M.: 2015, MNRAS **452**, 3064

Reid, M., Biretta, J., Junor, W., Muxlow, T., and Spencer, R.: 1989, ApJ **336**, 112

Reynaldi, V. and Feinstein, C.: 2013, MNRAS **435**, 1350

Reynolds, S. P.: 2009, ApJ **703**, 662

Roberts, D. H., Wardle, J. F., Lipnick, S. L., Selesnick, P. L., and Slutsky, S.: 2008, ApJ **676(1)**, 584

Robertson, D. S., Gubbay, J. S., and Legg, A. T.: 1973, *Australian Journal of Physics* **2**, 184

Robertson, J. G.: 1981, A&A **93**, 113

Romero, G. E., Chajet, L., Abraham, Z., and Fan, J. H.: 2000, A&A **360**, 57

Roos, N.: 1988, ApJ **334**, 95

Roos, N., Kaastra, J. S., and Hummel, C. A.: 1993, ApJ **409**, 130

Rudnick, L. and Owen, F. N.: 1976, BAAS **8**, 553

Rybicki, G. B. and Lightman, A. P.: 2008, *Radiative processes in astrophysics*, John Wiley & Sons

Ryle, M. and Windram, M. D.: 1968, MNRAS **138**, 1

Safouris, V., Hunstead, R., and Prouton, O.: 2003, *Australian Journal of Physics* **20(1)**, 1

Saikia, D. and Gupta, N.: 2003, A&A **405(2)**, 499

Saikia, D. J., Jamrozy, M., Konar, C., and Nandi, S.: 2010, in *25th Texas Symposium on Relativistic Astrophysics*, p. 14

Sanders, R. H.: 1983, ApJ **266**, 73

Sarazin, C. L.: 1988, S&T **76**, 639

Sault, R. and Wieringa, M.: 1994, A&AS 108

Sault, R. J., Hamaker, J. P., and Bregman, J. D.: 1996, A&AS **117**, 149

Scheuer, P.: 1974, MNRAS **166(3)**, 513

Scheuer, P.: 1982, in *Extragalactic radio sources*, pp 163–165, Springer

Scheuer, P. and Feiler, R.: 1996, MNRAS **282(1)**, 291

Schilizzi, R. T. and Ekers, R. D.: 1975, A&A **40**, 221

Schilizzi, R. T. and McAdam, W. B.: 1975, MmRAS **79**, 1

Schnitzeler, D. H. F. M.: 2008, *Ph.D. thesis*, Leiden University

Schwab, F.: 1984, in *Indirect Imaging. Measurement and Processing for Indirect Imaging*, Vol. 1, pp 333–346

Scott, J. S., Robertson, J. W., and Tarenghi, M.: 1977, A&A **59**, 23

Shakura, N. I. and Sunyaev, R. A.: 1973, A&A **24**, 337

Shu, F. H., Laughlin, G., Lizano, S., and Galli, D.: 2000, ApJ **535**, 190

Simkin, S. M.: 2001, in R. A. Laing and K. M. Blundell (eds.), *Particles and Fields in Radio Galaxies Conference*, Vol. 250 of *Astronomical Society of the Pacific Conference Series*, p. 467

Simkin, S. M., Bicknell, G. V., and Bosma, A.: 1984, ApJ **277**, 513

Simkin, S. M. and Ekers, R. D.: 1979, AJ **84**, 56

Simpson, C., Clements, D., Rawlings, S., and Ward, M.: 1993, MNRAS **262(4)**, 889

Sivakoff, G. R.: 2001, *MERLIN & VLA Observations of QSO 0800+ 608*, University of Manchester

Slee, O. B.: 1977, *Australian Journal of Physics Astrophysical Supplement* **43**, 1

Smith, H. E., Smith, E. O., and Spinrad, H.: 1976, PASP **88**, 621

Sokoloff, D. D., Bykov, A. A., Shukurov, A., Berkhuijsen, E. M., Beck, R., and Poezd, A. D.: 1998, MNRAS **299**, 189

Sparks, W. B., Golombek, D., Baum, S. A., Biretta, J., de Koff, S., Macchetto, F., McCarthy, P., and Miley, G. K.: 1995, ApJ **450**, L55

Steenbrugge, K. C. and Blundell, K. M.: 2008, MNRAS **388(4)**, 1457

Steffen, W.: 1997, *Vistas in Astronomy* **41(1)**, 71

Steffen, W., Zensus, J. A., Krichbaum, T. P., Witzel, A., and Qian, S. J.: 1995, A&A **302**, 335

Stirling, A. M., Spencer, R. E., Cawthorne, T. V., and Paragi, Z.: 2004, MNRAS **354**, 1239

Stocke, J. T., Burns, J. O., and Christiansen, W. A.: 1985, ApJ **299**, 799

Sun, M., Jones, C., Forman, W., Vikhlinin, A., Donahue, M., and Voit, M.: 2007, ApJ **657(1)**, 197

Sutherland, R. S., Bicknell, G. V., and Dopita, M. A.: 1993, ApJ **414**, 510

Tateyama, C., Kingham, K., Kaufmann, P., Piner, B., De Lucena, A., and Botti, L.: 1998, ApJ **500(2)**, 810

Taylor, A. R., Stil, J. M., and Sunstrum, C.: 2009, ApJ **702**, 1230

Taylor, G. B. and Zavala, R.: 2010, ApJ **722**, L183

Terquem, C. and Papaloizou, J. C. B.: 2000, A&A **360**, 1031

Thompson, A. R., Clark, B. G., Wade, C. M., and Napier, P. J.: 1980, ApJS **44**, 151

Tingay, S., Goeke, R., Bowman, J. D., Emrich, D., Ord, S., Mitchell, D. A., Morales, M. F., Booler, T., Crosse, B., Wayth, R., et al.: 2013, *Proceedings of the Astronomical Society of Australia* **30**, e007

Tomita, A., Maehara, H., Takeuchi, T. T., Nakanishi, K., Honma, M., Tutui, Y., and Sofue, Y.: 1999, PASJ **51**, 285

Ulrich, M.-H.: 1978, ApJ **221**, 422

Urry, C. M. and Padovani, P.: 1995, PASP **107(715)**, 803

van Breugel, W., Filippenko, A. V., Heckman, T., and Miley, G.: 1985a, ApJ **293**, 83

van Breugel, W., Heckman, T., and Miley, G.: 1984, ApJ **276**, 79

van Breugel, W., Miley, G., Heckman, T., Butcher, H., and Bridle, A.: 1985b, ApJ **290**, 496

van Breugel, W. J. M. and Dey, A.: 1993, ApJ **414**, 563

van Breugel, W. J. M., Heckman, T. M., Miley, G. K., and Filippenko, A. V.: 1986, ApJ **311**, 58

van der Laan, H.: 1962, MNRAS **124**, 125

Veilleux, S. and Osterbrock, D. E.: 1987, in C. J. Lonsdale Persson (ed.), *NASA Conference Publication*, Vol. 2466 of *NASA Conference Publication*

Venkatesan, T. C. A., Batuski, D. J., Hanisch, R. J., and Burns, J. O.: 1994, ApJ **436**, 67

Vicente, L., Charlot, P., and Sol, H.: 1996, A&A **312**, 727

Villar-Martin, M., Tadhunter, C., Morganti, R., Axon, D., and Koekemoer, A.: 1999, MNRAS **307(1)**, 24

Villar-Martin, M., Tadhunter, C., Morganti, R., Clark, N., Killeen, N., and Axon, D.: 1998, A&A **332**, 479

Villata, M. and Ferrari, A.: 1995, A&A 293

Villata, M., Raiteri, C., Sillanpää, A., and Takalo, L.: 1998, MNRAS **293(1)**, L13

Visnovsky, K., Impey, C. D., Foltz, C., Hewett, P., Weymann, R., and Morris, S.: 1992, ApJ **391**, 560

Vogt, C., Dolag, K., and Enßlin, T. A.: 2005, MNRAS **358(3)**, 732

Walker, R., Benson, J., Unwin, S., Lystrup, M., Hunter, T., Pilbratt, G., and Hardee, P.: 2001, ApJ **556(2)**, 756

Wall, J. V. and Cole, D. J.: 1973, *Australian Journal of Physics* **26**, 881

Wardle, J. and Kronberg, P.: 1974, ApJ **194**, 249

Wayth, R. B., Lenc, E., Bell, M. E., Callingham, J. R., Dwarakanath, K. S., Franzen,

T. M. O., For, B.-Q., Gaensler, B., Hancock, P., Hindson, L., Hurley-Walker, N., Jackson, C. A., Johnston-Hollitt, M., Kapińska, A. D., McKinley, B., Morgan, J., Offringa, A. R., Procopio, P., Staveley-Smith, L., Wu, C., Zheng, Q., Trott, C. M., Bernardi, G., Bowman, J. D., Briggs, F., Cappallo, R. J., Corey, B. E., Deshpande, A. A., Emrich, D., Goeke, R., Greenhill, L. J., Hazelton, B. J., Kaplan, D. L., Kasper, J. C., Kratzenberg, E., Lonsdale, C. J., Lynch, M. J., McWhirter, S. R., Mitchell, D. A., Morales, M. F., Morgan, E., Oberoi, D., Ord, S. M., Prabu, T., Rogers, A. E. E., Roshi, A., Shankar, N. U., Srivani, K. S., Subrahmanyan, R., Tingay, S. J., Waterson, M., Webster, R. L., Whitney, A. R., Williams, A., and Williams, C. L.: 2015, *Proceedings of the Astronomical Society of Australia* **32**, e025

Wegner, G., Colless, M., Saglia, R. P., McMahan, R. K. J., Davies, R. L., Burstein, D., and Baggley, G.: 1999, *VizieR Online Data Catalog* 730

Wilkins, D. C.: 1972, Phys. Rev. D **5**, 814

Wilkinson, P., Kus, A., Pearson, T., Readhead, A., and Cornwell, T.: 1986, in *Quasars*, Vol. 119, p. 165

Willson, M. A. G.: 1970, MNRAS **151**, 1

Wilson, T. L., Rohlfs, K., and Hüttemeister, S.: 2009, *Tools of radio astronomy*, Vol. 86, Springer

Wing, J. D. and Blanton, E. L.: 2011, AJ **141(3)**, 88

Woltjer, L.: 1959, ApJ **130**, 38

Worrall, D., Birkinshaw, M., and Cameron, R.: 1995, ApJ **449**, 93

Worrall, D., Birkinshaw, M., Laing, R., Cotton, W., and Bridle, A.: 2007, MNRAS **380(1)**, 2

Worrall, D. M.: 2009, A&A Rev. **17**, 1

Worrall, D. M. and Birkinshaw, M.: 2006, in D. Alloin (ed.), *Physics of Active Galactic Nuclei at all Scales*, Vol. 693 of *Lecture Notes in Physics, Berlin Springer Verlag*, p. 39

Worrall, D. M. and Birkinshaw, M.: 2014, ApJ **784**, 36

Worrall, D. M. and Birkinshaw, M.: 2017, *ArXiv e-prints*

Worrall, D. M., Birkinshaw, M., and Hardcastle, M. J.: 2001, MNRAS **326**, L7

Worrall, D. M., Birkinshaw, M., and Young, A. J.: 2016, MNRAS **458**, 174

Zavala, R. T. and Taylor, G. B.: 2005, ApJ **626**, L73

Zensus, J., Cohen, M., and Unwin, S.: 1995, ApJ **443**, 35

Zwicky, F., Herzog, E., Wild, P., Karpowicz, M., and Kowal, C. T.: 1961, *Catalogue of galaxies and of clusters of galaxies, Vol. I*